TU Delft

Delft University of Technology

3D Steering

Additive Manufacturing in Snake-Like Surgical Devices

Culmone, C.

DOI
10.4233/uuid:f2b07624-8a6d-41c9-b931-2423849182a7

Publication date
2022

Document Version
Final published version

Citation (APA)
Culmone, C. (2022). *3D Steering: Additive Manufacturing in Snake-Like Surgical Devices*. [Dissertation (TU Delft), Delft University of Technology]. https://doi.org/10.4233/uuid:f2b07624-8a6d-41c9-b931-2423849182a7

Important note
To cite this publication, please use the final published version (if applicable).
Please check the document version above.

Copyright
Other than for strictly personal use, it is not permitted to download, forward or distribute the text or part of it, without the consent of the author(s) and/or copyright holder(s), unless the work is under an open content license such as Creative Commons.

Takedown policy
Please contact us and provide details if you believe this document breaches copyrights.
We will remove access to the work immediately and investigate your claim.

This work is downloaded from Delft University of Technology.
For technical reasons the number of authors shown on this cover page is limited to a maximum of 10.

3D STEERING

Additive Manufacturing in Snake-Like Surgical Devices

Costanza CULMONE

Printed by: Gildeprint

Cover designed by: C. Culmone

All rights reserved. No part of this thesis may be reproduced by any means or transmitted in any form without the written permission of the author or, when appropriate, of the publisher of the publications.

Copyright © 2022 by C. Culmone

ISBN 978-94-6384-370-6

An electronic version of this dissertation is available at
http://repository.tudelft.nl/.

3D STEERING

Additive Manufacturing in Snake-Like Surgical Devices

Dissertation

for the purpose of obtaining the degree of doctor
at Delft University of Technology
by the authority of the Rector Magnificus prof.dr.ir. T.H.J.J. van der Hagen
Chair of the Board for Doctorates
to be defended publicly on Wednesday 28 September 2022 at 10:00 o'clock

by

Costanza CULMONE

Master of Science in Biomedical Engineering, University of Pisa, Italy
Born in Tolentino, Italy

This dissertation has been approved by the promotors

Composition of the doctoral committee:

Rector Magnificus,	chairperson
Prof. dr. ir. P. Breedveld	Delft University of Technology, promotor
Dr. ir. G. Smit	Delft University of Technology, copromotor
Independent members:	
Prof. dr. J. Dankelman	Delft University of Technology, The Netherlands
Prof. dr. M. van der Elst	Delft University of Technology, The Netherlands
Prof. dr. ir. R.H.M Goossens	Delft University of Technology, The Netherlands
Prof. dr. ir. J.L. Herder	Delft University of Technology, The Netherlands
Dr. ir E. van der Poorten	Katholieke Universiteit Leuven, Belgium

This work was supported by Netherlands Organization for Scientific Research (Nederlandse Organisatie voor Wetenschappelijk Onderzoek, NWO), domain Applied and Engineering Sciences (TTW), and which is partly funded by the Ministry of Economic Affairs. Grant number 12137, Bio-Inspired Maneuverable Dendritic Devices for Minimally Invasive Surgery.

Table of Contents

Summary vii

Samenvatting xi

1 Introduction 1
- 1.1 From open surgery to minimally invasive surgery . . . 2
- 1.2 Steerability and Follow-the-Leader motion . . . 4
- 1.3 Snake-like instruments . . . 4
- 1.4 Additive manufacturing . . . 6
- 1.5 Additive manufacturing in medical devices . . . 7
- 1.6 Goal of this thesis . . . 7
- 1.7 Approach and thesis outline . . . 8
- References . . . 9

Part 1 Real-Time Snake-Like Control

2 Follow-the-Leader Mechanisms in Medical Devices 15
- 2.1 Introduction . . . 17
- 2.2 Literature search methods . . . 18
  - 2.2.1 Scientific literature search . . . 18
  - 2.2.2 Patent literature search . . . 18
  - 2.2.3 Eligibility conditions . . . 18
- 2.3 Results . . . 19
  - 2.3.1 Literature search results . . . 19
  - 2.3.2 General categorizations . . . 19
  - 2.3.3 Steering of the device . . . 20
  - 2.3.4 Propagation of the device . . . 24
  - 2.3.5 Shape conservation of the device . . . 26
- 2.4 Discussion . . . 29
  - 2.4.1 Comparison of FTL device performance . . . 29
  - 2.4.2 Common steering and shape conservation strategies . . . 33
  - 2.4.3 Design combinations in FTL devices . . . 35
  - 2.4.4 Assessment of alternative solutions for FTL medical devices . . . 37
  - 2.4.5 Commercially available instruments . . . 38
  - 2.4.6 The future of FTL medical devices . . . 41
- 2.5 Conclusion . . . 42
- References . . . 42

3 Follow-the-Leader Shape Memory System for Minimally Invasive Surgery 51
3.1 Introduction . . . 53
3.2 State-of-the-art . . . 54
3.2.1 Snake-like surgical robots . . . 54
3.2.2 Mechanical shape-shifting devices . . . 55
3.3 Concept design . . . 56
3.3.1 Cable-driven FTL-propagation . . . 56
3.3.2 Memory mechanism . . . 58
3.4 Proof of concept prototype . . . 60
3.5 Functional evaluation . . . 62
3.6 Discussion . . . 63
3.6.1 MemoBox design . . . 63
3.6.2 Implementation in a surgical instrument . . . 65
3.6.3 Mechanical over mechatronics solutions . . . 66
3.7 Conclusion . . . 67
References . . . 68

Part 2 Additive Manufacturing and Compliant Solutions

4 Additive Manufacturing in Medical Instruments 75
4.1 Introduction . . . 77
4.2 Literature search methods . . . 78
4.2.1 Scientific literature research . . . 78
4.2.2 Eligibility criteria . . . 78
4.2.3 Literature search results . . . 78
4.3 Clinical application and novelty of AM devices . . . 80
4.3.1 Conventional general-purpose instruments . . . 80
4.3.2 Conventional specific-purpose instruments . . . 81
4.3.3 Unconventional general-purpose instruments . . . 82
4.3.4 Unconventional specific-purpose instruments . . . 85
4.4 Reasons for design of AM devices . . . 85
4.4.1 Customization . . . 85
4.4.2 Cost-effectiveness and disposability . . . 86
4.4.3 Accessibility . . . 86
4.4.4 Simple assembly and short production time . . . 87
4.4.5 MRI-compatibility and biocompatibility . . . 87
4.4.6 Prototyping and others . . . 88
4.5 Technology to manufacture AM devices . . . 88
4.5.1 AM technologies . . . 88
4.5.2 AM materials . . . 88
4.6 Discussion . . . 90
4.6.1 Properties and performance of AM devices . . . 90
4.6.2 Medical regulations and sterilization . . . 91
4.6.3 Production cost . . . 92
4.6.4 3D printing to help and 3D printing to challenge . . . 93

4.6.5 Temporal distribution and future trends . . . 93
4.6.6 Limitations of this study . . . 95
4.7 Conclusion . . . 95
References . . . 96

5 Non-Assembly 3D Printing for Compliant Surgical Devices 105
5.1 Introduction . . . 107
5.2 Conceptual design of the compliant shaft . . . 109
5.2.1 Design requirements . . . 109
5.2.2 Design choices . . . 110
5.3 Proof of concept — HelicoFlex . . . 112
5.4 Fabrication . . . 114
5.5 HelicoFlex performance . . . 116
5.5.1 Steering evaluation . . . 116
5.5.2 Payload test . . . 118
5.5.3 Actuation force test . . . 119
5.6 Discussion . . . 120
5.7 Conclusion . . . 123
References . . . 124

6 Steering Strategies of 3D Printed Steerable Instruments 129
6.1 Introduction . . . 131
6.2 Cable configuration strategies . . . 132
6.2.1 Parallel configuration . . . 133
6.2.2 Multi-actuation configuration . . . 133
6.2.3 Three-dimensional representation . . . 133
6.3 Instrument prototypes . . . 135
6.3.1 Design . . . 135
6.3.2 Fabrication . . . 137
6.4 Functionality test . . . 138
6.4.1 Background and goal . . . 138
6.4.2 Participants . . . 139
6.4.3 Experimental setup . . . 140
6.4.4 Task and procedure . . . 141
6.5 Results . . . 142
6.6 Discussion . . . 145
6.6.1 Experimental findings . . . 145
6.6.2 Limitation of this study and future recommendation . . . 147
6.7 Conclusion . . . 148
References . . . 148

7 Fully 3D Printed Compliant Surgical Grasper 151
7.1 Introduction . . . 153
7.1.1 State of the art . . . 153
7.1.2 Challenges in minimally invasive surgery . . . 154
7.1.3 Additive manufacturing for surgical devices . . . 154

7.1.4 Objective . . . 155
7.2 3D-GriP design . . . 156
7.2.1 Gripper design . . . 156
7.2.2 Steerable segment design . . . 157
7.2.3 Handgrip ergonomics . . . 157
7.2.4 Steering control . . . 158
7.2.5 Grasping control . . . 159
7.3 Prototype fabrication and assembly . . . 159
7.4 Experimental methods and results . . . 161
7.4.1 Bending angle measurements . . . 161
7.4.2 Steering force test . . . 162
7.4.3 Grasping force test . . . 165
7.5 Discussion . . . 167
7.5.1 Production and customization . . . 167
7.5.2 Performance and improvements . . . 168
7.5.3 Limitations and future studies . . . 169
7.6 Conclusion . . . 170
References . . . 170

Part 3 Surgical Grippers

8 3D Printed Surgical Grasper for Chordae Tendineae Repair 177
8.1 Introduction . . . 179
8.1.1 Mitral valve regurgitation . . . 179
8.1.2 State-of-the-art interventional techniques . . . 179
8.2 Design of the ChoRe . . . 181
8.2.1 Conventional procedure . . . 181
8.2.2 Design requirements . . . 181
8.2.3 Overall design . . . 182
8.2.4 Prototype manufacturing . . . 187
8.3 Functional test in bovine hearts . . . 188
8.3.1 Parameters of interest . . . 188
8.3.2 Material preparation . . . 188
8.4 Results . . . 189
8.5 Discussion . . . 190
8.5.1 A new concept for chord replacement . . . 190
8.5.2 Prototyping and testing . . . 192
8.6 Conclusion . . . 193
References . . . 193

9 3D Printed Surgical Grasper with Soft Pads for Gentle Grip 199
9.1 Introduction . . . 201
9.2 Design . . . 203
9.2.1 Soft pads . . . 203
9.2.2 3D printed gripper . . . 204

9.3 Methods . . . 205
9.3.1 Pinch force measurements . . . 205
9.3.2 Gripping force measurements . . . 206
9.4 Results . . . 207
9.4.1 Pinch force measurements . . . 207
9.4.2 Gripping force measurements . . . 208
9.5 Discussion . . . 209
9.6 Conclusion . . . 212
References . . . 212

10 Discussion **215**
10.1 Main findings of this thesis . . . 216
10.2 Limitations of the research . . . 218
10.3 Trends, challenges, and developments . . . 218
10.4 Conclusion . . . 221
References . . . 222

Acknowledgements **225**

Curriculum Vitae **227**

List of Publications **229**

Summary

The minimally invasive approach has revolutionized the standard in surgery. In conventional open procedures, the surgeon exposes the diseased area with a relatively large incision. Contrary to conventional surgery, in minimally invasive surgery, several small incisions are used to insert the surgical instruments and reach the target area, reducing the risk of infections and surgical trauma. The surgical instruments currently used are straight and rigid, allowing only straight paths to be followed. An alternative is passively flexible instruments, such as endoscopes and catheters, that require external guidance, e.g., the blood vessel wall, and therefore cannot provide a stable platform to operate. Areas with a high density, like the brain, or situations that demand to actively decide the path to follow, such as in the peripheral bronchi of the lungs, require snake-like instruments that are able to follow multi-curved paths and can maintain their position without external support. Because of the great potential advantages that these types of instruments could offer and because of the new surgical possibilities that might be explored, companies and researchers are working on creating solutions. However, the complexity of such instruments creates difficulties in the surgical implementation and remain a major challenge.

In this context, additive manufacturing, also known as 3D printing, offers a new paradigm for design, manufacturing, and assembly, allowing the production of complex geometries difficult to produce with conventional manufacturing. Using additive manufacturing might help to solve some of the major challenges in snake-like surgical instruments, such as a large number of components and long assembly time. Therefore, the main purpose of the research described in this thesis, is to explore how the combination of additive manufacturing and mechanical solutions can help in designing snake-like instruments, while minimizing the assembly and device complexity.

This thesis is organized into three parts as the main components of a snake-like surgical instrument: Part I, Control, focuses on the control side of the instrument with particular attention to mechanical solutions. Part II, Shaft, focuses on the possibility of fabricating snake-like instruments with additive manufacturing technology, and Part III, End-Effector, on the use of 3D printing to enhance end-effector functions.

In Part I, Chapter 2 introduces the so-called follow-the-leader behavior with a comprehensive overview of the medical devices in literature and proposes a classification based on their three main functions: steering (controlling the leader/end-effector orientation), propagation (advancing the device along a specific path), and conservation (memorizing the shape of path taken by the device). An interesting approach to follow-the-leader devices is the use of mechanical solutions to avoid a large number of actuators. Therefore, Chapter 3 presents an adjustable mechanical memory system able to impose a follow-the-leader motion to the steerable shaft of a med-

ical instrument without using actuators. The shape memory mechanism allows the real-time control of the path during the insertion and retraction of the instrument in the human body. The memory system was implemented in the MemoBox, a fully mechanical prototype able to create and follow discretized paths in 2D.

Part II focuses on additive manufacturing for the development of snake-like instruments. Chapter 4 presents a comprehensive overview of additively manufactured devices for treatment and diagnostics that have been found in the scientific literature. Devices vary for clinical applications, materials, and applied technology but also for the reasons behind the use of additive manufacturing. Two of the main advantages of additive manufacturing are possible customization and the possibility of producing complex geometries that are difficult, if not impossible, to fabricate with conventional manufacturing technologies. Chapter 5 explores additive manufacturing for minimizing the components in the fabrication of snake-like surgical instruments. The study begins introducing a new compliant element where torsion and axial stiffness are combined in a helicoid-based element. The compliant segment was then implemented in a new multi-steerable instrument. The instrument was then prototyped by having its two main components 3D printed: the shaft, with a rigid and a steerable part, and the handle based on a mirrored wrist-control. The prototype showed the ability to follow single and double curved paths. Chapter 6 presents a comparative analysis of the usability of the device presented in Chapter 5, with two different cable configurations: parallel configuration, in which each segment is driven by four independent cables, and multi-actuation configuration, where parallel and helical cables are simultaneously used to control the steerable shaft. The study showed no significant difference in the learning curves to operate the instrument, but participants experienced a significantly lower workload and expressed a net preference for the parallel configuration. Part II ends by proposing a new design that combines the two main advantages of additive manufacturing, customization and easy assembly, in a 3D printed steerable laparoscopic gripper (Chapter 7). The device consists of a pistol-grip handle with a joystick to control the steering motion and a trigger to control the gripper motion. A steerable element, a rigid shaft, and a compliant gripper form the end-effector. Compliant joints and snap-fit connectors are used to simplify assembly and reduce the number of components to just five 3D printed parts in total. The design, in combination with additive manufacturing, is easily adaptable to the needs of the surgeon.

Part III of this thesis presents two examples of how additive manufacturing can contribute to the design of customized end-effectors. Chapter 8 introduces an integrated 3D printed mechanism for the repair of chordae tendineae, the strings that attach the mitral valve to the wall of the heart and help the opening and closure of the valve. The device, composed of ten parts, was successfully tested in a bovine heart to evaluate its functionality. In Chapter 9, the compliant 3D printed gripper design presented in Chapter 7 is equipped with elastomeric soft pads reinforced with carbon-fiber fabric to maximize the contact area, prevent slippage, and reduce local high pinch forces. The gripper was 3D printed as a single component, and the soft pads were manually attached afterwards. The soft gripper was tested on soft tissue

by comparing its behavior with the reference gripper where metal patterned pads were attached showing. The test showed that the soft gripper generated a similar gripping force, but had a lower pinch force compared to the reference gripper.

This thesis shows that the combination of additive manufacturing and mechanical solutions has great potential in the design and development of surgical instruments with enhanced functionalities. Additive manufacturing allows us to think out of the box, take the chance of exploring creative solutions, and experiment without geometrical boundaries, paving the way for new devices and new procedures that once seemed like a distant dream.

Samenvatting

De minimaal-invasieve benadering heeft een revolutie teweeggebracht in de chirurgie. Bij conventionele, open procedures legt de chirurg het te behandelen gebied bloot met een relatief grote incisie. Bij minimaal invasieve chirurgie worden meerdere kleine incisies gebruikt om de chirurgische instrumenten in te brengen en het doelgebied te bereiken, waardoor het risico op infecties en chirurgisch trauma wordt verminderd. De chirurgische instrumenten die hier momenteel voor worden gebruikt zijn recht en rigide, waardoor in principe alleen rechte paden kunnen worden afgelegd. Als alternatief kunnen passieve flexibele instrumenten, zoals flexibele endoscopen en katheters, worden gebruikt, die een externe geleidingsstructuur in het lichaam nodig hebben, zoals bijvoorbeeld de wand van een bloedvat, en daarom geen stabiel platform kunnen bieden om te opereren. Operaties in complexe anatomie zonder aanwezige geleidingsstructuren, zoals bijvoorbeeld in de hersenen, of medische ingrepen in situaties die vereisen dat het te volgen pad actief moet worden gekozen, zoals in de vertakte perifere bronchiën van de longen, vereisen slangachtige instrumenten, die in staat zijn om meervoudig gekromde paden te volgen en die hun positie kunnen behouden zonder externe ondersteuning. Vanwege de vele potentiële voordelen die dit soort instrumenten kunnen bieden en vanwege de nieuwe chirurgische mogelijkheden die erdoor ontstaan, wordt er wereldwijd onderzoek gedaan aan het creëren van oplossingen voor slangachtige ontwerpen. De complexiteit van dergelijke instrumenten veroorzaakt echter problemen bij de chirurgische implementatie en vormt nog steeds een grote uitdaging.

In deze context biedt additieve fabricage, ook wel 3D-printen genoemd, een nieuw paradigma voor ontwerp, productie en assemblage, waardoor het mogelijk is om complexe geometrieën te vervaardigen, die moeilijk te produceren zijn met conventionele vervaardigingstechnieken. Het gebruik van additieve fabricatietechnologie kan helpen om een aantal grote uitdagingen van slangachtige chirurgische instrumenten op te lossen, zoals het grote aantal benodigde componenten en de lange montagetijd. Het belangrijkste doel van dit proefschrift is daarom om te onderzoeken hoe additieve fabricagetechnologie, gecombineerd met slimme mechanische oplossingen, kan helpen bij het ontwerp van slangachtige instrumenten, door de complexiteit van het instrument te minimaliseren en de assemblage te vereenvoudigen.

Dit proefschrift is opgedeeld in drie delen die corresponderen met de belangrijkste componenten van een slangachtig chirurgisch instrument. Deel I, Controle, richt zich op de controlekant van het instrument, met bijzondere aandacht voor mechanische oplossingen. Deel II, Schacht, richt zich op de mogelijkheid om slangachtige instrumenten te fabriceren met additieve fabricagetechnologie. Deel III, End-Effector, richt zich op het gebruik van 3D-printing om de functionaliteit van de tip van het instrument, waarmee het weefsel wordt gemanipuleerd, te verbeteren.

Deel I van dit proefschrift introduceert in Hoofdstuk 2 zogenaamd "volg-de-leider" gedrag waarmee slangachtige instrumenten kunnen worden bestuurd, met een uitgebreid overzicht van dergelijke instrumenten in de literatuur, ingedeeld op basis van hun drie hoofdfuncties: sturen (besturing van de leider/end-effector), voortbewegen (het manoeuvreren langs een specifiek pad) en vorm behouden (het onthouden van de vorm van het gevolgde pad). Een interessante benadering voor het ontwerp van volg-de-leider-instrumenten is het gebruik van zuiver mechanische oplossingen, om zo het gebruik van een groot aantal actuatoren te vermijden. Daarom presenteert Hoofdstuk 3 een instelbaar mechanisch vormgeheugensysteem dat in staat is om een volg-de-leider-beweging op te leggen aan de bestuurbare schacht van een slangachtig instrument, zonder gebruik te maken van actuatoren. Het vormgeheugenmechanisme maakt real-time instelling van het pad mogelijk, tijdens het inbrengen en terugtrekken van het instrument en is geïmplementeerd in de zogenaamde "MemoBox": een volledig mechanisch prototype dat in staat is om gediscretiseerde paden in 2D te creëren en te volgen.

Deel II van dit proefschrift richt zich op additieve fabricagemethoden voor de ontwikkeling van slangachtige instrumenten. Hoofdstuk 4 geeft een uitgebreid overzicht van additief gefabriceerde medische instrumenten voor behandeling en diagnostiek die zijn gevonden in de wetenschappelijke literatuur. Deze instrumenten variëren in klinische toepassing, materiaal en toegepaste technologie, maar ook in de reden voor het gebruik van additieve fabricage. Twee van de belangrijkste voordelen van additieve fabricage zijn de mogelijkheid tot personalisatie en de mogelijkheid om complexe geometrieën te produceren, die moeilijk, zo niet onmogelijk, te vervaardigen zijn met conventionele fabricagetechnologieën. Daarom onderzoekt Hoofdstuk 5 de mogelijkheid om het aantal componenten in de productie van slangachtige chirurgische instrumenten te minimaliseren met behulp van additieve fabricage. Dit onderzoek begint met de introductie van een nieuw compliant element, waarbij torsiestijfheid en axiale stijfheid zijn gecombineerd in een op een helicoïde gebaseerde structuur. Het compliante segment is vervolgens geïmplementeerd in een nieuw prototype van een multi-stuurbaar instrument dat bestaat uit twee 3D-geprinte hoofdcomponenten: een schacht, bestaande uit een rigide en een multi-stuurbaar deel met vijf individueel bestuurbare compliante segmenten, en een handvat waarmee de schacht via gespiegelde polsbediening kan worden bestuurd. Het prototype toont aan dat het mogelijk is om enkel- en dubbelgekromde paden te volgen. Hoofdstuk 6 presenteert een vergelijkende analyse van het in Hoofdstuk 5 gepresenteerde instrument, waarin de besturing voor de gebruiker met twee verschillende kabelconfiguraties wordt vergeleken: een parallelle configuratie, waarbij elk segment wordt aangedreven door vier onafhankelijke kabels, en een multi-actuatie configuratie, waarbij parallelle en helixvormige kabels gelijktijdig worden gebruikt om de stuurbare schacht aan te sturen. Uit de resultaten van een experiment met proefpersonen blijkt dat er geen significant verschil zit in de leercurves met beide instrumenten. De deelnemers hadden echter een significant lagere werklast bij de parallelle configuratie en gaven hier netto hun voorkeur aan. Deel II eindigt in Hoofdstuk 7 met een bijzonder, nieuw ontwerp waarin de twee belangrijkste

voordelen van additieve fabricage, maatwerk en eenvoudige montage, worden gecombineerd in een 3D-geprinte stuurbare laparoscopische grijper. Het instrument bestaat uit een handvat met pistoolgreep, waarbij een joystick wordt gebruikt om te sturen en een trekker om te grijpen. De rigide schacht eindigt in een stuurbare tip met een compliante grijper. Compliante gewrichten en klikverbindingen zijn gebruikt om de montage te vereenvoudigen en het aantal componenten te verminderen tot slechts vijf 3D-geprinte onderdelen in totaal. Het ontwerp is, in combinatie met 3D-printing, op eenvoudige wijze aanpasbaar aan de behoeften van de chirurg.

Deel III van dit proefschrift presenteert twee voorbeelden van geavanceerde 3D-geprinte end-effectoren. Hoofdstuk 8 introduceert een bijzonder geïntegreerd, 3D-geprint mechanisme, ontwikkeld voor het herstel van de zogenaamde chordae tendineae; de peesdraden die de mitralisklep aan de wand van het hart bevestigen en helpen bij het openen en sluiten van de klep. Het mechanisme, bestaande uit tien onderdelen, is met succes uitgetest in een runderhart om de functionaliteit ervan te evalueren. In Hoofdstuk 9 wordt het in Hoofdstuk 7 gepresenteerde compliante 3D-geprinte grijperontwerp uitgerust met zachte binnenlagen van een met koolstofvezel versterkt elastomeer om het contactoppervlak met weefsel te maximaliseren, wegglijden te voorkomen en om lokale hoge puntkrachten te verminderen. De grijper is 3D-geprint als een enkel onderdeel en de zachte binnenlagen zijn daarna handmatig bevestigd. De zachte grijper is getest op zacht weefsel, waarbij het gedrag is vergeleken met een referentiegrijper waaraan geribbelde metalen contactoppervlakken waren bevestigd. Uit de test bleek dat de zachte grijper een vergelijkbare grijpkracht genereerde, maar een lagere knijpkracht had in vergelijking met de referentie grijper.

Dit proefschrift laat zien dat de combinatie van additieve fabricagetechnologie met slimme mechanische oplossingen veel potentieel heeft bij het ontwerpen en ontwikkelen van chirurgische instrumenten met een sterk verbeterde functionaliteit. Additieve fabricage stelt ons in staat om buiten bestaande ontwerpgrenzen te komen en om nieuwe, creatieve oplossingen te verkennen en ermee te experimenteren zonder geometrische limitatie. Dit maakt de weg vrij voor nieuwe instrumenten en voor bijzondere procedures waarvan we tot op heden alleen maar konden dromen.

1

Introduction

1

1.1. From open surgery to minimally invasive surgery

The word surgery has its origin in the Greek work χειρουργία *(kheírourgía)* that, translated, means handwork, (χείρ hand and εργον work) [1].Is surgery still only manual labor or, can new technologies and findings help the clinicians in achieving new results?

Thirst for knowledge has played a fundamental role in the development of new surgical technologies. Since the beginning of their history, humans have learned how to make tools and use them to improve their life quality, from agriculture to health. One of the first pieces of evidence of surgery dates back to the Neolithic period (10,000-4,500 BC) with the practice of trepanation in which the skull was drilled or scraped to reduce the intracranial pressure and cure diseases [2]. Across centuries, breakthroughs have defined the development of surgery, such as the germ theory of disease by Louis Pasteur or the discovery of penicillin by Alexander Fleming. Until the late 20th century, open surgery was considered the standard in surgery. In conventional open surgery, a relatively large incision directly exposes the diseased area allowing the surgeon to visualize and access the inside of the human body [3] (Figure 1.1).

In 1982, the advent of the high-resolution endoscope paved the way for a new approach: minimally invasive surgery (MIS) [4]. In MIS, one or several incisions of few millimeters long, are used as an entry port to the human body, and instruments with long, straight, and rigid shafts are used to reach the diseased area, making the procedure less invasive for the patient but more challenging for the surgeon [5] (Figure 1.1). Even though more difficult to perform, MIS has significant advantages compared to conventional open surgery, such as shorter recovery time, lower risks of infection, less scar tissue, and therefore cosmetic benefits [6, 7].

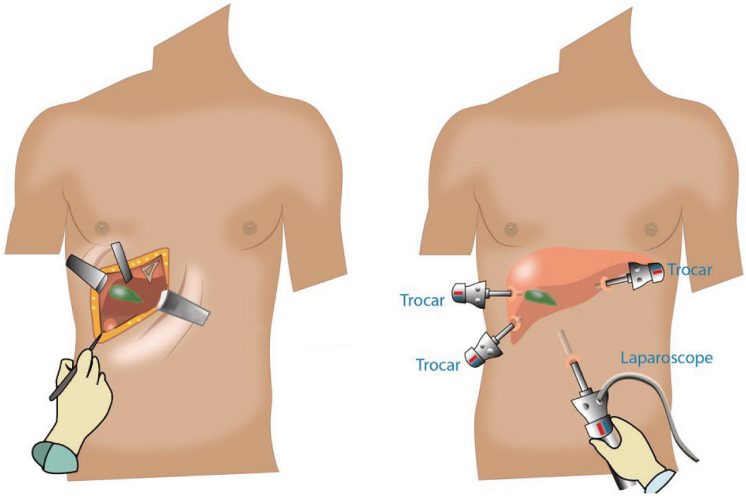

Figure 1.1: Surgical approaches. Open surgery, with one large opening (left), Minimally invasive surgery, with multiple small incisions (right). Adapted from [8].

In limiting the size of the incision, the instrument maneuverability decreases, forcing the surgeon to operate in more challenging conditions. Whereas open surgery allows for direct visualization and access to the organs, which can be directly touched, in MIS, the surgeon can only count on two-dimensional camera images projected on a flat monitor [9]. Due to the long and straight nature of the instruments, surgeons are forced to adopt an unnatural stance with consequent fatigue and loss of dexterity [10]. Moreover, minimizing the size of the incision reduces the number of degrees of freedom from six in open surgery to four in MIS (Figure 1.2a) and creates the so-called fulcrum effect, mirroring the surgeon's hand movements and limiting the workspace to a cone shape with the trocar as the apex (Figure 1.2b) [9].

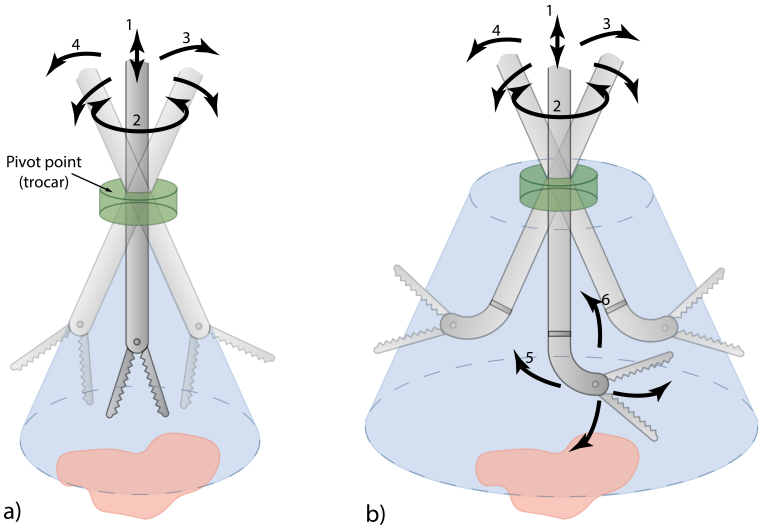

Figure 1.2: Degrees of freedom of surgical instruments a) in open surgery and b) in minimally invasive surgery. In minimally invasive surgery, the fulcrum effect limits the degrees of freedom to four and mirrors the movement of the surgeon due to the small incision through which the instrument is inserted.

In improving the surgeon's workspace and dexterity, the location of the operative area plays a fundamental role. In the abdominal area, inflation of the abdomen is a common practice to expand and enlarge the surgeon's workspace. However, in some procedures, such as cardiovascular interventions, inflation is not an option, and the natural pathways, such as blood vessels, are used to reach the diseased area by means of passively flexible instruments, e.g., catheters. Such passively flexible instruments need external guidance to move forwards and cannot provide a stable operating platform because they are not rigid and therefore not self-supporting. The need for instruments able to generate pathways by themselves by means of **self-supporting** and **self-guiding** becomes clear in natural orifice transluminal endoscopic surgery (NOTES); a minimally invasive procedure in which surgeons use the mouth, nostrils, vagina, and other natural orifices to enter the human body [11, 12]. In delicate, difficultly accessible anatomic areas such as the brain, the instrument cannot use

existing pathways to reach the location of concern, and snake-like instruments with self-supporting and self-guiding properties become increasingly essential to improve the surgeon's dexterity and, therefore, the positive outcome of the procedure.

1.2. Steerability and Follow-the-Leader motion

A number of research groups worldwide have analyzed the problem of instrument maneuverability, and many solutions have been proposed [13, 14]. The integration of a steerable component on the distal end of the device allows re-orientation of the end-effector, keeping the rigid shaft steady in place. LaproFlex (DEAM, Amsterdam, The Netherlands) (DEAM 2019), FlexDex (FlexDex, Brighton, MI, USA) [15], and SILS™ Hand Instruments (Medtronic, Minneapolis, MN, USA)[16] are examples of handheld steerable instruments available in the market. However, steerability in these devices is still limited due to rigid shafts which do not permit navigation along curves with multiple radii.

To overcome the rigidity of the shaft, research has been carried out on the integration of additional flexible components at the end of the rigid shaft to increase maneuverability and on applying control strategies to navigate over more complex paths [17]. One of the most applied strategies is the so-called follow-the-leader (FTL) motion. FTL motion, also known as path following, was first proposed by Choset and Henning in segmented snake-like robots [18]. In FTL-motion, the user steers the most distal segment of the robot, the so-called "leader." The leader creates the trajectory that is taken over by the follower segments, mimicking the obstacle-avoiding motion of a snake through its environment (Figure 1.3). Therefore, the user only controls the position of the first, most distal segment, whereas the steering information is stored and passed back to the follower segments. The described mechanism applies to all the segments of the robot: the pose of each segment slides backward to the follower segments once the robot moves forward. In snake-like robots, FTL motion is mainly applied to search and rescue strategies and general inspections, e.g., in pipelines of collapsed buildings after an earthquake. In these contexts, even if the robot has to move in confined spaces, it can rely on the relatively stiff surrounding environment that can be used to generate motion [18, 19]. Moreover, different from the surgical field, in search and rescue, dimensional constraints are much larger, allowing the actuators to be embedded directly into the segments.

1.3. Snake-like instruments

Snake-like medical devices can be subdivided into three main categories: alternating, telescopic, and shape-shifting systems. Within the alternating systems, the only commercially available FTL device is the Flex® Robotic System (Medtronics Corp., Raynham, MS, USA) with real-time control [20]. With its 10 mm diameter, the Flex® Robotic System uses the patient's mouth as the entry port to have access to the oropharynx, hypopharynx, and larynx. The internal alternating FTL system is based on a friction-based locking system between rigid cylindrical links and spherical joints. The system consists of two concentric tubes that alternate between rigid and

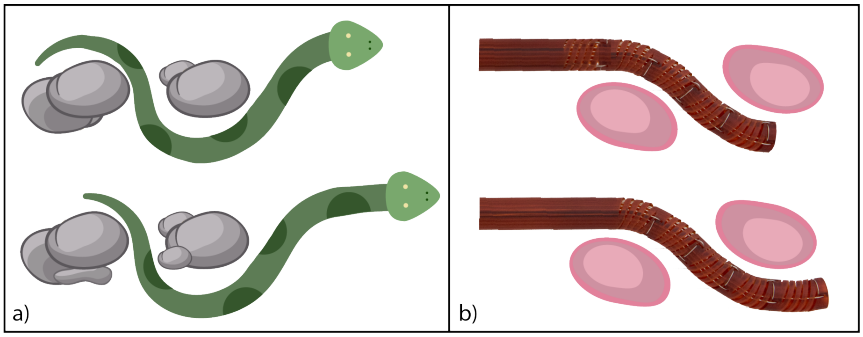

Figure 1.3: Analogy of serpentine locomotion in medical devices. a) A snake's body follows its head avoiding rocks on its path. b) Similarly, the body of a snake-like medical device follows its end-effector, avoiding anatomical obstacles on its path.

flexible states, allowing for a specific path to be followed in real-time.

Telescopic systems mainly consist of concentric tube continuum robots. These robots are based on pre-curved elastic elements nested concentrically into each other [21, 22]. Sliding and rotating the tubes relative to each other allow for an FTL motion. However, due to the pre-defined pre-curved properties, only a few simple paths can be followed precisely, and they require a priori planning of the trajectory [23].

Shape-shifting systems instead are based on the individual control of the steerable segments by means, for instance, of electric actuators. In these systems, the surgeon steers the leader segment while the following segments assume the shape and position of the segment in front of them as the instrument moves ahead. The shape is memorized in a computerized actuation system in which each degree of freedom requires its dedicated actuator to transfer the shape among the follower segments. The actuators are usually placed at the proximal part of the instrument, separated from the shaft, using a system of cables to transfer the actuator motion to the segments [24]. Increasing the number of degrees of freedom increases the complexity of the system.

A first attempt to decrease the complexity, *avoiding* the use of electric actuators, has been made by Helselmans *et al.* [17, 25], who developed two mechanical master-slave shape-shifting FTL systems. In one of the systems, called MemoFlex, a pre-curved steel rod is read out by the master that passes the curve information to a Ø5 mm slave shaft, which mimics the shape of the rod [25]. In the second system, the shaft segments are steered through a certain path by means of control points guided by pre-defined physical tracks [17]. Both systems show the potential of fully mechanical solutions for snake-like instruments. However, both systems are based on pre-defined tracks that cannot be changed in real-time by the surgeon and have to be determined beforehand pre-operatively. Besides, both systems have a complex mechanical design that requires a large number of components making the manufacturing and assembly time-consuming and expensive.

1

1.4. Additive manufacturing

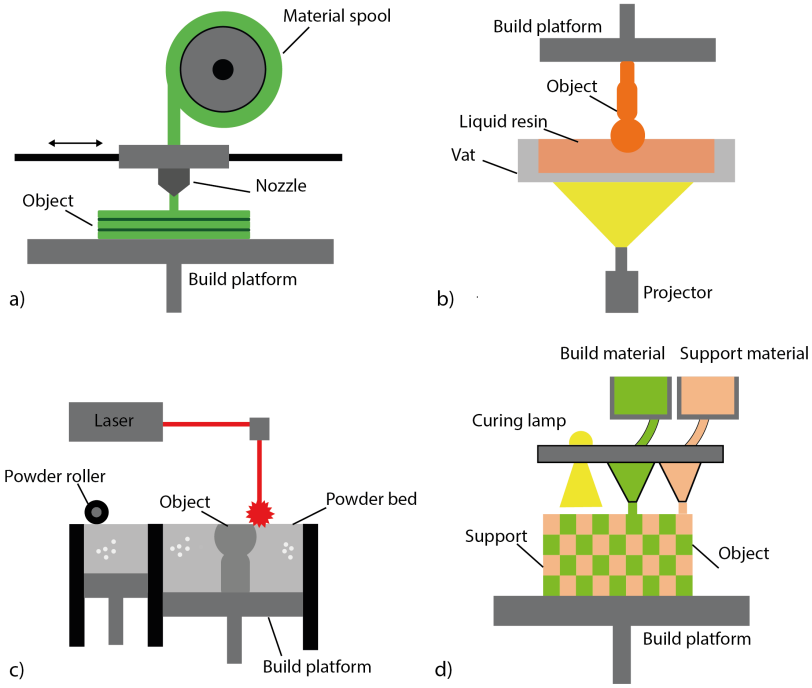

Figure 1.4: Most used additive manufacturing technology in the fabrication of instruments for diagnostic and surgery. In material extrusion technology a), a thermoplastic material is extruded via a nozzle and deposited on a build platform. Due to the low temperature of the build platform, the semi-melted material hardens in the 3D object. In Vat photopolymerization technology b), a liquid photopolymer resin contained in a vat is selectively cured layer by layer by means of a heat source (laser or UV light) to build the object. In powder bed fusion technology c), particles are melted together layer by layer using energy from an electron beam or a laser. In multijet technology d), different materials, such as photopolymers or metals, can be used to build a 3D object hardening layer by layer the material using a light or heat source.

A new perspective on the design, manufacturing, and assembly of medical devices is offered by additive manufacturing (AM), also known as 3D printing. With AM, a computer-aided design (CAD) model can be directly fabricated with a layer-by-layer process. The first appearance of AM was in the early 80s, and in 1984 the first AM technology, stereolithography, was patented [26]. Stereolithography uses a light source (e.g., laser) to harden a single layer of photopolymer resin; the process repeats until the entire object is printed. The importance of AM rapidly increased. In 1987, the first commercial version of the 3D printer was commercialized, and applications further increased because of high reductions in the cost of printers [27].

Different AM technologies are available today, and the American Society for Testing and Materials (ASTM) has defined a Standard Terminology for AM Technologies in which they identify seven main categories: binder jetting, direct energy deposition, material extrusion, material jetting, powder bed fusion, sheet lamination, and

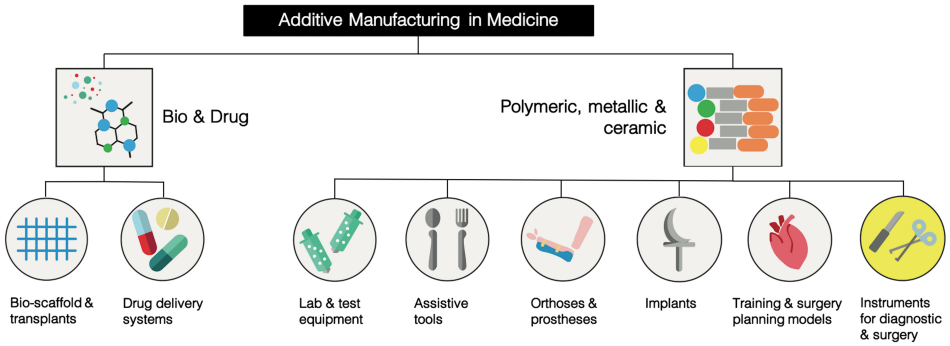

Figure 1.5: Classification of medical fields related to additive manufacturing. The first level of the classification concerns the material used to print whereas the second level is the medical field of application.

Vat photopolymerization. Figure 1.4 shows the most used AM technologies for the production of instruments for diagnostic and surgery.

1.5. Additive manufacturing in medical devices

In the medical field, AM has grown in importance due to the possibility of designing customized tools both for the clinician and patient needs [28]. AM has been applied in many medical fields such as tissue engineering [29], drug delivery systems [30], laboratory equipment [31], assistive tools such as customized cutlery to help people with chronic diseases in their daily life [32], orthoses and prostheses [33]. implants [34], anatomical models [35], surgical guides [36], and medical instruments for diagnostics and surgery (Figure 1.5).

AM enables the production of complex geometries that would be difficult to produce with conventional manufacturing technologies. Enabling an increased geometrical complexity allows the integration of more functionalities in a single component, reducing the assembly time. Many research groups take advantage of additive manufacturing in the field of medical instruments [37]. Examples of steerable devices manufactured using AM are presented by Morimoto *et al.* [38], who used AM in concentric tube continuum robots, Mintenbeck *et al.* ([39], who applied AM in the manufacturing of the segments, and Jelinek *et al.* [40] in the production of a steerable surgical grasper. However, such instruments are still based on components meant to be produced with conventional manufacturing methods, therefore, designed with a large number of parts.

1.6. Goal of this thesis

The field of minimally invasive surgery is progressing towards a continuous reduction of the invasiveness of the procedure to minimize the trauma for the patient. The integration of follow-the-leader motion into flexible surgical devices allows the instrument to pass through tortuous anatomical paths avoiding sensitive structures and

accessing difficult anatomic areas. However, the design complexity of such systems is still high, and the number of components is large, requiring much assembly time and very high associated costs. Novel mechanical solutions in combination with the new design and manufacturing possibilities of additive manufacturing might tackle these challenges.

Therefore, in this thesis, we combine ***mechanical solutions*** and ***additive manufacturing technology*** to design steerable instruments while minimizing the assembly and the device complexity. This research aims to provide an innovative approach to design 3D printed steerable surgical instruments where the integration of multiple functions into a single component allows simplification of the entire design.

1.7. Approach and thesis outline

This thesis is divided into three parts: control, shaft, and end-effector, considering the main components of a snake-like surgical instrument, (Figure 1.6):

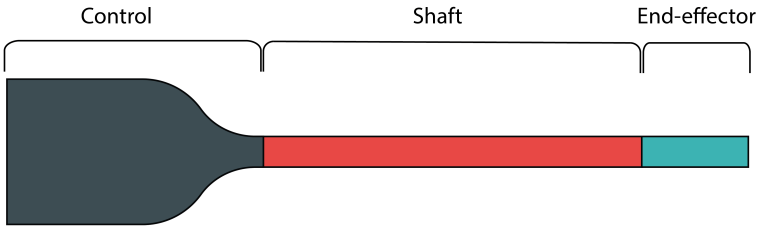

Figure 1.6: Main components of a snake-like surgical instrument representing the three parts of this thesis.

Part I Control:Real-time snake-like control. **Chapter 2** presents a research and patent literature review of solutions for follow-the-leader motion in medical devices. When it comes to the control of snake-like systems, it has been shown that mechanical solutions can be an option [17, 25]. However, the only fully mechanical real-time control system, presented in the literature, is composed out of hundreds of parts that make the system too large for implementation in a medical device [41]. For this reason, **Chapter 3** presents an innovative programmable shape memory system, fully mechanical, based on a shape-shifting mechanism with the number of components strongly decreased as well as its size.

Part II Shaft: Additive manufacturing and compliant solutions. **Chapter 4** explores additive manufacturing technology for surgical and diagnostic instruments giving a critical perspective. Exploiting the possibilities given by additive manufacturing in combining multiple functionalities in a single component, in **Chapter 5**, a novel compliant steerable instrument with fully mechanical control is presented. Particular attention is given to the reduction in the number of components. Both the shaft and the control handle are manufactured as two single compliant parts, highly simplifying conventional designs. **Chapter 6** presents a comparative analysis of the instrument designed in **Chapter 5** routed with two different cable configurations. An experiment involving 12 participants investigated the maneuverability and control of the steer-

able instruments in terms of task performance time, learning curve, and partecipants' preferences. The second part of this thesis ends with **Chapter 7**, where the design of the instrument in **Chapter 5** is developed further into a new fully 3D printed compliant handheld grasper to achieve omnidirectional steering.

Part III End-Effector: Surgical grippers. In the last part of this thesis, two examples of 3D printed end-effectors for different surgical scenarios are presented. **Chapter 8** presents a new grasping mechanism for repairing chordae tendineae (tendinous strands) in the heart in case of mitral valve regurgitation, a heart pathology in which the heart valve does not close properly due to the breakage of such strands. In **Chapter 9**, the end-effector of the compliant grasper from **Chapter 7** is equipped with adhesive pads and evaluated on its pinch force and capability in case of tissue slippage.

Finally, the three parts are joined and discussed in the Discussion and Conclusion (**Chapter 10**).

References

[1] R. A. Fisher, K. Ahmed, and P. Dasgupta, *Introduction to Surgery for Students* (Springer, 2017).

[2] R. S. Solecki, R. L. Solecki, and A. P. Agelarakis, *The proto-neolithic cemetery in Shanidar Cave*, 7 (Texas A&M University Press, 2004).

[3] R. Bittner, *The standard of laparoscopic cholecystectomy,* Langenbeck's archives of surgery **389**, 157 (2004).

[4] S. D. S. Peter and G. W. Holcomb III, *History of minimally invasive surgery,* Atlas of Pediatric Laparoscopy and Thoracoscopy , 1 (2008).

[5] A. Munasinghe, B. Singh, N. Mahmoud, M. Joy, D. Chang, F. Penninckx, and O. Faiz, *Reduced perioperative death following laparoscopic colorectal resection: results of an international observational study,* Surgical endoscopy **29**, 3628 (2015).

[6] M. J. Mack, *Minimally invasive and robotic surgery,* Jama **285**, 568 (2001).

[7] M. S. L. Liem, Y. Van Der Graaf, C. J. Van Steensel, R. U. Boelhouwer, G.-J. Clevers, W. S. Meijer, L. P. S. Stassen, J. P. Vente, W. F. Weidema, and A. J. P. Schrijvers, *Comparison of conventional anterior surgery and laparoscopic surgery for inguinal-hernia repair,* New England Journal of Medicine **336**, 1541 (1997).

[8] *Types of surgery and endoscopy,* (2019), https://www.thesurgeonscollective.com.au/treatments/types-of-surgery-open-laparoscopic-endoscopy-gastroscopy-colonoscopy-perth, Accessed: 2021-03-01.

[9] G. H. Ballantyne, *The pitfalls of laparoscopic surgery: challenges for robotics and telerobotic surgery,* Surgical Laparoscopy Endoscopy & Percutaneous Techniques **12**, 1 (2002).

[10] R. Berguer, *Surgical technology and the ergonomics of laparoscopic instruments,* Surgical endoscopy **12**, 458 (1998).

[11] B. Shrestha, *Natural orifi ce transluminal endoscopic surgery (notes)-an emerging technique in surgery,* Journal of Nepal Medical Association **51** (2011).

[12] B. Azizi Koutenaei, E. Wilson, R. Monfaredi, C. Peters, G. Kronreif, and K. Cleary, *Robotic natural orifice transluminal endoscopic surgery (r-notes): Literature review and prototype system,* Minimally Invasive Therapy & Allied Technologies **24**, 18 (2015).

[13] J. Burgner-Kahrs, D. C. Rucker, and H. Choset, *Continuum Robots for Medical Applications: A Survey,* IEEE Transactions on Robotics **31**, 1261 (2015).

[14] E. A. Arkenbout, P. W. Henselmans, F. Jelínek, and P. Breedveld, *A state of the art review and categorization of multi-branched instruments for notes and sils,* Surgical endoscopy **29**, 1281 (2015).

[15] *Flexdex surgical,* (2020), https://flexdex.com/, Accessed: 2020-05-09.

[16] Medtronic, *Silstm hand instruments,* (2020), https://www.medtronic.com/covidien/en-us/products/hand-instruments-ligation/sils-hand-instruments.html#sils-clinch, Accessed: 2020-05-09.

[17] P. Henselmans, C. Culmone, D. Jager, R. van Starkenburg, and P. Breedveld, *The memoflex ii, a non-robotic approach to follow-the-leader motion of a snake-like instrument for surgery using four predetermined physical tracks,* Medical Engineering & Physics **86**, 86 (2020).

[18] H. Choset and W. Henning, *A follow-the-leader approach to serpentine robot motion planning,* Journal of Aerospace Engineering **12**, 65 (1999).

[19] P. Liljebäck, K. Y. Pettersen, Ø. Stavdahl, and J. T. Gravdahl, *A review on modelling, implementation, and control of snake robots,* Robotics and Autonomous systems **60**, 29 (2012).

[20] M. Corporation, *Flex® robotic system: Expanding the reach of surgery®,* (2021), https://medrobotics.com/gateway/flex-system-int/, Accessed: 2021-02-22.

[21] R. J. Webster, J. M. Romano, and N. J. Cowan, *Mechanics of precurved-tube continuum robots,* IEEE Transactions on Robotics **25**, 67 (2009).

[22] P. E. Dupont, J. Lock, B. Itkowitz, and E. Butler, *Design and control of concentric-tube robots,* IEEE Transactions on Robotics **26**, 209 (2010).

[23] H. B. Gilbert and R. J. Webster, *Can concentric tube robots follow the leader?* in *2013 IEEE international conference on robotics and automation* (IEEE, 2013) pp. 4881–4887.

[24] H. Lee, K. G. Kim, J. H. Seo, and D. K. Sohn, *Natural orifice transluminal endoscopic surgery with a snake-mechanism using a movable pulley,* The International Journal of Medical Robotics and Computer Assisted Surgery **13**, e1816 (2017).

[25] P. W. Henselmans, G. Smit, and P. Breedveld, *Mechanical follow-the-leader motion of a hyper-redundant surgical instrument: Proof-of-concept prototype and first tests,* Proceedings of the Institution of Mechanical Engineers, Part H: Journal of Engineering in Medicine **233**, 1141 (2019).

[26] C. W. Hull, *Apparatus for production of three-dimensional objects by stereolithography,* United States Patent, Appl., No. 638905, Filed (1984).

[27] D. Hoang, D. Perrault, M. Stevanovic, and A. Ghiassi, *Surgical applications of three-dimensional printing: a review of the current literature & how to get started,* Annals of Translational Medicine **4** (2016).

[28] C.-Y. Liaw and M. Guvendiren, *Current and emerging applications of 3d printing in medicine,* Biofabrication **9**, 024102 (2017).

[29] A. Youssef, S. J. Hollister, and P. D. Dalton, *Additive manufacturing of polymer melts for implantable medical devices and scaffolds,* Biofabrication **9**, 012002 (2017).

[30] M. Palo, J. Holländer, J. Suominen, J. Yliruusi, and N. Sandler, *3d printed drug delivery devices: perspectives and technical challenges,* Expert Review of Medical Devices **14**, 685 (2017).

[31] W. Lee, D. Kwon, W. Choi, G. Y. Jung, A. K. Au, A. Folch, and S. Jeon, *3d-printed microfluidic device for the detection of pathogenic bacteria using size-based separation in helical channel with trapezoid cross-section,* Scientific Reports **5**, 7717 (2015).

[32] T. Nozaki, T. Murakami, T. Shimono, K. Ohnishi, and R. Oboe, *Development of meal assistance device for patients with spinal cord injury,* in *Advanced Motion Control (AMC), 2016 IEEE 14th International Workshop on* (IEEE, 2016) pp. 388–393.

[33] J. ten Kate, G. Smit, and P. Breedveld, *3d-printed upper limb prostheses: a review,* Disability and Rehabilitation: Assistive Technology **12**, 300 (2017).

[34] N. Xu, F. Wei, X. Liu, L. Jiang, H. Cai, Z. Li, M. Yu, F. Wu, and Z. Liu, *Reconstruction of the upper cervical spine using a personalized 3d-printed vertebral body in an adolescent with ewing sarcoma,* Spine **41**, E50 (2016).

[35] D. B. Jones, R. Sung, C. Weinberg, T. Korelitz, and R. Andrews, *Three-dimensional modeling may improve surgical education and clinical practice,* Surgical innovation **23**, 189 (2016).

[36] M. Randazzo, J. M. Pisapia, N. Singh, and J. P. Thawani, *3d printing in neurosurgery: a systematic review,* Surgical neurology international **7**, S801 (2016).

[37] C. Culmone, G. Smit, and P. Breedveld, *Additive manufacturing of medical instruments: A state-of-the-art review,* Additive Manufacturing **27**, 461 (2019).

[38] T. K. Morimoto and A. M. Okamura, *Design of 3-D Printed Concentric Tube Robots,* IEEE Trans. Robotics **32**, 1419 (2016).

[39] J. Mintenbeck, M. Siegfarth, R. Estaña, and H. Wörn, *Flexible instrument for minimally invasive robotic surgery using rapid prototyping technology for fabrication,* (2014) pp. 1085–1090.

[40] F. Jelínek, R. Pessers, and P. Breedveld, *DragonFlex Smart Steerable Laparoscopic Instrument,* Journal of Medical Devices **8**, 015001 (2014).

[41] P. W. J. Henselmans, S. Gottenbos, G. Smit, and P. Breedveld, *The Memo Slide: An explorative study into a novel mechanical follow-the-leader mechanism,* Proceedings of the Institution of Mechanical Engineers, Part H: Journal of Engineering in Medicine **231**, 1213 (2017).

Part 1

Real-Time Snake-Like Control

2

Follow-the-Leader Mechanisms in Medical Devices

Published as:
Culmone, C., Yikilmaz S. F., Trauzettel F., and Breedveld, P. "Follow-The-Leader Mechanisms in Medical Devices: A Review on Scientific and Patent Literature". IEEE Reviews in Biomedical Engineering, (2021), doi: 10.1109/RBME.2021.3113395

Abstract

Conventional medical instruments are not capable of passing through tortuous anatomy as required for natural orifice transluminal endoscopic surgery due to their rigid shaft designs. Nevertheless, developments in minimally invasive surgery are pushing medical devices to become more dexterous. Amongst devices with controllable flexibility, so-called Follow-The-Leader (FTL) devices possess motion capabilities to pass through confined spaces without interacting with anatomical structures. The goal of this literature study is to provide a comprehensive overview of medical devices with FTL motion. A scientific and patent literature search was performed in five databases (Scopus, PubMed, Web of Science, IEEExplore, Espacenet). Keywords were used to isolate FTL behavior in devices with medical applications. Ultimately, 35 unique devices were reviewed and categorized. Devices were allocated according to their design strategies to obtain the three fundamental sub-functions of FTL motion:*steering*, (controlling the leader/end-effector orientation), *propagation*, (advancing the device along a specific path), and *conservation* (memorizing the shape of the path taken by the device). A comparative analysis of the devices was carried out, showing the commonly used design choices for each sub-function and the different combinations. The advantages and disadvantages of the design aspects and an overview of their performance were provided. Devices that were initially assessed as ineligible were considered in a possible medical context or presented with FTL potential, broadening the classification. This review could aid in the development of a new generation of FTL devices by providing a comprehensive overview of the current solutions and stimulating the search for new ones.

2.1. Introduction

In the last decades, minimally invasive surgery (MIS) has shown many benefits over open surgery, due to a reduction in the size of incisions made by the surgeon [1–3]. Ultimately, MIS leads to less scar tissue, bleeding, infections, and hospital time [4–6]. Conventional MIS involves the use of rigid, slender instruments inserted into the body via trocars. In some cases, such as in laparoscopic surgery, the surgeon's maneuverability and vision can be improved by creating an open space by inflating the body with carbon dioxide.

However, this technique cannot always be used. In some procedures, natural anatomic pathways such as blood vessels can be used to reach the target area using passively flexible instruments, e.g., flexible endoscopes or catheters. However, in situations in which natural pathways cannot be used to reach the target area, external guidance, and support of the instruments is necessary. This issue becomes fundamental in natural orifice transluminal endoscopic surgery (NOTES), in which surgeons use the mouth, nostrils, rectum, and other natural orifices to enter the human body [7–10]. In these scenarios, rigid or passively flexible instruments are limited in their dexterity, which negatively impacts the positive outcome of the procedure [11]. It is therefore important to design medical devices that have high dexterity and additional degrees of freedom (DOF) to reach targets in confined anatomical structures. Features like controllable flexibility have been used in the design of many medical devices [12, 13]. Controllable flexibility allows for surgical instruments to access target locations in a flexible state while providing rigid support during the procedure phase.

Another important feature is the device control strategy that is the way to navigate the instrument into the body and plan the pathway. One of the most applied control strategies is the so-called Follow-The-Leader (FTL) motion, first proposed by Choset and Henning in snake-like hyper redundant robots [14]. These robots possess bio-inspired serpentine locomotion in which the body of the robot follows its tip. This motion allows the device to reach a target in a confined space from one entry point without relying on reaction forces from the environment. A definition of FTL motion for a medical instrument is given by Burgner-Kahrs *et al.* [15], stating that these devices must *"operate in a so-called follow-the-leader manner where their body conforms approximately to the path taken by their end-effector without relying on anatomical interaction forces."* This behavior makes it possible to avoid obstacles at all times during advancement towards a target or retraction from a target, without applying significant force to any anatomy.

The goal of this study is to provide a comprehensive overview of methods used to achieve FTL motion in medical devices from both scientific and patent literature. For inclusion in this study, the device should be mechanically described and, a physical or a virtual prototype should be presented. Moreover, the device should memorize and propagate along the path taken by the end-effector to comply with the FTL motion. The devices found in the literature are classified based on the mechanical aspects providing their FTL motion.

2.2. Literature search methods

2.2.1. Scientific literature search

The scientific literature search was conducted using the Scopus, PubMed, Web of Science, and IEEExplore databases. Because the goal was to provide a comprehensive overview of medical devices that have been designed to have FTL motion ability, the query was organized in three main aspects named: *behavior*, *object*, and *application*. All of these aspects had to be present in the found papers to merit their inclusion in this study. The behavior terms of the query specify the nature of the devices' motion. Here, *follow the leader*, shape memor*, path follow*, snake-like*, and *serpentine* were used as search terms to capture this aspect. In the object category, *device*, instrument*, catheter**, and *manipulator** were specified to define the type of device sought, in this case, any type of medical device. Finally, the application category specified the medical application in which the sought devices could be used; **medic*, surg*, interven*, *scop*, inspec*, diagnos*, treat**, and *therap** were specified for this term. The query was restricted to title, abstract, and keywords because these areas contain the essence of the article.

The query was formulated as follows: (*"follow the leader*" OR "shape memor*" OR "path follow*" OR "snake like" OR "serpentine") AND (catheter* OR instrument* OR device* OR manipulator) AND (*medic* OR surg* OR interven* OR *scop* OR inspec* OR diagnos* OR treat* OR therap**). The search was limited to English written documents only, and no time limitations were given. The query was aimed at isolating results about devices that have an FTL mechanism and are used in medical applications. The overlapping documents among different databases were filtered out. The query was discussed and formulated by all the authors of this review. The appearance of each word used in the query was further checked in the title, abstract, and keywords to evaluate its relevance for the search.

2.2.2. Patent literature search

The patent literature search was conducted using the Espacenet database. The query was limited to search within classification A61: *Medical or veterinary science; hygiene*, and further limited to titles and abstracts ("ta"). The query was expressed as follows: (*ta = "follow the leader" OR ta = "path follow*" OR ta = "snake like" OR ta = "serpentine*") AND (ta any "catheter*" OR ta any "instrument*" OR ta any "device*" OR ta any "manipulator*") AND cpc = "A61"*. Because the search was already within the medical classification A61, the application category became redundant and was omitted. The term *shape memor** was also omitted from this query, as even though within the context of FTL motion, it refers to the ability of a device to remember its physical shape, most often the term is used in materials science, leading to too many irrelevant results. Finally, the results were filtered to show English results only.

2.2.3. Eligibility conditions

In order to be deemed eligible for inclusion, an item of literature had to demonstrate a clear medical application, have met all of the conditions for FTL motion set out by Burgner-Kahrs *et al.* [15] in Section 2.1, which means be able to memorize and

propagate the path taken by the end-effector, and have disclosed the mechanical design of the presented robot, either as a physical prototype or virtual model. Papers containing only algorithms or clinical trials of FTL devices without mechanical background information were not included.

In many cases, FTL systems are not designed for medical purposes but rather for search and rescue or inspection in an industrial setting [16, 17]. These systems face fundamentally different design requirements as compared to medical robots, often directly using their environment to provide the reaction forces necessary for movement, a strategy that is undesirable in the medical field due to the risk of tissue damage. This results in methods of locomotion that are significantly different from those designed to interact with human tissue (e.g., wheels [18], continuous tracks [19], or legs [20]. Finally, these robots are simply much larger than their medical counterparts [21, 22], which are designed to operate in confined spaces at comparatively small scales while maintaining biocompatibility and sterility and interacting with human tissue. Solutions for search and rescue or industrial inspections were therefore not included in the study.

The performance of the presented devices did not affect their selection. For example, some devices cannot carry their weight and therefore need a surface to operate on [23] or need to be operated hanging down [24]. In these cases, if the FTL motion is still present and independent from the environment in at least one plane, the paper was included.

2.3. Results

2.3.1. Literature search results

The literature search yielded 6638 scientific papers and 158 patents. Of the located pieces of scientific literature, 3119 results were located using Scopus, 2376 were sourced using the Web of Science database, 876 results were found on PubMed, and 267 on IEEExplore Figure 2.1. Duplicates were removed by comparing titles with a Matlab script that selected 3997 individual scientific papers (last update: June 2021). The titles and abstracts of the found papers and patents were manually checked to exclude documents dealing with topics different from FTL motion in medical devices. This selection resulted in 175 potentially relevant scientific papers and 21 patents. The full texts of these documents were then read and examined based on the eligibility conditions by the authors. The references were also checked to find other relevant papers or patents. Finally, 43 documents were selected from the scientific and patent literature, covering in total 35 different FTL devices. The final results were discussed and checked by all the authors.

2.3.2. General categorizations

In order to categorize the devices found in the literature, the concept of FTL motion was divided into three sub-functions: *steering*, *propagation*, and *conservation*, as shown in Figure 2.2. The principle is that any device capable of FTL motion must possess all three sub-functions. An FTL system must be able to:

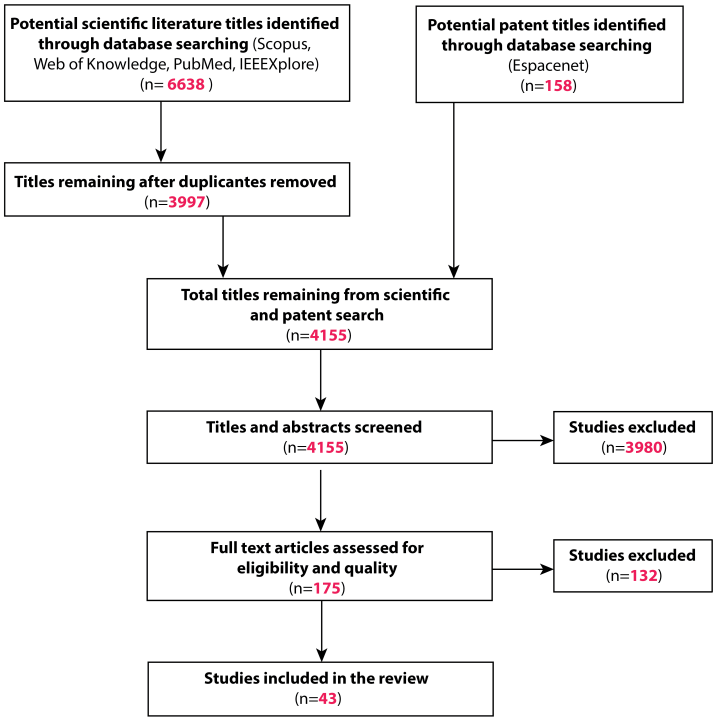

Figure 2.1: Four-phases flow diagram for the scientific and patent literature.

1. *Steer* the leader/end-effector to the desired orientation.

2. *Propagate* along a specific path towards a target.

3. *Conserve* the shape of the path taken by the leader/end-effector.

Each sub-function was further divided into the *type* of solution to achieve the sub-function, Figure 2.2. Each type of solution was then analyzed considering the *method* to generate forces for the given sub-function. Since patents often intentionally cover a variety of suitable actuation method, the most emphasized method was assumed for the purposes of classification. Throughout this review, the word "proximal" is used to indicate the shaft segments that are closest to the operator or handle of the device, whereas "distal" is used for the segments that are close to the end-effector of the device.

2.3.3. Steering of the device

For FTL devices, steering the device essentially means manipulating the orientation of the leader/end-effector. The steering classification concerns the location of the steering actuator(s) - either inside or outside the body. *Steering/Inside the body*

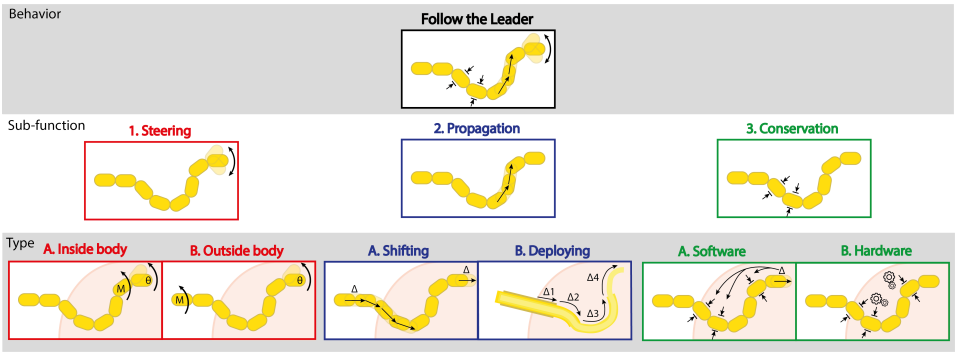

Figure 2.2: Schematic representation of Follow-The-Leader motion divided into three sub-functions. 1. Steering, 2. Propagation, 3. Conservation. Each sub-function is further analyzed considering the actuator location, propagation manner, and constraint type, respectively.

indicates that the actuation unit is embedded in the part of the device that must be inserted into the body of the patient (e.g., the shaft or the steerable segments). *Steering/Outside the body* means that the actuation systems of the robot are not inserted into the body of the patient, but remain in a module of the robot (e.g., handle or controller) that is kept outside of the patient.

The steering motion is generated by forces that actuate the segment leader/end-effector. The found methods by which these forces are generated in steering both inside and outside the body have been subdivided into six groups:

(a) motor torque or force

(b) thermal deformation force

(c) elastic relaxation force

(d) electromagnetic (EM) force

(e) cable tension force

(f) hydraulic force

In these groups the leader segment changes orientation because (a) a torque is applied to its joint by a motor; (b) it is attached to wires that change their shape with heat; (c) it wants to assume the orientation with the lowest potential energy; (d) it is attracted by an electromagnetic force pivoting it in a certain direction; (e) it is pulled by a cable that bends or pivots the segment towards a certain direction; (f) it is filled with a pressurized liquid.

Steering/Inside body

This group consists of devices that have actuators embedded within the parts that enter the body of the patient [23, 25–31]. Most of these devices have segments

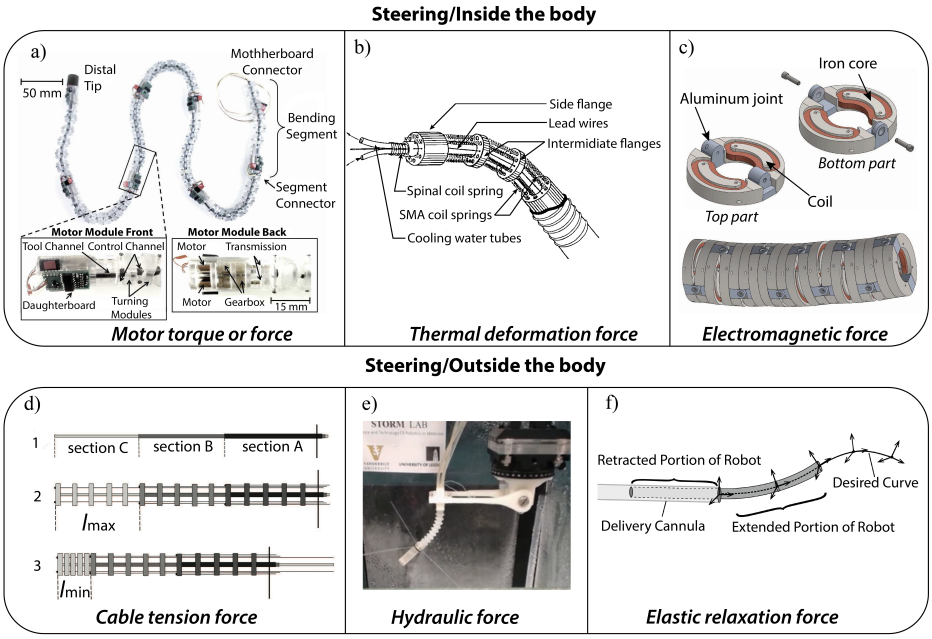

Figure 2.3: Examples of actuators inside and outside the body of a Follow-The-Leader (FTL) devices. a) Continuum robot endoscope. The motors in the motor modules reel in the cables attached to the segment connectors to articulate the segments [23] (©[2014] IEEE). b) Inside structure of an active endoscope controlled by SMA actuators. The SMA coils contract when heated up and relax when cooled down with cooling water. The SMA coils are attached to flanges that bend by activating the SMA actuators [26] (©[1988] IEEE). c) CAD model of a hyper-redundant FTL system. Each segment is composed of two grey rings. The grey rings are attached to each other using aluminum joints. The coil (red) around the iron core generates a magnetic field if current runs through it. Depending on the current direction, the rings swivel relative to their neighbors because of electromagnetic attraction/repulsion. Adapted from [29, 30] (©[2015] IEEE). d) Two-dimensional schematic view of an extendable, tendon-driven continuum robot, adapted from [35]. The robot body is divided into three sections, with distal section C at the top and proximal section A at the bottom and connected to a control unit (not shown). Each section A-C contains five disks loosely placed around a backbone tube in the middle, with the tube connected to the top disc. The three backbone tubes of sections A-C fit concentrically into one another and are individually retractable. The top disc of section C connects to three tendons that pass freely through the system to the control unit. Similarly, the top disc of section B connects to three other tendons, and the top disc of section C connects to a third set of three tendons. In total, nine tendons are controlled by the control unit, as well as the length of the telescopic backbone tubes. If the distal tube is retracted, section C collapses. Permanent magnets are oriented in a repelling sequence to ensure equal distance when the concentric backbones are deployed. e) Hydraulic actuated device. The pressurized water in the main body bends the device in different directions, adapted from [36]. f) Concentric tube device. The tubes bend in the direction of the least internal tension. Operating this precisely results in steering [37] (©[2015] IEEE).

with embedded motors that control the joint rotation of each segment individually by applying torque [27, 28, 31]. A unique case is a device proposed by Chen *et al.*, shown in Figure 2.3a [23]. This particular device uses motors embedded in the segments to reel in cables and bend the segments with cable tension. Systems that steer by means of shape memory alloy (SMA) wires, also referred to as SMA actuators [32, 33], are also considered to have an actuation inside the body of the patient

[25, 26]. Actuation by SMA wires is carried out using a material phase change. By changing the temperature of SMA wires, the atomic arrangement of the material changes [34], reshaping the wire. If these wires are attached to segments of the FTL device, their deformation can re-orient the segment. If the temperature is precisely and actively controlled, the deformation of the SMA wire can be regulated, making the steering (semi-) continuous continuous (Figure 2.3b) [26]. If the SMA wire is only set to achieve the threshold for total deformation, the segments have a binary control assuming only their extreme orientations when activated [25]. Note that in these devices, the temperature increases due to current flow through electrical resistance within the wires. One of the analyzed devices instead uses electromagnetic (EM) force to pivot the segment to its extremes in one DOF, obtaining binary steering for each segment, see Figure 2.3c [29, 30]. The EM force is generated within the segments and is therefore categorized as an actuator inside the body.

Steering/Outside body

This group consists of devices that have actuators in the proximal handle or controller, external to the parts that enter the body of the patient. For most of these devices, the steering is achieved using cables [24, 35, 38–60]. Pulling or releasing the cables changes the curvature of the device's segments. Tensile force on the cables can be applied by actuators located outside the body, e.g., electromotors [24, 35, 38–43, 46–48, 50–58, 60, 61] or manually [44, 45, 49, 59]. The number of DOF achievable by any given steerable segment is dependent on the number of cables controlling it; two cables result in one DOF, whereas three or four cables result in bending in two DOF. A common arrangement for these devices consists of rigid spacer disks that guide the cables along the shaft of the device, with these disks attached to [38] or arranged around one compliant element [35, 51, 52], running the entire length of the shaft (Figure 2.3d). As this design is analogous to a vertebral column, the central element is often referred to as the "backbone" [62]. In devices with multiple steerable segments, the cables controlling a given segment simply pass through the disks of the segments they are not intended to control and are anchored only to the segment they control. By pulling at the steering cables a local bending torque, which directly relates to the length of the moment arm relative to their backbone, is applied, causing the segment to steer. Cables can also be substituted by pressurized liquids. The combination of more than two jets bends the segments in two DOF [36], Figure 2.3e.

Elastic relaxation forces are used for steering devices composed of pre-curved concentric tubes [37, 63–69]. Pre-curved concentric tube devices consist of plastically bent tubes aligned concentrically, Figure 2.3f. Here, steering is essentially the result of the elastic interaction of the tubes. The tubes naturally want to bend in a certain direction, therefore applying elastic relaxation forces. By rotating and translating the tubes with respect to each other, the pre-curved sections will change their orientation [37]. The rotations and translations of the tubes are achieved using actuators outside the body. As the motion comes from the internal elastic forces of the tubes, these devices do not need cable guiding disks or the creation of space between a backbone and a tendon to allow moment arms to apply forces [70]. These types of systems are

also called invertebrate robots due to the lack of a backbone compared to tendon-driven devices. They are quite popular in the field of medical instruments because their working principle allows the construction of very thin devices [71, 72] compared to cable-driven devices. In cable-driven devices, the bending torque depends on the length of the moment arm relative to the backbone, requiring a certain thickness for functioning.

2.3.4. Propagation of the device

The propagation classification concerns the advancement method only of the shaft of the device. The propagation of an FTL device is essentially the movement of the device shaft along a path towards a target. The device shaft can either advance in a shifting manner or a deploying manner. *Shifting propagation*, as defined by Ikuta *et al.*, means that the entire device shaft is part of the advancing movement [26]. All segments will advance the same distance simultaneously. *Deploying propagation* means that a distal segment of the shaft can advance while its proximal segments remain stationary.

The methods found for generating the forces to provide shifting or deploying propagating motion have been subdivided into two groups:

(a) *motor force* (e.g., rack and pinion or lead screw spindle)

(b) *manual force* (e.g., surgical handle or manual insertion)

Shifting propagation

This group consists of devices that propagate by advancing all segments of the shaft simultaneously. Most of the found devices advance with an electric motor to continuously have precise control and information of the displacement [24, 26, 27, 29, 30, 36, 39, 42, 43, 47, 48, 50, 55–58], Figure 2.4a. Conversely, some prototypes do not have real-time information on device advancement, thus they are programmed to steer segments on time for a constant advancement speed [23, 25, 31]. Other devices are designed for manual insertion and have other aids to account for the insertion depth [28, 44, 45, 59]. An example of the latter is the semi-automatic snake robot for NOTES shown in Figure 2.4b. The device is inserted manually, and its insertion depth is tracked by a trans-anal endoscopic microsurgery (TEM) trocar equipped with hall-effect sensors [28]. Another manually operated device that does not need an external tracer module is the hyper-redundant surgical instrument shown in Figure 2.4c. The manually actuated passive rack and pinion mechanism advances the device by turning a crank, which creates a direct kinematic relation between the crank rotation and the forward motion of the device [44].

Deploying propagation

This group consists of devices that propagate by advancing the relative distal segments of the shaft while the relative proximal segments of the device remain stationary, e.g., in Figure 2.4d, tubes 3 and 2 remain stationary while tube 1 advances. Since concentric tube systems propagate a tube while another remains stationary,

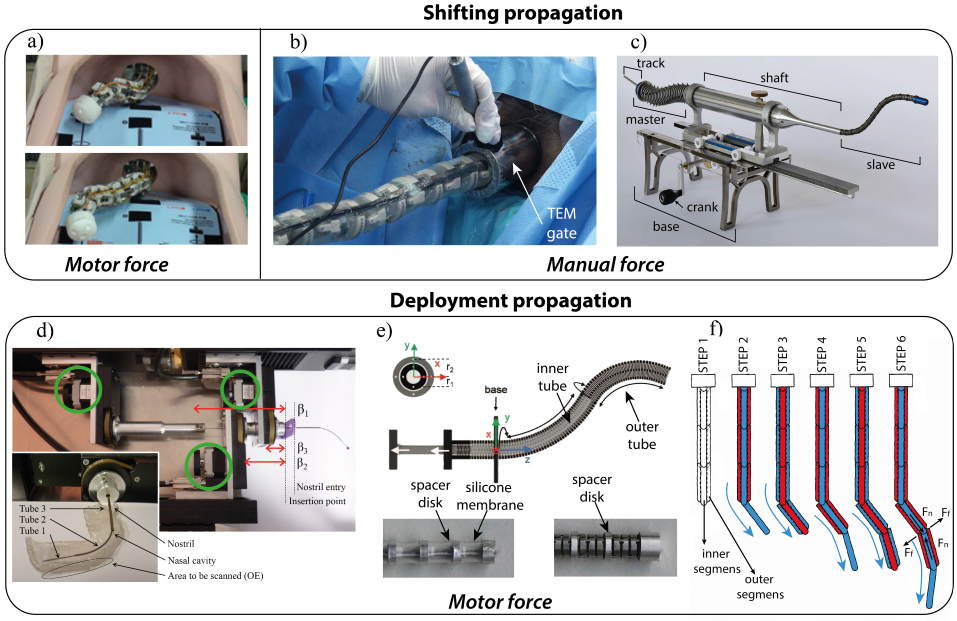

Figure 2.4: Examples of Follow-The-Leader (FTL) devices with shifting or deploying propagation. a) Example of shifting propagation in which all segments are independently controlled by dedicated motors on the external control unit. For the advancing motion, an additional motor moves the whole system, adapted from [47]. b) Snake robotic colonoscope design concept named "hold the snake". The trans-anal endoscopic microsurgery (TEM) gate is placed in the patient's anus, and the robot is inserted through the TEM gate manually by a medical staff member. Electric motors embedded into the shaft segments control the steering and memorize the shape [28]. c) MemoFlex hyper-redundant mechanical surgical FTL instrument, adapted from [44]. The crank drives a rack and pinion construction that translates the track – a pre-bent stainless-steel rod that defines the 3D path to be followed. During the forward motion of the instrument, the track moves through the master module in the direction of the shaft. The master module follows the shape of the moving track and is connected via cables to the slave module that copies the shape of the master. As the track moves through the master, the slave follows the shape of the track and thereby displays FTL motion over the fixed shape of the track. d) Example of a concentric tube device designed for optical biopsy applications driven by stepper motors (encircled in green) [65] (©[2017] IEEE). e) Tendon-driven continuum robot with an inner tube placed inside an outer tube. The spacer disks and silicone membrane provide a smooth concentric sliding motion, adapted from [38] (©[2017] IEEE). f) Highly Articulated Robotic Probe (HARP). The inner and the outer tube alternate their stiffness during propagation: flexible while advancing (blue), stiff when stationary (red). Cables run through the segments of the inner and outer tubes. Tensioning the cables compresses the segments and generates normal forces (F_n) at their contact surfaces, thus locking the shape. The friction forces (F_f) between the contact surfaces of the segments keep the configuration locked, adapted from [53].

these systems usually advance in a deploying manner by means of linear motor force. Three different types of concentric mechanisms have been found in the literature: pre-curved concentric tubes, steerable concentric devices, and alternating devices. *Pre-curved concentric tubes* [37, 63–69], often referred to as telescoping mechanisms [66], slide concentrically by means of a linear motor force, see Figure 2.4d. *Steerable concentric devices* [35, 38, 49, 51, 52, 60, 61] use the same deployment mechanism, but since this devices are not pre-curved, an additional force is required

to actively steer the tubes. A particular type of such a concentric mechanism is based on spacer disks that cannot be fixed to the backbone since the backbone extends. To keep the equal distribution of disks along the backbone, the loose disks contain mutually repelling permanent magnets. This means that the individual disks in the mechanism behave as separated by a spring, but unlike a spring, which has a minimum compressed length, the magnetic field can be compressed until there is no space between the magnets [38], see Figure 2.4e. The third type of concentric mechanism is the so-called *alternating devices* that switch the stationary part of the system [40, 41, 46, 53]. Instead of having multiple concentric tubes telescopically advancing one after another, these systems only have two concentric parts that switch in propagation; when the inner segments advance, the outer segments are stationary and vice versa, making it a deploying propagation. An example of this is shown in Figure 2.4f. As an alternative to this concentric version, the two alternating shafts can also be aligned parallel to each other [54].

2.3.5. Shape conservation of the device

Conserving the shape of an FTL device means assuming the shape of the path taken by the leader/end-effector during the entire propagation and memorize it. This means that the advancing segments of the device are essentially constrained in their movement. The constraint can be applied through the software or the hardware of the device. A *software constraint* means that the movement of the segment is determined by a computerized controller that maintains the configuration of the shaft of the device. Without a controlled actuation, this segment would be physically free to reconfigure. In practice, this implies that there is no dedicated mechanism other than the actuation system used for steering, which can preserve the global shape and pose of the shaft. In other words, the shape constraint is virtual, existing only in the control software of the device. Conversely, a *hardware constraint* means that a physical mechanism determines the movement of the segment. Note that the mechanism could still be activated using a controller, but the constraint on the movement of the segment is physical. The physical constraint can be applied in the handle or the shaft of the device. Naturally, the constraint type is closely related to the advancement method, as the shape is often conserved by the method of propagating.

Software constraint

This group consists of devices that maintain their shape using a software constraint, where advancing segments have a virtually assigned direction. For this group, the shape is held by maintaining the position of the steering actuation. In devices with electric motors, the shape taken by the segment is held by holding the torque at each joint [27, 28, 31] (Figure 2.5a). In devices with cables, the position taken by the segments is kept by holding the tension on each segment [23, 24, 39, 42, 43, 47, 48, 50, 55–58], and in devices with hydraulic actuation by holding the pressure [36] see Figure 2.5b. Devices with SMA actuators hold the shape by maintaining the right temperature for each segment [25, 26] (Figure 2.5c), whereas devices with electromagnets conserve their shape by maintaining the magnetic force [29, 30], Figure 2.3c. When propagating, the segments change their orientation to compensate for

the change in configuration due to the device translation. This behavior can be achieved with inverse kinematics where the device configuration becomes the input for the computerized actuation and/or path planning algorithms that may use cost-functions to minimize the configuration perturbation.

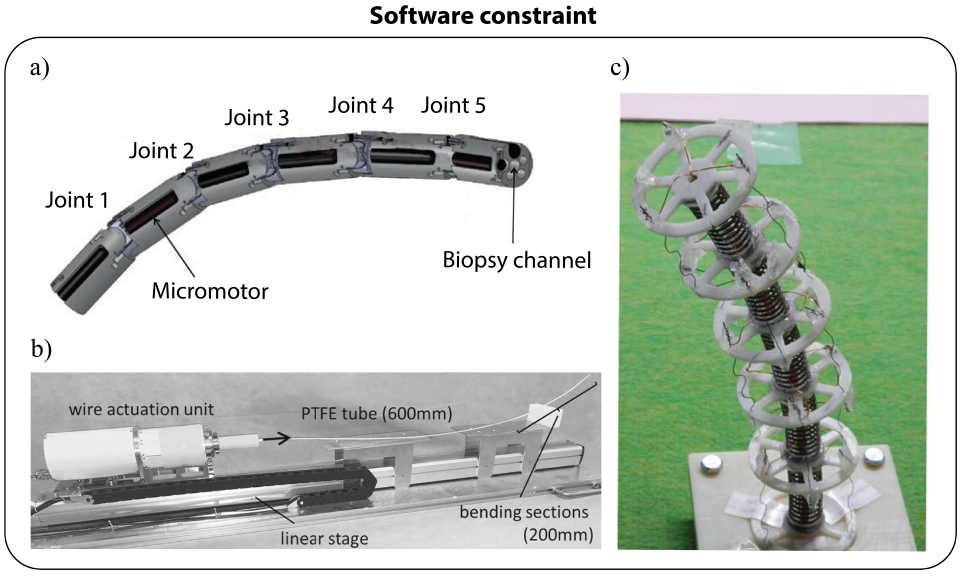

Figure 2.5: Examples of software constraints. a) Motor-based articulated robot. Each DOF is controlled by a motor placed directly into the steerable shaft. The shape is conserved holding the torque. Adapted from [27] ©[2013] IEEE). b) Cable-driven catheter for transbronchial biopsy. The catheter uses a cable-driven push/pull mechanism to control the three steerable segments. The user uses a joystick to actively steer the end-effector and follow the path [42]. c) Manipulator based on SMA actuators. Each segment is controlled by three SMA actuators [25].

Hardware constraint

This group consists of devices where the shaft segments are physically constrained to advance only in the desired direction by a mechanism inside the shaft or the handle of the device. The found methods that generate the forces for shape conservation in devices based on hardware constraints can be subdivided into four groups:

(a) *steering actuation force*

(b) *friction force*

(c) *interlocking geometry force*

(d) *elastic interaction force*

where the shape of the device is maintained by (a) holding the actuation of the steering mechanisms (e.g., by applying torque or maintaining cable tension), (b)

using friction forces in the shaft to prevent segment motion, (c) using interlocking structures in the shaft to prevent segment motion, or (d) leveraging the superposition of elastic interaction forces seeking minimum potential energy.

Most devices leveraging deploying propagation depend on advancing individual segments of the shaft in a particular sequence for the shape conservation method to work. These devices are classified as having a hardware constraint given by steering actuation forces [35, 38, 51, 52, 60, 61]. An example is shown in Figure 2.6a. The proximal segments of the device are advanced first and are steered along the desired path. Once the endpoint of its insertion movement has been reached, the segment stops moving and holds its shape. Thereby, it acts as a guide for a distal, concentrically aligned segment that begins a movement physically constrained to the path taken by the now stationary proximal segment. Since the leader segment is concentrically guided by its proximal follower segments, the device shape always conforms to the path taken by the leader.

The hardware constraint in pre-curved concentric tube devices is given by the elastic relaxation forces of the concentric tubes. If the (stationary) proximal tube has a strongly dominant stiffness relative to the (propagating) distal tube, the (stationary) proximal tube is considered to be a hardware constraint for the (propagating) distal tube [63]. However, if the tubes have similar stiffnesses, the device shape is determined by the superposition of the tube shapes [37, 64–69]. This means that the tubes have to re-orientate collectively to maintain the desired configuration being a hardware constraint for each other. The difference between these concentric tube mechanisms is schematically shown in Figures 2.6b-c. Due to the presence of pre-curved shapes, pre-curved concentric tube devices are limited in the paths they can follow [73].

As opposed to pre-curved concentric tube devices, in alternating devices, the concentric/parallel parts can be alternately locked and fixed in shape so that each of those two parts forms the stationary guide for the other as it propagates. This forms a hardware constraint for the concentric/parallel propagating part that slides along it. The alternating devices found in the literature use friction forces [40, 41, 46, 53, 54] or geometry locks [49] to hold the configuration of the stationary part. The friction force is achieved by compressing the segments with cable tension [40, 41, 53, 54], or by pinching the steering cables with piezo-electric deformation [46], Figure 2.6d. Geometry locking activated by cable tension or SMA actuators in an alternating device is proposed in the patent of Sadaat *et al.* [49]. Other interesting examples are the devices presented by Henselmans *et al.* [44, 45, 59], in which a geometry lock is used in the control handle outside the body to constrain the motion of the segments inside the body. Having the hardware constraint placed into the handle allows for larger space to design a dedicated locking mechanism that acts directly on the actuation of the segment. The locking mechanisms designed by Henselmans *et al.* contain either pre-curved rods [44] (Figure 2.4c), pre-programmed physical tracks [59], or programmable physical tracks, such as the system shown in (Figure 2.6e) [45].

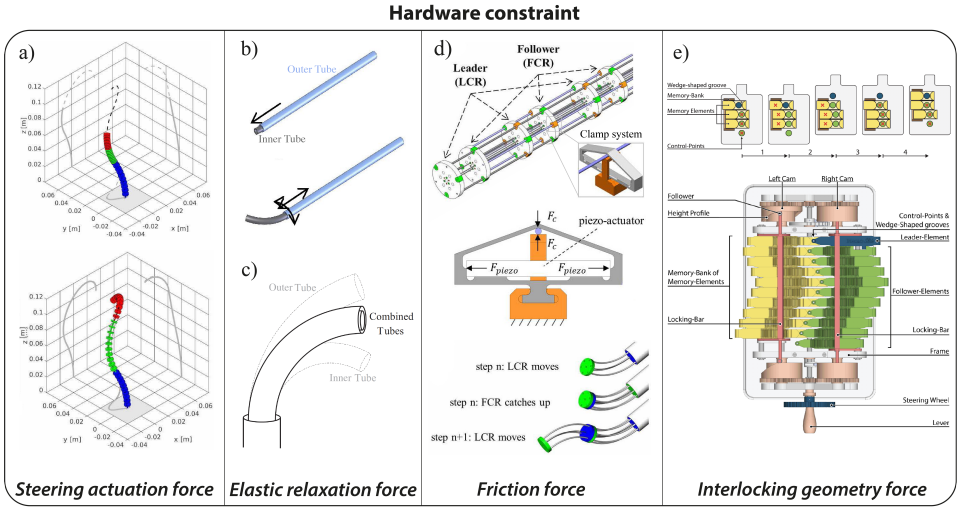

Figure 2.6: Examples of hardware constraints. a) FTL continuum robot. The segments are deployed in order from the most proximal (blue) to the middle (green), and finally the most distal segment (red). The shape of a relative proximal segment is held by the steering cables while its relative distal segments advance concentrically through this fixed curve. Thus, the relative proximal segments form physical constraints to the advancement of the leader/end-effector towards the target [51] (©[2016] IEEE). b) A pair of continuum concentric tubes with relative infinite stiffness of the outer tube (blue). When the inner tube (grey) is retracted, the outer tube dominates the stiffness and therefore the shape. When a portion of the inner tube slides out, the inner tube relaxes to its initial curvature [68] (©[2006] IEEE). c) A pair of continuum concentric tubes with similar stiffness. A superposition of both inner and outer tubes with differently bent aligns the tubes in an intermediate position. The systems hold the configuration with elastic interaction forces, adapted from [74] (©[2006] IEEE). d) The device consists of two identical tendon-driven continuum robots: the follower continuum robot (FCR) and the leader continuum robot (LCR). A clamp system, based on piezo-actuators, pinches the tendons, holding the configuration of the LCR and the FCR, alternately, adapted from [46]. e) The MemoSlide programmable cam. The left figure shows the mechanism responsible for the MemoSlide shifting in which the main components of the mechanism are the leader element (blue), the follower control-points (green), and the memory elements (yellow). A red cross indicates when one of these components is geometrically locked. The right figure shows a top view of the proof-of-concept prototype. The memory and follower elements have teeth on the upper surface. These teeth interlock with the teeth on the bottom surface of the locking-bars (red). When the lever is rotated, the left and right cam operate the sequence. The two bars move out of phase, alternatively locking and releasing the follower and memory-elements, adapted from [45].

2.4. Discussion

2.4.1. Comparison of FTL device performance

Path following ability

One of the primary design goals of FTL medical devices is to allow better access to sites in tortuous anatomy whereas reducing the potential for patient injury due to contact between the shaft of the device and the surrounding tissue. Apart from the risk of injury, poor path-following may also result in longer procedure times, thereby increasing cost [75, 76]. With this in mind, it is naturally of interest to compare FTL devices found in the literature by their relative leader-following capability. This

Table 2.1: Deviation from the propagation path reported by nine FTL devices found in the literature. Publications reporting path deviation data provided either the absolute value in mm (shown in columns 2-4) or as the deviation per unit inserted length, reported in percent (columns 5-7). Table sorted in ascending order of mean percentage deviation. Unreported data is marked with a "-".

	Deviation (mm)			Deviation (%)		
First author (year)	Min.	Mean	Max.	Min.	Mean	Max.
Dupourqué (2019)	-	0.54	-	-	0.27	-
Chen (2014)	13.50	15.00	29.50	1.50	1.60	3.20
Zhang (2019)	2.00	3.35	4.80	1.20	1.60	2.90
Gilbert (2015)	-	2.00	-	-	2.50	-
Amanov (2021)	-	-	-	-	2.60	14.00
Amanov (2017)	6.70	5.00	10.00	9.60	7.10	14.00
Gao (2019)	0.16	-	1.78	0.27	-	3.00
Granna (2016)	-	-	0.81	-	-	5.00
Henselmans (2019)	15.00	-	40.00	13.00	-	36.00

section further compares the reported procedure times, the forces exerted by devices on their environments, and their sizes.

Different metrics may be used to evaluate the path-following ability of a device, such as a root mean square (RMS) error [65] or an overlaid motion footprint [44]. The most common metric, however, is the deviation of the device from its intended path, expressed either as an absolute value or as a percentage of the insertion length of the device being evaluated (Figure 2.7). Many publications do not provide a quantitative assessment of path-following ability, and path deviation depends heavily upon many factors, such as propagation speed, insertion length, and the number and nature of the curves along the path. This makes it difficult to meaningfully identify relationships between device classifications and leader-following ability. Nevertheless, it is interesting to gain a qualitative insight into the capabilities of devices proposed in the literature. Table 2.1 shows the deviation values for nine of the devices found in the literature.

Another important aspect is the ability of the device to precisely follow the described path not only during the device insertion but also during retraction. Only a handful of papers explicitly stated that the device is capable of reversed FTL motion [24, 28, 44–46, 50, 53, 59, 61]. Concentric tubes [61] or alternating devices, such as the HARP [46, 53], can reverse the advancing order of the concentric elements, whereas manually-actuated systems are manually pulled backward [28], or the insertion movement is inverted; i.e., the crank is turned in the opposite direction [44, 45, 59]. However, even if not explicitly stated, electromechanically actuated devices with independent segments should be capable of backward motion by reversing the actuator motion.

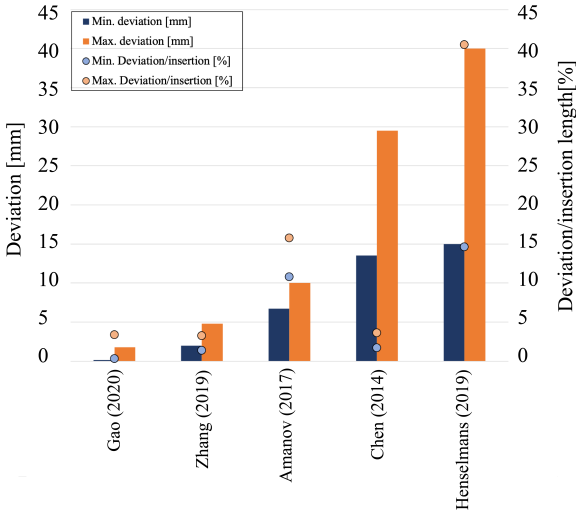

Figure 2.7: Accuracy comparison of the devices that explicitly reported the deviation from the path of the device. The minimum (blue) and maximum (orange) deviation are shown as bars. The dot markers show deviation as a percentage of insertion length, where blue signifies the minimum absolute value and orange the maximum absolute value. The two devices with the lowest reported deviation steer the leader with cables from outside the body, advance in a shifting manner with linear actuators, and apply a software constraint to the device.

Propagation speed

To justify the use of an FTL device in a procedure that can also be carried out conventionally, the device should potentially be safer, more accurate, and enable faster procedure times. The decrease in time, in fact, should not compromise the procedure safety, and the device should not damage the surrounding tissues but rather increase the accuracy of the procedure. Propagation speed, however, is often not explicitly reported as a performance metric and can be affected by the surgeon's experience, and most of the literature deals with an early-stage technology not yet optimized for speed. Information on procedure time is mentioned in only a few publications presenting pre-clinical studies and clinical trial results. The FTL system proposed by Gao *et al.* [43], for example, shows an increased procedure time when performing a ventriculostomy and tumor biopsy in patients with normal anatomy, whereas reporting a significantly reduced procedure time in patients with abnormal anatomy. The HARP device proposed by Degani *et al.*, [40, 41] reports procedure times comparable to operations performed with other robotic platforms for epiglottectomy on a cadaver [77].

Tissue reaction force and operating force

Another relevant performance metric is the magnitude of the forces exerted on the device's surrounding anatomical structures. By decreasing the force applied to the surrounding tissues, potential damage to these tissues can be reduced [42, 47]. Again, only a few publications measured and reported this aspect. For example, the robotic

catheter for transbronchial biopsy proposed by Dupourqué *et al.* reduced the reaction forces measured with a force sensor on the phantom wall from 0.94 N with a manual catheter to 0.13 N and the average path deviation from 0.95 mm to 0.54 mm [42].

The operating forces of some devices are also measured to assess the possibility of supporting other equipment, ensuring stability during the procedure. For example, the robotic endoscope proposed by Lee *et al.* [47] allows the insertion of medical instruments through the central lumen of the device while holding a load of up to 15 N applied either axially or laterally at the distal tip of the device without changing its shape. This was manually measured using a push/pull gauge applied to the end-effector of the device. Likewise, Kang *et al.* stated that their device, shown in Figure 2.6d, ensures an operating force of approximately 4-8 N at an advancement speed of 1.5 mm/s [46]. In this case, the force was measured by externally pushing the device end-effector with a force sensor constrained to a linear stage.

Size

One of the major determinants of potential applications for a flexible medical device is the device's shaft diameter, and 19 publications were found that explicitly reported the diameters and lengths of their respective proposed devices. On the one hand, the shaft diameter is directly related to the surgical application the device is designed for. When the application is for instance in the gastrointestinal tract, the device can reach a diameter of 13 mm [78], whereas in applications such as neurosurgery 3.5 mm in diameter is the maximum [43]. On the other hand, the mechanism used to achieve FTL motion also requires a certain minimum shaft diameter. It was found that devices with actuators located inside the body (Figure 2.8, actuator location "A") have larger diameters than devices with actuators located outside the body (Figure 2.8, actuator location "B"). Pre-curved concentric tube devices with elastic relaxation as steering mechanism (Figure 2.8, steering mechanism "c") have the smallest diameters, followed by devices that apply cable tension (Figure 2.8, steering mechanism "e") from outside the body. Notable exceptions are the devices proposed by Kang *et al.* [46], which has no steering actuators but six shape locking actuators for each segment located inside the body, and the one proposed by Lee *et al.* [47], which is originally designed for NOTES and for which the authors propose many potential size reduction options.

Medical Applications

FTL devices have been developed for different medical fields due to the ability to move through tortuous paths and avoid obstacles (Figure 2.9). Gastrointestinal applications such as gastroscopy or colonoscopy are one of the major application fields [26, 31, 49, 50]. Conventional flexible endoscopes are passively inserted into the colon. However, high forces can be applied to the colon walls increasing the patient's discomfort and creating difficulties for the clinician [79]. Having active navigation during colonoscope insertion would avoid high stress to the colon walls and open new possibilities in diagnostic and treatment for gastrointestinal pathologies.

Chen *et al.* [23] proposed an FTL device able to follow the curves of the colon without relying on the anatomical wall and therefore simplifying the insertion, decreasing the chance of wall damage and patient discomfort. Other examples of FTL sys-

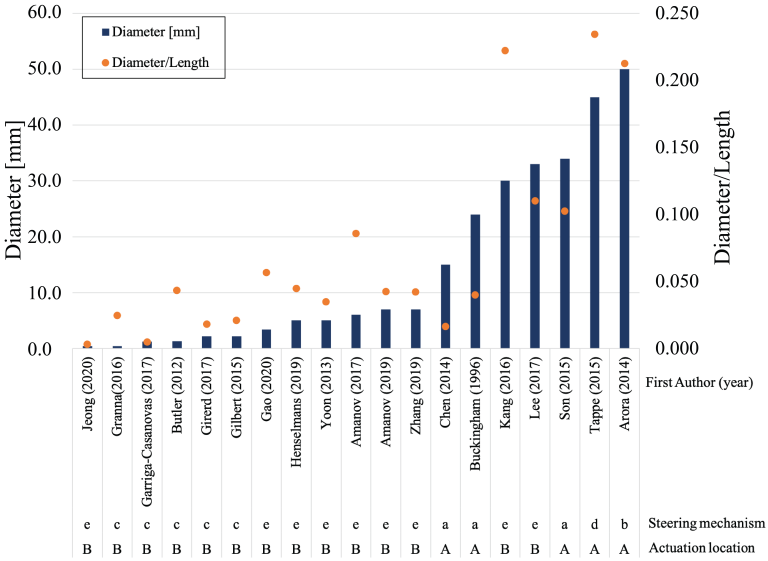

Figure 2.8: Size comparison of the devices with explicitly reported maximum diameter and length, in ascending order of shaft diameter (blue bars). The orange markers show the ratio of diameter to length of each device. The first authors and the device classification are shown underneath the graph; A: actuators inside body, B: actuators outside the body, a: motor torque force, b: thermal deformation force, c: elastic relaxation force, d: electromagnetic force, e: cable tension force.

tems are the device by Gao *et al.* [43] and Yoon *et al.* [56] that find their application in neurosurgery. Gao *et al.* proposed a device for endoscopic third ventriculostomy and tumor biopsy. The device uses FTL motion to minimize tissue trauma while reaching the operation site. Yoon *et al.* designed a device for endoscopic maxillary sinus surgery able to follow the tortuous path through the nasal cavity [55]. Transluminal procedures are also a possible application of FTL devices due to their ability to move in confined spaces and provide a stable platform to operate [27, 45, 47]. Bajo *et al.* proposed an FTL device for transurethral bladder resection that allows the surgeon to operate without *a priori* knowledge with full control of the end-effector DOF [39]. Another possible application is endoscopic biopsies; for example, in organs such as the lungs, the diagnostic sensitivity of biopsies - the success rate of the procedure - is lower than 25% in the peripheral airways due to the difficulties in reaching and extracting the biopsy samples [80].

Dupourqué *et al.* proposed a device for transbronchial biopsy in which the FTL motion enhances the surgeon's maneuverability in reaching the peripheral bronchi of the lungs [42]. Applications can also be found for cardiovascular surgery [41], endovascular interventions [60], and extra-vascular procedures where the FTL device cannot rely on the vessels' wall to follow the desired path [54]. Other possible applications of FTL devices are optical biopsies [65], application of cochlear implants [67], and treating epilepsy with laser ablation of the hippocampus [66].

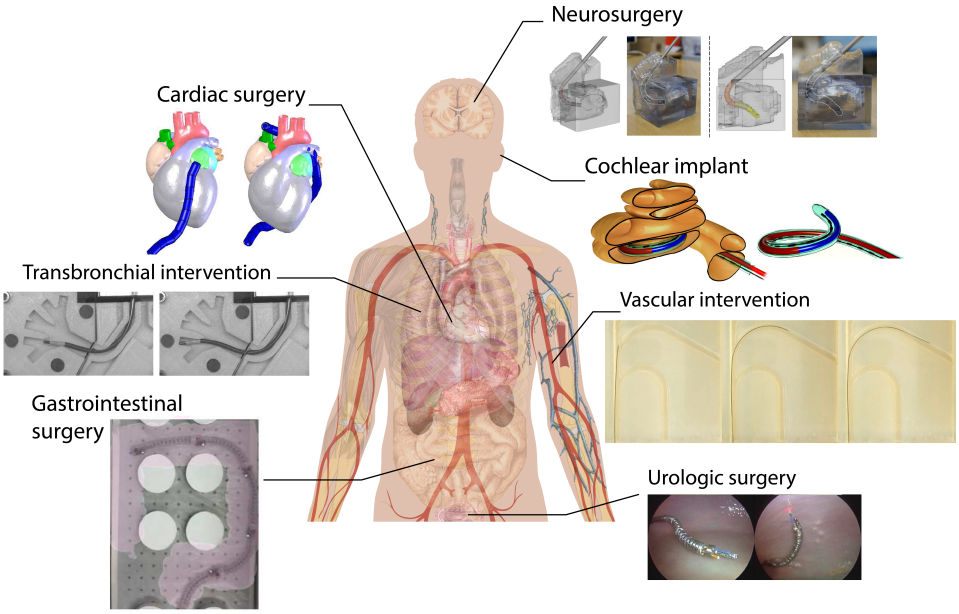

Figure 2.9: Medical applications of FTL devices. Cardiac surgery, adapted from [40] (©[2006] IEEE); neurology, adapted from [55](©[2018] IEEE); cochlear implant [67]; transbronchial intervention, adapted from [42]; vascular intervention, adapted from [60] (©[2020] IEEE); gastrointestinal surgery [23] (©[2014] IEEE); urology, adapted from [39] (©[2013] IEEE).

2.4.2. Common steering and shape conservation strategies

Steering

A widespread design approach in the steering of FTL devices is the combination of actuators located outside the body with tendons transmitting the forces generated by the actuators to the tip of the device. All but one of the 20 devices using tendons to steer the device utilize this strategy. Looking at the published size (Figure 2.8) and performance data (Table 2.1), it becomes clear that the goal of this strategy is to use precise motor control to steer a thinner shaft, a goal achieved with some success. Whereas systems using *elastic relaxation* tend to have smaller diameters Figure 2.8), they tend to have a mediocre path deviation per unit inserted length when compared to cable *tension* based devices. The accuracy of concentric tube robots tends to be highly dependent on the task and the design of the tubes. The tube shapes are specifically designed to achieve optimal pathing and advancement towards the target [81, 82]. Therefore, these devices are often designed for a particular medical procedure that requires a path with a specific, near-constant shape, e.g., neurological procedures [83], treatment of hydrocephalus [63], a biopsy of olfactory cells [64], or cochlear implant insertion [67]. Table 2.1 shows the published path deviation data; Gilbert *et al.* [66] and Granna *et al.* [67] are both *steering/outside body, elastic relaxation* devices, whereas Chen *et al.* [23] utilize tendons combined with actuation

inside the body.

Furthermore, SMA and EM actuators were only found to be used as actuators inside the body [25, 29, 30]. This is most likely since these technologies can create individual actuators that are smaller than standard electric motors, leading designers to attempt to integrate them into the shaft of a device. However, this strategy does not necessarily result in smaller steerable shafts; in Figure 2.8, it can be seen that these devices possess diameters of over 40 mm.

Shape conservation

Software constraints were found to be used by 17 out of 35 systems. These devices were universally found to use their steering actuation to conserve their shape, most likely because this is the simplest way for an electromechanically controlled system to hold its shape: if the actuator maintains its position, the device should stay in the same configuration. This simplicity precludes other additional shape locking strategies such as friction, interlocking geometry, or elastic interactions, as they would add complexity with no real benefit.

Conversely, hardware constraints were used by 18 out of 35 devices with a variety of shape conservation strategies. For example, almost all concentric tube robots utilized their elastic relaxation properties to retain their shape, whereas geometry locking systems were engaged either by cable tension or SMA actuators. Friction locks were used exclusively by three FTL devices, such as the one shown in Figure 2.4f. All three of these devices [40, 41, 46, 53, 54] consist of alternating systems that realize FTL motion due to their ability to alternatingly advance while locking and unlocking their shape.

Two mechanisms were found by which friction was translated to the stiffness of the shaft. Kang *et al.* used friction between piezoelectric clamps and tendons to prevent the tendons from moving relative to the shaft, thereby locking the system's shape [46]. On the other hand, the systems developed by Degani *et al.* and Chen *et al.* used the friction between rigid shaft elements to conserve the shape of the device [40, 54]. Degani's design applies tension on all of the steering wires simultaneously to compress the shaft elements together in the axial direction, whereas Chen's system possesses a dedicated tendon used to compress the elements together. These differing strategies further appear to affect device diameters; Chen *et al.* report a diameter of 6 mm, although as this system uses two parallel shafts, its overall diameter increases to at least 12 mm at the widest point. Degani's design is concentric, but also reports a size of 12 mm. Kang *et al.* cite a much larger diameter of 30 mm due to miniaturization limits with the piezoelectric clamps [46], supporting the argument that including any kind of actuator, even actuators that are already highly miniaturized, in the shaft of a device leads to much larger device diameters.

2.4.3. Design combinations in FTL devices

The designs proposed in the literature tend to cluster around certain combinations of design choices, as shown by Table 2.2. Whereas eight combinations of the two types for each sub-function are theoretically possible (Figure 2.10), only four are published. For example, every single one of the seven devices utilizing actuators inside

Table 2.2: Existing combinations of the three FTL sub-functions in the devices found in the literature. Sub-functions: 1. steering, 2. propagation, 3. conservation. The devices combine types A or B from each sub-function to achieve FTL motion.

Sub-function			Description	Number of devices	References
1	2	3			
A	A	A	Actuation inside body, Shifting propagation, Software constraint	7	[23, 25–29, 31]
B	A	A	Actuation outside body, Shifting propagation, Software constraint	10	[24, 36, 39, 42, 43, 47, 48, 50, 55, 58]
B	A	B	Actuation outside body, Shifting propagation, Hardware constraint	3	[44, 45, 59]
B	B	B	Actuation outside body, Deploying propagation, Hardware constraint	15	[35, 37, 38, 46, 49, 53, 54, 60, 61, 63, 64, 66–69]

the body controls its segments individually, enabling them to propagate in a shifting manner with software constraints. Actuation inside the body is usually less preferred than actuation outside the body due to limits in the miniaturization of the actuation components. However, with the great progress in soft robotics, new solutions can be investigated, leading to combined systems with, for example, actuation inside the body with deployment propagation.

Conservation and propagation are closely related, as the manner of propagation can intrinsically provide shape conservation, particularly in systems that deploy to propagate. All of the 15 devices that advance in a deploying manner use hardware constraints to conserve the shape of the path taken by the leader/end-effector and have actuators located outside the body. Deploying devices exclusively use hardware constraints as their alternating nature means that at least one of the concentric shafts always serves as a physical constraint, making software constraints redundant. Conversely, 17 of the 20 devices propagating in a shifting manner apply a software constraint, as shifting propagation requires individual control of the segments that is commonly combined with feedback control to impose software constraints as discussed in Section 2.3.5. The remaining three devices [44, 45, 59] apply a hardware constraint to the segment shape. Unlike hardware constraints in deploying devices, hardware constraints in shifting devices are located outside the body alongside the actuation system. These constraints act directly on the actuation of a given segment. This constrained actuation is further mechanically coupled to the device translation, resulting in a shifting propagation. The devices proposed by Henselmans *et al.* have a physical track (a programmed cam or a pre-curved rod) that serves as the physical constraint for the segment actuation in the controller [44, 59]. The physically constrained actuation is then transferred with cables to the instrument shaft. Thus, relocating the concentric physical constraint mechanism to a module outside the main body results in a shifting propagation with a hardware constraint. While it is difficult to directly compare devices based on the number of DOF, the inherent expense of including additional actuators in any given robotic system makes it desirable to increase the number of DOF controllable per actuator. Most of the surveyed devices showed a ratio of between 0.5 and 1.5 DOF per actuator. Some devices with hard-

ware constraints showed, however, a higher number of DOF per actuator. Devices with hardware constraints showed a higher number of DOF per actuator. Notable outliers are [44, 59] (with a geometry lock in the handle control), and the alternating device proposed by Degani *et al.* [40], which showed 28, 36, and 17 DOF/actuator, respectively.

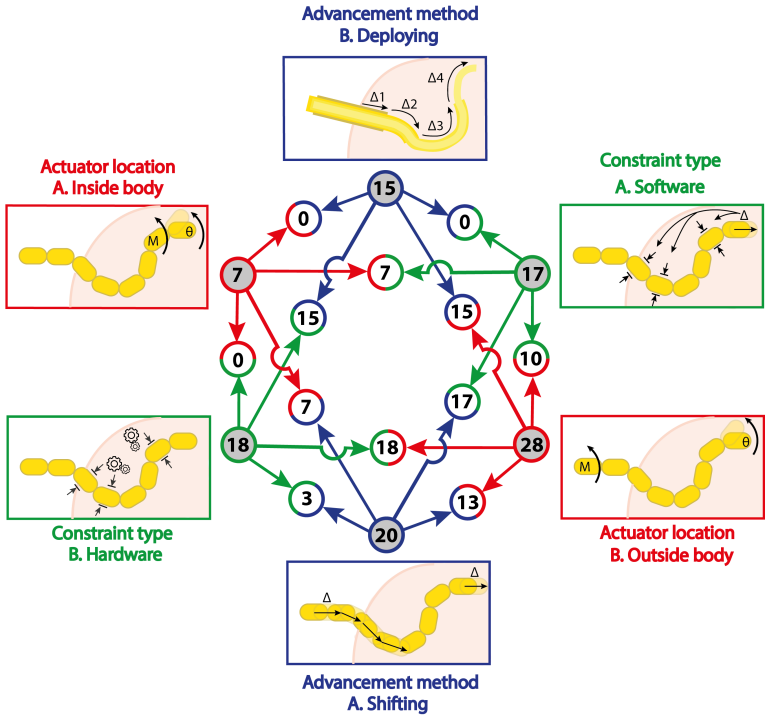

Figure 2.10: Overview of combined sub-functions to achieve FTL motion in medical devices. Three FTL sub-functions steering, propagation, and conservation, associated with the colors red, blue, and green, respectively, are each executed in either type A or B. The number of devices found in the literature that are allocated to each type, is noted in the grey nodes close to the schematic drawings. For example, from the 35 devices 20 advance in a shifting manner (blue: Advancement method A. Shifting) and the remaining 15 devices advance in a deploying manner (blue: Advancement method B. Deploying). The cross combination of two sub-function types is shown in white nodes between the arrows associated with the sub-functions. The color of the perimeter and arrows correspond to the sub-function with the same color. For example, from the 20 devices that propagate in a shifting manner, seven have actuators inside the body (red arrow from A. Inside body and blue arrow from A. Shifting) and 13 have actuators outside the body (red arrow from B. band blue arrow from A. Shifting).

2.4.4. Assessment of alternative solutions for FTL medical devices

Medical devices with FTL potential: Many devices found in the literature contain two of the three sub-functions to achieve FTL motion. Various devices with pneumatic or hydraulic actuation show potential for FTL capabilities with pneumatic or hydraulic actuators. A device excluded uses two pneumatically extensible and bendable seg-

ments in series, Figure 2.11a [84, 85]. Steering each segment is achieved by filling the fluid chambers inside the segment, whereas their configuration is hold using granular jamming, a mechanism used in medical devices or soft robotics to adjust the system stiffness [86, 87]. Keeping a similar configuration to the one proposed by Ranzani *et al.*, an FTL motion could have been achieved using a deploying mechanism to propagate the shape, as for the concentric tubes.

Another excluded device uses hydraulic bellows inside a catheter of 3 mm in diameter to steer the segments [88], Figure 2.11b. Depending on the pressure, the bellows stretch or shrink the segments on one side, making them bend. The system contains special valves that allow for independent control of each segment. The authors claim that the device operates with safe pressures for blood vessels and uses saline solution as a hydraulic fluid. If steering with bellows would be coupled to the displacement of the catheter, FTL motion could be achieved by steering with hydraulic forces that could also be used to hold the path configuration.

An interesting locking mechanism that could be applied for FTL motion is the pneumatic expansion of tubes to lock segments in their orientation of the device shown in Figure 2.11c [89]. Alternating devices, such as the devices shown in Figure 2.4f and 2.7d, could use this locking mechanism to memorize the shape.

FTL motion as a combination between tool and shaft propagation: Many of the reviewed solutions are designed to act as a guide for other instruments, such as biopsy forceps. While this review focused solely on devices with the shaft that performs FTL motion, it is possible that a surgical instrument, inserted through a working channel of the shaft, could take the role of the leader segment, thereby creating a combination instrument/shaft FTL device. This could be advantageous from a human-machine interface perspective, as the forward propagation of the shaft as a whole would be intrinsically tied to the pose of the inserted instrument instead of being a separately-controlled function.

FTL devices with nonmedical applications: As stated in the introduction, many FTL devices have a nonmedical application. This often means that their design is not applicable to medical devices. A few exceptions have been found for FTL devices that have similar design constraints or have the potential to be miniaturized. The device presented by Dong *et al.* features an inspection/repair robot for gas turbines [90]. Some of the specifications are a minimum of 25 DOF, maximum tip diameter of 15 mm, and 1200 mm arm length. The device is steered with cables by actuators outside the segments, advances in a shifting manner with a motor, and applies a software constraint where the steering actuation holds the configuration. Another device, designed for search and rescue operations, uses so-called growth navigation [91], Figure 2.12. The steering is achieved by increasing the length of the device on one side. A pump with air pressure supplied actuates the increase in length. The device advances in a deploying manner with air pressure, and the shape is conserved by a physical constraint where air pressure holds the configuration of the device. The device is also able to retract from a straight position.

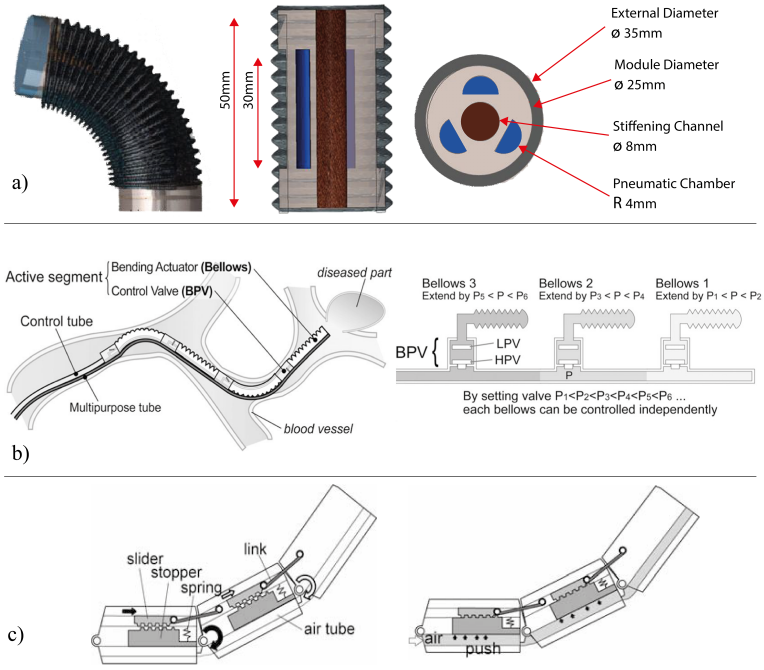

Figure 2.11: Examples of medical devices with FTL potential. a) Fluid actuated segment. Three pneumatic chambers can fill up with air. Combining the inflation of these chambers can bend the segment in various directions. If all chambers are filled, the segment elongates straightly. The stiffening channel (brown) serves as a backbone and contains coffee grains that serve as a granular interlocking substance. The grains in the stiffening channel can be compressed by a vacuum, stiffening the channel, and keeping the orientation of the segment. Adapted from [85] (©[2013] IEEE). b) Hydraulic actuated active catheter. The catheter maneuvers through a blood vessel towards the target. The control tube supplies the fluid to all control valves. Depending on the pressure of the fluid supplied from the control tube, the valve opens and the fluid enters the bellow, making it expand [88] (©[2012] IEEE). c) Pneumatically actuated shape locking mechanism. When the segments bend, the links displace the sliders. The sliders contain teeth that can interlock with the stoppers. If air flows into the air tube, the air tube expands and pushes the stoppers upwards compressing the springs. The interlocking teeth prevent the sliders from moving which fixes the position of the links and therefore the orientation of the segments. If the air leaves the air tube, the compressed springs reset the stoppers downwards. Adapted from [89].

2.4.5. Commercially available instruments

Five of the devices found in the literature are or were commercially available. In 1996, Buckingham and Graham presented the first prototype of a device that had servo motors embedded inside the segments [31]. According to the authors' evaluation, the manipulator had to be five times smaller and place the actuation outside the main body of the device to be used for surgeries. The authors suggested having a device with actuators outside the shaft would help miniaturization. In 2002 Buckingham presented the commercialized version of the prototype proposed in 1996: OC Robotics. The OC Robotics 10 DOF snake arm robot is a tendon-driven device with

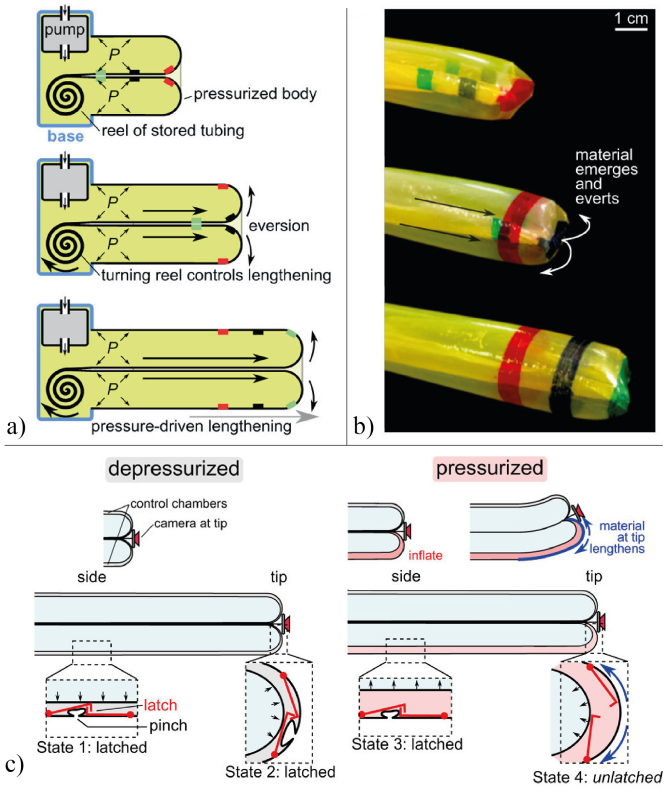

Figure 2.12: Soft robot with growth navigation. a) A schematic side section view of the deploying robot. Air is pumped into the device, reeling out the stored tubing as it everts from the center. b) Picture of the device. c) Steering mechanism. The device has control chambers on the outer edge that contain a series of latches. These latches pinch the outer edge of the control chamber, essentially decreasing its length. The latches behave differently depending on their position (side or tip) and the state of the control chamber (depressurized or pressurized), giving four States. Adapted from [91].

actuators outside the shaft and is commercially available for search and rescue or repair operations [92]. In 2003, OC Robotics patented FTL technology for medical devices [48] and was awarded for NOTES robotic development in 2011 [93]. OC Robotics was mentioned in a review in 2012 [94], including one medical device, but so far, there are no FTL medical devices commercially available from OC Robotics.

Another patented device presented by Saadat *et al.* is affiliated with USGI Medical® [49]. The patent contains a shape locking mechanism that is used in the commercially available catheter from USGI medical® [95]. However, the commercialized catheter does not have a propagating mechanism and associated shape conservation method as described in the patent.

Another device was patented by Donhowe *et al.* [50] in 2013 and today is commercially provided by Intuitive Surgical® as Ion™ [96]. The device, used in bronchoscopy to perform biopsies in the lungs, has a shaft diameter of 3.5 mm and uses path

planning before the intervention with the help of a computed tomography scan to pre-plan its insertion and the retraction. The path is, therefore, predefined and cannot be changed during navigation. Moreover, Ion™ bases its propagation on the surrounding anatomies, and a shape lock mechanism provides rigid support for the biopsy needle. A fiber optic shape sensor measures the full shape of the device during the insertion. A multicenter study is ongoing, but positive preliminary results have already been published [97, 98].

Virtuoso surgical is a start-up [99] basing its technology on the concentric tube robot presented in the work of Gilbert*et al.* [66]. The system is intended to enhance dexterity compared to rigid endoscopes when operating in a single port surgery. Even if the FTL motion seems to have not yet been implemented in the system, future works could propose new generations of endoscopes able to follow and memorize the desired path.

Finally, the HARP, presented by Degani *et al.* (Figure 2.4f), is provided by Medrobotics® (MA, USA) as Flex® Robotic System [100]. The Flex® Robotic System has been tested in cadaveric transoral surgery [77] and evaluated in its performance in various studies [101], showing promising results in colon rectus inspections and in transoral procedures where the mouth is used as the entry port for the surgical procedure [102, 103].

2.4.6. The future of FTL medical devices

Most of the works analyzed in this review, 35 out of 43, have been published within the last ten years. This indicates that the field of FTL medical devices is still in the development phase and that new solutions are expected in the upcoming years. With the advent of soft robotics, research on new materials is being carried out, opening the way to new possibilities for FTL devices. Shape memory alloys (SMA) are widely used in the medical field due to their MRI- and bio-compatibility. In this review, an example of their application is given by Arora *et al.* [25] that use SMA wires to steer their device. Electro-active polymers (EAP) change their stiffness depending on the applied voltage, and they represent a valid alternative to conventional actuation methods. However, even if widely used in general purpose soft robotics [104], EAP scarcely find their application in medical devices due to their need for high voltage, low response time, and low exerted forces [105]. Elastomers such as polydimethylsiloxane (PDMS) are often used in soft robotic systems for minimally invasive surgery [105] due to their low cost, easy availability, and MRI-compatibility. Elastomers are often used in Flexible Fluidic Actuators (FFA), allowing changes in stiffness using air or liquids and avoiding electrical sources [106, 107]. These properties could be used to create an FTL motion in concentric mechanisms. Interesting materials that find application in medical devices are hydrogels. Hydrogels respond to temperature, chemical, magnetic, or electrical stimuli by expanding or shrinking, changing their rigidity and shape [108]. Interesting results have been achieved in the fabrication of soft grippers [109, 110], showing potential for FTL medical devices.

An important aspect that must be taken into consideration is the use of devices as disposable or reusable instruments. Looking at robotic systems, such as the da

Vinci® robotic system (Intuitive Surgical Inc., Sunnyvale, CA, USA), having robotic arms with embedded electronics and miniaturized components leads to a short life span for the instruments and high costs of maintenance [111]. In this scenario, additive manufacturing technology, also known as 3D printing, could open new opportunities for disposable and customized shafts and end-effectors due to the possibility of modifying the design considering surgeon's and patient's needs [112–114]. The implementation of this new technology, together with the implementation of FTL motion in surgical devices, represents a step forward to more personalized medicine.

2.5. Conclusion

FTL motion was divided into three fundamental sub-functions: steering, propagation, and conservation. As each sub-function has two types of solutions, eight combinations are possible, of which only half were found in the literature. Despite being often proposed in medical devices, no FTL devices were found based on pneumatic mechanisms. Device specifications were mostly task-specific although some patterns were apparent for certain design choices. For example, a smaller diameter was chosen for devices with actuators outside the body, in particular pre-curved concentric tube devices. The largest number of DOF per actuator was achieved by devices using hardware constraints to conserve their shape. FTL devices have great potential in the medical field, especially in procedures with abnormal anatomies and unpredictable situations. In this work, we provided a detailed overview of the solutions currently available for FTL devices, reflecting on current limitations and future perspectives. This review offers the foundation that will aid in the development of an innovative generation of medical devices.

References

[1] P. Gavriilidis and K. Katsanos, *Laparoscopic versus open transverse colectomy: a systematic review and meta-analysis,* World journal of surgery **42**, 3008 (2018).

[2] J. A. Warren and M. Love, *Incisional hernia repair: minimally invasive approaches,* Surgical Clinics **98**, 537 (2018).

[3] M. Honda, H. Kumamaru, T. Etoh, H. Miyata, Y. Yamashita, K. Yoshida, Y. Kodera, Y. Kakeji, M. Inomata, H. Konno, *et al.*, *Surgical risk and benefits of laparoscopic surgery for elderly patients with gastric cancer: a multicenter prospective cohort study,* Gastric Cancer **22**, 845 (2019).

[4] N. Kulkarni and T. Arulampalam, *Laparoscopic surgery reduces the incidence of surgical site infections compared to the open approach for colorectal procedures: a meta-analysis,* Techniques in coloproctology , 1 (2020).

[5] T. Xu, S. M. Hutfless, M. A. Cooper, M. Zhou, A. B. Massie, and M. A. Makary, *Hospital cost implications of increased use of minimally invasive surgery,* JAMA surgery **150**, 489 (2015).

[6] H. Hwang, J.-E. Myung, J. W. Yi, S.-S. Lee, and J. Park, *Laparoscopic surgery versus*

open surgery for gastric cancer: big data analysis based on nationwide administrative claims data, Annals of Surgical Treatment and Research **99**, 138 (2020).

[7] B. Shrestha, *Natural orifi ce transluminal endoscopic surgery (notes)-an emerging technique in surgery,* Journal of Nepal Medical Association **51** (2011).

[8] B. Azizi Koutenaei, E. Wilson, R. Monfaredi, C. Peters, G. Kronreif, and K. Cleary, *Robotic natural orifice transluminal endoscopic surgery (r-notes): Literature review and prototype system,* Minimally Invasive Therapy & Allied Technologies **24**, 18 (2015).

[9] B. Dallemagne, S. Perretta, P. Allemann, M. Asakuma, and J. Marescaux, *Transgastric hybrid cholecystectomy,* Journal of British Surgery **96**, 1162 (2009).

[10] Z. Mitros, B. Thamo, C. Bergeles, L. Da Cruz, K. Dhaliwal, and M. Khadem, *Design and modelling of a continuum robot for distal lung sampling in mechanically ventilated patients in critical care,* Frontiers in Robotics and AI **8** (2021).

[11] T. Rahimli, T. Hidayetov, Z. Yusifli, H. Memmedzade, T. Rajabov, and K. Aghayev, *Endoscopic endonasal approach to giant pituitary adenomas. surgical outcomes and review of the literature.* World Neurosurgery (2021).

[12] L. Blanc, A. Delchambre, and P. Lambert, *Flexible medical devices: Review of controllable stiffness solutions,* Actuators **6**, 23 (2017).

[13] A. Loeve, P. Breedveld, and J. Dankelman, *Scopes too flexible... and too stiff,* IEEE pulse **1**, 26 (2010).

[14] H. Choset and W. Henning, *A follow-the-leader approach to serpentine robot motion planning,* Journal of Aerospace Engineering **12**, 65 (1999).

[15] J. Burgner-Kahrs, D. C. Rucker, and H. Choset, *Continuum Robots for Medical Applications: A Survey,* IEEE Transactions on Robotics **31**, 1261 (2015).

[16] H. Komura, H. Yamada, and S. Hirose, *Development of snake-like robot acm-r8 with large and mono-tread wheel,* Advanced Robotics **29**, 1081 (2015).

[17] P. Liljebäck, K. Y. Pettersen, Ø. Stavdahl, and J. T. Gravdahl, *A review on modelling, implementation, and control of snake robots,* Robotics and Autonomous systems **60**, 29 (2012).

[18] Z. Cao, D. Zhang, B. Hu, and J. Liu, *Adaptive path following and locomotion optimization of snake-like robot controlled by the central pattern generator,* Complexity **2019** (2019).

[19] G. Granosik and J. Borenstein, *Integrated joint actuator for serpentine robots,* IEEE/ASME Transactions On Mechatronics **10**, 473 (2005).

[20] S. Inagaki, T. Niwa, and T. Suzuki, *Follow-the-contact-point gait control of centipede-like multi-legged robot to navigate and walk on uneven terrain,* in *2010 IEEE/RSJ International Conference on Intelligent Robots and Systems* (IEEE, 2010) pp. 5341–5346.

[21] L. Tang, J. Wang, Y. Zheng, G. Gu, L. Zhu, and X. Zhu, *Design of a cable-driven hyper-redundant robot with experimental validation,* International Journal of Advanced Robotic Systems **14**, 1729881417734458 (2017).

[22] Q. Fu and C. Li, *Robotic modelling of snake traversing large, smooth obstacles reveals stability benefits of body compliance,* Royal Society open science **7**, 191192 (2020).

[23] Y. Chen, J. Liang, and I. W. Hunter, *Modular continuum robotic endoscope design and path planning,* in *2014 IEEE International Conference on Robotics and Automation (ICRA)* (IEEE, 2014) pp. 5393–5400.

[24] D. Palmer, S. Cobos-Guzman, and D. Axinte, *Real-time method for tip following navigation of continuum snake arm robots,* Robotics and Autonomous Systems **62**, 1478 (2014).

[25] A. Arora, Y. Ambe, T. H. Kim, R. Ariizumi, and F. Matsuno, *Development of a maneuverable flexible manipulator for minimally invasive surgery with varied stiffness,* Artificial Life and Robotics **19**, 340 (2014).

[26] K. Ikuta, M. Tsukamoto, and S. Hirose, *Shape memory alloy servo actuator system with electric resistance feedback and application for active endoscope,* in *Proceedings. 1988 IEEE International Conference on Robotics and Automation* (IEEE, 1988) pp. 427–430.

[27] K.-W. Kwok, K. H. Tsoi, V. Vitiello, J. Clark, G. C. Chow, W. Luk, and G.-Z. Yang, *Dimensionality reduction in controlling articulated snake robot for endoscopy under dynamic active constraints,* IEEE Transactions on robotics **29**, 15 (2012).

[28] J. Son, C. N. Cho, K. G. Kim, T. Y. Chang, H. Jung, S. C. Kim, M.-T. Kim, N. Yang, T.-Y. Kim, and D. K. Sohn, *A novel semi-automatic snake robot for natural orifice transluminal endoscopic surgery: preclinical tests in animal and human cadaver models (with video),* Surgical endoscopy **29**, 1643 (2015).

[29] S. Tappe, J. Pohlmann, J. Kotlarski, and T. Ortmaier, *Towards a follow-the-leader control for a binary actuated hyper-redundant manipulator,* in *2015 IEEE/RSJ International Conference on Intelligent Robots and Systems (IROS)* (IEEE, 2015) pp. 3195–3201.

[30] S. Tappe, J. Kotlarski, T. Ortmaier, M. Dörbaum, A. Mertens, and B. Ponick, *The kinematic synthesis of a spatial, hyper-redundant system based on binary electromagnetic actuators,* in *2015 6th International Conference on Automation, Robotics and Applications (ICARA)* (IEEE, 2015) pp. 211–216.

[31] R. Buckingham and A. Graham, *Computer controlled redundant endoscopy,* in *1996 IEEE International Conference on Systems, Man and Cybernetics. Information Intelligence and Systems (Cat. No. 96CH35929)*, Vol. 3 (IEEE, 1996) pp. 1779–1783.

[32] J. M. Jani, M. Leary, A. Subic, and M. A. Gibson, *A review of shape memory alloy research, applications and opportunities,* Materials & Design (1980-2015) **56**, 1078 (2014).

[33] M. M. Kheirikhah, S. Rabiee, and M. E. Edalat, *A review of shape memory alloy actuators in robotics,* in *Robot soccer world cup* (Springer, 2010) pp. 206–217.

[34] M. Qidwai and D. Lagoudas, *On thermomechanics and transformation surfaces of polycrystalline niti shape memory alloy material,* International journal of plasticity **16**, 1309 (2000).

[35] E. Amanov, T.-D. Nguyen, and J. Burgner-Kahrs, *Tendon-driven continuum robots with extensible sections—a model-based evaluation of path-following motions,* The International Journal of Robotics Research **40**, 7 (2021).

[36] F. Campisano, S. Caló, A. A. Remirez, J. H. Chandler, K. L. Obstein, R. J. Webster III, and P. Valdastri, *Closed-loop control of soft continuum manipulators under tip follower actuation,* The International Journal of Robotics Research **40**, 923 (2021).

[37] C. Bergeles, A. H. Gosline, N. V. Vasilyev, P. J. Codd, J. Pedro, and P. E. Dupont, *Concentric tube robot design and optimization based on task and anatomical constraints,* IEEE Transactions on Robotics **31**, 67 (2015).

[38] E. Amanov, J. Granna, and J. Burgner-Kahrs, *Toward improving path following motion: hybrid continuum robot design,* in *2017 IEEE international conference on robotics and automation (ICRA)* (IEEE, 2017) pp. 4666–4672.

[39] A. Bajo, R. B. Pickens, S. D. Herrell, and N. Simaan, *Constrained motion control of multisegment continuum robots for transurethral bladder resection and surveillance,* in *2013 IEEE International Conference on Robotics and Automation* (IEEE, 2013) pp. 5837–5842.

[40] A. Degani, H. Choset, A. Wolf, and M. A. Zenati, *Highly articulated robotic probe for minimally invasive surgery,* in *Proceedings 2006 IEEE International Conference on Robotics and Automation, 2006. ICRA 2006.* (IEEE, 2006) pp. 4167–4172.

[41] A. Degani, H. Choset, A. Wolf, T. Ota, and M. A. Zenati, *Percutaneous intrapericardial interventions using a highly articulated robotic probe,* in *The First IEEE/RAS-EMBS International Conference on Biomedical Robotics and Biomechatronics, 2006. BioRob 2006.* (IEEE, 2006) pp. 7–12.

[42] L. Dupourqué, F. Masaki, Y. L. Colson, T. Kato, and N. Hata, *Transbronchial biopsy catheter enhanced by a multisection continuum robot with follow-the-leader motion,* International journal of computer assisted radiology and surgery **14**, 2021 (2019).

[43] Y. Gao, K. Takagi, T. Kato, N. Shono, and N. Hata, *Continuum robot with follow-the-leader motion for endoscopic third ventriculostomy and tumor biopsy,* IEEE Transactions on Biomedical Engineering **67**, 379 (2019).

[44] P. W. Henselmans, G. Smit, and P. Breedveld, *Mechanical follow-the-leader motion of a hyper-redundant surgical instrument: Proof-of-concept prototype and first tests,* Proceedings of the Institution of Mechanical Engineers, Part H: Journal of Engineering in Medicine **233**, 1141 (2019).

[45] P. W. J. Henselmans, S. Gottenbos, G. Smit, and P. Breedveld, *The Memo Slide: An explorative study into a novel mechanical follow-the-leader mechanism,* Proceedings of the Institution of Mechanical Engineers, Part H: Journal of Engineering in Medicine **231**, 1213 (2017).

[46] B. Kang, R. Kojcev, and E. Sinibaldi, *The first interlaced continuum robot, devised to intrinsically follow the leader,* PloS one **11**, e0150278 (2016).

[47] H. Lee, K. G. Kim, J. H. Seo, and D. K. Sohn, *Natural orifice transluminal endoscopic surgery with a snake-mechanism using a movable pulley,* The International Journal of Medical Robotics and Computer Assisted Surgery **13**, e1816 (2017).

[48] R. Buckingham and A. Graham, *Robotic positioning of a work tool or sensor,* (2003), uS Patent App. 10/370,190.

[49] V. Saadat, R. C. Ewers, and E. G. Chen, *Shape lockable apparatus and method for advancing an instrument through unsupported anatomy,* (2004).

[50] C. Q. Donhowe, A. Belson, K. J. Donhowe, K. R. Krieg, E. M. Storne, T. J. Yorkey, and J. Zhang, *Method and system for steerable medical device path definition and following during insertion and retraction,* (2013).

[51] M. Neumann and J. Burgner-Kahrs, *Considerations for follow-the-leader motion of extensible tendon-driven continuum robots,* in *2016 IEEE International Conference on Robotics and Automation (ICRA)* (2016) pp. 917–923.

[52] T.-D. Nguyen and J. Burgner-Kahrs, *A tendon-driven continuum robot with extensible sections,* in *2015 IEEE/RSJ International Conference on Intelligent Robots and Systems (IROS)* (2015) pp. 2130–2135.

[53] H. M. Choset, A. Wolf, and M. A. Zenati, *Steerable, follow the leader device,* (2018), uS Patent App. 10,076,235.

[54] Y. Chen, J. H. Chang, A. S. Greenlee, K. C. Cheung, A. H. Slocum, and R. Gupta, *Multi-turn, tension-stiffening catheter navigation system,* in *2010 IEEE International Conference on Robotics and Automation* (IEEE, 2010) pp. 5570–5575.

[55] H.-S. Yoon, J. H. Jeong, and B.-J. Yi, *Image-Guided Dual Master–Slave Robotic System for Maxillary Sinus Surgery,* IEEE Transactions on Robotics **34**, 1098 (2018).

[56] H.-S. Yoon, H.-J. Cha, J. Chung, and B.-J. Yi, *Compact design of a dual master-slave system for maxillary sinus surgery,* in *2013 IEEE/RSJ International Conference on Intelligent Robots and Systems* (IEEE, 2013) pp. 5027–5032.

[57] H.-S. Yoon and B.-J. Yi, *A 4-dof flexible continuum robot using a spring backbone,* in *2009 International Conference on Mechatronics and Automation* (IEEE, 2009) pp. 1249–1254.

[58] Z. Zhang, J. Dequidt, J. Back, H. Liu, and C. Duriez, *Motion control of cable-driven continuum catheter robot through contacts,* IEEE Robotics and Automation Letters **4**, 1852 (2019).

[59] P. Henselmans, C. Culmone, D. Jager, R. van Starkenburg, and P. Breedveld, *The memoflex ii, a non-robotic approach to follow-the-leader motion of a snake-like instrument for surgery using four predetermined physical tracks,* Medical Engineering & Physics **86**, 86 (2020).

[60] S. Jeong, Y. Chitalia, and J. P. Desai, *Design, modeling, and control of a coaxially aligned steerable (coast) guidewire robot,* IEEE Robotics and Automation Letters **5**, 4947 (2020).

[61] B. Qi, Z. Yu, Z. K. Varnamkhasti, Y. Zhou, and J. Sheng, *Toward a telescopic steerable robotic needle for minimally invasive tissue biopsy,* IEEE Robotics and Automation Letters **6**, 1989 (2021).

[62] I. D. Walker, *Continuous Backbone "Continuum" Robot Manipulators,* ISRN Robotics **2013**, 1 (2013).

[63] E. J. Butler, R. Hammond-Oakley, S. Chawarski, A. H. Gosline, P. Codd, T. Anor, J. R. Madsen, P. E. Dupont, and J. Lock, *Robotic neuro-emdoscope with concentric tube augmentation,* in *2012 IEEE/RSJ International Conference on Intelligent Robots and Systems* (IEEE, 2012) pp. 2941–2946.

[64] C. Girerd, A. V. Kudryavtsev, P. Rougeot, P. Renaud, K. Rabenorosoa, and B. Tamadazte, *Slam-based follow-the-leader deployment of concentric tube robots,* IEEE Robotics and Automation Letters **5**, 548 (2020).

[65] C. Girerd, K. Rabenorosoa, P. Rougeot, and P. Renaud, *Towards optical biopsy of olfactory cells using concentric tube robots with follow-the-leader deployment,* in *2017 IEEE/RSJ International Conference on Intelligent Robots and Systems (IROS)* (IEEE, 2017) pp. 5661–5887.

[66] H. B. Gilbert, J. Neimat, and R. J. Webster, *Concentric tube robots as steerable needles: Achieving follow-the-leader deployment,* IEEE Transactions on Robotics **31**, 246 (2015).

[67] J. Granna, T. S. Rau, T.-D. Nguyen, T. Lenarz, O. Majdani, and J. Burgner-Kahrs, *Toward automated cochlear implant insertion using tubular manipulators,* in *Medical Imaging 2016: Image-Guided Procedures, Robotic Interventions, and Modeling*, Vol. 9786 (International Society for Optics and Photonics, 2016) p. 97861F.

[68] P. Sears and P. Dupont, *A steerable needle technology using curved concentric tubes,* in *2006 IEEE/RSJ international conference on intelligent robots and systems* (IEEE, 2006) pp. 2850–2856.

[69] A. Garriga-Casanovas and F. Rodriguez y Baena, *Complete follow-the-leader kinematics using concentric tube robots,* The International Journal of Robotics Research **37**, 197 (2018).

[70] J. Burgner-Kahrs, H. B. Gilbert, J. Granna, P. J. Swaney, and R. J. Webster, *Workspace characterization for concentric tube continuum robots,* in *2014 IEEE/RSJ International Conference on Intelligent Robots and Systems* (IEEE, 2014) pp. 1269–1275.

[71] H. B. Gilbert, D. C. Rucker, and R. J. Webster III, *Concentric tube robots: The state of the art and future directions,* in *Robotics Research* (Springer, 2016) pp. 253–269.

[72] A. W. Mahoney, H. B. Gilbert, and R. J. Webster III, *A review of concentric tube robots: modeling, control, design, planning, and sensing,* The Encyclopedia of MEDICAL ROBOTICS: Volume 1 Minimally Invasive Surgical Robotics , 181 (2019).

[73] H. B. Gilbert and R. J. Webster, *Can concentric tube robots follow the leader?* in *2013 IEEE international conference on robotics and automation* (IEEE, 2013) pp. 4881–4887.

[74] R. J. Webster, A. M. Okamura, and N. J. Cowan, *Toward active cannulas: Miniature snake-like surgical robots,* in *2006 IEEE/RSJ international conference on intelligent robots and systems* (IEEE, 2006) pp. 2857–2863.

[75] R. E. Perez and S. Schwaitzberg, *Robotic surgery: finding value in 2019 and beyond,* Ann Laparosc Endosc Surg **4**, 51 (2019).

[76] I. G. Jeong, Y. S. Khandwala, J. H. Kim, D. H. Han, S. Li, Y. Wang, S. L. Chang, and B. I. Chung, *Association of robotic-assisted vs laparoscopic radical nephrectomy with perioperative outcomes and health care costs, 2003 to 2015,* Jama **318**, 1561 (2017).

[77] P. J. Johnson, C. M. R. Serrano, M. Castro, R. Kuenzler, H. Choset, S. Tully, and U. Duvvuri, *Demonstration of transoral surgery in cadaveric specimens with the medrobotics flex system,* The Laryngoscope **123**, 1168 (2013).

[78] M. Kay and R. Wyllie, *Colonoscopy, polypectomy, and related techniques,* in *Pediatric gastrointestinal and liver disease* (Elsevier, 2011) pp. 650–667.

[79] A. J. Loeve, P. Fockens, and P. Breedveld, *Mechanical analysis of insertion problems and pain during colonoscopy: why highly skill-dependent colonoscopy routines are necessary in the first place... and how they may be avoided,* Canadian Journal of Gastroenterology **27**, 293 (2013).

[80] D. P. Steinfort, Y. H. Khor, R. L. Manser, and L. B. Irving, *Radial probe endobronchial ultrasound for the diagnosis of peripheral lung cancer: systematic review and meta-analysis,* European Respiratory Journal **37**, 902 (2011).

[81] C. Bedell, J. Lock, A. Gosline, and P. E. Dupont, *Design optimization of concentric tube robots based on task and anatomical constraints,* in *2011 IEEE international conference on robotics and automation* (IEEE, 2011) pp. 398–403.

[82] J. Burgner, D. C. Rucker, H. B. Gilbert, P. J. Swaney, P. T. Russell, K. D. Weaver, and R. J. Webster, *A telerobotic system for transnasal surgery,* IEEE/ASME Transactions on Mechatronics **19**, 996 (2013).

[83] X. Yang, S. Song, L. Liu, T. Yan, and M. Q.-H. Meng, *Design and optimization of concentric tube robots based on surgical tasks, anatomical constraints and follow-the-leader deployment,* IEEE Access **7**, 173612 (2019).

[84] T. Ranzani, G. Gerboni, M. Cianchetti, and A. Menciassi, *A bioinspired soft manipulator for minimally invasive surgery,* Bioinspiration & biomimetics **10**, 035008 (2015).

[85] M. Cianchetti, T. Ranzani, G. Gerboni, I. De Falco, C. Laschi, and A. Menciassi, *Stiff-flop surgical manipulator: Mechanical design and experimental characterization of the single module,* in *2013 IEEE/RSJ international conference on intelligent robots and systems* (IEEE, 2013) pp. 3576–3581.

[86] L. Blanc, A. Pol, B. François, A. Delchambre, P. Lambert, and F. Gabrieli, *Granular jamming as controllable stiffness mechanism for medical devices,* in *Micro to MACRO Mathematical Modelling in Soil Mechanics* (Springer, 2018) pp. 57–66.

[87] N. G. Cheng, M. B. Lobovsky, S. J. Keating, A. M. Setapen, K. I. Gero, A. E. Hosoi, and K. D. Iagnemma, *Design and analysis of a robust, low-cost, highly articulated manipulator enabled by jamming of granular media,* in *2012 IEEE international conference on robotics and automation* (IEEE, 2012) pp. 4328–4333.

[88] K. Ikuta, Y. Matsuda, D. Yajima, and Y. Ota, *Pressure pulse drive: A control method for the precise bending of hydraulic active catheters,* IEEE/ASME Transactions on Mechatronics **17**, 876 (2011).

[89] A. Yagi, K. Matsumiya, K. Masamune, H. Liao, and T. Dohi, *Rigid-flexible outer sheath model using shape lock mechanism by air pressure and wire driven curving mechanism,* in *World Congress on Medical Physics and Biomedical Engineering 2006* (Springer, 2007) pp. 3108–3111.

[90] X. Dong, D. Axinte, D. Palmer, S. Cobos, M. Raffles, A. Rabani, and J. Kell, *Development of a slender continuum robotic system for on-wing inspection/repair of gas turbine engines,* Robotics and Computer-Integrated Manufacturing **44**, 218 (2017).

[91] E. W. Hawkes, L. H. Blumenschein, J. D. Greer, and A. M. Okamura, *A soft robot that navigates its environment through growth,* Science Robotics **2** (2017).

[92] R. Buckingham, *Snake arm robots,* Industrial Robot: An International Journal (2002).

[93] O. Robotics, *Swrda awards oc robotics research grant to develop surgical snake-arm robot,* (2011), https://www.ocrobotics.com/news/swrda-awards-oc-robotics-research-grant-to-develop-surgical-snakearm-robot/, Accessed: 2021-02-22.

[94] R. Bloss, *Snake-like robots "reach" into many types of applications,* Industrial Robot: An International Journal (2012).

[95] L. L. Swanstrom, R. Kozarek, P. J. Pasricha, S. Gross, D. Birkett, P.-O. Park, V. Saadat, R. Ewers, and P. Swain, *Development of a new access device for transgastric surgery,* Journal of gastrointestinal surgery **9**, 1129 (2005).

[96] I. Surgical, *Iontm by intuitivetm. a robotic-assisted endoluminal platform for minimally invasive peripheral lung biopsy,* (2021), https://www.intuitive.com/en-us/products-and-services/ion, Accessed: 2021-02-22.

[97] E. Folch, M. Pritchett, J. Reisenauer, D. Ost, A. Majid, S. Fernandez-Bussy, C. Keyes, M. Parikh, J. Diaz-Mendoza, R. Casal, *et al.*, *A prospective, multi-center evaluation of the clinical utility of the ion endoluminal system-experience using a robotic-assisted bronchoscope system with shape-sensing technology,* in *A110. ADVANCES IN INTERVENTIONAL PULMONOLOGY* (American Thoracic Society, 2020) pp. A2719–A2719.

[98] A. Agrawal, D. K. Hogarth, and S. Murgu, *Robotic bronchoscopy for pulmonary lesions: a review of existing technologies and clinical data,* Journal of Thoracic Disease **12**, 3279 (2020).

[99] V. S. Inc., *Virtuoso surgical,* (2021), https://virtuososurgical.net/, Accessed: 2021-09-09.

[100] M. Corporation, *Flex® robotic system: Expanding the reach of surgery®,* (2021), https://medrobotics.com/gateway/flex-system-int/, Accessed: 2021-02-22.

[101] S. Mattheis, P. Hasskamp, L. Holtmann, C. Schäfer, U. Geisthoff, N. Dominas, and S. Lang, *Flex robotic system in transoral robotic surgery: the first 40 patients,* Head & neck **39**, 471 (2017).

[102] M. Remacle, V. Prasad, G. Lawson, L. Plisson, V. Bachy, and S. Van der Vorst, *Transoral robotic surgery (tors) with the medrobotics flex™ system: first surgical application on humans,* European Archives of Oto-Rhino-Laryngology **272**, 1451 (2015).

[103] N. Sethi, M. Gouzos, V. Padhye, E. Ooi, A. Foreman, S. Krishnan, and J. Hodge, *Transoral robotic surgery using the medrobotic flex® system: the adelaide experience,* Journal of robotic surgery **14**, 109 (2020).

[104] I. D. Walker, D. M. Dawson, T. Flash, F. W. Grasso, R. T. Hanlon, B. Hochner, W. M. Kier, C. C. Pagano, C. D. Rahn, and Q. M. Zhang, *Continuum robot arms inspired by cephalopods,* in *Unmanned Ground Vehicle Technology VII*, Vol. 5804 (International Society for Optics and Photonics, 2005) pp. 303–314.

[105] M. Runciman, A. Darzi, and G. P. Mylonas, *Soft robotics in minimally invasive surgery,* Soft robotics **6**, 423 (2019).

[106] M. Cianchetti, C. Laschi, A. Menciassi, and P. Dario, *Biomedical applications of soft robotics,* Nature Reviews Materials **3**, 143 (2018).

[107] M. Manti, V. Cacucciolo, and M. Cianchetti, *Stiffening in soft robotics: A review of the state of the art,* IEEE Robotics & Automation Magazine **23**, 93 (2016).

[108] Y. Lee, W. Song, and J.-Y. Sun, *Hydrogel soft robotics,* Materials Today Physics **15**, 100258 (2020).

[109] E. Palleau, D. Morales, M. D. Dickey, and O. D. Velev, *Reversible patterning and actuation of hydrogels by electrically assisted ionoprinting,* Nature communications **4**, 1 (2013).

[110] J. Zheng, P. Xiao, X. Le, W. Lu, P. Théato, C. Ma, B. Du, J. Zhang, Y. Huang, and T. Chen, *Mimosa inspired bilayer hydrogel actuator functioning in multi-environments,* Journal of Materials Chemistry C **6**, 1320 (2018).

[111] R. Prewitt, V. Bochkarev, C. L. McBride, S. Kinney, and D. Oleynikov, *The patterns and costs of the da vinci robotic surgery system in a large academic institution,* Journal of robotic surgery **2**, 17 (2008).

[112] C. Culmone, P. W. Henselmans, R. I. van Starkenburg, and P. Breedveld, *Exploring non-assembly 3d printing for novel compliant surgical devices,* Plos one **15**, e0232952 (2020).

[113] T. K. Morimoto and A. M. Okamura, *Design of 3-D Printed Concentric Tube Robots,* IEEE Trans. Robotics **32**, 1419 (2016).

[114] K. Oliver-Butler, Z. H. Epps, and D. C. Rucker, *Concentric agonist-antagonist robots for minimally invasive surgeries,* in *Proc. SPIE 10135, Medical Imaging 2017: Image-Guided Procedures, Robotic Interventions, and Modeling*, Vol. 10135 (2017) p. 1013511.

3

Follow-the-Leader Shape Memory System for Minimally Invasive Surgery

Accepted as:
Culmone, C., Jager D. J., and Breedveld, P. "MemoBox: A Mechanical Follow-the-Leader system for Minimally Invasive Surgery". Frontiers in Medical Technology, (2022)

Abstract

With the increase in Natural Orifice Transluminal Endoscopic Surgery procedures, there is an increasing demand for surgical instruments with additional degrees of freedom, able to travel along tortuous pathways and guarantee dexterity and high accuracy without compromising the surrounding environment. The implementation of follow-the-leader motion in surgical instruments allows propagating the decided shape through its body and moving through curved paths avoiding sensitive areas. Due to the limited operational area and therefore the instrument size, the steerable shaft of these instruments is usually driven by cables that are externally actuated. However, a large number of degrees of freedom requires a great number of actuators, increasing the system complexity. Therefore, our goal was to design a new memory system able to impose a follow-the-leader motion to the steerable shaft of a medical instrument without using actuators. We present a memory mechanism to control and guide the cable displacements of a cable-driven shaft able to move along a multi-curved path. The memory mechanism is based on a programmable physical track with a mechanical interlocking system. The memory system, called MemoBox, was manufactured as a proof of concept demonstration model, measuring 70x64x6 mm^3 with 11 programmable elements and featuring a minimum resolution of 1 mm. The prototype shows the ability to generate and shift complex 2D pathways in real-time controlled by the user.

3.1. Introduction

Minimally invasive surgery (MIS) aims at reducing the invasiveness of a surgical procedure by using small incisions as the entry port of the human body. By reducing the incision size, the chance of exposure-related infections, pain, and recovery time decrease drastically. A step forward has been made with the introduction of Natural Orifice Transluminal Endoscopic Surgery (NOTES), in which surgeons can operate and enter the human body using natural orifices such as mouth, nose, or anus [1–3]. For instance, Endoscopic Endonasal Surgery (EES) is a NOTES procedure in which the nostrils are the entry port to reach and remove tumors at the base of the skull, such as those occurring in the pituitary gland. The pituitary gland is difficult to reach because the nostrils create a narrow passage that limits the maneuverability of the tools. Therefore, by using conventional straight and rigid instruments, some tumors cannot be reached or removed entirely, and patients require further treatment [4, 5]. Instruments such as flexible endoscopes or catheters usually have a passively flexible shaft, and only in some of them, the end-segment can be actively controlled and articulated. These instruments usually need support from the surrounding environments that constrain and guide them through organs such as the intestines or the blood vessels. However, soft tissues and delicate anatomies, such as those in the skull base and around the pituitary gland, cannot provide enough support for such instruments, leading to the need for having instruments capable of self-support and self-guidance.

In 1999, Choset and Henning minted the new term "Follow-the-Leader" (FTL), also known as path following, to refer to a new kind of motion behavior of segmented snake-like robots [6]. In FTL-motion, the user steers the head (the most distal segment) of the robot. The pose information is stored and passed back to the other segments in order to let them assume the same pose once they have translated to the same location in space. Therefore, the user only controls the position of the first segment, the so-called "leader". At the same time, the other segments follow the trajectory created by the leader, mimicking the obstacle-avoiding motion of a snake through its environment. The controlled navigation of FTL-instrumentation can be a valuable alternative not only in EES but in many other surgical scenarios. Applications can also be found in interventional bronchoscopy, in which a steerable bronchoscope is inserted into the bronchi to perform diagnostic biopsies. Bronchi branches are delicate and thin, and when the target lesion is located in a peripheric area of the lungs, the diagnostic sensitivity, which is the percentage of successfully diagnosed lesions, is very low (<25%) [7]. FTL-instruments could bring bronchoscopy to a higher level and help the surgeon to navigate through peripheric bronchi and increase the diagnostic sensitivity. Another possible application is in the trans-catheter replacement of cardiac valves such as the aortic valve [8] or mitral valve [9]. During these procedures, the femoral artery for the aortic valve, or the femoral vein for the mitral valve, are used to insert the catheter and bring the new valve to the heart. Especially in the mitral valve replacement, the catheter needs to navigate through the beating heart to position the new valve correctly. During navigation, FTL-instruments could help the surgeon to precisely control the motion for catheter insertion and retraction.

3.2. State-of-the-art

3.2.1. Snake-like surgical robots

FTL-motion has been implemented into a number of surgical instruments. Snake-like robots based on a hyper-redundant structure have each rigid segment connected to the adjacent segment(s) by means of rigid joints. Those rigid joints are usually driven by individual embedded actuators (intrinsic). Having individual actuators allows direct control over the segment; however, miniaturization is challenging [10, 11]. Therefore, possible applications are limited to procedures such as colonoscopy, in which the diameter of the instruments can be larger than 10 mm [12–14]. Miniaturization is instead possible with actuators placed outside the main body of the instrument (extrinsic), leading to fewer spatial limitations [15, 16], less issues with sterilization [17], and possible low-cost disposable use [18, 19]. Surgical robots can also be categorized into two main groups considering the shape propagation method: shape-deploying and shape-shifting [20, 21] Figure 3.1.

Shape deploying robots mainly comprise telescopic robots and alternating robots. Telescopic robots are usually concentric tube continuum robots based on pre-curved elastic components concentrically nested into each other. Motors are placed outside the robot and enable sliding and rotation of the tubes over one another. Due to the difference in stiffness of the concentric tubes, the robot can create various paths [22, 23]. These robots can achieve FTL-motion by controlling the actuation mechanism; however, FTL-motion is limited to specific paths related to the pre-curves of the elastic tubes, requiring prior planning of the trajectory [24, 25]. The research group of Burgner-Kahrs developed a hybrid cable-driven continuum robot in which a telescopic backbone is combined with magnetic spacer disks to control the arc lengths and the curvature of the bending section during the FTL-motion [16, 26]. They also present an alternative hybrid continuum robot in which two nested Nitinol tubes, equipped with spacer disks, use a cable-driven actuation method to achieve FTL-motion [27]. An evaluation of these two robots showed that they were able to perform specific

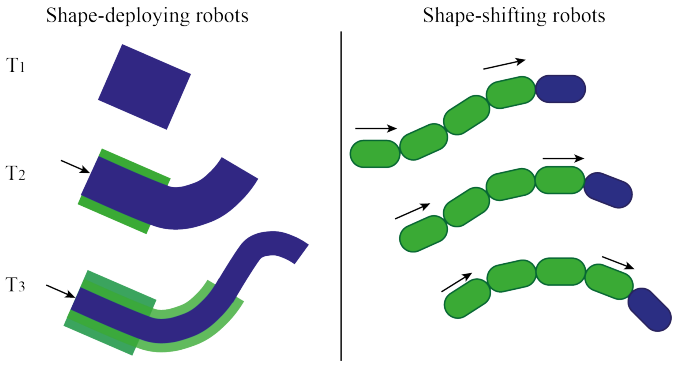

Figure 3.1: Categorization of FTL surgical robots with extrinsic actuators: shape-deploying (left) and shape-shifting robots (right). Blue indicates the leader segment and green the follower segment(s). T_1, T_2, and T_3 indicate three different phases of the shape propagation.

single and double-curved paths.

Alternating robots are based on actively stiffening their components in an alternating fashion to create the desired path [21]. The Highly Articulated Robot Probe (HARP), also known as CardioArm or FlexRobotic System [28], is based on a friction-based locking system between rigid cylindrical links and spherical joints [29–31]. The alternation between a rigid and a limp state of two concentric tubes allows the robot to follow a specific path decided in real-time by the user. However, due to the large dimensions (Ø10 mm in the commercialized version), applications are limited to the colon, rectum, or laryngopharyngeal complex [28, 32].

In shape-shifting robots, the position and steering angle of the first distal segment are actively controlled by the user, whereas the following segments assume the steering angle and position of the segment in front of them as the instrument moves ahead. Usually, surgical robots that belong to this group are made of a large number of segments (hyper-redundant). The segments are steered by cables and individually controlled by electric motors placed at the proximal part of the instrument and therefore separated from the robot's snake-like body [33–35]. In these robots, each degree of freedom (DOF) requires a dedicated actuator as transferring back the shape among the follower segments requires simultaneous control of all the segments. The use of a large number of motors leads to a complexity higher than strictly necessary for FTL-motion that, in principle, only needs to actively control the pose of the leader segment and passively transfer it to the follower segments.

3.2.2. Mechanical shape-shifting devices

A first attempt to avoid the use of electrical actuators in shape-shifting devices is a fully mechanically-controlled and cable-driven instrument developed by Henselmans *et al.* [36]. They developed a master-slave system in which a pre-curved steel rod is read out by the master, which passes the pose information to a Ø5 mm slave shaft that mimics the shape of the steel rod. A second fully mechanically-controlled and cable-driven prototype is the so-called MemoFlex II [20]. This device has a snake-like shaft of 16 segments that are steered by steering cables. The steering cables are fixed to control points, and the main body of the device (also called revolver) allows their backward and forward motion. To define the path of the control points, a track ring that contains fixed curved grooves representing pre-defined physical tracks rotates around the revolver and guides the control points. A chassis synchronizes the rotation of the track ring with the forward motion of the snake-like shaft using coupled grooves so that the motion of the shaft will correspond with the pre-defined curvature of the fixed tracks.

Although both these instruments function quite well, they have the drawback of being designed to follow a pre-defined path. By using pre-operative MRI or CT imaging data, the surgeon, determines the path to be followed beforehand without the possibility of changing direction or adjusting the position of the shaft during the procedure, limiting his/her action. The goal of this research is to design a fully mechanical memory system able to achieve an FTL-motion for shape-shifting mechanisms. The new memory system should memorize the pose information of the leader segment

and propagate the shape to the follower segments. The mechanism should be able to perform a variety of different path shapes, such as single, double, or multi-curved paths. Moreover, the FTL-motion should be adjustable in real-time without a priori knowledge of the path.

3.3. Concept design

3.3.1. Cable-driven FTL-propagation

Shape-shifting devices are usually based on cable-driven mechanisms that offer the possibility of having a high number of degrees of freedom while keeping the diameter of the shaft small. The minimum number of cables for steering one segment in two DOF is three. The use of four cables, placed in diametrically opposite positions in the shaft cross-section, allows antagonistic movement of the cables, simplifying their control. Figure 3.2 shows that when a steerable segment is bent to an angle α by applying a specific displacement Δs to a steering cable, the antagonistic cable is displaced by the same Δs in the opposite direction. Thus, passing the displacement Δs of the leader segment to the follower segments allows an FTL-motion in a shape-shifting device. Figure 3.2 shows an example of a multi-steerable shaft with 16 segments. Each segment is controlled by four cables and has two DOF. In an FTL-motion of the shaft, the displacement Δs of leader segment 1 shifts back to the follower segment 2. Then, leader segment 1 will assume a new pose, and the new displacement Δs will be pass backward to follower segment 2. The process will continue until reaching the target.

Figure 3.3a shows a 2D representation of an FTL system with six segments. The bending angle of the leader segment (blue in Figure 3.3a) corresponds to a translation along the y-axis of the corresponding control point (also blue). As previously discussed, due to the symmetry of the system, the displacement Δs of the tensioned cable is equal to the released Δs of the antagonist cable. By steering the leader seg-

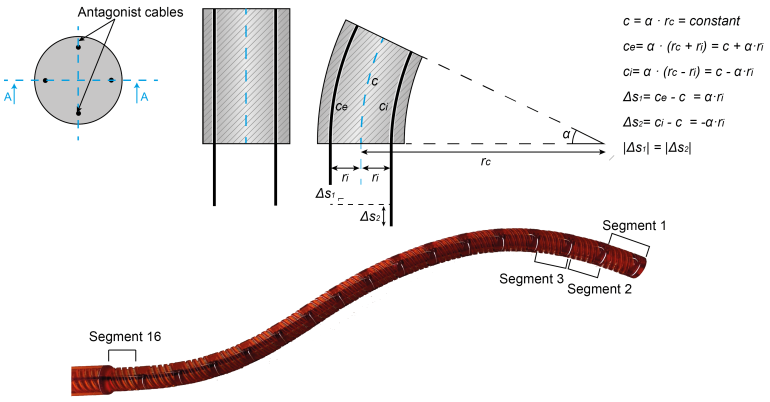

Figure 3.2: Cable-driven segments. Four-cable control of a steerable segment and an example of a Ø 8 mm cable-driven shaft with 16 segments. Segment 1 is the leader segment. Adapted from [20].

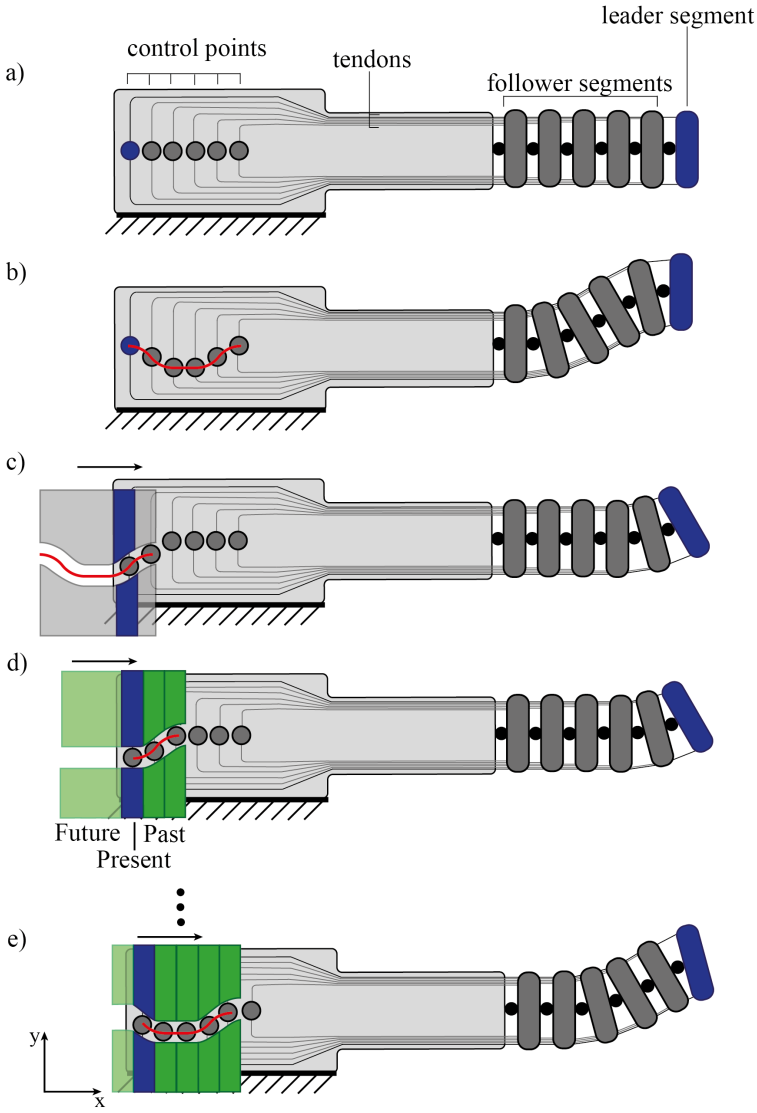

Figure 3.3: Schematic representation of a six-segmented system employing Follow-The Leader (FTL) propagation. a) Main components of a cable-driven FTL system, showing: the control points (grey circles) with the leader control point that controls the leader segment in blue, the cables, and the follower segments. b) A path is defined by individually controlling the control points. c) A pre-defined physical track, superimposed to the system, can substitute the individually controlled points giving a pre-defined path. d-e) The pre-defined physical track is replaced by a programmable physical track composed out of a number of steering elements that can be individually translated along the y-axis and locked into position. Light green represents the future, blue represents the present, and dark green the past. The red line represents the path.

ment, memorizing its pose, and advancing the system forward along the x-axis, the information is passed backward. This information is the displacement of the leader control point passes to the second control point, the information of the second control point to the third, and so on (Figure 3.3b). The three actions, steering, memorizing, and advancing, are repeated until reaching the target area. In the representation of Figure 3.3b, each control point has to be independently actuated to pass back its position to the follower segment and to take the new position from the previous control point. By superimposing a pre-defined physical track on the set of control points, we pass from an FTL-mechanism that acts directly on the control points to an FTL-mechanism integrated into the pre-defined physical track. This means that, in an ideal situation, a fixed physical track is capable of taking over the role of the single actuators and perform a pre-programmed path (Figure 3.3c).

Using a pre-defined physical track, however, means that the track cannot be changed in real-time but can only follow the pre-defined path, which is a disadvantage [20]. Discretizing the pre-defined physical track into a set of steering elements that can be translated into position and locked gives a solution (Figures 3.3d-e). In such a programmable physical track, the steering elements can be divided into three groups resembling the past, the present, and the future. The past (dark green) corresponds to the steering elements already translated into position and locked. The present (blue) corresponds to the steering element that will be the next one to assume a new position, and therefore the leader element that controls the leader segment of the tip. The future (light green) corresponds to the steering elements not yet defined in their position. The main functions that such a programmable memory system must provide are then:

I Steering the leader segment by translating the leader control point

II Memorizing the position given to the leader control point

III Advancing while passing the pose information memorized backwards to the follower control points (leader to second, second to third, etc.)

Pre-defined physical tracks can pass the pose information backward (III) but do not allow the position to be controlled in real-time (I-II).

3.3.2. Memory mechanism

As shown in Figure 3.4, to program a path, the steering element representing the present (blue) must be decoupled from the past (Phase 1: decoupling) and moved to a position of the user's choice (Phase 2: steering). In this phase, the future steering elements (light green) are locked to the present steering element and travel with it as a single part. When the desired position is reached, the present steering element is coupled again with the past (Phase 3: coupling), the system is advanced one step forwards (Phase 4: advancing), and a new steering element becomes the blue present. This new present steering element is then again decoupled from the past, and the cycle repeats. The past (dark green) remains locked in place, and, as the

cycle repeats, more steering elements are added to the past to form a programmable path, visualized by the red lines in Figure 3.4.

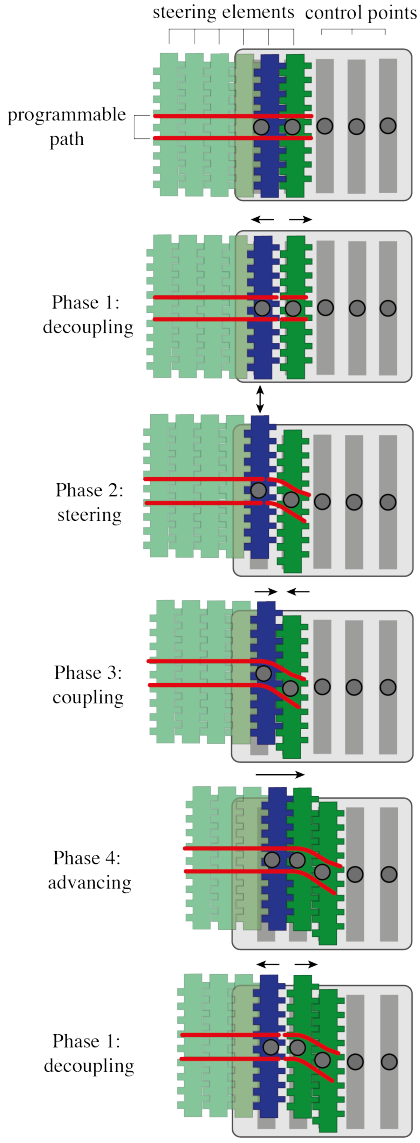

Figure 3.4: Memory mechanism showing the programmable path (red lines) and the steering elements (light green for the future, blue for the present, dark green for the past). The control points are represented by the grey dots. The figure shows the four phases required to create a real-time FTL-motion: Phase 1. Decoupling the future and the present from the past. Phase 2. Steering the element that represents the present to a new position. Phase 3. Coupling the present and the past again to memorize the new position. Phase 4. Advancing the programmable physical track along the control points to pass the pose information backward.

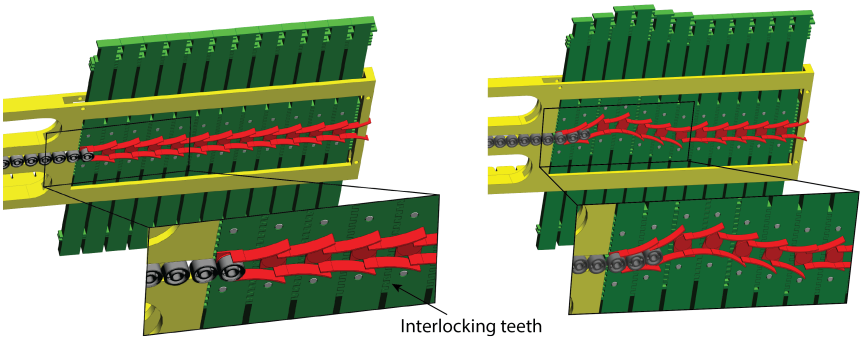

Figure 3.5: Detail of the steering element (green), guiding units (red), and control points (dark grey). At the left, the steering elements and the guiding units form a straight path. At the right, they form a curved path.

Figure 3.5 shows a close up of the programmable physical track in a 3D representation. The steering elements (green in Figure 3.5) create a discretized path by interlocking with each other due to teeth positioned at their sides. For smooth steering of the control points over the programmable physical track, we equipped the steering elements with guiding units (red in Figure 3.5). These guiding units have thin-walled flexible lateral flaps and interpolate the discrete information from the steering elements into a smoothly curved path to guide the control points (dark grey in Figure 3.5). Each guiding unit is connected to the corresponding steering element via a pin that enables its rotation.

3.4. Proof of concept prototype

A proof of concept MemoBox prototype was manufactured in order to test the functioning of the programmable physical track proposed in the previous section, Figure 3.6. The prototype was designed by keeping in mind the size of the pre-defined physical tracks of the MemoFlex II (60x30x4 mm^3) [20]. The MemoBox mechanism is surrounded by a rectangular clear Acrylic frame (light grey) that is split into two parts; the top part guiding the memory mechanism and the bottom part guiding the control points. The bottom part of the Acrylic frame contains slots that guide sliding bars (dark grey) with the control points, represented by Ø3 mm ball bearings. The sliding bars represent the connection with the cables of the snake-like instrument, and they can only translate sideways. As the programmable physical track must slide over the control points to transfer the path (Figure 3.4) along the x-axis, the steering elements are mounted into a moving support frame (yellow) and coupled together by a pre-tensioned leaf spring (grey).

In order to decouple the past steering elements from the present and future steering elements, the present steering element is engaged by a steering element selector, blue in Figure 3.6. By pushing it manually downwards, the steering element selector creates a space between the past and the present. Unlocking the past from the

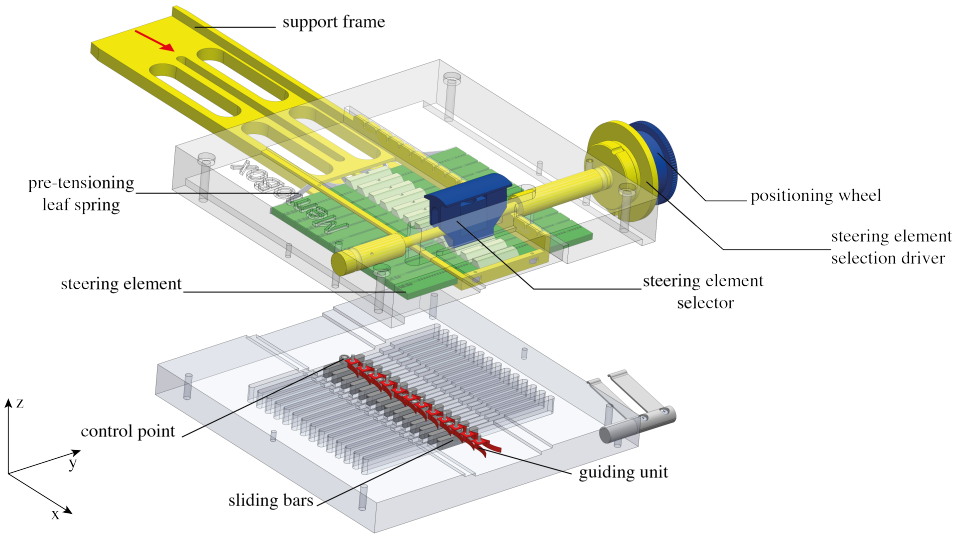

Figure 3.6: Exploded view of the MemoBox CAD model. The steering elements are shown in green and the guiding units in red. The steering elements are positioned in a support frame (yellow) that slides over the control points (dark grey ball bearings) connected to sliding bars (dark grey) along the x-axis. In order to determine a new position for the present steering element, the steering element selector (blue) engages the present steering element, and the positioning wheel (blue) enables its translation along y-axis. When the new position is achieved, the steering element selector disengages the present steering element, and the pre-tensioned leaf spring pushes back the steering elements in order to lock them in position. The programmable physical track slides over the control points by rotating the steering element selection driver (yellow) in the direction of the red arrow (x-axis).

present enables the translation along the y-axis (y-translation) of the present and future steering elements without interfering with the stored path. Once the position of the present is defined, the steering element selector disengages the present steering element, and the pre-tensioning leaf spring pushes the present back together to the past reconnecting all the steering elements. The y-translation of the present steering element is controlled by a positioning wheel that is connected to the steering element selector, blue in Figure 3.6, by means of an endless screw. When the steering element selector engages the present steering element, its y-translation can be set by rotating the positioning wheel in both directions with a resolution of 1 mm per step (0.5 mm tooth thickness, 0.5 mm gap between two teeth). The maximum travel range (y-translation) between adjacent segments was limited to 2 mm in either direction to avoid creating an irregular path that would be unable to guide the ball bearings (control points) smoothly. Finally, a knob named the steering element selection driver, yellow in Figure 3.6, can be used to move forward and backward the programmable physical track along the control points.

The steering elements were machined out of an aluminum plate by means of Electric Discharge Machining (EDM). Sliding parts, such as the support frame, the positioning wheel, the steering element selection driver, and the sliding bars, were

made out of brass to minimize friction. All springs in the system were made out of stainless spring steel. The frame was made of clear Acrylic to facilitate visualization and analysis of the mechanism's behavior and the motion of the control points over the path (Figure 3.7).

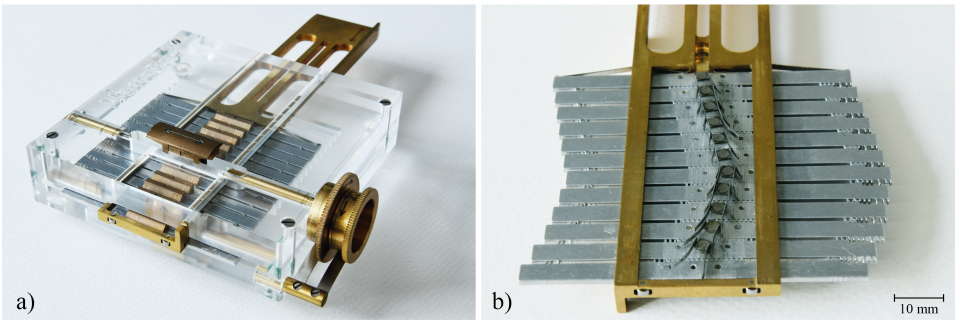

Figure 3.7: The MemoBox prototype. a) Top view of the prototype. b) A detail of the smooth path formed by the guiding units.

3.5. Functional evaluation

The MemoBox prototype was used to test the setting mechanism of the programmable track and to evaluate its smooth propagation on the control points and their guiding units. MemoBox is able to follow a wide range of single and double or multi curved paths (Figure 3.8).

Figure 3.9 shows the sequence of motions to form a triangular path; from the starting position, in which the control points are in their initial straight position and still separated from the steering elements, to the ending position, in which all the steering elements are engaged to form the path and have slid over all the control points. Considering the behavior of a hypothetical steerable shaft (as shown in Figure 3.2), in the beginning, the shaft will then be straight, whereas, in the end, it will take a double-curved position due to the translation of the control points. The

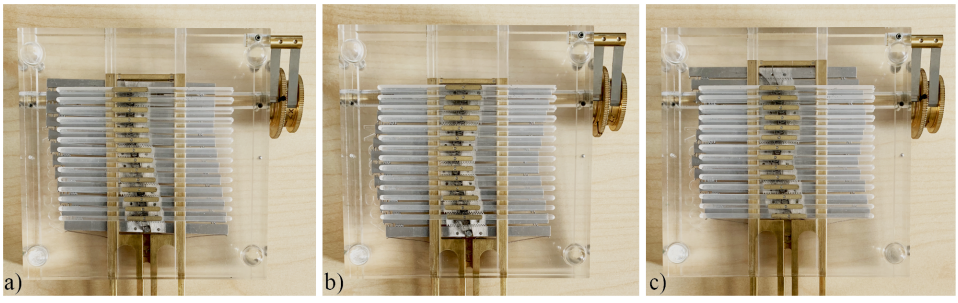

Figure 3.8: Different paths followed by MemoBox: a) single curve; b) double curve; c) multi curve.

action sequence of the user follows the four main phases listed in Section 3.3.1. First, the selector is pushed down to engage the present steering element and space it to the past steering elements. Once the present steering element is engaged, the new position can be selected by turning the positioning wheel clockwise or counterclockwise, depending on the direction the present steering element has to take. When the new position is decided for, the selector is released, reconnecting the present steering element with the past steering elements, and allowing the pose information to be memorized. Then, the selection driver is turned clockwise, and the next present steering element is selected, allowing the starting of a new cycle and moving the control points along the generated track. The programmable physical track works in both directions; by turning the selection driver counterclockwise, the control points follow the created path backward till they are in the neutral straight position again. This corresponds with the situation in a real surgical scenario, where the snake-like instrument will be able to follow the same path for reaching the target area and for retraction, avoiding sensitive organs or tissues on the way in and out of the patient. The QR code at the end of this chapter provides the link to the video of the user sequence of actions and the behavior of MemoBox.

3.6. Discussion

3.6.1. MemoBox design

In this paper, we developed a new, fully mechanical, programmable physical track for controlling snake-like surgical instruments. MemoBox is based on the principle that instead of using 14 actuators to perform an FTL-motion, one for each control point, the control points can be controlled by superimposing a mechanical memory system. The new memory system is based on a discrete geometrical interlocking mechanism between 11 steering elements. The steering elements form the shape that is followed by the control points. The control points, 14 in our prototype, represent the number of segments of the shaft. Therefore, the steering elements can hypothetically change in number from the control points as they belong to two independent assemblies in the MemoBox with guiding units in-between. This mechanism is more reliable and stiffer as compared to continuous friction-based mechanisms, such as in alternating robots because it avoids error accumulation along the path. MemoBox allows for single, double or, multi-curved paths that can be adjusted at any time during the motion.

In our prototype, steering element discretization is 1 mm with a maximum travel range of ±2 mm from one steering element to the next. In combination with an Ø8 mm steerable shaft like the one in Figure 3.2, with the cables placed concentrically in a Ø6.4 mm ring, the shaft can reach a bending angle of 180 degrees with a cable displacement of ±10 mm. This means that, with a maximum travel range of ±2 mm, the shaft can reach an angle of 180 degrees in five subsequent steps of the mechanical memory system, with 36 degrees per step. If, instead, we consider a Ø5 mm shaft with cables placed in a Ø4 mm ring, the shaft would reach the same bending angle in three steps of the mechanical memory system. In our prototype this resolution was considered sufficient [20]. However, the resolution can be further improved by

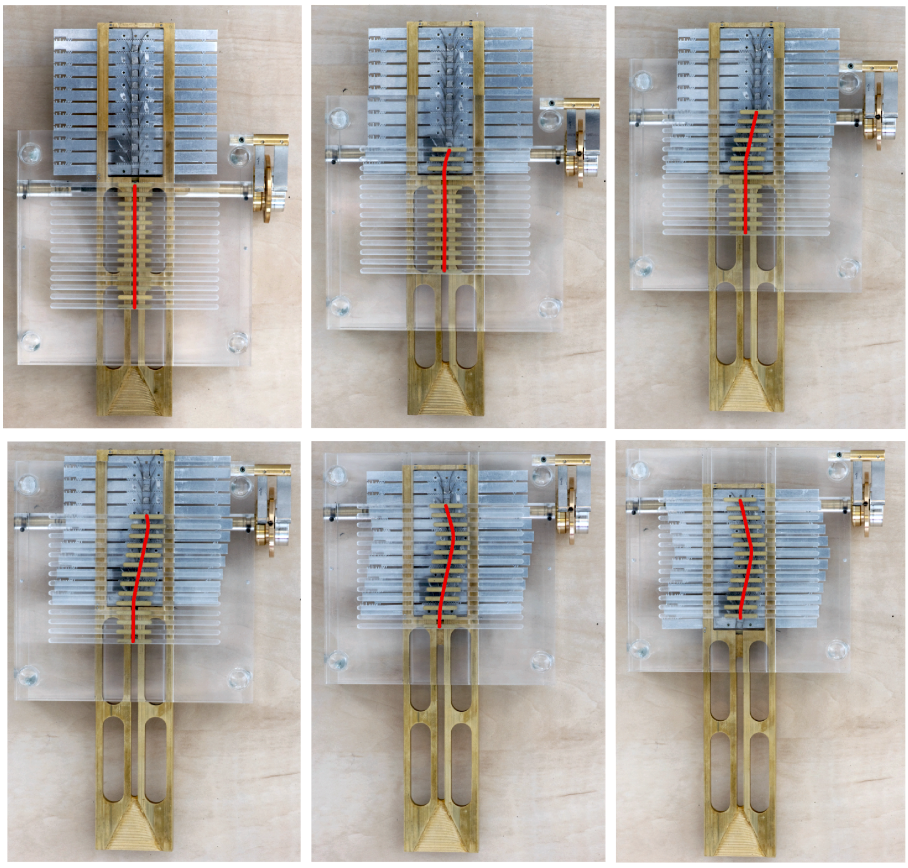

Figure 3.9: MemoBox following a triangular path, corresponding to a double curved shape in a snake-like shaft. The programmable physical track slides over the control points step-by-step, and each time the selected steering element takes the new position decided by the user.

decreasing the tooth width and spacing. Moreover, MemoBox is a modular system and the number of steering elements can be adapted depending on the number of DOF needed for the selected procedure. In our prototype, the 11 steering elements can each take five possible positions: two positions when the steering element translates upwards along the y-axis, two when it translates downwards, and one of it remains in the middle with respect to the follower segment. Therefore, there are theoretically 511 possible paths that the mechanical memory can perform.

MemoBox used guiding units with flexible stainless-steel flaps to interpolate the discretized information of the steering elements in a smooth path. However, due to limitations in the flexibility of the flaps, the travel range between two adjacent elements cannot be greater than ±2 mm in order to not create irregularities. An alternative solution to increase the travel range and thus achieve a larger bending angle with fewer steering elements in the instrument shaft, could be the implementation

of a continuous compliant element connected to the steering elements to create a smooth and continuous path.

Although the user of the memory system has a continuous path in mind, our MemoBox requires translation of this continuous motion into a discrete input. At each step, the user selects the present steering element, defines the new position, and moves the memory one step forward. Even though the control points move smoothly from one position to another, the sequence of motion set by the user remains discretized. The discretization of the FTL movement is, however, an intrinsic characteristic of FTL surgical robotic systems, as the pathway is always programmed in a step-wise manner related to the number and length of the segments.

MemoBox represents only one module of the overall system, and therefore a complete evaluation of the FTL error cannot be carried out here. However, one of the main factors that influence the FTL error in our MemoBox is the discretized angle resulting from the resolution in the translation of the steering elements. The 1 mm resolution allows the segments of the previously considered Ø8 mm compliant shaft to make discrete steps at an interval of 18 degrees. Therefore, considering a segment length of 10 mm, the maximum discretization error would be around 1.5 mm, given by half of the 18 degrees angle at 1 mm discretization multiplied by the length of the steerable segment. The acceptable error mainly depends on the surgical application. An error of 1.5 mm is comparable with the error of similar FTL systems [27, 37] and, although still too large for sinus surgery [38], is tolerated in procedures such as colonoscopy [12]. Scaling down the resolution of the steering elements would reduce the discretization error and expand the application range. Besides the discretization, FTL behavior would also be affected by friction, flexible behavior of the steering cables, and a possibility of cable buckling. All those factors should be considered beforehand when designing the overall system [20].

Besides MemoBox, the literature contains only one other mechanically programmable physical track called MemoSlide [39]. One of the difficulties encountered in MemoSlide was miniaturization. In MemoBox, greater miniaturization has been achieved by replacing MemoSlide's complex alternating mechanism to memorize the path by a much simpler shape shifting mechanism. By using a shape-shifting mechanism, the number of components halved because the mechanism is based on only one memory system. Moreover, MemoSlides uses wedges that create a discretized path. In MemoBox, the flexible flaps of the guiding units replace the wedges and ensure a smooth path for the ball bearings. We, therefore, decreased the size of the programmable physical track from 145x125x25 mm^3 of the MemoSlide to 70x64x6 mm^3 of our MemoBox with a reduction in edge length of 50% by keeping the same discretization and the same number of programmable segments.

3.6.2. Implementation in a surgical instrument

MemoBox was designed as a programmable physical track able to guide a surgical shaft along tortuous paths with an FTL-motion avoiding sensitive organs or tissues. Being a proof of concept, we designed a 2D system able to control cables of the steerable shaft in one plane. However, in a real scenario, the steerable shaft needs to

move in 3D. The integration of MemoBox into a system such as MemoFlex II [20] allows transforming a system based on pre-defined physical tracks into one that can be controlled in real-time, giving the possibility of adjusting the path during the surgical procedure. MemoFlex II is based on the combined work of four physical tracks, two for each plane, Figure 3.10a. Each pair of physical tracks control two antagonistic cables for each segment of the steerable shaft. The four physical tracks are placed in an external cylinder that rotates around the main body of the instrument. The external cylinder is coupled with an external chassis to combine the steering motion with the forward and backward motion of the instrument. Substituting the four pre-defined physical tracks with the MemoBox mechanism will result in the instrument schematically shown in Figure 3.10b. The figure shows a side view of the instrument where only two of the integrated MemoBoxes are visible, one for the motions in the xz-plane and the other for the motions on the yz-plane. The four MemoBoxes in this schematic mechanism are controlled by means of two pivotable rings, light blue in Figure 3.10b. The use of these rings allows the user to control antagonist MemoBoxes in a synchronized fashion. The rings are connected to the main body of the instrument via a frame, grey in Figure 3.10b, each with two spherical joints, depicted in orange. Control knobs are connected to the rings to select and control the position of the present steering elements. Following the design of the MemoFlex II, the rotational motion of the yellow external cylinder that houses the four MemoBoxes can be coupled with the sliding motion, forward and backward, in the z-axis. The coupling can be done similarly as in the MemoFlex II, with an external chassis, but for the sake of clarity, this external chassis is not shown in Figure 3.10b. MemoBox was prototyped as a first proof-of-concept and was therefore designed as a 2D planar design. Future work will focus on integrating the MemoBox into a 3D system, thereby reshaping the mechanism into a curved design.

3.6.3. Mechanical over mechatronics solutions

When comparing mechatronic and fully mechanical FTL solutions, one of the advantages of using mechatronics is that each DOF is individually controlled by a dedicated actuator. Having independent control over each DOF generally makes such a system more versatile, e.g., not only suited to propagate tracks initiated by the end-effector but also suited for changing the entire track at one time. A limitation of mechatronics FTL-systems as compared to mechanical ones is the associated high complexity and related costs [40]. For example, to control a snake-like tip with 16 segments, each having 2 DOF, with each of the four steering cable connected to a motor, 64 electric motors need to be precisely synchronized, as compared to only four MemoBoxes. Using 64 motors, including sensors, gearboxes, and controls, will greatly increase complexity and costs as well as the overall size of the system. In an attempt to reduce the system size, miniature electric motors can be used as an alternative. However, miniature motors can deliver only limited power, which would result, with the use of miniature gearboxes, in slow responsiveness of the system. Reducing the number of motors by making mechanical connections between antagonistic steering cables would lead to 30 motors and 30 mechanical linkages or pulleys, which will still lead to a very complex system as compared to our approach with four Memoboxes.

Therefore, mechatronic and mechanical solutions should be considered complementary and chosen depending on the specific procedure. When mechanical solutions are not able to ensure the precision and versatility requested, mechatronics systems provide a valuable solution that justifies the costs.

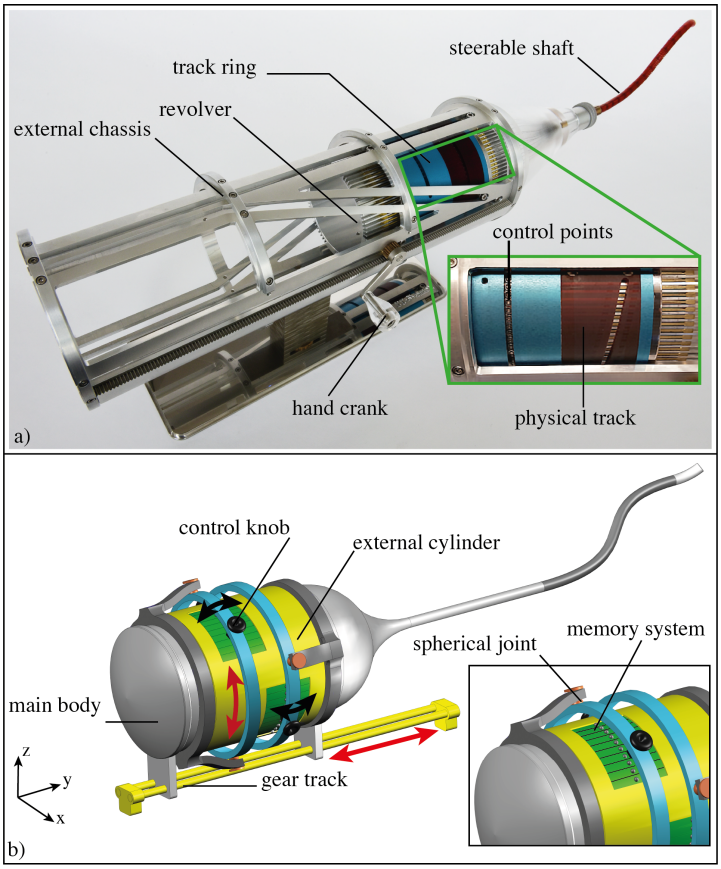

Figure 3.10: Integration of the MemoBox system into a surgical instrument with an FTL-motion. a) MemoFlex II device [20]. The close-up shows a physical track and the control points. b) An artistic impression of the final system integrated with four MemoBox programmable physical tracks. The main body (grey) slides over a gear track (yellow). The sliding motion of the main body is coupled with the rotational motion of the external cylinder (yellow) in which the programmable physical tracks are placed (green). At each step, a new position of the present steering element is decided by using the two double-joystick, one for each plane (black). The control knobs are attached to the main body by means of support with two spherical joints (orange in the close-up).

3.7. Conclusion

In this work, we presented a new programmable, mechanically-actuated physical track to guide a steerable shaft through tortuous paths with FTL-motion. A 2D proof of

concept prototype, called MemoBox, was manufactured able to memorize the pathways that are selected in real-time by the user and transform these pathways into the input of a snake-like multi-steerable shaft. Mechanical FTL solutions provide advantages over mechatronics solutions in controlling a high number of degrees of freedom, whereas mechatronics solutions can guarantee more versatility and precision. Mechanical and mechatronics FTL solutions should be therefore considered complementary and chosen depending on the specific surgical procedure. FTL-instrumentation can make a difference in many surgical scenarios, such as colonoscopy, interventional bronchoscopy, or skull base surgery. MemoBox represents a step forward in designing advanced snake-like surgical instruments without the use of actuators and electronics components.

References

[1] J. S. Schneider, J. Burgner, R. J. Webster III, and P. T. Russell III, *Robotic surgery for the sinuses and skull base: What are the possibilities and what are the obstacles?* Current opinion in otolaryngology & head and neck surgery **21**, 11 (2013).

[2] E. G. Sheu and D. W. Rattner, *Natural Orifice Transluminal Endoscopic Surgery (NOTES™) BT - The SAGES Manual Operating Through the Endoscope*, edited by M. Kroh and K. M. Reavis (Springer International Publishing, 2016) pp. 463–474.

[3] C. H. Snyderman, H. Pant, and R. Carrau, *Transnasal Endoscopic Skull Base and Brain Surgery* (2011) pp. 83–91.

[4] T. Rahimli, T. Hidayetov, Z. Yusifli, H. Memmedzade, T. Rajabov, and K. Aghayev, *Endoscopic endonasal approach to giant pituitary adenomas. surgical outcomes and review of the literature.* World Neurosurgery (2021).

[5] S. Yano, T. Hide, and N. Shinojima, *Efficacy and complications of endoscopic skull base surgery for giant pituitary adenomas,* World neurosurgery **99**, 533 (2017).

[6] H. Choset and W. Henning, *A follow-the-leader approach to serpentine robot motion planning,* Journal of Aerospace Engineering **12**, 65 (1999).

[7] D. P. Steinfort, Y. H. Khor, R. L. Manser, and L. B. Irving, *Radial probe endobronchial ultrasound for the diagnosis of peripheral lung cancer: systematic review and meta-analysis,* European Respiratory Journal **37**, 902 (2011).

[8] M. J. Reardon, N. M. Van Mieghem, J. J. Popma, N. S. Kleiman, L. Søndergaard, M. Mumtaz, D. H. Adams, G. M. Deeb, B. Maini, H. Gada, *et al.*, *Surgical or transcatheter aortic-valve replacement in intermediate-risk patients,* New England Journal of Medicine **376**, 1321 (2017).

[9] C. Culmone, A. Ali, M. Scali, A. Menciassi, and P. Breedveld, *Chore: A device for transcatheter chordae tendineae repair,* Proceedings of the Institution of Mechanical Engineers, Part H: Journal of Engineering in Medicine **233**, 712 (2019).

[10] S. Tappe, J. Pohlmann, J. Kotlarski, and T. Ortmaier, *Towards a follow-the-leader control for a binary actuated hyper-redundant manipulator,* in *2015 IEEE/RSJ International Conference on Intelligent Robots and Systems (IROS)* (IEEE, 2015) pp. 3195–3201.

[11] S. Tappe, D. Yu, J. Kotlarski, and T. Ortmaier, *Model reduction methods for optimal follow-the-leader movements of binary actuated, hyper-redundant robots,* in *Computational Kinematics* (Springer, 2018) pp. 35–43.

[12] Y. Chen, J. Liang, and I. W. Hunter, *Modular continuum robotic endoscope design and path planning,* in *2014 IEEE International Conference on Robotics and Automation (ICRA)* (IEEE, 2014) pp. 5393–5400.

[13] J. Son, C. N. Cho, K. G. Kim, T. Y. Chang, H. Jung, S. C. Kim, M.-T. Kim, N. Yang, T.-Y. Kim, and D. K. Sohn, *A novel semi-automatic snake robot for natural orifice transluminal endoscopic surgery: preclinical tests in animal and human cadaver models (with video),* Surgical endoscopy **29**, 1643 (2015).

[14] J. D. Waye, *Quo vadis: another new colonoscope,* Official journal of the American College of Gastroenterology| ACG **102**, 267 (2007).

[15] H. Lee, K. G. Kim, J. H. Seo, and D. K. Sohn, *Natural orifice transluminal endoscopic surgery with a snake-mechanism using a movable pulley,* The International Journal of Medical Robotics and Computer Assisted Surgery **13**, e1816 (2017).

[16] T.-D. Nguyen and J. Burgner-Kahrs, *A tendon-driven continuum robot with extensible sections,* in *2015 IEEE/RSJ International Conference on Intelligent Robots and Systems (IROS)* (2015) pp. 2130–2135.

[17] N. Miner, *Cleaning, disinfection and sterilization of heat-sensitive endoscopes in,* Endoscopy **10**, 50355 (2013).

[18] P. L. Anderson, R. A. Lathrop, S. D. Herrell, and R. J. Webster, *Comparing a mechanical analogue with the da vinci user interface: Suturing at challenging angles,* IEEE robotics and automation letters **1**, 1060 (2016).

[19] P. L. Anderson, R. A. Lathrop, and R. J. Webster III, *Robot-like dexterity without computers and motors: a review of hand-held laparoscopic instruments with wrist-like tip articulation,* Expert review of medical devices **13**, 661 (2016).

[20] P. Henselmans, C. Culmone, D. Jager, R. van Starkenburg, and P. Breedveld, *The memoflex ii, a non-robotic approach to follow-the-leader motion of a snake-like instrument for surgery using four predetermined physical tracks,* Medical Engineering & Physics **86**, 86 (2020).

[21] B. Kang, R. Kojcev, and E. Sinibaldi, *The first interlaced continuum robot, devised to intrinsically follow the leader,* PloS one **11**, e0150278 (2016).

[22] P. E. Dupont, J. Lock, B. Itkowitz, and E. Butler, *Design and control of concentric-tube robots,* IEEE Transactions on Robotics **26**, 209 (2010).

[23] R. J. Webster, J. M. Romano, and N. J. Cowan, *Mechanics of precurved-tube continuum robots,* IEEE Transactions on Robotics **25**, 67 (2009).

[24] H. B. Gilbert, J. Neimat, and R. J. Webster, *Concentric tube robots as steerable needles: Achieving follow-the-leader deployment,* IEEE Transactions on Robotics **31**, 246 (2015).

[25] C. Girerd, K. Rabenorosoa, P. Rougeot, and P. Renaud, *Towards optical biopsy of olfactory cells using concentric tube robots with follow-the-leader deployment,* in *2017 IEEE/RSJ International Conference on Intelligent Robots and Systems (IROS)* (IEEE, 2017) pp. 5661–5887.

[26] M. Neumann and J. Burgner-Kahrs, *Considerations for follow-the-leader motion of extensible tendon-driven continuum robots,* in *2016 IEEE International Conference on Robotics and Automation (ICRA)* (2016) pp. 917–923.

[27] E. Amanov, J. Granna, and J. Burgner-Kahrs, *Toward improving path following motion: hybrid continuum robot design,* in *2017 IEEE international conference on robotics and automation (ICRA)* (IEEE, 2017) pp. 4666–4672.

[28] M. Corporation, *Flex® robotic system: Expanding the reach of surgery®,* (2021), https://medrobotics.com/gateway/flex-system-int/, Accessed: 2021-02-22.

[29] A. Degani, H. Choset, A. Wolf, and M. A. Zenati, *Highly articulated robotic probe for minimally invasive surgery,* in *Proceedings 2006 IEEE International Conference on Robotics and Automation, 2006. ICRA 2006.* (IEEE, 2006) pp. 4167–4172.

[30] M. Mahvash and M. Zenati, *Toward a hybrid snake robot for single-port surgery,* in *2011 Annual International Conference of the IEEE Engineering in Medicine and Biology Society* (IEEE, 2011) pp. 5372–5375.

[31] T. Ota, A. Degani, D. Schwartzman, B. Zubiate, J. McGarvey, H. Choset, and M. A. Zenati, *A highly articulated robotic surgical system for minimally invasive surgery,* The Annals of thoracic surgery **87**, 1253 (2009).

[32] E. Funk, D. Goldenberg, and N. Goyal, *Demonstration of transoral robotic supraglottic laryngectomy and total laryngectomy in cadaveric specimens using the medrobotics flex system,* Head & neck **39**, 1218 (2017).

[33] X. Dong, D. Axinte, D. Palmer, S. Cobos, M. Raffles, A. Rabani, and J. Kell, *Development of a slender continuum robotic system for on-wing inspection/repair of gas turbine engines,* Robotics and Computer-Integrated Manufacturing **44**, 218 (2017).

[34] L. Dupourqué, F. Masaki, Y. L. Colson, T. Kato, and N. Hata, *Transbronchial biopsy catheter enhanced by a multisection continuum robot with follow-the-leader motion,* International journal of computer assisted radiology and surgery **14**, 2021 (2019).

[35] D. Palmer, S. Cobos-Guzman, and D. Axinte, *Real-time method for tip following navigation of continuum snake arm robots,* Robotics and Autonomous Systems **62**, 1478 (2014).

[36] P. W. Henselmans, G. Smit, and P. Breedveld, *Mechanical follow-the-leader motion of a hyper-redundant surgical instrument: Proof-of-concept prototype and first tests,* Proceedings of the Institution of Mechanical Engineers, Part H: Journal of Engineering in Medicine **233**, 1141 (2019).

[37] Z. Zhang, J. Dequidt, J. Back, H. Liu, and C. Duriez, *Motion control of cable-driven continuum catheter robot through contacts,* IEEE Robotics and Automation Letters **4**, 1852 (2019).

[38] H.-S. Yoon, J. H. Jeong, and B.-J. Yi, *Image-Guided Dual Master–Slave Robotic System for Maxillary Sinus Surgery,* IEEE Transactions on Robotics **34**, 1098 (2018).

[39] P. W. J. Henselmans, S. Gottenbos, G. Smit, and P. Breedveld, *The Memo Slide: An explorative study into a novel mechanical follow-the-leader mechanism,* Proceedings of the Institution of Mechanical Engineers, Part H: Journal of Engineering in Medicine **231**, 1213 (2017).

[40] W. F. Abdelmoaty, C. M. Dunst, C. Neighorn, L. L. Swanstrom, and C. W. Hammill, *Robotic-assisted versus laparoscopic unilateral inguinal hernia repair: a comprehensive cost analysis,* Surgical endoscopy **33**, 3436 (2019).

Figure 3.11: Video of the user sequence of actions and the behavior of MemoBox.

Part 2

Additive Manufacturing and Compliant Solutions

4

Additive Manufacturing in Medical Instruments

Published as:
Culmone, C., Gerwin S., and Breedveld P. "Additive manufacturing of medical instruments: A state-of-the-art review." Additive Manufacturing, 27 (2019): 461-473.

Abstract

Goal: Additive manufacturing, also known as 3D printing, has begun to play a significant role in the field of medical devices. This review aims to provide a comprehensive overview and classification of additively manufactured medical instruments for diagnostics and surgery by identifying medical and technical aspects. Methods: A scientific literature search on additively manufactured medical instruments was conducted using the Scopus database. Results: We categorized the relevant articles (71) by considering the novelty of each proposed instrument and its clinical application. Then, we analyzed the relevant articles by examining the reasons behind choosing additive manufacturing technology to produce instruments for diagnostics and surgery. Possible customization (27%) and Cost-effectiveness (23%) were the main reasons expressed. Technical specifications of the additive manufacturing technology and the material used were also analyzed, and a tendency of using material extrusion technology (35% of the applications) and polymeric materials (86% of the applications) was shown. Conclusions: Additive manufacturing is opening the door to a new approach in the production of medical devices, which allows the complexity of their designs to be pushed to the extreme. However, we found that technical limitations need to be tackled and important aspects such as sterilization or debris contamination are still not considered to be relevant factors during the design and fabrication process. Keeping in mind the challenges of such a new field, additive manufacturing technology can be considered as a great opportunity to provide easy access to healthcare in developing countries as well as an important step toward patient-specific medicine.

4.1. Introduction

Additive manufacturing (AM), also known as 3D printing or rapid prototyping, is rapidly changing the perspective of how medical devices have to be designed and what can be produced and prototyped. With AM technology, a computer-aided design (CAD) model can be directly transformed into a 3D object, built layer-by-layer, in a relatively short time and with low cost, avoiding the long processes of conventional fabrication methods.

This technology emerged in the 1980s and rapidly increased in importance owing to the possibility of designing tailored tools both for patient and clinician needs [1]. When the first commercial version of the 3D printer was launched in the market in 1987, applications further increased because of high reductions in the cost of printers [2]. As shown in Figure 4.1, AM has been applied in a number of medical fields such as tissue engineering to design personalized scaffolds or artificial tissues and organs for transplants [3–9]; drug delivery systems [10, 11]; laboratory equipment such as probes [12] and portable test tools to detect specific medical parameters such as cortisol in the saliva [13]; assistive tools such as customized cutlery to help people with chronic diseases in their daily life [14]; orthoses and prostheses for developing countries, where the population cannot afford expensive devices [15–17]; implant [18–20]; anatomical models for both surgical planning and procedure training particularly in cases of rare pathologies [21–23]; surgical guides for screw insertions [24]; and in recent years, medical instruments for diagnostics and surgery.

In 2017, the Food and Drug Administration (FDA) published the first version of guidelines for AM of medical instruments [25]. However, to the authors' knowledge, neither an overview of the currently existing 3D-printed instruments for diagnostics and surgery nor an analysis of their common characteristics exists.

In this review, we provide a complete overview of the current state of the art in the AM of medical instruments used for diagnostics and surgery. We categorize the instruments considering the application as well as the reasons related to the use of the applied 3D printing method.

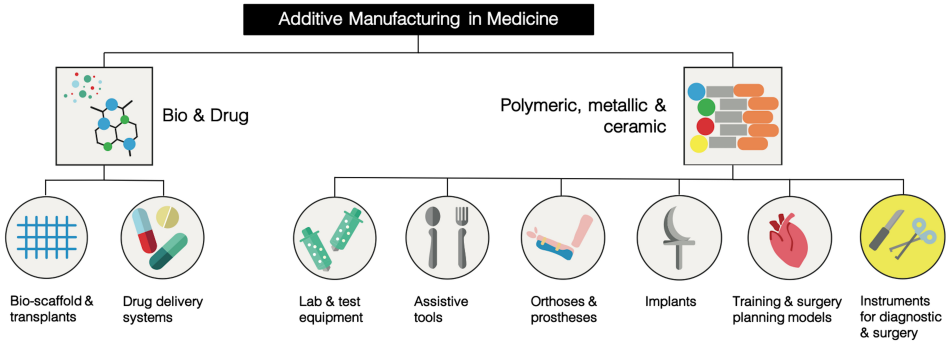

Figure 4.1: Classification of medical fields related to additive manufacturing. The first level of classification concerns the material used and the second level the medical field of application. This review paper focuses on instruments for diagnostic and surgery (highlighted in yellow).

4.2. Literature search methods

4.2.1. Scientific literature research

A scientific literature search was conducted using the Scopus database on the AM of medical instruments used for diagnostics and surgery. The choice for Scopus database rather than other databases, such as Web of Science or PubMed, is due to its completeness in journal titles, the possibility of using nested Boolean searches, and its classification of articles in multiple subject areas which allows achieving a wider range of articles [26]. The search keywords of the query were organized into three categories: (1) fabrication technology (3D print*, additive manufactur*, rapid prototyp*), (2) product class (instrument, tool, prototype, device, appliance, equipment), and (3) application area (med*, surg*, diagnos*). We decided to use only general terms in all categories to have a broader search query and we excluded specific terms such as the specific AM technologies, specific types of instruments, and specific names of interventions. We did not limit the search to a particular period; however, we decided to crop the result to include only the English articles in the subject area of "Engineering" and "Medicine." We searched in titles, abstracts, and keywords of the documents. Our complete search query was TITLE-ABS-KEY (("3D print*" OR "additive manufactur*" OR "rapid* prototyp*") AND (instrument OR tool OR prototype OR device OR appliance OR equipment) AND (med* OR surg* OR diagnos*)) AND (LIMIT-TO (SUBJAREA, "ENGI") OR LIMIT-TO (SUBJAREA, "MEDI")) AND (LIMIT-TO (LANGUAGE, "English")).

4.2.2. Eligibility criteria

In this review, we define a medical instrument as a tool for examining or treating patients. The tool must be directly in contact with the patient but is not meant to stay into the body for more than the duration of the examination or treatment. Considering the three categories used for the search keywords, in Category (1), "fabrication technology," we considered the seven main categories of AM technologies defined by the Standard Terminology for AM Technologies (ASTM): binder jetting, direct energy deposition, material extrusion, material jetting, powder bed fusion, sheet lamination, and Vat photopolymerization [27]. Bioprinting and drug printing were excluded. In Category (2), "product class," we included surgical instruments used inside the body, as well as diagnostic instruments used to examine the patient from the outside. Because we focused on medical instrumentation, we excluded surgical guides developed for navigation during surgery, as well as 3D-printed anatomic models for surgical planning and training, implants, prostheses, orthoses, probes, and drug portable devices. In Category (3), "application area," we considered eligible all the instruments used in the medical domain except for laboratory tools that are not directly in contact with the patient.

4.2.3. Literature search results

The search resulted in 2616 scientific articles, the titles and abstracts of which were scanned. We selected 53 articles that fulfilled the eligibility criteria. Besides analyzing the results obtained with the search query, we also checked the references of the

Table 4.1: Author(s), year of publication, clinical application, and corresponding category in the classification of relevant articles for conventional medical instruments. Conventional General Purpose (C-GP); Conventional Specific Purpose (C-SP).

Author(s)	Publication year	Clinical Application	Classification
George et al.	2017	General surgery	C-GP
Paraskevopoulos	2016	Intracranial surgery	C-GP
Singh et al.	2016	Microsurgery	C-GP
del Junco et al.	2015	Endoscopic and laparoscopic equipment	C-GP
Rankin et al.	2014	Open surgery	C-GP
Wong and Pfahnl	2014	General surgery	C-GP
Wong	2015	General surgery	C-GP
Yamamoto et al.	2015	General surgery	C-GP
Ibrahim et al.	2015	General surgery	C-GP
Kondor et al.	2013	General surgery	C-GP
Kondor et al.	2013	General surgery	C-GP
Fuller et al.	2014	Bone reduction	C-GP
Băilă et al.	2016	General surgery	C-GP
Băilă et al.	2016	Dental procedure	C-GP
Kaleev et al.	2017	General surgery	C-GP
Sanchez-Tamayo and Wachs	2018	Robotic surgery	C-GP
Aguilera-Astudillo et al.	2016	Diagnostics	C-GP
Yamamoto et al.	2018	Endoscopic surgery	C-GP
Rothenberg et al.	2017	Ultrasound-guided aspiration	C-SP
Gálvez et al.	2016	Assisted ventilation	C-SP
Way et al.	2015	Assisted ventilation	C-SP
Kontio et al.	2012	Mandible fracture correction	C-SP
Way	2018	Flow rate control	C-SP
Walter et al.	2017	Polyp dissection in colonoscopy	C-SP
Navajas and Hove	2017	Transconjunctival vitrectomy	C-SP
Cook et al.	2015	Specific Ventilation Imaging	C-SP
del Junco et al.	2015	Urine flow kidney-bladder	C-SP
Ko et al.	2016	Mucosal/submucosal dissection	C-SP
Walker et al.	2016	Breast Brachytherapy	C-SP
Ulmeanu et al.	2016	Tracheostomy	C-SP
Steinemann et al.	2018	Distal esophageal mucosectomy	C-SP

selected articles to include the ones not captured by the query. We found 18 additional articles, resulting in 71 total articles. The obtained information was analyzed from different perspectives. First, we considered the clinical application and the novelty of the devices. Then, we reviewed the articles on the reason for using the AM technology. Finally, technical information related to the AM technology used in the field of medical instruments was retrieved.

4.3. Clinical application and novelty of AM devices

We categorized the instruments considering their novelty and clinical application (Figure 4.2). We considered a device to be a "conventional instrument" when its basic design was based on traditional instruments used in diagnostics and surgery such as surgical tweezers. A completely new design was, instead, categorized as an "unconventional instrument." Each of these categories was further split into two subcategories considering the clinical application. We defined a device designed for diagnostic or surgical approaches that could be used in different types of procedures as a "general purpose instrument." Laparoscopic or endoscopic generic instruments fall into this category. On the contrary, we defined a device designed for only one particular type of surgery as a "specific-purpose instrument," for example, polyps dissection in the colon (Figure 4.2). Articles in which a conventional instrument is proposed are grouped in Table 4.1 and those that propose an unconventional instrument are listed in Table 4.2.

4.3.1. Conventional general-purpose instruments

A straightforward use of AM is to try and produce medical instruments that are identical to those manufactured by conventional methods, such as molding or machining. General surgical kits were presented by George *et al.* [28], Wong *et al.* [29, 30], Ibrahim *et al.* [31], and Kondor *et al.* [32]. Surgical kits are generally composed of tweezers, needle drivers, hemostats, retractors, forceps, and scalpels and are designed to perform relatively common surgical procedures (Figure 4.3a).

Other research groups focused only on one such instrument with [32, 34–39] or without [40–42] changes in its design. While Singh *et al.* [40] presented a fully assembled microsurgery tweezer, Paraskevopoulos [34] introduced a modified burr hole: a device used in intracranial procedures as the entry port to stabilize a range of endoscopic instruments (Figure 4.3b). The modified design of this device is meant to allow for solo surgeries. The approach used by Băilă *et al.* [43, 44] was different; they printed a general-purpose dental elevator that was manufactured in two pieces with two different AM technologies: Vat photopolymerization for the handle and power

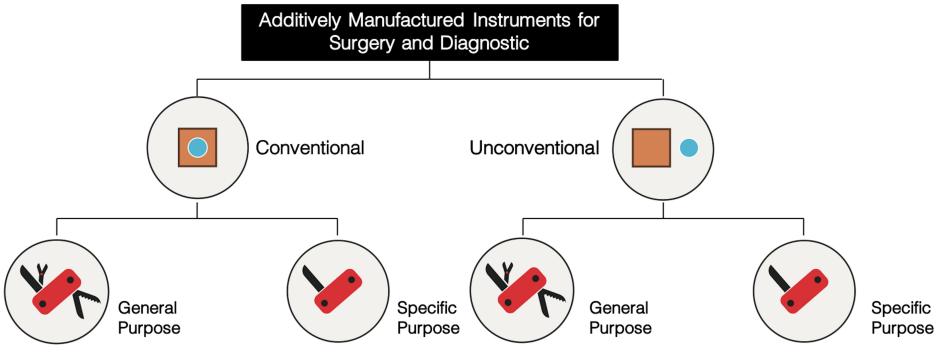

Figure 4.2: Classification of additively manufactured medical instruments for diagnostics and surgery.

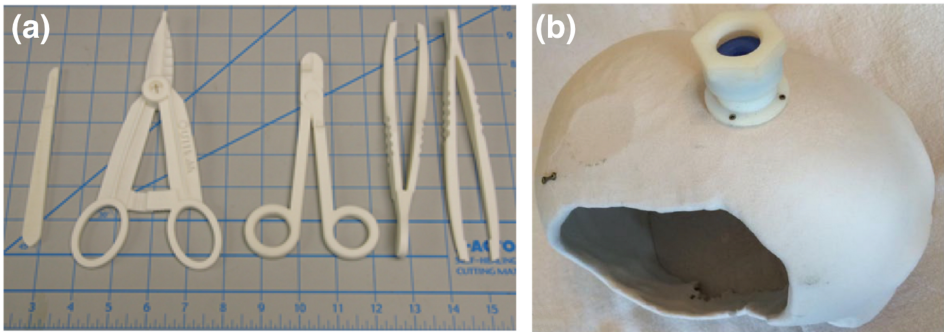

Figure 4.3: Examples of "conventional general-purpose" instruments: (a) surgical kit: scalpel, hemostat, needle driver, and forceps [33]; (b) modified burr hole presented by Paraskevopoulos [34].

bed fusion for the beak. The choice of printing only a part of an instrument was made also by Sanchez-Tamayo *et al.* [45], who tried to manufacture grippers and cutting tools for integration into surgical robots. An AM diagnostic device was presented by Aguilera-Astudillo *et al.* [46], who designed a stethoscope in which the chest piece was manufactured using a 3D printer.

4.3.2. Conventional specific-purpose instruments

An interesting approach to AM is to use the 3D printing process to partly modify the design of conventional instruments to perform specific procedures. The changes made to the design are mostly related to the functionality [47–51] or size [52–56]. An example of functionality change is given by the reciprocating syringe of Rothenberg *et al.* [47] for image-guided aspiration, as shown in Figure 4.4a. In a conventional syringe, sucking small parts of solid organs or fluids while maintaining the vacuum often needs the help of an assistant. The reciprocating syringe uses a double lumen structure allowing the physician to perform a solo procedure by inverting the movement of the syringe plunger. A modification of the conventional equipment for specific ventilation imaging, which is a technique used to measure the air distribution in the lungs, was performed by Cook *et al.* [51]. They proposed an alternative bypass flow attachment that was completely manufactured using 3D printing technology and could substitute a significant number of components with only one part.

Navajas and Hove [53] provided an example of size change using 3D printing in the fabrication of a trocar-cannula for transconjunctival vitrectomy, a procedure during which the gel-like material in the eye is substituted by a saline solution. In this case, the functionality of the trocar-cannula is not changed, but because of the 3D printing technology, the size can be customized considering the surgical instrumentations used during the procedure. A similar approach was taken by Walker *et al.* [55] in designing measuring tools to estimate the size of a probe used in lumpectomy, a breast cancer removal procedure (Figure 4.4b). The overall design of the measuring tools, a handle with a sphere on top, is the same as that of the probe. However, by using AM, the size of the sphere can be changed to diameters ranging from 1.5 to 5 cm depending

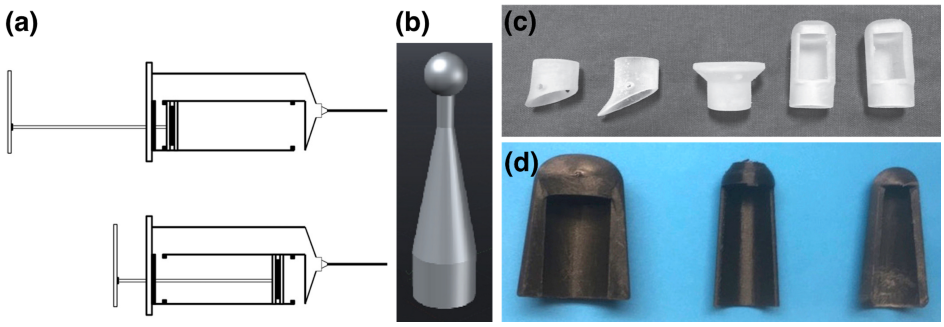

Figure 4.4: Examples of "conventional specific-purpose" instruments: (a) sketch of reciprocating syringe by Rothenberg *et al.* [47]; (b) CAD of measuring tool designed by Walker *et al.* to choose the appropriate probe for lumpectomy procedure [55]; (c) caps designed to be added to a conventional gastroscope to perform different types of biopsies [58]; (d) retractors for distal esophageal mucosectomy [59].

on the patient's needs. In this way, an appropriate probe can be chosen by avoiding unnecessary sterilization of probes of the wrong size.

Furthermore, AM can be used to fabricate additional parts for standard devices or procedures. Walter *et al.* [57] presented a cap that can be added to a conventional colonoscope to enhance the field of view of the instrument and detect the presence of polyps in the colon. Using AM allowed the size of the cup for different colonoscopes to be customized. Ko *et al.* [58] also printed a set of caps (Figure 4.4c). The caps were added to a conventional gastroscope and the shape was varied depending on the procedure to be performed. For example, a cap with a wide end was used to perform esophageal biopsies - removal of a small piece of tissue. Figure 4.4d shows a space holder proposed by Steinemann *et al.* [59], which was used to better expose the esophagus wall during the suturing phase of mucosectomy, a partial resection of the bowel wall, and enhance the final result.

4.3.3. Unconventional general-purpose instruments

AM has opened the doors to create new designs for medical instruments, some of which are impossible to manufacture by conventional methods. These instruments are generally designed for minimally invasive surgical procedures, during which one of the most important aspects is the maneuverability of the instrument inside the human body.

AM technology can be used to fabricate steerable surgical instruments [60–66]. The DragonFlex is a new concept of a laparoscopic grasper, fully 3D printed with seven degrees of freedom (DOFs), to give the surgeon the possibility to steer the instrument inside a patient's body [60] (Figure 4.5a). A smart steerable needle was presented by Sahlabadi *et al.* [66], in which the shaft was 3D printed and guided by Nitinol wires.

Many research groups focused their work on new designs for continuum robots and manipulators [67–69, 71–75]. Morimoto *et al.* [71], Oliver-Butler *et al.* [67], and Amanov *et al.* [73] proposed concentric tube structures based on the sliding motion

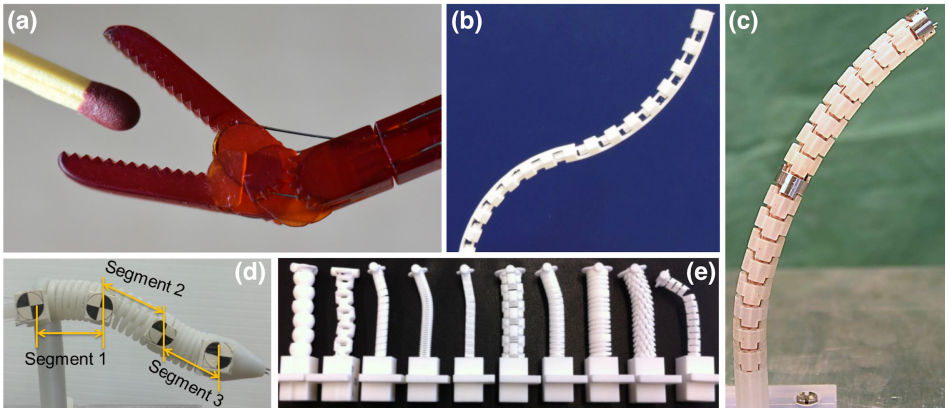

Figure 4.5: Examples of "unconventional general purpose" instruments: (a) steerable laparoscopic grasper with seven degrees of freedom; (b) 3D printed concentric tube robot [67]; (c) cable-driven continuum robot [68]; (d) the snake-like system presented by Kim *et al.* [69]; (e) different structures of the overtube presented by professor Lueth's group [70].

of one tube into the other to achieve a snake-like motion (Figure 4.5b). In these concentric tube structures, the number of elements is usually kept to a minimal, and the 3D printing material and design properties are used to increase the steerability. The same principle was used by Kim *et al.* [69] to implement a snake-like system made of three segments fully assembled (Figure 4.5d). A similar continuum robot was presented by Mintenbeck *et al.* [68] but, in contrast to concentric tube structures that usually decrease the number of parts, the body of this robot was made of multiple elements that were grouped into two cable-driven segments able to move with four DOFs, as shown in Figure 4.5c. The research group led by Professor Lueth [76] proposed a branched overtube system to be used in combination with conventional endoscopes and endoscopic instruments. The system was fully 3D printed and the control was purely mechanical. They presented different structures for the overtube system and the configuration of the branched unit, as well as different materials that can be used for the production of the device [70, 77, 78] (Figure 4.5e).

Other interesting examples of "unconventional general-purpose" medical instruments concern positioning and stabilizing systems [79–82], such as the one designed by Boehler *et al.* [79]. The stabilizing system is able to modulate the needle insertion for biopsy intervention by estimating the patient's movements related to the breathing cycle. In this case, AM allows the system to be magnetic resonance imaging (MRI)-compatible.

Force sensors manufactured using AM are also part of this category, owing to the novelty in their design, which aims to directly integrate the sensor into a catheter [83], or a trocar [84] in one printing step. Finally, García *et al.* [85] presented a new 3D-printed device to perform trans-anal endoscopic surgical procedures that is able to provide an adequate workspace without inflating the rectum. In this case, AM allows the device to be modified according to the patient's needs.

Table 4.2: Author(s), year of publication, clinical application, and corresponding category in the classification of relevant articles for unconventional medical instruments. Unconventional General-Purpose (U-GP); Unconventional Specific-Purpose (U-SP).

Author(s)	Publication year	Clinical Application	Classification
Morimoto and Okamura	2016	Minimally invasive procedure	U-GP
Oliver-Butler et al.	2017	Endoscopic procedure	U-GP
Jelínek et al.	2014	Minimally invasive surgery	U-GP
Jelínek et al.	2015	Minimally invasive surgery	U-GP
Jelínek et Breedveld	2015	Minimally invasive surgery	U-GP
Qi et al.	2016	Minimally invasive surgery	U-GP
Amanov et al.	2015	Minimally invasive surgery	U-GP
Boehler et al.	2016	MR-guided percutaneous procedure	U-GP
Entsfellner et al.	2014	Ear Nose Throat (ENT) surgery	U-GP
Krieger et al.	2017	Endoscopic surgery	U-GP
Mintenbeck et al.	2014	Minimally invasive surgery	U-GP
Cortes-Rodicio et al.	2017	PET-guided biopsy	U-GP
Seneci et al.	2015	Laparoscopic surgery	U-GP
Coemert et al.	2017	Minimally invasive surgery	U-GP
Nowell et al.	2017	Endonasal surgery	U-GP
Roppenecker et al.	2013	Single-port gastroenterology surgery	U-GP
Kesner and Howe	2011	Force measurement in catheter	U-GP
Roppenecker et al.	2012	Single port surgery	U-GP
Seneci et al.	2017	General surgery	U-GP
Schmitz et al.	2017	General surgery	U-GP
Sakes et al.	2018	Minimally invasive surgery	U-GP
Sahlabadi et al.	2017	Percutaneous intervention	U-GP
Fontanelli et al.	2017	Minimally invasive robotic surgery	U-GP
Kim et al.	2015	Neurosurgery	U-GP
García et al.	2018	Trans-anal endoscopic procedure	U-GP
Saafi et al.	2018	Laparoscopic surgery	U-GP
Zizer et al.	2016	Endoscopic submucosal dissection	U-SP
Chen et al.	2016	Cervical intraepithelial neoplasia	U-SP
Krieger et al.	2016	Partial nephrectomy	U-SP
Epaminonda et al.	2016	Cervical cancer	U-SP
Menikou et al.	2017	Pain palliation bone cancer	U-SP
Peikari et al.	2011	Transrectal brachytherapy	U-SP
Maeda et al.	2015	Endoscopic submucosal dissection	U-SP
Traeger et al.	2014	Endoscopic submucosal dissection	U-SP
Yiallouras et al.	2014	Prostate cancer	U-SP
Roppenecker et al.	2012	Endoscopic submucosal dissection	U-SP
Rugg et al.	2016	Scanning fiber endoscope (SFE)	U-SP
Myloas and Damianou	2014	Brain cancer	U-SP
Dikici et al.	2018	Hysterectomy	U-SP

4.3.4. Unconventional specific-purpose instruments

The "unconventional specific-purpose" category clusters works in which the authors identified a specific procedure or disease, and used the AM technology to design an innovative instrument. Five of the found articles presented instruments to treat or provide palliative care for different types of cancer [86–90]. Chen *et al.* [86] introduced a new inexpensive thermo-coagulator to treat cervical neoplasia, an anomalous growth of cells in the female cervix (Figure 4.6a) while Menikou *et al.* [88] proposed an MRI-compatible device for pain palliation in bone cancer using thermal ablation (Figure 4.6b). A 3D-printed device for brachytherapy, a treatment via rectum in which radioactive sources are placed directly in contact with the area of interest was proposed by Peikari *et al.* [91]. A new device was also proposed by Dikici *et al.* [92] to perform a particular gynecological surgery during which the uterus is removed with a laparoscopic approach. The AM technology was used by Rugg *et al.* [93] to fabricate a tailored handpiece to hold the scanning fiber endoscope, a particular instrument used to acquire dental images without using X-ray.

Figure 4.6c shows an interesting application for the implantation of cell sheets. Maeda *et al.* [94] proposed a device to implant cell sheets after the removal of gastrointestinal tumors in which the cell-sheet carrier was 3D printed. Finally, the branched overtube system presented by Professor Lueth's group was modified, in order to be suitable for a specific surgery during which a gastrointestinal tumor was removed [95–97] (Figure 4.6d). The overtube system was tested in the laparoscopic environment as well to remove small kidney tumors [98].

4.4. Reasons for design of AM devices

Conventional manufacturing technologies are widely known and people have significant knowledge on the possibilities and limits of such technologies. Thus, it is interesting to analyze the reasons why AM technology was used to produce the medical instruments found in the literature. In Figure 4.7, we highlighted eight reasons for the choice of AM expressed in the articles, which if not explicitly expressed by the authors were found on a careful analysis conducted by the authors of this review. Multiple reasons are often mentioned in the same article.

4.4.1. Customization

One of the main reasons expressed in the articles (27%) is the possibility of customization. Customization can concern patients, in which case instruments are customized in their dimension or design not only to meet the patient's anatomy, but also the clinician's needs for more intuitive ergonomics and user-friendliness [41]. The surgical kit presented by Kondor *et al.* [32] is an example; it was designed to be modified according to the needs of the patient or the surgeon. Customization of the instrumentation can also be performed considering the procedure. The instrument can then change in its size for adaptation to conventional devices, such as colonoscopes or endoscopes [57, 58] (Figure 4.4c) or considering the specific size of the tumor [98].

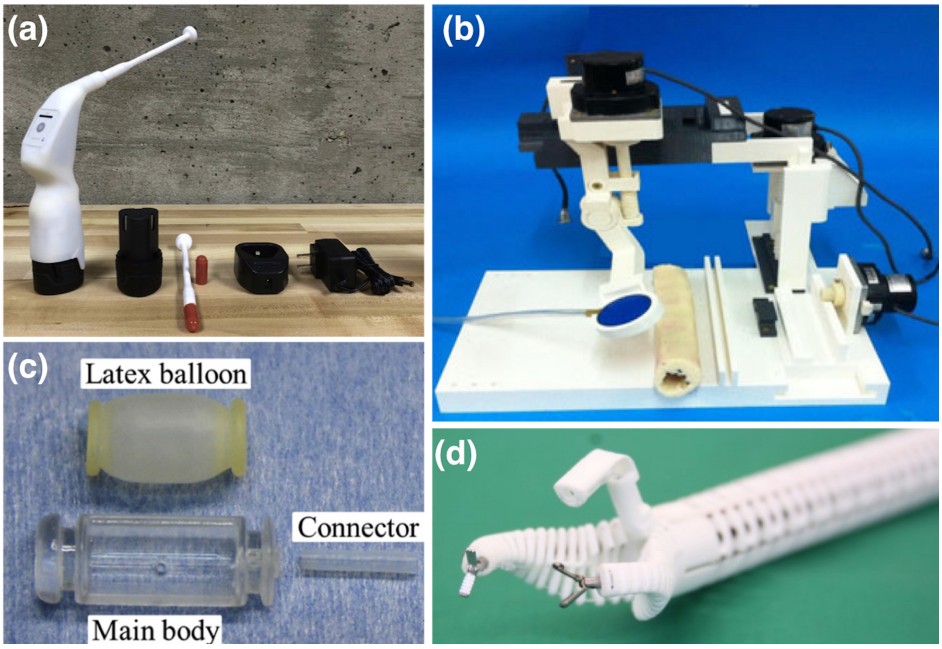

Figure 4.6: Examples of "unconventional specific-purpose" instruments: (a) thermo-coagulator to treat a type of gynecological cancer [86]; (b) MRI-compatible device for pain palliation in bone cancer [88]; (c) device to implant cell sheets [94]; (c) detail of the branched end of the overtube system proposed by Professor Lueth's group [96].

4.4.2. Cost-effectiveness and disposability

Many articles (31) justified the choice for AM owing to a considerable reduction in production cost. Ten of these articles estimated the incurred cost. Some of them considered only the price of the material [41, 51, 52, 93], some others carried out a complete evaluation of the expenses considering the material, cost of printer, payment of an expert for the design process, duration of printing, and post-processing [56]. Walker *et al.* emphasized the advantage of using the AM technology to avoid unnecessary sterilization cycles of ultrasounds probes [55]. The probe has a lifespan of 100 sterilizations. Therefore, avoiding unnecessary sterilization of the probes using measuring 3D printed tools decreases the cost of the entire procedure (Figure 4.4b). Directly connected with the cost-effectiveness and customization is the possibility of making disposable instruments. AM offers a low-cost production method, allowing customization on-demand of the instruments for patient-specific procedures [35, 98].

4.4.3. Accessibility

Eight articles emphasized the importance of AM in terms of accessibility: the possibility of having access to healthcare in remote areas. Developing countries, military expeditions, and space missions are the main scenarios proposed. The opportunity is related not only to the low costs of the AM technology [31, 41, 86] but also to the

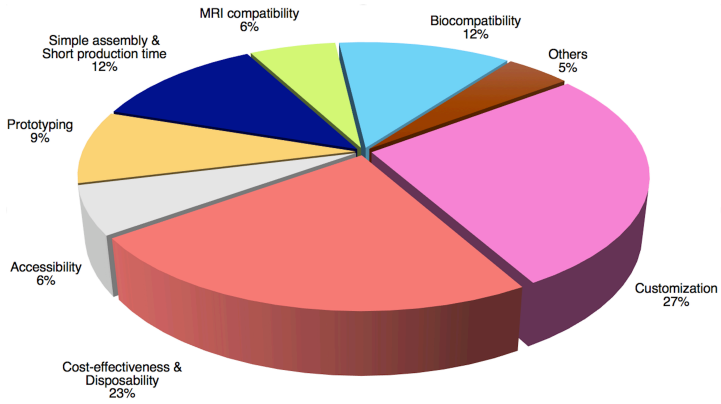

Figure 4.7: Various reasons related to the choice of using additive manufacturing to print medical instruments for diagnostics and surgery.

possibility of providing an open-source library in which the basic design of instruments is uploaded and offered for free [32].

4.4.4. Simple assembly and short production time

AM is categorized as a rapid prototyping technology as it offers a more rapid fabrication process compared to conventional manufacturing. In a number of articles (16), the reason for choosing AM is related to the necessity of having a quick turnaround during the design process. An additional advantage of AM is that the production and assembly time do not increase with the complexity of the design, allowing a reduction in the number of components while increasing the complexity of a single element [63, 96]. As a result, the design evaluation as well as the optimization phase can be carried out in a shorter time [48].

4.4.5. MRI-compatibility and biocompatibility

Depending on the medical application, an important aspect is the MRI-compatibility of the device proposed. A significant number of articles (8) highlighted the advantage of AM in fabricating instruments with material properties compatible with MRIs. Another fundamental property that is taken into consideration in various articles (16) is the biocompatibility of the medical instrument. Biocompatibility is mainly related to the material used. There are two main polymers used in the reviewed articles, where their use is justified by their biocompatibility; polylactic acid (PLA) is described in three articles, and PA2200, a type of polyamide is described in six articles. Metals such as stainless steel, alumina–zirconia composites, or cobalt–chromium alloys are also used to fabricate medical instruments owing to their biocompatibility but their use is limited compared to that of polymeric-based materials.

4.4.6. Prototyping and others

When conventional manufacturing methods are used in the first phases of a design process, the time required for the production of a prototype can be extremely long. The tuning phase to optimize and ameliorate the functionality of the design can be even longer. For this reason, in many articles (12) AM was used to fabricate the first prototype as a proof-of-concept [81, 82, 92]. Often, the 3D-printed prototype was used to test the design properties, by using the actual size of the device [84] or by giving it larger dimensions [74]. In a few articles (6), the reason behind the choice for AM is more related to material properties [44] or particular design configurations that are difficult to fabricate [78].

4.5. Technology to manufacture AM devices

4.5.1. AM technologies

The term "additive manufacturing" groups a large number of technologies. Owing to its novelty, many types of classifications can be found in the literature. In this review, we used the categorization given by the ASTM organization, which provides seven well-defined groups of AM technologies [27]. Figure 4.8 shows the percentages related to the use of these technologies to manufacture medical instruments. Clearly, the most applied technology is material extrusion (ME) with 35% of the applications. The ME technology is based on the extrusion and deposition of thermoplastic material through a nozzle. The semi-melted material in contact with the low-temperature platform rapidly hardens and solidifies keeping the 3D shape. ME includes fused deposition modeling (FDM), which is the cheapest process currently available in the market [99].

Powder bed fusion (PBF) uses energy from laser or electron beam to melt layer by layer particles together, while in material jetting (MJ) drops of liquid material are deposited on a platform and cured with UV light every layer. PBF together with MJ are widely used (26% and 21%, respectively), while Vat photopolymerization (VP) is used only in nine cases (11%). In VP a vat of liquid photopolymer is selectively exposed to a laser beam which polymerized layer by layer the material to create solid parts. VP includes techniques such as stereolithography (SLA) and digital light process (DLP). Ulmeanu *et al.* [56] presented the only application of binder jetting technology (BJ) in the production of medical instruments. BJ uses liquid bonding agent on powder material to build 3D structures layer by layer.

Direct energy deposition (DED) uses energy to directly melt the material while is deposited on the platform, while sheet lamination (SL) stacks and laminates sheets of material using processes such as ultrasonic welding. In the literature analyzed for this review, both DED and SL were not used to produce medical instruments; this could be owing to the limitation in material choice. Five of the articles did not mention the specific technology applied but only the material.

4.5.2. AM materials

The choice of materials is directly related to the technology used. We decided to divide the materials into three main categories: polymer-based, metals, and ceramic-

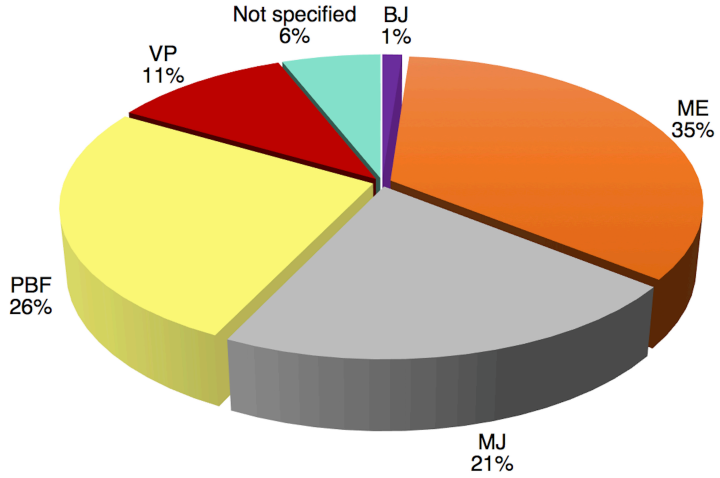

Figure 4.8: Various additive manufacturing technologies used to print medical instruments (see text for abbreviations). Direct energy deposition (DED) and sheet lamination (SL) are not presented in the chart because no articles were found using these technologies. The percentages are calculated considering the number of applications that can be multiple in the same article.

based. The group with the largest number of applications (86%) is that of polymer-based materials (Figure 4.9c). This is in line with the analysis of the technologies presented in the previous section in which only PBF and BJ allow the use of metals and ceramic-based materials. Polymer-based materials include acrylonitrile butadiene styrene (ABS), which is used in 21 different applications, PLA, polyamides (nylon), polycarbonates (PC), resins, and rubber-like materials. When not specified, the material category (polymer-based) was deduced from the technology applied owing to the direct correlation between the material and type of printer used and categorized as "others." There was a single application with polycaprolactone (PLC), which was included into "others" [73] (Figure 4.9a). The large use of polymer-based materials is partially related to biocompatibility, as for PLA, and biodegradability as for PA2200 polyamides raw powder (certificated as biocompatible according to ENISO 10993-1) [98].

Compared to polymer-based materials, metals are rarely used; they are applied only in 12% of the cases (11 applications). Stainless steel (SS) is most commonly used (6 applications), while both titanium (Ti) alloy cobalt–chromium (Co–Cr) alloy are each applied in two cases (Figure 4.9b). We found the use of ceramic materials in three applications: ceramic-filled epoxy resin and alumina-zirconia composite in the DragonFlex steerable laparoscopic grasping forceps of Jelínek *et al.* [60, 62] and in the personalized tools for tracheostomy, a surgical procedure to help the breathing, by Ulmeanu *et al.* [56].

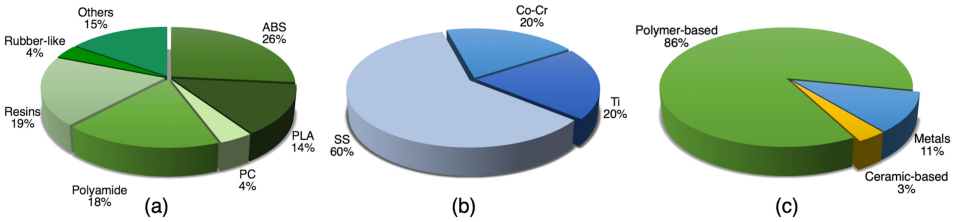

Figure 4.9: Materials used to 3D print medical instruments. (a) Percentages of different polymeric-based materials used to print medical instruments (see text for abbreviations); (b) percentages of different metallic materials used to print medical instruments; (c) percentages of different categories of materials used to print medical instruments.

4.6. Discussion

In this review, we provided an overview of the AM of medical instruments for diagnostics and surgery found in the literature, considering the novelty and clinical application. We analyzed the reasons related to the choice of using AM, the technologies, and the materials used. In this section, we will focus on properties and performance, the medical regulations and sterilization of additively manufactured medical instruments, the production cost, and the use of this technology to expand healthcare in developing countries, as well as to allow new surgical procedures.

4.6.1. Properties and performance of AM devices

Widely accepted advantages related to the use of AM are the simplicity of the manufacturing phase and the possibility of making complex shapes without increasing complexity in the fabrication process. However, due to the novelty of AM, there are still issues to be tackled, regardless of the specific technology. The AM processes create inhomogeneity in the material. Inhomogeneity creates anisotropic behavior of the material and can lead to unpredictable ruptures of the printed parts [71, 80, 84]. Another main cause of weaknesses in AM parts is print orientation [74]. Changing the orientation of printing can alter the stiffness of a printed part, as shown by Entsfellner *et al.* who printed a compliant mechanism in different directions [80]. Wong and Nowell *et al.* noticed weaknesses when forces are applied transversally to a 3D printed layer [29, 74]. Print orientation can also affect the cross-section of the printed part [71], but it is not the only factor that plays an important role during the printing process. Different printers and materials with the same technology can alter the final design [71, 93].

Accuracy is another important factor in AM; the higher the accuracy of the printer, the more the 3D printed device will correspond to the designed CAD model. VT is most accurate, but limitations in material choice limit its use in the medical field [62]. PBF is less accurate than VT, causing changes in design properties such as decreased flexibility of thin structures due to increased thickness of the layers [78]. Despite this, PBF offers the possibility to print without any support material due to the powder bed that creates support itself [71]. MJ allows the use of materials

with properties ranging from high stiffness to great flexibility. Nevertheless, it is necessary to remove a considerable amount of support material with consequences on the surface properties of the printed part [62]. ME is the most used AM technology due to its simplicity and the availability of cheap printers. However, ME needs support material [55], a controlled extrusion temperature and specific nozzle size depending on the material used [73]. It is therefore clear that, regardless the specific AM technology, the CAD model must be modified considering limitations and accuracy of the printer [35, 53, 56, 71], but also considering the results given by printing attempts and iterations [28, 62].

In Section 4.5.2 we pointed out that the majority of the materials used are polymer-based. Many polymers, such as PLA or nylon, are widely used in the medical field and for this reason already certificated for their biocompatible properties. However, polymers can change their properties over time. PLA becomes stiffer after some time [73] while some of the epoxy resins used in SLA change due to their photosensitivity [62]. The use of a polymer-based material also influences the mechanical properties of medical instruments. Brittleness and limitations in exerted forces [40] are reasons why AM is often considered to produce disposable instruments.

Nevertheless, there are advantages that only AM can provide. Boehler *et al.* presented a variable stiffness spherical joint printed using the multi-material properties of the MJ [79]. They printed a rigid polymer and a rubber-like material together in a single component. Roppenecker *et al.* printed a snake-like system designed as multiple pieces, but printed as a single structure, playing with tolerances in between the different elements [70]. Moreover, compliant mechanisms and joints can be printed [80], as well as different surface patterns [63], playing with material properties and thickness.

4.6.2. Medical regulations and sterilization

In 2017, the FDA issued a new guideline to share technical aspects on the use of AM technologies to fabricate medical devices [25]. The guideline covers all steps: from the design process to the test phase and sterilization. One of the critical aspects on the production of medical devices using AM is maintaining tight tolerances. Depending on the AM technology used, it can be challenging to keep the correct dimensions and geometry, especially in small-scale applications [56], and to produce identical pieces respecting tolerances. Another important factor that is almost never considered in the analyzed articles is the possibility of debris remaining even after sterilization, owing to the complex shape of the device. Any medical device needs to be sterilized before direct contact with the patient. However, the more complex the instrument geometry, the more difficult the sterilization process.

According to the Centers for Disease Control and Prevention, there are many sterilization techniques, such as autoclave, hydrogen peroxide gas plasma, and ethylene oxide gas [100]. The autoclave, which uses steam under pressure at a high temperature (121 °C or 134 °C), is nontoxic and allows quick cycles of sterilization. However, it can damage instruments printed with certain polymeric materials that have a relatively low melting point. For example, PLA becomes soft at 60 °C [51]

and ABS deteriorates at 88 °C [53]. The autoclave can be used with instruments printed with the PA 2200 polymer, but in this case, sterilization can be done only one time because, after the first use, the blood contamination cannot be eliminated [78]. Ethylene oxide gas and hydrogen peroxide gas plasma are low-temperature sterilization methods (below 60 °C) with a cycle duration of 12–24 h and 28–75 min, respectively [100]. However, ethylene oxide gas may be toxic and FDA recommends to use it as a last resort [101]. Hydrogen peroxide gas plasma is safe for the body and the environment. Both ethylene oxide gas plasma and hydrogen peroxide gas plasma can be used with additively manufactured instruments, but none of the covered studies have implemented these sterilization methods.

An interesting approach is suggested by three articles [29, 41, 55]. Due to the high temperature with which the material is extruded using FDM, it could be possible to consider the process as self-sterilizing (if the piece is printed in a sterile platform and environment), according to the polymerase chain reaction (PCR) test for bacteria load [41]. However, only 90% of the instruments printed by Kondor *et al.* were considered accurately sterilized directly after the printing process [32].

The overall conclusion is that even if some studies show an interest in the sterilization phase, many of them (42 studies) do not take this aspect into consideration. The choice of using AM in the early prototyping phase can explain the lack of concern in the sterilization phase. However, owing to the connection between complexity of design and difficulties in the sterilization process, it would be preferable to consider sterilization as a priority in the development of additively manufactured medical devices.

4.6.3. Production cost

AM is often considered as an inexpensive method of fabrication, and if we consider only the material cost, this is indeed frequently true [52, 80, 93]. However, there are various factors that must be considered. In order to design a medical instrument, an expertise in CAD modeling is necessary and the labor cost of a designer can be approximately $100–150 per hour [38]. The CAD software license can have an annual cost of approximately $2000 or more and even if free software packages are available, paid software packages are often necessary for complex geometries. Moreover, the design of fine mechanical systems needs a long refinement phase to adapt the CAD design to the 3D-printed results, increasing the labor cost of the designer. A considerable difference in cost is attributed to the type of printer used. FDM is the cheapest technology currently available [99] and the printer cost is approximately $2500 [41, 55, 59]. However, considering a similar build volume, printers such as multijet (MJ technology), stereolithography (VP technology), or selective laser sintering (PBF technology) have considerably higher costs, Table (4.3). Other factors that must be taken into consideration are post-processing, sterilization, and energy usage. Among the relevant articles analyzed, only two of them provided a detailed analysis of the costs; in both cases, the FDM technology was used [55, 56].

Table 4.3: Examples of 3D printers available in the market for fused deposition modeling (FDM), multijet (MUJ), stereolithography (SLA), and selective laser sintering (SLS), considering a similar build volume.

Printing process (printing technology)	Name	Company	Build Volume (cmxcmxcm)	Min. thickness layer (μm)	Material	Cost (€)
FDM (ME)	Ultimaker 2	Ultimaker	23.0x22.5x20.5	20	polymeric	2,500
FDM (ME)	AW3D HDX	Airwolf 3D	30.5x20.3x30.5	60	polymeric	3,500
MUJ (MJ)	ProJet 3510	3D Systems	29.8x18.5x20.3	32-16	polymeric	69,500
Polyjet (MJ)	Objet Eden	Stratasys	25.5x20.0x25.2	16	polymeric	19,800
SLA (VP)	ProJet6000	3D Systems	25.0x25.0x25.0	50	polymeric	200,000
SLA (VP)	Form 2	Formlabs	14.5x17.5x14.5	25-100	polymeric	4,000
SLS (PBF)	Elite P3600	TPM	36.0x36.0x60.0	130	polymeric	150,000
SLS (PBF)	ProX series	3D Systems	38.1x33.0x46.0	100	polymeric	500,000

4.6.4. 3D printing to help and 3D printing to challenge

Looking at the reasons behind the choice of using AM for medical instruments, it is clear that two major application groups can be distinguished: instruments made to help people in developing countries and instruments made to tackle new challenges in terms of design complexity and technical possibilities. Five of the analyzed articles presented ideas to expand the access to medical instrumentation in developing countries. Moreover, there are many non-profit organizations, such as the ILab/Haiti, which introduce AM to the locals in order to provide critical medical equipment such as umbilical cord clamps or oxygen splitters in a shorter time with an effective reduction in cost [102]. A similar project is implemented in Tanzania, where the ReFab Dar organization is exploring the opportunity of recycling plastic to produce medical supplies such as circumcision kits [103]. The intent of these non-profit organizations is obviously good, but there are still some challenges to be addressed, such as the energy supply required to run the 3D printers and the sterilization of instruments produced [102]. Moreover, there are a number of projects that base the material supply on recycling plastic but the consequences of this choice are not completely clear in terms of durability, mechanical properties, and sterilization. Another important issue that should be taken into consideration is the possibility of damage to the 3D printers and the need for experts to repair them. Simplifying the 3D printing process is one of the actions for expanding the accessibility and attaining faster and ready-to-use instruments.

A completely opposite trend in AM is to push its boundaries further in the design of highly complex devices capable of performing a new generation of medical procedures. Continuum robots are part of this group [67, 69, 71, 73]. These robots are designed to navigate to inaccessible areas of the human body that are impossible to treat with conventional instrumentation.

4.6.5. Temporal distribution and future trends

AM began to gain importance in the 1980s. Figure 4.10 shows how this technology has strongly increased its impact in the field of medical instruments for diagnostics and surgery only in the last eight years. In fact, we did not use any time limitation in our query and no relevant articles dated before 2011 were found. Compared to other medical fields, such as orthoses or surgical planning models, the interest in

medical instruments for diagnostics and surgery had grown later [104, 105]. This is probably related to the design complexity, advanced functionality, and miniature dimensions of medical instrumentation. The earliest designs for both orthotic and surgical models were only static models based on the images acquired by means of computed tomography scan or MRI without post-processing. On the contrary, it is often not possible to print medical instruments with the exact same design as used with conventional manufacturing to achieve the same functionality. The upward trend can then be considered as the consequence of an increase in knowledge of AM technologies.

In this review, we only considered the seven main categories of AM defined by ASTM. However, new technologies have been invented and tested in the last years. Microscale medical instruments for minimally invasive surgery have been printed by Cohen *et al.* with the innovative technique of Electrochemical FABrication (EFAB) in which, alternating layers of sacrificial material and structural material, the final device is produced with a layer thickness of 4 μm [106]. Other promising techniques in the micro/nanoscale are Projection Microstereolithography (PμSL) and Direct Ink Writing (DIW) which are widely explained by Mao *et al.* [107]. PμSL is a 3D printing technology similar to the SLA in which liquid photosensitive materials are polymerized. The high resolution of this technology is given by the combination of a single exposure per layer and the use of micromirror arrays to define the projected mask. DIW is similar to FDM, however, the material is not extruded due to an increase in heat but usually under pressure by exploiting the high viscosity of the material to keep the shape before the post-processing phase. These techniques are mainly used in the bioprinting field, but, given the possibility of printing different types of materials, among which polymers and metals, at a reasonably large volume, possible future applications can be seen in the production of micro-instrumentation, such as instruments for eye surgery, or soft actuators [108].

Improving conventional AM, an interesting direction is followed by Mangat *et al.* [109]. They use FDM to produce an enhanced material for medical applications by embedding natural fiber into conventional PLA. This idea can find applications not only in bioprinting but also in medical instruments where having tendons directly embedded into the device can lead to a faster assembly as well as more complex geometry in tendon-driven instruments.

Finally, a remarkable new technology is Continuous Liquid Interface Production (CLIP) developed to overcome limitations of SLA [110]. This technology, allows a 3D object to be built continuously without any stop between layers and at a higher speed than in SLA by keeping high resolution [111, 112]. The great potential shown by this technology can be foreseen in customization of medical instruments directly before or during surgery due to the high printing speed which allows for on-demand kits in a short time. High-resolution technologies, although still in an initial stage, as well as modified conventional AM have a great impact in the design of medical instruments leading to new designs impossible to produce with conventional manufacturing technologies.

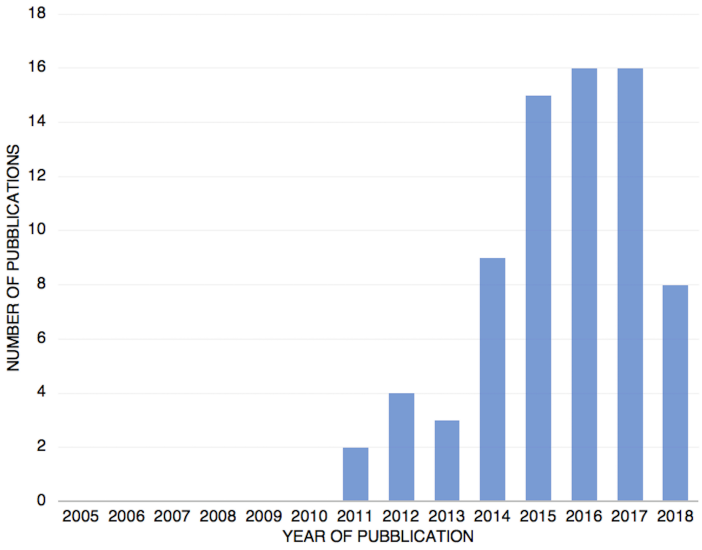

Figure 4.10: Temporal distribution of relevant articles found in the literature.

4.6.6. Limitations of this study

This review focuses on the AM of medical instruments for diagnostics and surgery taking into consideration only the seven technologies listed by the ASTM. However, the combination of additive and subtractive manufacturing technologies has not been considered as well as AM technologies such as the EFAB technology able to print medical devices in a microscale [106, 113]. Because we only considered articles in which the use of AM is specified, we did not cover papers without a description of the fabrication technology or the material used. A number of AM surgical guides are presented in the literature, mostly in dental interventions and orthopedic surgeries, but they are not included in this review. A comprehensive overview of such devices is provided by Dahake *et al.* [114] and Popescu *et al.* [115].

4.7. Conclusion

This review article provides an overview of the AM of medical instruments used for diagnostics and surgery. We categorized the medical instruments according to the clinical application, novelty, reasons behind the choice of using AM, and the technical characteristics of the AM technologies used. Using AM means having considerable freedom in terms of complexity of the design compared to conventional manufacturing. Several research groups are pushing the boundaries of AM to achieve instruments with advanced functionalities. However, sterilization issues are often ignored. AM is often considered to be an inexpensive and rapid method to produce on-demand medical instruments. The basic material used to print prototypes can be considered inexpensive but the printing technology used is often expensive. On the other hand,

the AM technology is opening the door to a personalized treatment that will help people with rare diseases or uncommon anatomy. Moreover, the simple production provides an easier access to healthcare for people who live in developing countries or remote areas. Making use of AM, without disregarding the practical aspects of such a sensitive field, is therefore a great opportunity for designers to develop a new generation of medical instruments with a great impact on society.

References

[1] C.-Y. Liaw and M. Guvendiren, *Current and emerging applications of 3d printing in medicine,* Biofabrication **9**, 024102 (2017).

[2] D. Hoang, D. Perrault, M. Stevanovic, and A. Ghiassi, *Surgical applications of three-dimensional printing: a review of the current literature & how to get started,* Annals of Translational Medicine **4** (2016).

[3] D. W. Hutmacher, *Scaffolds in tissue engineering bone and cartilage,* Biomaterials **21**, 2529 (2000).

[4] S. Singh, S. Ramakrishna, and R. Singh, *Material issues in additive manufacturing: A review,* Journal of Manufacturing Processes **25**, 185 (2017).

[5] S. Derakhshanfar, R. Mbeleck, K. Xu, X. Zhang, W. Zhong, and M. Xing, *3d bioprinting for biomedical devices and tissue engineering: A review of recent trends and advances,* Bioactive materials **3**, 144 (2018).

[6] N. Nagarajan, A. Dupret-Bories, E. Karabulut, P. Zorlutuna, and N. E. Vrana, *Enabling personalized implant and controllable biosystem development through 3d printing,* Biotechnology advances **36**, 521 (2018).

[7] J. K. Placone and A. J. Engler, *Recent advances in extrusion-based 3d printing for biomedical applications,* Advanced healthcare materials **7**, 1701161 (2018).

[8] N. Poomathi, S. Singh, C. Prakash, R. V. Patil, P. Perumal, V. A. Barathi, K. K. Balasubramanian, S. Ramakrishna, and N. Maheshwari, *Bioprinting in ophthalmology: current advances and future pathways,* Rapid Prototyping Journal (2019).

[9] A. Youssef, S. J. Hollister, and P. D. Dalton, *Additive manufacturing of polymer melts for implantable medical devices and scaffolds,* Biofabrication **9**, 012002 (2017).

[10] J. S. Akmal, M. Salmi, A. Mäkitie, R. Björkstrand, and J. Partanen, *Implementation of industrial additive manufacturing: Intelligent implants and drug delivery systems,* Journal of functional biomaterials **9**, 41 (2018).

[11] M. Palo, J. Holländer, J. Suominen, J. Yliruusi, and N. Sandler, *3d printed drug delivery devices: perspectives and technical challenges,* Expert Review of Medical Devices **14**, 685 (2017).

[12] W. Lee, D. Kwon, W. Choi, G. Y. Jung, A. K. Au, A. Folch, and S. Jeon, *3d-printed microfluidic device for the detection of pathogenic bacteria using size-based separation in helical channel with trapezoid cross-section,* Scientific Reports **5**, 7717 (2015).

[13] M. Zangheri, L. Cevenini, L. Anfossi, C. Baggiani, P. Simoni, F. Di Nardo, and A. Roda, *A simple and compact smartphone accessory for quantitative chemiluminescence-based lateral flow immunoassay for salivary cortisol detection,* Biosensors and Bioelectronics **64**, 63 (2015).

[14] T. Nozaki, T. Murakami, T. Shimono, K. Ohnishi, and R. Oboe, *Development of meal assistance device for patients with spinal cord injury,* in *Advanced Motion Control (AMC), 2016 IEEE 14th International Workshop on* (IEEE, 2016) pp. 388–393.

[15] J. ten Kate, G. Smit, and P. Breedveld, *3d-printed upper limb prostheses: a review,* Disability and Rehabilitation: Assistive Technology **12**, 300 (2017).

[16] Y.-a. Jin, J. Plott, R. Chen, J. Wensman, and A. Shih, *Additive manufacturing of custom orthoses and prostheses–a review,* Procedia CIRP **36**, 199 (2015).

[17] J. S. Cuellar, G. Smit, A. A. Zadpoor, and P. Breedveld, *Ten guidelines for the design of non-assembly mechanisms: The case of 3d-printed prosthetic hands,* Proceedings of the Institution of Mechanical Engineers, Part H: Journal of Engineering in Medicine **232**, 962 (2018).

[18] M. Salmi, J. Tuomi, K.-S. Paloheimo, M. Paloheimo, R. Björkstrand, A. A. Mäkitie, K. Mesimäki, and R. Kontio, *Digital design and rapid manufacturing in orbital wall reconstruction,* in *Innovative Developments in Design and Manufacturing* (CRC Press, 2009) pp. 357–360.

[19] J. Poukens, P. Laeven, M. Beerens, G. Nijenhuis, J. V. Sloten, P. Stoelinga, and P. Kessler, *A classification of cranial implants based on the degree of difficulty in computer design and manufacture,* The International Journal of Medical Robotics and Computer Assisted Surgery **4**, 46 (2008).

[20] N. Xu, F. Wei, X. Liu, L. Jiang, H. Cai, Z. Li, M. Yu, F. Wu, and Z. Liu, *Reconstruction of the upper cervical spine using a personalized 3d-printed vertebral body in an adolescent with ewing sarcoma,* Spine **41**, E50 (2016).

[21] M. Salmi, *Possibilities of preoperative medical models made by 3d printing or additive manufacturing,* Journal of medical engineering **2016** (2016).

[22] I. Gibson, L. K. Cheung, S. P. Chow, W. L. Cheung, S. L. Beh, M. Savalani, and S. H. Lee, *The use of rapid prototyping to assist medical applications,* Rapid Prototyping Journal **12**, 53 (2006).

[23] D. B. Jones, R. Sung, C. Weinberg, T. Korelitz, and R. Andrews, *Three-dimensional modeling may improve surgical education and clinical practice,* Surgical innovation **23**, 189 (2016).

[24] M. Randazzo, J. M. Pisapia, N. Singh, and J. P. Thawani, *3d printing in neurosurgery: a systematic review,* Surgical neurology international **7**, S801 (2016).

[25] FDA, *Technical Considerations for Additive Manufactured Medical Devices - Guidance for Industry and Food and Drug Administration Staff* (2017) p. 31.

[26] J. C. F. de Winter and D. Dodou, *A surge of p-values between 0.041 and 0.049 in recent decades (but negative results are increasing rapidly too),* PeerJ **3**, e733 (2015).

[27] A. C. F. o. A. M. Technologies and A. C. F. o. A. M. T. S. F. . on Terminology, *Standard Terminology for Additive Manufacturing Technologies* (ASTM International, 2012).

[28] M. George, K. R. Aroom, H. G. Hawes, B. S. Gill, and J. Love, *3d printed surgical instruments: The design and fabrication process,* World Journal of Surgery **41**, 314 (2017).

[29] J. Y. Wong and A. C. Pfahnl, *3d printing of surgical instruments for long-duration space missions,* Aviation Space and Environmental Medicine **85**, 758 (2014).

[30] J. Y. Wong, *Ultra-portable solar-powered 3d printers for onsite manufacturing of medical resources,* Aerospace Medicine and Human Performance **86**, 830 (2015).

[31] A. M. S. Ibrahim, R. R. Jose, A. N. Rabie, T. L. Gerstle, B. T. Lee, and S. J. Lin, *Three-dimensional printing in developing countries,* Plastic and Reconstructive Surgery - Global Open **3**, e443 (2015).

[32] S. Kondor, C. G. Grant, P. Liacouras, M. J. R. Schmid, L. Michael Parsons, V. K. Rastogi, L. S. Smith, B. Macy, B. Sabart, and C. Macedonia, *On demand additive manufacturing of a basic surgical kit,* Journal of Medical Devices **7**, 030916 (2013).

[33] M. George, H. Hawes, K. Aroom, B. S. Gill, and J. Love, *Inguinal hernia repair using 3d printed surgical instruments in the cadaveric model: A feasibility study,* Global Surgery **3**, 1 (2017).

[34] D. Paraskevopoulos, *Specification Analysis, Design, and Prototyping of a Burr Hole Endoscope Stabilization Device,* Surgical Innovation **23**, 613 (2016).

[35] M. del Junco, Z. Okhunov, R. Yoon, R. Khanipour, S. Juncal, G. Abedi, A. Lusch, and J. Landam, *Development and initial porcine and cadaver experience with three-dimensional printing of endoscopic and laparoscopic equipment,* Journal of Endourology-rology **29**, 58 (2015).

[36] I. Yamamoto, R. Ota, R. Zhu, M. Lawn, T. Ishimatsu, T. Nagayasu, K. Takagi, and T. Koji, *Research on seamless development of surgical instruments based on biological mechanisms using cad and 3d printer,* Bio-Medical Materials and Engineering **26**, S341 (2015).

[37] S. Kondor, C. G. Grant, P. Liacouras, and M. Schmid, *Personalized surgical instruments,* Journal of Medical Devices **7** (2013), 10.1115/1.4024487.

[38] S. M. Fuller, D. R. Butz, C. B. Vevang, and M. V. Makhlouf, *Application of 3-dimensional printing in hand surgery for production of a novel bone reduction clamp,* Journal of Hand Surgery **39**, 1840 (2014).

[39] I. Yamamoto, K. Kishikawa, Y. Kondo, M. Lawn, T. Nagayasu, N. Yamasaki, and K. Matsumoto, *Development of a finger like multi-joint articulated surgical retractor for use in endoscopic surgery,* Journal of Vibroengineering **20**, 1194 (2018).

[40] R. Singh, A. Suri, S. Anand, and B. Baby, *Validation of reverse-engineered and additive-manufactured microsurgical instrument prototype,* Surgical Innovation **23**, 606 (2016).

[41] T. M. Rankin, N. A. Giovinco, D. J. Cucher, G. Watts, B. Hurwitz, and D. G. Armstrong, *Three-dimensional printing surgical instruments: Are we there yet?* Journal of Surgical Research **189**, 193 (2014).

[42] A. A. Kaleev, L. N. Kashapov, N. F. Kashapov, and R. N. Kashapov, *Application of reverse engineering in the medical industry,* IOP Conference Series: Materials Science and Engineering **240** (2017), 10.1088/1757-899X/240/1/012030.

[43] D.-I. Băilă, I.-G. Ghionea, O.-C. Mocioiu, S. Ćuković, M.-E. Ulmeanu, C.-I. Tarbă, and L.-V. Lazăr, *Design of handle elevators and atr spectrum of material manufactured by stereolithography,* in *Product Lifecycle Management for Digital Transformation of Industries*, edited by R. Harik, L. Rivest, A. Bernard, B. Eynard, and A. Bouras (Springer International Publishing, Cham, 2016) pp. 309–318.

[44] D. I. Băilă, C. V. Doicin, C. M. Cotruț, M. E. Ulmeanu, I. G. Ghionea, and C. I. Tarbă, *Sintering the beaks of the elevator manufactured by direct metal laser sintering (dmls) process from co - cr alloy,* Metalurgija **55**, 663 (2016).

[45] N. Sanchez-Tamayo and J. Wachs, *Collaborative robots in surgical research: A low-cost adaptation,* ACM/IEEE International Conference on Human-Robot Interaction , 231 (2018).

[46] C. Aguilera-Astudillo, M. Chavez-Campos, A. Gonzalez-Suarez, and J. L. Garcia-Cordero, *A low-cost 3-d printed stethoscope connected to a smartphone,* Proceedings of the Annual International Conference of the IEEE Engineering in Medicine and Biology Society, EMBS , 4365 (2016).

[47] S. Rothenberg, S. Abdullah, and J. Hirsch, *3D Printing Prototypes for Healthcare Professionals: Creating a Reciprocating Syringe,* Journal of Digital Imaging **30**, 566 (2017).

[48] Y. Way, A. Mohamad, and Aesyhah, *The application of rapid prototyping technology and Quality Functional Deployment (QFD) approach in enhancing the endotracheal tube holder model in medical application,* MATEC Web of Conferences **35**, 2 (2015).

[49] R. Kontio, R. Björkstrand, M. Salmi, M. Paloheimo, K.-S. Paloheimo, J. Tuomi, and A. Mäkitie, *Designing and Additive Manufacturing A Prototype for A Novel Instrument for Mandible Fracture Reduction,* Surgery: Current Research (2012), 10.4172/2161-1076.S1-002.

[50] Y. Way, *Product Development and Cost Analysis of Fabricating the Prototype of Roller Clamp in Intravenous (I.V) Tubing Medical Devices using Fused Deposition Modeling (FDM) Technology,* IOP Conference Series: Materials Science and Engineering **290**, 12023 (2018).

[51] F. R. Cook, E. T. Geier, A. K. Asadi, R. C. Sá, and G. K. Prisk, *Rapid Prototyping of Inspired Gas Delivery System for Pulmonary MRI Research,* 3D Printing and Additive Manufacturing **2**, 196 (2015).

[52] J. A. Gálvez, A. F. Simpao, Y. Dori, K. Gralewski, N. H. McGill, M. L. Rivera, N. Delso, H. Khan, M. A. Rehman, and J. E. Fiadjoe, *Not Just a Pretty Face: Three-Dimensional Printed Custom Airway Management Devices,* 3D Printing and Additive Manufacturing **3**, 160 (2016).

[53] E. V. Navajas and M. ten Hove, *Three-Dimensional Printing of a Transconjunctival Vitrectomy Trocar-Cannula System,* Ophthalmologica **237**, 119 (2017).

[54] M. del Junco, R. Yoon, Z. Okhunov, G. Abedi, C. Hwang, B. Dolan, and J. Landman, *Comparison of Flow Characteristics of Novel Three-Dimensional Printed Ureteral Stents Versus Standard Ureteral Stents in a Porcine Model,* Journal of Endourology **29**, 1065 (2015).

[55] J. M. Walker, D. A. Elliott, C. D. Kubicky, C. R. Thomas, and A. M. Naik, *Manufacture and evaluation of 3-dimensional printed sizing tools for use during intraoperative breast brachytherapy,* Advances in Radiation Oncology **1**, 132 (2016).

[56] M. Ulmeanu, C. Doicin, D. Baila, A. Rennie, C. Neagu, and S. Laha, *Comparative evaluation of optimum additive manufacturing technology to fabricate bespoke medical prototypes of composite materials,* Materiale Plastice **52**, 416 (2015).

[57] B. M. Walter, A. Hann, R. Frank, and A. Meining, *A 3D-printed cap with sideoptics for colonoscopy: A randomized ex vivo study,* Endoscopy **49**, 808 (2017).

[58] W. J. Ko, G. W. Song, S. P. Hong, C. I. Kwon, K. B. Hahm, and J. Y. Cho, *Novel 3D-printing technique for caps to enable tailored therapeutic endoscopy,* Digestive Endoscopy **28**, 131 (2016).

[59] D. C. Steinemann, P. C. Müller, M. Apitz, F. Nickel, H. G. Kenngott, B. P. Müller-Stich, and G. R. Linke, *An ad hoc three dimensionally printed tool facilitates intraesophageal suturing in experimental surgery,* Journal of Surgical Research **223**, 87 (2018).

[60] F. Jelínek, R. Pessers, and P. Breedveld, *DragonFlex Smart Steerable Laparoscopic Instrument,* Journal of Medical Devices **8**, 015001 (2014).

[61] F. Jelínek, T. Diepens, S. Dobbenga, G. Van Der Jagt, D. Kreeft, A. Smid, R. Pessers, and P. Breedveld, *Method for minimising rolling joint play in the steerable laparoscopic instrument prototype DragonFlex,* Minimally Invasive Therapy & Allied Technologies **24**, 181 (2015).

[62] F. Jelínek and P. Breedveld, *Design for Additive Manufacture of Fine Medical Instrumentation—DragonFlex Case Study,* Journal of Mechanical Design **137**, 111416 (2015).

[63] C. A. Seneci, J. Shang, A. Darzi, and G.-Z. Yang, *Rapid manufacturing with selective laser melting for robotic surgical tools: Design and process considerations,* (2015) pp. 824–830.

[64] C. A. Seneci, G. Gras, P. Wisanuvej, J. Shang, and G. Z. Yang, *3D printing of improved needle grasping instrument for flexible robotic surgery,* (2017) pp. 2524–2530.

[65] A. Sakes, K. Hovland, G. Smit, J. Geraedts, and P. Breedveld, *Design of a novel three- dimensional-printed two degrees-of-freedom steerable electrosurgical grasper for minimally invasive surgery,* Journal of Medical Devices, Transactions of the ASME **12**, 011007 (2018).

[66] M. Sahlabadi, K. Jezler, and P. Hutapea, *Novel Steerable Smart Needle With a Built-In Recovery Mechanism for Multiple Actuations,* ASME 2017 Conference on Smart Materials, Adaptive Structures and Intelligent Systems , V002T04A012 (2017).

[67] K. Oliver-Butler, Z. H. Epps, and D. C. Rucker, *Concentric agonist-antagonist robots for minimally invasive surgeries,* in *Proc. SPIE 10135, Medical Imaging 2017: Image-Guided Procedures, Robotic Interventions, and Modeling*, Vol. 10135 (2017) p. 1013511.

[68] J. Mintenbeck, M. Siegfarth, R. Estaña, and H. Wörn, *Flexible instrument for minimally invasive robotic surgery using rapid prototyping technology for fabrication,* (2014) pp. 1085–1090.

[69] Y. Kim, S. S. Cheng, and J. P. Desai, *Towards the development of a spring-based continuum robot for neurosurgery,* Medical Imaging 2015: Image-Guided Procedures, Robotic Interventions, and Modeling **9415**, 94151Q (2015).

[70] D. B. Roppenecker, A. Pfaff, J. A. Coy, and T. C. Lueth, *Multi Arm Snake - Like Robot Kinematics,* (2013) pp. 5040–5045.

[71] T. K. Morimoto and A. M. Okamura, *Design of 3-D Printed Concentric Tube Robots,* IEEE Trans. Robotics **32**, 1419 (2016).

[72] P. Qi, C. Zhang, J. Li, Z. Li, J. S. Dai, and K. Althoefer, *A compact continuum manipulator system with enhanced steering abilities for robot-assisted surgery,* Proceedings of the IEEE RAS and EMBS International Conference on Biomedical Robotics and Biomechatronics , 49 (2016).

[73] E. Amanov, T.-D. Nguyen, and J. Burgner-Kahrs, *Additive manufacturing of patient-specific tubular continuum manipulators,* in *Medical Imaging 2015: Image-Guided Procedures, Robotic Interventions, and Modeling*, Vol. 9415, edited by R. J. W. III and Z. R. Yaniv, International Society for Optics and Photonics (SPIE, 2015) pp. 420 – 428.

[74] R. Nowell, B. Shirinzadeh, L. Lai, J. Smith, and Y. Zhong, *Design of a 3-DOF parallel mechanism for the enhancement of endonasal surgery,* IEEE/ASME International Conference on Advanced Intelligent Mechatronics, AIM , 749 (2017).

[75] A. Schmitz, A. J. Thompson, P. Berthet-Rayne, C. A. Seneci, P. Wisanuvej, and G. Z. Yang, *Shape sensing of miniature snake-like robots using optical fibers,* (2017) pp. 947–952.

[76] Y. S. Krieger, D. B. Roppenecker, I. Kuru, and T. C. Lueth, *Multi-Arm Snake-Like Robot,* (2017) pp. 2490–2495.

[77] D. B. Roppenecker, M. F. Traeger, J. D. Gumprecht, and T. C. Lueth, *How to design and create a cardan shaft for a single port robot by selective laser sintering,* in *ASME International Mechanical Engineering Congress and Exposition*, Vol. 45196 (American Society of Mechanical Engineers, 2012) pp. 49–58.

[78] S. Coemert, M. F. Traeger, E. C. Graf, and T. C. Lueth, *Suitability Evaluation of various Manufacturing Technologies for the Development of Surgical Snake-like Manipulators from Metals Based on Flexure Hinges,* Procedia CIRP **65**, 1 (2017).

[79] Q. Boehler, M. Vedrines, S. Abdelaziz, P. Poignet, and P. Renaud, *Design and evaluation of a novel variable stiffness spherical joint with application to MR-compatible robot design,* (2016) pp. 661–667.

[80] K. Entsfellner, I. Kuru, T. Maier, J. D. Gumprecht, and T. C. Lueth, *First 3D printed medical robot for ENT surgery - Application specific manufacturing of laser sintered disposable manipulators,* (2014) pp. 4278–4283.

[81] J. Cortes-Rodicio, G. Sanchez-Merino, M. A. Garcia-Fidalgo, and I. Tobalina-Larrea, *A novel stereotactic frame for real PET-guided biopsies: A preclinical proof-of-concept,* Physica Medica **41**, 124 (2017).

[82] H. Saafi, C. Preault, M. A. Laribi, and S. Zeghloul, *A Novel Kinematic of a 4 d.o.fs Haptic Device Based on the Delta Robot Architecture,* in *Advances in Service and Industrial Robotics*, edited by C. Ferraresi and G. Quaglia (Springer International Publishing, Cham, 2018) pp. 699–706.

[83] S. B. Kesner and R. D. Howe, *Design Principles for Rapid Prototyping Forces Sensors using 3D Printing.* (2011) pp. 866–870.

[84] G. A. Fontanelli, L. R. Buonocore, F. Ficuciello, L. Villani, and B. Siciliano, *A novel force sensing integrated into the trocar for minimally invasive robotic surgery,* in *2017 IEEE/RSJ International Conference on Intelligent Robots and Systems (IROS)* (IEEE, 2017) pp. 131–136.

[85] J. I. R. García, J. M. S. Velasco, M. V. Suárez, A. C. Pereira, V. Sosa, and J. L. C. Rodríguez, *Design Engineering in Surgery. How to Design, Test and Market Surgical Devices Made With 3 D Printing?* Cirugia Espanola **96**, 198 (2018).

[86] J. Chen, T. Pickett, A. Langell, A. Trane, B. Charlesworth, K. Loken, S. Lombardo, and J. T. Langell, *Industry-academic partnerships: An approach to accelerate innovation,* Journal of Surgical Research **205**, 228 (2016).

[87] E. Epaminonda, T. Drakos, C. Kalogirou, M. Theodoulou, C. Yiallouras, and C. Damianou, *MRI guided focused ultrasound robotic system for the treatment of gynaecological tumors,* The International Journal of Medical Robotics and Computer Assisted Surgery **12**, 46 (2016).

[88] G. Menikou, C. Yiallouras, M. Yiannakou, and C. Damianou, *MRI-guided focused ultrasound robotic system for the treatment of bone cancer,* International Journal of Medical Robotics and Computer Assisted Surgery **13**, e1753 (2017).

[89] C. Yiallouras, N. Mylonas, and C. Damianou, *MRI-compatible positioning device for guiding a focused ultrasound system for transrectal treatment of prostate cancer,* International Journal of Computer Assisted Radiology and Surgery **9**, 745 (2014).

[90] N. Mylonas and C. Damianou, *MR compatible positioning device for guiding a focused ultrasound system for the treatment of brain deseases,* The International Journal of Medical Robotics and Computer Assisted Surgery **10**, 1 (2014).

[91] M. Peikari, T. K. Chen, E. C. Burdette, and G. Fichtinger, *Section-thickness profiling for brachytherapy ultrasound guidance,* in *Medical Imaging 2011: Visualization, Image-Guided Procedures, and Modeling*, Vol. 7964 (International Society for Optics and Photonics, 2011) p. 79640R.

[92] S. Dikici, B. Aldemir Dikici, H. Eser, E. Gezgin, Ö. Başer, S. Şahin, B. Yılmaz, and H. Oflaz, *Development of a 2-dof uterine manipulator with LED illumination system as a new transvaginal uterus amputation device for gynecological surgeries,* Minimally Invasive Therapy & Allied Technologies **27**, 117 (2018).

[93] A. L. Rugg, L. Y. Nelson, M.-A. I. Timoshchuk, and E. J. Seibel, *Design and Fabrication of a Disposable Dental Handpiece for Clinical Use of a New Laser-Based Therapy-Monitoring System,* Journal of Medical Devices **10**, 011005 (2015).

[94] M. Maeda, N. Kanai, S. Kobayashi, T. Hosoi, R. Takagi, T. Ohki, Y. Muragaki, M. Yamato, S. Eguchi, F. Fukai, and T. Okano, *Endoscopic cell sheet transplantation device developed by using a 3-dimensional printer and its feasibility evaluation in a porcine model,* Gastrointestinal Endoscopy **82**, 147 (2015).

[95] E. Zizer, D. Roppenecker, F. Helmes, S. Hafner, Y. Krieger, T. Luth, and A. Meining, *A new 3D-printed overtube system for endoscopic submucosal dissection: first results of a randomized study in a porcine model,* Endoscopy **48**, 762 (2016).

[96] M. F. Traeger, D. B. Roppenecker, M. R. Leininger, F. Schnoes, and T. C. Lueth, *Design of a spine-inspired kinematic for the guidance of flexible instruments in minimally invasive surgery,* in *IEEE International Conference on Intelligent Robots and Systems* (2014) pp. 1322–1327.

[97] D. B. Roppenecker, A. Meining, G. Horst, H. Ulbrich, and T. C. Lueth, *Interdisciplinary development of a single-port robot,* in *2012 IEEE International Conference on Robotics and Biomimetics, ROBIO 2012 - Conference Digest* (2012) pp. 612–617.

[98] Y. S. Krieger, D. B. Roppenecker, J. U. Stolzenburg, and T. C. Lueth, *First step towards an automated designed Multi-Arm Snake-Like Robot for minimally invasive surgery,* in *IEEE RAS and EMBS International Conference on Biomedical Robotics and Biomechatronics* (2016) pp. 407–412.

[99] M. P. Chae, W. M. Rozen, P. G. McMenamin, M. W. Findlay, R. T. Spychal, and D. J. Hunter-Smith, *Emerging Applications of Bedside 3D Printing in Plastic Surgery,* Frontiers in Surgery **2**, 1 (2015).

[100] W. A. W. A. Rutala 1948- and D. J. D. J. Weber 1951-, *Guideline for disinfection and sterilization in healthcare facilities, 2008,* .

[101] H. Shintani, *Ethylene oxide gas sterilization of medical devices,* Biocontrol science **22**, 1 (2017).

[102] A. D. Dotz, *A pilot of 3d printing of medical devices in haiti,* in *Technologies for development* (Springer, 2015) pp. 33–44.

[103] *ReFab Dar,* http://www.refabdar.org/, Accessed:2018-07-17.

[104] D. Freeman and L. Wontorcik, *Stereolithography and prosthetic test socket manufacture: A cost/benefit analysis,* JPO: Journal of Prosthetics and Orthotics **10**, 17 (1998).

[105] M. McGurk, A. A. Amis, P. Potamianos, and N. M. Goodger, *Rapid prototyping techniques for anatomical modelling in medicine.* Annals of the Royal College of Surgeons of England **79**, 169 (1997).

[106] A. Cohen, R. Chen, U. Frodis, M. Wu, and C. Folk, *Microscale metal additive manufacturing of multi-component medical devices,* Rapid Prototyping Journal **16**, 209 (2010).

[107] M. Mao, J. He, X. Li, B. Zhang, Q. Lei, Y. Liu, and D. Li, *The emerging frontiers and applications of high-resolution 3D printing,* Micromachines **8**, 113 (2017).

[108] M. Wehner, R. L. Truby, D. J. Fitzgerald, B. Mosadegh, G. M. Whitesides, J. A. Lewis, and R. J. Wood, *An integrated design and fabrication strategy for entirely soft, autonomous robots,* Nature **536**, 451 (2016).

[109] A. S. Mangat, S. Singh, M. Gupta, and R. Sharma, *Experimental investigations on natural fiber embedded additive manufacturing-based biodegradable structures for biomedical applications,* Rapid Prototyping Journal **24**, 1221 (2018).

[110] M. Degnan, *3D Printing Techniques and Processes*, Project Learning with 3D Printing (Cavendish Square Publishing LLC, 2017).

[111] J. R. Tumbleston, D. Shirvanyants, N. Ermoshkin, R. Janusziewicz, A. R. Johnson, D. Kelly, K. Chen, R. Pinschmidt, J. P. Rolland, A. Ermoshkin, *et al.*, *Continuous liquid interface production of 3d objects,* Science **347**, 1349 (2015).

[112] R. L. Truby and J. A. Lewis, *Printing soft matter in three dimensions,* Nature **540**, 371 (2016).

[113] J. Gafford, Y. Ding, A. Harris, T. McKenna, P. Polygerinos, D. Holland, C. Walsh, and A. Moser, *Shape Deposition Manufacturing of a Soft, Atraumatic, and Deployable Surgical Grasper,* Journal of Mechanisms and Robotics **7**, 021006 (2015).

[114] S. W. Dahake, A. M. Kuthe, M. B. Mawale, and A. D. Bagde, *Applications of medical rapid prototyping assisted customized surgical guides in complex surgeries,* Rapid Prototyping Journal **22**, 934 (2016).

[115] D. Popescu and D. Laptoiu, *Rapid prototyping for patient-specific surgical orthopaedics guides: A systematic literature review,* Proceedings of the Institution of Mechanical Engineers, Part H: Journal of Engineering in Medicine **230**, 495 (2016).

5

Non-Assembly 3D Printing for Compliant Surgical Devices

Published as:
Culmone, C., Henselmans, P. W., van Starkenburg, R. I., and Breedveld, P. "Exploring non-assembly 3D printing for novel compliant surgical devices". PLOS One, 15.5 (2020), e0232952.

Abstract

In minimally invasive surgery, maneuverability is usually limited and a large number of degrees of freedom (DOF) is highly demanded. However, increasing the DOF usually means increasing the complexity of the surgical instrument leading to long fabrication and assembly times. In this work, we propose the first fully 3D printed (in all its parts except for the actuation cables and their fixation) handheld, multi-steerable device. The proposed device is mechanically actuated, and possesses five serially controlled segments. We designed a new compliant segment providing high torsion and axial stiffness as well as a low bending stiffness by merging the functions of four helicoids and a continuum backbone. Compliant segments were combined to form the compliant shaft of the new device. In order to control this compliant shaft, a control handle was designed that mimics the shaft structure. A prototype called the HelicoFlex was built using only three 3D printed parts. HelicoFlex, with its 10 degrees of freedom, showed a fluid motion in performing single and multi-curved paths. The multi-steerable instrument was 3D printed without any support material in the compliant shaft itself. This work contributes to enlarge the body of knowledge regarding how additive manufacturing could be used in the production of multi-steerable surgical instruments for personalized medicine.

5.1. Introduction

Over the last decades, one of the most significant innovations in surgery is the transition from open surgery to minimally invasive surgery (MIS). In open surgery, the area of interest is directly exposed, and depending on the specific procedure, the incision can be relatively large [1, 2]. However, increasing the size of the incision means increasing the risk of infection as well as the recovery time for the patient [3, 4]. Conversely, MIS strives to reduce the incision size by using smaller instruments and indirect visualization using endoscopes. However, using conventional tools that are straight, long, and rigid while decreasing the size of the incision, has a high impact on the maneuverability of the instruments and the reachability of the area of interest. The problem is evident in Natural Orifice Transluminal Endoscopic Surgery (NOTES) which uses natural orifices such as mouth, nose, or anus as the entry port of the body [5, 6]. For instance, Endoscopic Endonasal Surgery (EES) is a NOTES procedure in which the nostrils are the entry port to reach and remove tumors at the base of the skull. A common procedure is the removal of adenomas in the pituitary gland. The narrow corridor through the nostrils limits the maneuverability of the used rigid instruments.

Research groups have analyzed the problem of instrument maneuverability, and many devices have been proposed [7]. The use of the well-known da Vinci® robotic system (Intuitive Surgical Inc., Sunnyvale, Ca, USA) with integrated EndoWrist technology: a two degrees of freedom (DOF) mechanism for steering into the distal end of the surgical instruments, increases surgeon dexterity in a laparoscopy scenario allowing procedures in which high maneuverability is required [8] (Figure 5.1).

However, steerability is still limited due to rigid instrument shafts which do not permit navigation through curves with multiple radii [10]. Moreover, miniaturized pulleys, which are at the base of the EndoWrist design, guide the cables, provoking fatigue and limiting the lifespan to a maximum of ten sterilization cycles, increasing

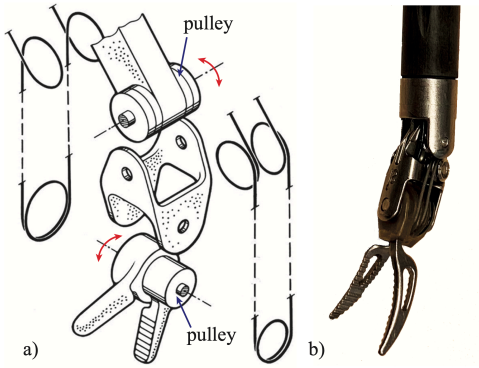

Figure 5.1: Endo Wrist Grasper. a) Schematic exploded view of the Endo Wrist in which the different driving cables, pulleys, and rivets are shown, adapted from Breedveld *et al.* [9], based on the EndoWrist patent [10], and b) a Ø 8 mm Endo Wrist Grasper. In the EndoWrist, the two pulleys are positioned perpendicular to each other provide two DOF (red arrows).

the overall costs [11].

In order to overcome the rigidity of the shaft, research has been focused on the integration of an additional flexible component at the end of the rigid shaft, allowing maneuvering over more complex curvatures and expanding the motion beyond the 2 DOF EndoWrist. The flexibility of the additional component can be obtained using continuum structures. Multi-steerable instruments based on continuum structures can be compared with "invertebrates" due to their ability to form continuous curves [12, 13]. Examples of continuum structures are concentric telescopic tube robots [14] composed of concentric precurved tubes placed into one another. The control of the rotation and the translation of the tubes relative to each other allows the formation of curved shapes [14, 15]. Another approach is using a single- or a multi-backbone structure. In a single-backbone structure, a single element supports the entire flexible segment. This element can be made of shape memory alloys [16], springs [17], flexible tubes [18], or variable stiffness mechanisms [19, 20]. Multi-backbone structures are based on multiple elements, for example parallel rods, that equally contribute to the motion of the flexible tip [21].

Regardless of the number of backbones used, multi-steerable instruments require a method of actuation. Types of actuation are based on hydraulic and pneumatic principles, as well as shape memory alloys [7]. However, tendon-driven actuation remains most commonly used in medical applications due to the possibility of minimizing the size of the tip while at the same time controlling a large number of DOF [22]. In an attempt to control the complex motion of such a multi DOF shaft, each DOF can be individually controlled and actuated using independent electric motors. Due to their relatively large size, these motors should then be placed outside the patient at the control side of the instrument. However, the use of a large number of motors generally results in high production costs, difficulties in sterilization, and unsuitability for disposable use [23]. Moreover, a system with a large number of motors requires a large footprint, reducing the workspace for the surgeon near the patient.

In an attempt to solve these problems, manually actuated instruments such as the HelixFlex proposed by Gerboni *et al.* or the multi-backbone elbow device presented by Riojas *et al.*, have been developed, presenting a completely different approach by being multi-steerable and at the same time handheld [24, 25]. These instruments are fully mechanically actuated with no need for electric motors. Fan *et al.* [26] give a comprehensive overview of handheld (multi-)steerable instruments and Anderson *et al.* [27] of their control methods. Although the proposed handheld devices meet the requirements in terms of flexibility, miniaturization, and maneuverability, they are still very complex, containing numerous complex-shaped parts, impairing the assembly process, and making the device unsuited for sterilization or low-cost disposable use.

Additive manufacturing (AM), also referred to as three-dimensional (3D) printing, might provide a solution. AM enables a computer-aided design (CAD) to be directly converted into a 3D object with a layer by layer printing process. AM allows the production of structures with complex geometries that cannot be produced with conventional fabrication techniques. Moreover, this increase in geometrical complexity allows for the integration of more functionality into a single part, consequently reducing the need for assembling multiple parts. Many research groups are exploiting

this technology in the field of medical instruments [28]. An example is given by the manipulator presented by Mintenbeck *et al.* in which AM was used in the fabrication of the steerable segments [29]. Morimoto and Okamura applied AM into concentric tube robots investigating different materials and 3D printing technology [30], whereas at the Technical University of Munich researchers developed a 3D printed overtube to enhance the properties of conventional flexible endoscopes [31, 32].

Although problems such as steerability and miniaturization have been addressed, design complexity is still high and the number of components is still large, hindering the reduction of assembly time. Therefore, this study explores the use of AM for the development of a manually actuated tendon-driven multi-steerable surgical device, intending to simplify its fabrication and assembly process to make it suitable for disposable use. A new device called HelicoFlex was developed as a first explorative case to combine easy manufacture with very high steering performance. HelicoFlex is the first handheld device that is printed in only three parts with five steerable segments, which enables the control of 10 DOF. In the first part of the paper, we will explore new geometries to find a design paradigm to combine the characteristics of a compliant shaft and minimize the number of parts while using AM. In the second part of the paper, we present the entire design and study its behavior in performing complex curves.

5.2. Conceptual design of the compliant shaft

5.2.1. Design requirements

The compliant shaft of our instrument should allow high steerability in terms of multiple DOF to follow tortuous paths and complex curves with different radii. The device should, therefore, include multiple segments that are serially connected and each bendable in 2 DOF. Each segment should have a high axial and torsional stiffness, whereas a relatively low bending stiffness is preferred. Axial stiffness is required for reliable control of the compliant shaft whereas torsional stiffness is required to endure axial torques that arise from external loads. On the contrary, low bending stiffness is preferred as it improves the bendability of the entire shaft and limits the required tensile forces on the steering cables, reducing the forces required for actuation and resulting in lower friction forces in the system. For application in MIS, the diameter of the compliant shaft should not exceed 10 mm [33], integrating at least one lumen to allow for the insertion of additional instruments (e.g., biopsy forceps) or tools to visualize and operate on the area of interest. Guidance and fixation of cables are two of the most challenging functionalities within a tendon-driven device, and therefore often have a significant influence on the shape, fabrication, and assembly process of the device, especially in multi-steerable instruments that incorporate many cables. An effective and scalable method for integrating the functionalities of cable guidance and fixation in preferably one single component was therefore a key research topic in the design of our instrument. Finally, the new compliant shaft should preferably be 3D printed without support material, which is sacrificial material needed to print specific overhangs, in order to reduce the post-processing time after the printing process.

5.2.2. Design choices

Conventional steerable instruments are generally based on a chain of connected rigid elements. In the specific case of EndoWrist, steering in two directions is provided by a series of miniature pulleys placed perpendicular to each other and individually controlled by driving cables looped around the pulleys (Figure 5.1). As the diameter of the pulleys is too small as compared to the thickness of the driving cables, the cables suffer from fatigue, reducing the lifespan of the EndoWrist to only ten procedures [34]. In our design, we aimed at avoiding pulleys by using a cable guidance system that does not generate fatigue. Moreover, we aimed at greatly expanding EndoWrist's motion to 10 DOF while merging all its rigid-linked frame properties into one 3D printed compliant component without using support, combining high axial and torsional stiffness with low bending stiffness. We strived to have at least one lumen and containing simple means to guide and fix 20 actuation cables, to facilitate fast and easy assembly.

Compliant segment design

A compliant structure that combines high axial stiffness with low bending stiffness can be created by using a thin beam serving as a continuous backbone at the center of a steering segment (Figure 5.2a).

However, a thin beam is not torsion stiff. Increasing the diameter of the beam would provide higher torsion stiffness, yet would also increase its bending stiffness. Thus, an additional element has to be added to ensure torsion stiffness. A helicoid is a compliant element able to provide high torsion stiffness and low bending stiffness. In our design, we decided to combine these two elements: a continuous thin central backbone around which a helicoid runs (Figure 5.2b). Four helicoids were evenly placed around the centerline to provide a more homogeneous torsion stiffness as compared to only one helicoid (Figure 5.2c). The pitch of each helicoid was kept equal to the length of the backbone, meaning that each helicoid makes one full turn

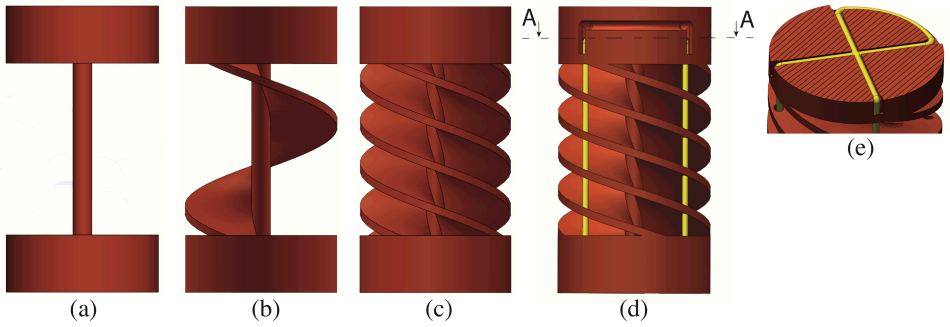

Figure 5.2: Schematic drawing of a 3D-printed compliant shaft segment with actuation cables in yellow. (a) A solid backbone gives a high axial stiffness; (b) a helicoid increases torsion stiffness; (c) increasing the number of helicoids makes the system more homogeneous; (d) holes are added to guide four actuation cables through the helicoids; and (e) the segment is completed with an additional structure to loop and fasten the actuation cables.

within the length of the backbone.

Finally, we defined the exact shape of the four helicoids. As shown in the cross-section in Figure 5.3a, we started with a thin rectangular shape for the helicoids. However, at the inside of these helicoids, cracks can be provoked by excessive bending. By increasing the thickness of the helicoids, we can ensure that the helicoids would touch each other at their outer edge, thus creating a stop for the bending (Figure 5.3b). However, increasing the thickness of the helicoid at the outer edge while keeping the rectangular shape would increase the bending stiffness as, in this case, more material is added to the backbone. Therefore, we decided to change the rectangular shape into a T-shape (Figure 5.3c), keeping a low bending stiffness while at the same time limiting the maximum bending angle.

Cable fixation method

As previously discussed, cable fixation is an important aspect that can affect the robustness of the device, causing malfunctioning or breakages. In our compliant design, we decided on an alternative cable fixation method avoiding soldering or gluing in the shaft. Exploring friction-based fixation methods led us to a solution in which the cables are looped inside the structure. As shown in Figure 5.2e, by looping a cable into a cross-shaped groove in the transversal plane of the segment and bending both its ends 90 degrees in the pulling direction, we obtain two independent actuation cables positioned at an angle of 90 degrees and connected in a sturdy cable fixation

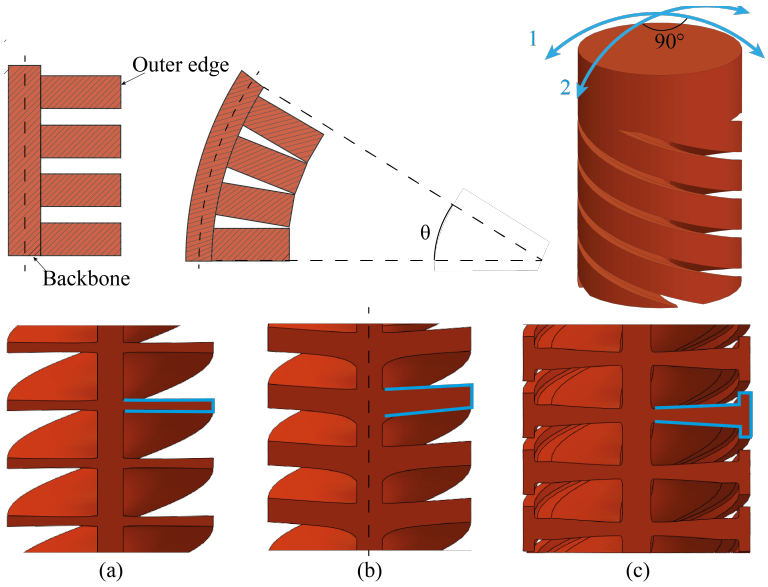

Figure 5.3: Helicoids shape design. Top: Sketch of a compliant segment in a straight and bent position with light blue arrows showing the two DOF per segment; each segment being able to bend in two perpendicular directions. Bottom: different shapes of the helicoids cross-section: (a) thin rectangular shape, (b) thick rectangular shape, (c) T-shape.

point (Figure 5.2d). Fixating four actuation cables per segment was realized by adding two cable fixation points on top of each other, rotated over 180 degrees. The total height of the resulting fixation module was 3 mm, leading to a total segment length of 12 mm. For our prototype, we decided to use an outer diameter of 8 mm.

5.3. Proof of concept — HelicoFlex

After characterizing a single 3D printed segment of the compliant shaft, we designed the entire HelicoFlex (Figure 5.4). The instrument is composed of only three components: a compliant shaft and a compliant handle with a rigid shaft in between. We designed a handle with a compliant structure equivalent to the compliant shaft. The compliant shaft and the handle were connected using cables that actuate the device with a serial control method, described by Fan *et al.* [26], in which the compliant shaft mirrors the movement of the compliant handle (Figure 5.4a).

The compliant shaft of the device is composed out of compliant segments (Ø 8 mm, length 12 mm) stacked on top of each other to create a modular shaft in which the number of segments can be changed according to the number of DOF required. We decided for a shaft with five compliant segments, resulting in a total of 10 DOF at a length of 60 mm (Figure 5.4b). Each compliant segment has a backbone of Ø 1 mm and is actuated by four cables that are fixed at the segment location, as shown in Figure 5.2e, and run along the compliant shaft in a cable-ring configuration. Each segment is twisted around its heartline over 18 degrees as compared to the previous segment in order to avoid overlapping of the 20 parallel-running cables.

The *rigid shaft* (Ø 8 mm, 120 mm long) is printed in one part together with the compliant shaft and guides the cables from the compliant shaft to the handle through dedicated grooves running along its entire length (Figure 5.4b).

The *compliant handle* is connected to the rigid shaft by means of a press-fit mechanism, and its design is based on a large version of the compliant shaft (Figure 5.4d). The handle contains an inner backbone and an outer helical structure. The inner backbone has a structure similar to the compliant shaft, containing five segments with a diameter of 8 mm and a length of 18.5 mm. The outer helical structure of the handle has an outer diameter of 29 mm and contains holes through which the cables run. Running the cables through the handle at a larger diameter than in the compliant shaft creates not only additional space for precise fixation of the cables but also creates an amplification factor between the handle and the compliant shaft. Assuming that there is no friction, no play, no compression of the printed parts, and no stretching of the cables, the amplification factor can be calculated using the following equation:

$$\gamma = \beta \frac{D_{\text{handle}}}{D_{\text{shaft}}} \tag{5.1}$$

where γ is the desired bending angle of the tip, β is the corresponding bending angle of the handle, D_{handle} is the diameter of the cable ring in the compliant handle, and D_{shaft} is the diameter of the cable ring in the compliant shaft. In order to guide the cables

smoothly from the shaft to the handle, an amplification component was designed at the distal side of the handle to gently amplify the cable distance from 6.5 mm to 22 mm. The amplification component guides the cables smoothly through partly covered S-shaped grooves while avoiding buckling. The amplification component is covered by a hive-inspired structure with holes. The hive structure facilitates the 3D printing process by enabling precise printing of cable grooves, avoiding clogging (Figure 5.4f).

In the handle, cables were fixated via dog point set screws to enable easy fine-tuning. The ends of all cables were collected and stored inside the end cap (Figure 5.4c), attached to the handle by a press-fit mechanism. Four lumens with a diameter of 1.75 mm run through the entire device to enable the insertion of thin, flexible

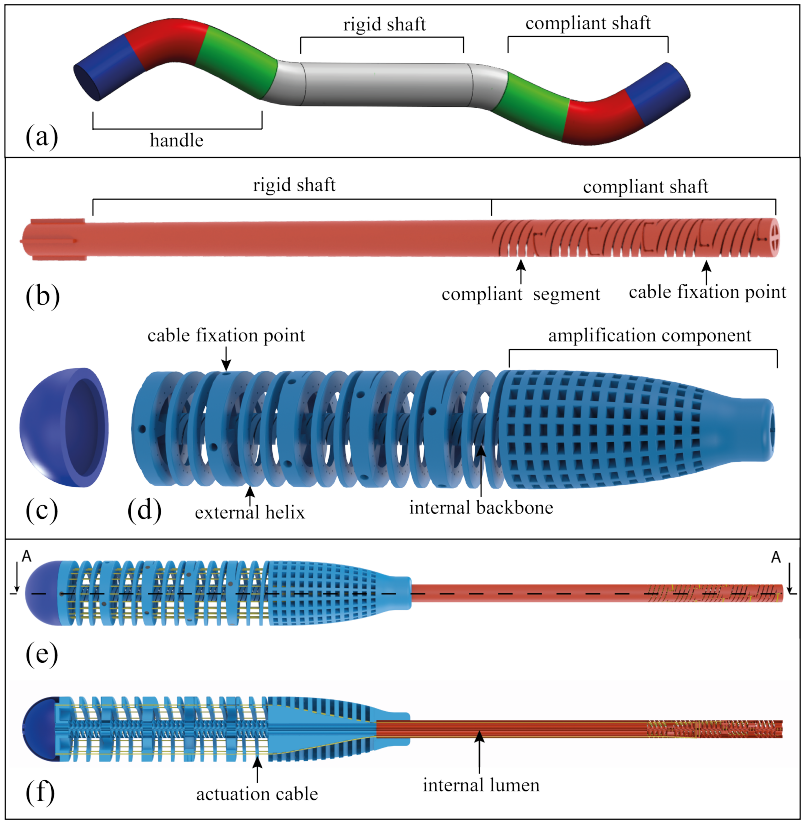

Figure 5.4: Phases in the development of the HelicoFlex. (a) Chosen serial control method in which each colored segment of the compliant handle controls the corresponding mirrored segment of the compliant shaft; (b) compliant shaft connected to rigid shaft in which a compliant segment and a cable fixation point are highlighted; (c) end cap in which the loose ends of the actuation cables are stored; (d) compliant handle in which the external helix, the internal backbone, a cable fixation point at the handle side and the amplification component, to gently increase the distance between the cables from Ø 6.5 mm in the shaft to Ø 22 mm in the handle, are highlighted; (e) assembly; and (f) cross-section, showing one of the internal lumens and two actuation cables.

instruments such as biopsy forceps, or thin, fiberoptic endoscopes to visualize the site of interest.

5.4. Fabrication

Considering the small size of some of HelicoFlex's features, we selected the AM technology taking into account the resolution achievable by the printer. A Perfactory® 4 Mini XL (EnvisionTec GmbH, Gladbeck, Germany), with a layer height in the vertical z-axis of 25 µm, was used to fabricate all three parts of the device. The used printer is based on Vat photopolymerization technology and uses the so-called Digital Light Processing (DLP) in which the combined work of a light source and a projector hardens the liquid resin layer by layer [35]. We printed our prototype using the R5 epoxy photopolymer resin (EnvisionTec GmbH, Gladbeck, Germany).

Both the handle and the shaft were printed vertically with the long axis parallel to the vertical z-axis of the printer. As DLP printing technology requires overhanging structures to be printed with support material, this would require a rather elaborate post-processing step in the removal of support material within the detailed helical structure. A number of studies carried out in the field of additive manufacturing for support structures show, however, that support structures are not always necessary providing that the length of overhanging layers is limited [36–40]. Following these studies, we decided to print the segments of the compliant shaft without support, using three general rules (Figure 5.5): reducing the overhang angle (α), limiting the length of bridges (B), and shortening overhanging structures (L).

The *overhang angle* is the angle between printed layers (i.e., the critical angle). Increasing the layer thickness while keeping the number of revolutions of the helicoid as well as the length of the segment equal, increases the overhang angle between

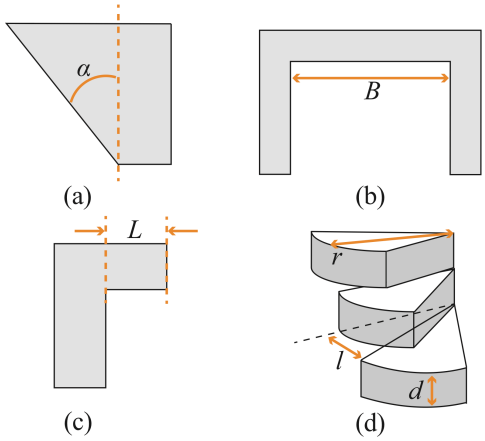

Figure 5.5: Rules to print without support: (a) reducing overhang angle α; (b) limiting the length of bridges B; (c) shortening overhanging structure L; (d) the rules applied in our helicoid: reducing the overhang angle by increasing the pitch or reducing radius r at a given layer thickness d will decrease the overhang l and improve the possibility of self-support.

two layers and thus the need for support. Therefore, by keeping the layer thickness small (25 µm) and the pitch of the helix equal to its height, the overhang angle is kept narrow, and the helicoids can support themselves. Bridges define the distance between two unconnected points; limiting the length of the bridges avoids the use of support material. The role of the amplification component is to guide the cables through curved grooves. However, using solid material in such a long element would clog the grooves. Therefore, the hive structure was used to create short grooves, while at the same time avoiding long bridges that would have been created if rings had been used as cable guidance during the vertical 3D printing process. Overhanging structures are shapes that stick out horizontally parallel to the building platform. In our design, combining helicoids with a central backbone allows the compliant shaft to be printed without extra support due to the constant presence of support (the backbone) in the structure [41].

Applying these rules, we printed the entire compliant shaft without any support in a single printing run. Printing without support led to a strong reduction in post-processing time with an additional advantage that eliminating support material from the printing process resulted in smooth surfaces without debris that could cause malfunctioning of the mechanism, especially in elements with a small size. Printing the handle and the shaft vertically allowed the grooves for the cables to remain open along the entire length of the shaft and the handle. The handle and the shaft were printed all together in 26 hours. After the printing, all the parts were placed in an ultrasonic cleaner for a few minutes.

Figure 5.6: The assembled HelicoFlex prototype showing a single curved shape.

In order to control the compliant shaft, each segment must be coupled with the corresponding segment in the handle using the corresponding actuation cables. Running all 20 cables (stainless-steel Ø 0.2 mm) through the shaft and the handle took around 5 hours. In the handle, the cables were fixated by dog point set screws to allow fine-tuning in this prototype. Although it was possible to tap directly into the 3D printed material, this could have created points of brittleness in the handle.

We, therefore, decided to place threaded inserts that allow the cable to be fine-tuned multiple times. During the assembly, the instrument was vertically placed and each cable was straightened by weights of 3 grams before fixation in the handle. The entire HelicoFlex prototype is shown in Figure 5.6.

5.5. HelicoFlex performance

5.5.1. Steering evaluation

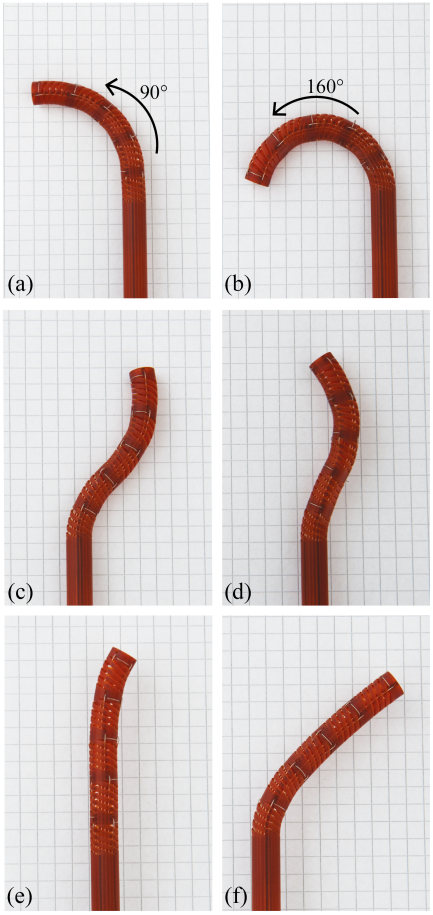

Figure 5.7: HelicoFlex compliant shaft bent in various shapes: (a) 90 degrees single curved shape; (b) 160 degrees single curved shape, reaching the maximum bending angle of the compliant shaft in performing a C-shape; (c) double curved with equal radii; (d) double curved with different radii; e) only the distal segment controlled; and (f) only the proximal segment controlled.

Simulating navigation through tortuous paths, the tip was moved along curves with different radii and shapes to evaluate the performance of the device, Figure 5.7. The prototype was able to perform single curved shapes with different angles (Figures

5.7a-b) and double curved shapes with different radii (Figures 5.7c-d). Moreover, the device allowed controlling each segment individually (Figures 5.7e-f). At an angle of 160 degrees, the maximum bending angle of the compliant shaft was reached because the outsides of the helicoids touched each other in the inner bend (see Figure 5.3).

Besides moving the device over different angles and shapes, we also evaluated the possibility of using the internal lumen. The device allows the insertion of a flexible fiberoptic endoscope into one of its four lumens while leaving the other three lumens free for the insertion of multiple surgical instruments, such as a biopsy forceps, as shown in Figure 5.8a. Moreover, a bendable rod can be placed inside one of the lumens of the handle and can be shaped to hold the desired position (Figure 5.8b). The fluid motion, as well as the easy maneuverability of the HelicoFlex prototype, can be seen in the video linked to the QR code at the end of this chapter.

Figure 5.8: Pictures of the HelicoFlex prototype. (a) Close-up of the compliant shaft of the HelicoFlex with a flexible biopsy forceps in one lumen and a flexible fiber optics endoscope in the second; (b) bendable metal rod inserted into one of the lumens to create a certain shape in the compliant shaft and keep it in position.

5.5.2. Payload test

For the instrument to be useful in a surgical setting, it must be able to withstand external loading. The bending stiffness of the HelicoFlex was therefore measured at the tip of the shaft. The shaft was tested in three different poses: straight, 90 degrees single curved, and in a double curved shape. To ensure that the poses were maintained during testing, 3D printed blocks were manufactured to properly constrain the handle in the required pose.

The setup consisted of a load cell (S-Beam LSB 200 FUTEK Advanced Sensor Technology Inc., CA, USA, controlled by a custom-made LabView script) mounted on a linear stage (Thorlabs PT1/M-Z8, with additional KDC101 controllers, controlled by Thorlabs Kinesis software). The linear stage drove the vertical displacement of the load cell with a low, constant speed of 0.5 mm/s, as to induce a defined displacement of the prototype shaft. The load cell measured the generated tip force as a result of the induced displacement and the elasticity of the shaft. To ensure a precise and consistent point contact with the tip, a steel ball (Ø 10 mm) was screwed on the load cell. The prototype was placed perpendicularly to the linear stage movement (Figure 5.9a).

For the single and the double curved shapes, the force was measured in two different directions: vertical (perpendicular to the plane of the curved shape) and axial (along the prototype main axis) for the single curved shape, and vertical and horizontal (in the plane of the curved shape) for the double curved shape (Figure 5.10). For the straight shape, the force was measured in the vertical direction. Different directions were achieved by simply rotating the prototype. Due to possible variations given by the 3D printing process and the post assembly, three prototypes were tested in each pose, and each measurement was repeated ten times. Data were acquired from the moment the load cell touched the shaft tip up to a displacement of 9 mm and analyzed using a Matlab R2020a script (Figure 5.9b).

Figure 5.10 shows the average peak force in the tested configurations for three

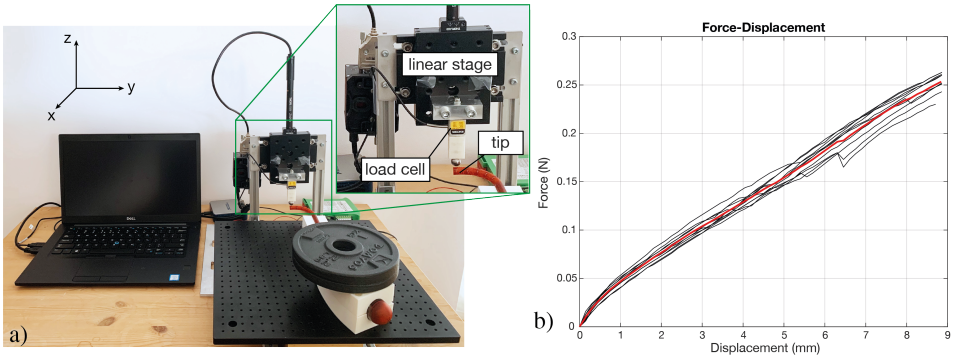

Figure 5.9: Setup of the payload test and an example of data acquired for the vertical direction. a) In the close-up different parts of the setup are highlighted. b) The experimental results for prototype 1 in single curved shape. The red line in the plot represents the averaged data.

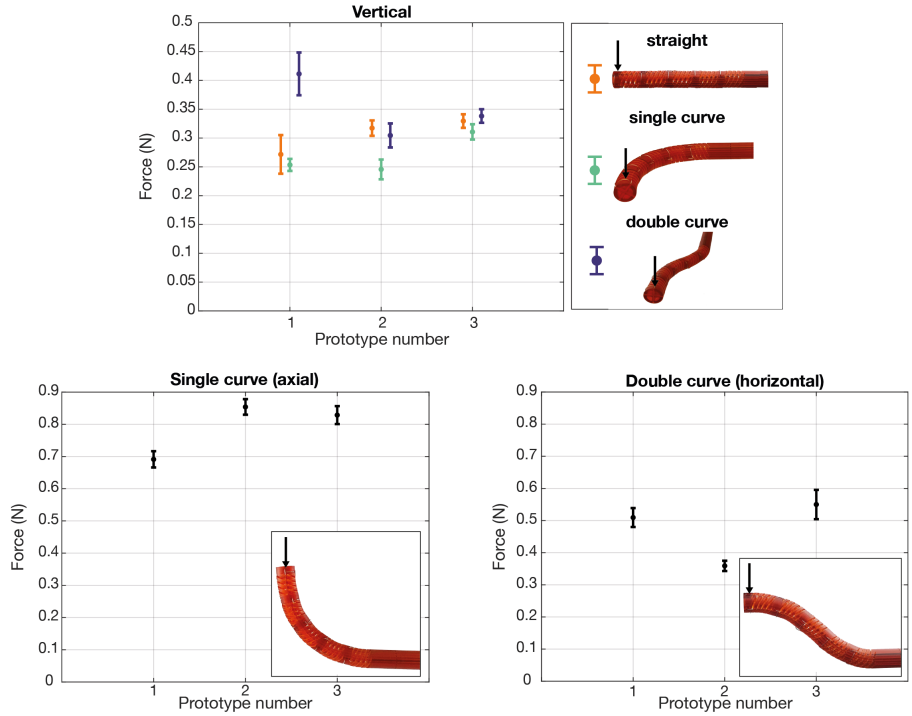

Figure 5.10: Plots of the average and the standard deviation of the peak-force for each different pose and prototype tested. The black arrows in the pictures indicate the direction of the displacement.

prototypes in each pose. The bending stiffness in the vertical direction for the straight shape was in the range of 0.030-0.035 N/mm. For the single curved shape, the bending stiffness in the vertical direction was in the range of 0.026-0.034 N/mm, while higher bending stiffness was measured in the axial direction (0.077-0.095 N/mm). For the double curved shape, the measured bending stiffness ranged between 0.033-0.045 N/mm and 0.039-0.061 N/mm vertical and horizontal direction, respectively.

5.5.3. Actuation force test

HelicoFlex was designed as a manually powered device. To evaluate the actuation force required from the user to bend the steerable shaft with and without load, a setup similar to the payload test was used. We analyzed the required force to bend the proximal segment of the handle. Due to its high flexibility, the handle bends under its own weight if not supported. Therefore, except for the proximal segment that was left free, the handle was supported with a 3D printed block and the amplification component was constrained to stabilize the prototype. A load cell was mounted on a linear stage. The linear stage allowed the vertical displacement of the load cell with a low, constant speed of 0.5 mm/s. The prototype was perpendicularly placed with respect to the linear stage, with the proximal segment of the handle underneath the

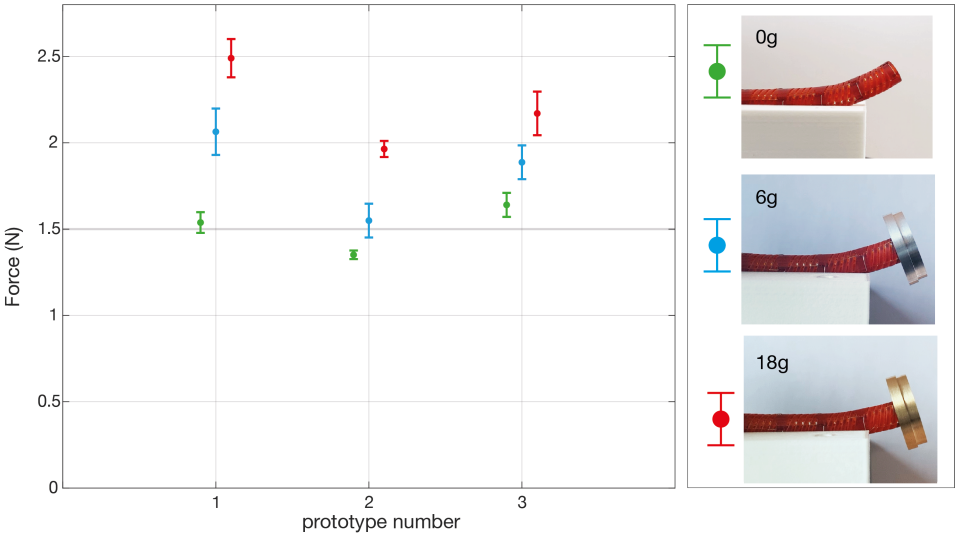

Figure 5.11: Peak force measured to bend the proximal segment of the handle with the tip loaded with 0 g, 6 g, and 18 g. The pictures on the right show the bending angle of the tip in the three conditions at the maximum proximal handle displacement (3 mm).

load cell. To ensure consistent contact with the proximal segment of the handle, a steel ball (Ø 10 mm) was screwed on the load cell. Data were acquired for a vertical displacement of 3 mm of the proximal segment of the handle. Three prototypes were each tested with three different loads applied at the tip of the steerable shaft: 0 g, 6 g, and 18 g. These loads were manufactured from aluminum (6 g) and brass (18 g) as to have the same volume, shape, and center of mass, but different weights. The measurements (three prototypes for three conditions) were repeated ten times for each condition (0 g, 6 g, 18 g). Data were analyzed using a MatlabR2020a script.

Figure 5.11 shows the average peak force at 3 mm of displacement for the three conditions for each prototype. The peak force was in the range of 1.35-1.65 N, 1.55-2.00 N, and 1.95-2.50 N respectively for 0 g, 6 g, and 18 g applied. As expected, the force that the user must apply to the handle increases with the load carried by the tip. Moreover, the bending angle of the tip of the steerable shaft decreases as the load carried on the shaft increases: from the straight position, we measured 32 degrees for 0 g, 22 degrees for 6 g, and 18 degrees for 18 g.

5.6. Discussion

In this work, we presented the world's first fully 3D printed handheld multi-steerable instrument with five individually controlled compliant segments providing a total of 10 DOF. One of the requirements expressed in Section 5.2.1 was the simplification of the assembly. In the conventional design of the EndoWrist, each part of the steerable

shaft is designed for a single function as a result of which the device contains a significant number of parts that all have to be individually handled during the assembly phase, which requires a large amount of time and work. In order to greatly simplify the assembly, we integrated all the functionalities in the combined single shape of the helicoids, the backbone, and the cable fixation points, giving to the segment high axial and torsion stiffness and low bending stiffness with easy and reliable fixation of cables. In HelicoFlex, we integrated all these functionalities in a five-segmented compliant shaft, with a complex and unusual shape, yet 3D printed in only one printing job. HelicoFlex shows a fluid motion and easy maneuverability during the performance of multiple shapes allowing added multi-functionality due to the presence of the four lumens. The maximum bending angle that can be obtained is 160 degrees, which is much larger than the bending angle guaranteed by commercialized instruments such as the LaparoFlex (DEAM, Amsterdam, The Netherlands) or the Autonomy Laparo-Angle (Cambridge Endoscopic Devices, Framingham, MA, USA), which usually ranges over ±60 degrees. The 8 mm diameter of the shaft was chosen equal to the diameter of most EndoWrist instruments and as a proof of concept in this paper. However, smaller diameters seem feasible without creating essential changes in the design.

The payload test showed that the bending stiffness of the steerable shaft is directly related to the direction of the external force. When the force was applied vertically, the bending stiffness ranged from 0.026 N/mm to 0.045 N/mm in the single curved and double curved shape, respectively. The bending stiffness increased when the force was applied on the plane of the curved shape, ranging between 0.039 and 0.061 N/mm (double curved shape). The maximum bending stiffness of almost 0.1 N/mm was measured when the external force was in the axial direction. To reach a bending stiffness suitable for surgical applications, it may be possible to increase the diameter of the internal backbone of the steerable shaft or the thickness of the helicoids. Also, it would be interesting to study how the material employed in the printing process affects the mechanical properties of the device. However, it is good to keep in mind that a balance has to be found between bending stiffness and more fatigue for the surgeon. The variance between the different prototypes is probably related to the 3D printing process and the minimal differences in manual straightening of the cables.

The general feeling while controlling the HelicoFlex is the easy maneuverability of the handle. Having a low bending stiffness reduces the forces required for actuation. We found that the actuation force increases linearly with the weight on the tip: increasing the load from 0 g to 6 g and from 0 g to 18 g required, respectively, 0.033-0.058 N and 0.033-0.047 N per added gram. Furthermore, the application of weight to the tip of the shaft influences the bending angle, which decreases with heavier loads. As currently designed, the prototype has a low bending stiffness not only in the steerable shaft but also in the handle, which bends under the weight of the shaft. Therefore, a higher bending stiffness would be desirable. Future research will focus on finding a good balance between the bending stiffness of the handle and the fatigue for the user.

The main goal of this work was to simplify the fabrication and assembly process of a multi-steerable device by using 3D printing technology to make it suited for disposable use. This led to a new type of continuous structure based on helicoids

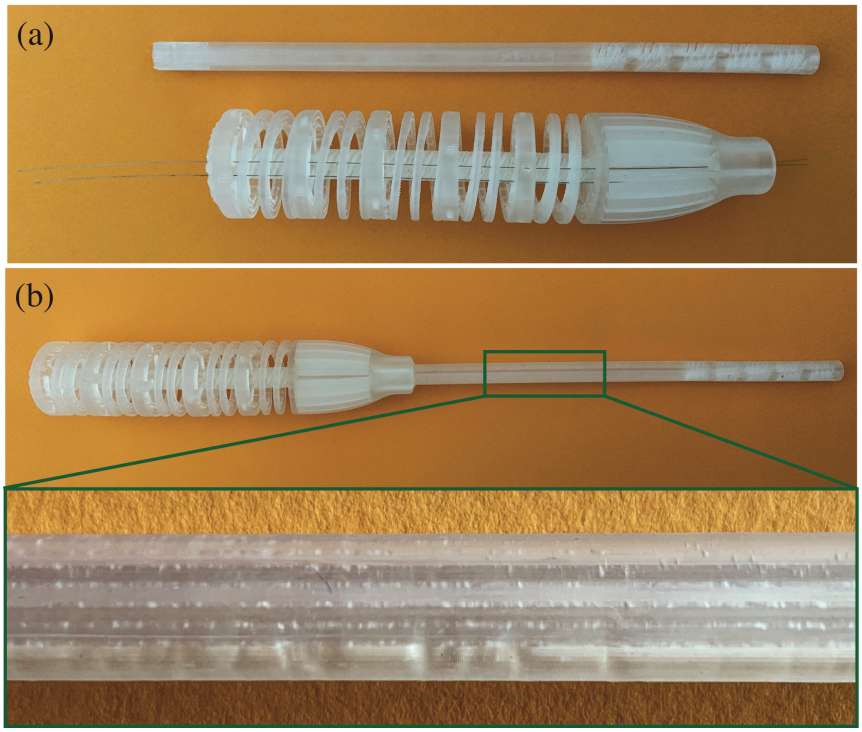

Figure 5.12: HelicoFlex printed with the E-Shell 600 biocompatible resin from (EnvisionTec GmbH, Gladbeck, Germany). (a) The shaft and the handle disassembled with two cables run through the handle. (b) The prototype assembled without cables with a close-up in which is visible how the grooves are clogged by liquid resin.

that could be printed without support. Moreover, we showed that it is possible to print an entire instrument out of one part, excluding the cables required for steering. In this prototype, we decided to use dog point set screws to fix the cables in the handle as this allows for easy fine-tuning of the prototype. Yet, we also experimented with cyanoacrylate glue that proved to be a fast and durable, much simpler alternative in the handle fixation (the cable fixation was tested tensioning the cable up to 1500 g for one hour with no sign of failure). The friction-based cable fixation in the compliant shaft required no other action than just looping the cables, which drastically decreased the assembly time. The entire device was printed in 26 hours, whereas threading and fixing the 20 cables took around 5 hours in this prototype. The handle and the shaft were printed with a layer thickness of 25 µm. Printing the same design with a layer thickness of 50 µm would drastically reduce the printing time to 13 hours, with only minor effects on the quality of the device. We found that the combination of helicoids with a continuum backbone limits the overhang angle between layers. In this way, we could avoid support material in the compliant shaft, which resulted in smoother surfaces without the presence of debris.

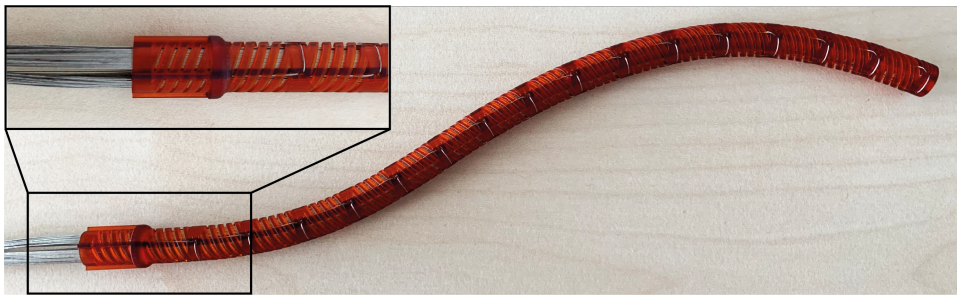

Figure 5.13: Example of 16 compliant segments combination with a close-up of the 64 actuation cables running through the Ø 8 mm shaft.

In our prototype, we used a non-biocompatible acrylic resin especially developed for prototyping. The use of this resin helped in the tuning phase to analyze and improve the design quality of the prototype. Biocompatible resins, such as E-Shell600, are provided by EnvisionTec as well. However, using this resin, results are decent but not yet sufficient due to the lower viscosity of this resin, which makes the cable grooves more difficult to be printed (Figure 5.12).

Using AM, the HelicoFlex can, in future surgical applications, be customized considering the surgery, the patients, and the surgeons' needs, as well as made MRI-compatible by replacing steel cables by Dyneema. In the future, more tests to investigate the maneuverability of this new multi-steerable instrument in narrow environments will be performed as well as different materials and sizes, increasing our knowledge in this emerging new field of 3D printed medical devices.

Using 3D printing is often considered a cheaper method of fabrication as compared to conventional manufacturing. However, it can be accounted as such only in specific cases (i.e., the production of complex devices that cannot easily be manufactured of molded conventionally) and if the necessary fine-tuning and testing time is taken into account (i.e., high initial costs for calibrating the settings of the printer, an expert who is able to tune and evaluate carefully how the design can be improved considering its use, long iteration phases to reach good results). Therefore, we believe that the real strength of AM is the capability of printing structures that are impossible to produce with conventional manufacturing and being able to integrate multiple functions into a single complex-shaped part. In a further elaboration, the number of segments can be increased, even more, reaching with the used cables and dimensions, a maximum length of 16 segments in a compliant shaft with 32 DOF (Figure 5.13). A multi-steerable structure this complex yet simple to assemble is a great step forward in the history of medical instrumentation.

5.7. Conclusion

In this work, we have presented the first 3D printed multi-steerable device. We have shown that by adapting the design of a device to the fabrication capabilities of additive manufacturing, we have integrated multiple functionalities of different conventional

elements into a single part, extensively decreasing the assembly time of a tendon-driven multi-steerable device for disposable medical use. The potential has been shown in a prototype: HelicoFlex. The handheld device, made out of three components, had five tendon-driven steerable segments for a total of 10 serially controlled DOF. HelicoFlex has shown a fluid motion and satisfactory results in performing different shapes. We have shown the high potential of additive manufacturing technology in building multi-steerable surgical instruments, limiting the number of components, and avoiding support material. HelicoFlex strives to contribute to the first generation of multi-steerable 3D printed instruments for MIS.

References

[1] R. Bittner, *The standard of laparoscopic cholecystectomy,* Langenbeck's archives of surgery **389**, 157 (2004).

[2] C. W. Akins, *Full sternotomy through a minimally invasive incision: a cardiac surgeon's true comfort zone,* The Annals of thoracic surgery **66**, 1429 (1998).

[3] M. J. Mack, *Minimally invasive and robotic surgery,* Jama **285**, 568 (2001).

[4] M. S. L. Liem, Y. Van Der Graaf, C. J. Van Steensel, R. U. Boelhouwer, G.-J. Clevers, W. S. Meijer, L. P. S. Stassen, J. P. Vente, W. F. Weidema, and A. J. P. Schrijvers, *Comparison of conventional anterior surgery and laparoscopic surgery for inguinal-hernia repair,* New England Journal of Medicine **336**, 1541 (1997).

[5] E. G. Sheu and D. W. Rattner, *Natural Orifice Transluminal Endoscopic Surgery (NOTES™) BT - The SAGES Manual Operating Through the Endoscope,* (Springer International Publishing, 2016) pp. 463–474.

[6] C. H. Snyderman, H. Pant, and R. Carrau, *Transnasal Endoscopic Skull Base and Brain Surgery* (2011) pp. 83–91.

[7] J. Burgner-Kahrs, D. C. Rucker, and H. Choset, *Continuum Robots for Medical Applications: A Survey,* IEEE Transactions on Robotics **31**, 1261 (2015).

[8] G. S. Guthart and J. K. Salisbury, *The Intuitive/sup TM/telesurgery system: overview and application,* in *Proceedings 2000 ICRA. Millennium Conference. IEEE International Conference on Robotics and Automation. Symposia Proceedings (Cat. No. 00CH37065)*, Vol. 1 (IEEE, 2000) pp. 618–621.

[9] P. Breedveld, H. G. Stassen, D. W. Meijer, and J. J. Jakimowicz, *Manipulation in laparoscopic surgery: overview of impeding effects and supporting aids,* Journal of laparoendoscopic & Advanced surgical Techniques **9**, 469 (1999).

[10] A. J. Madhani and J. K. Salisbury, *Wrist mechanism for surgical instrument for performing minimally invasive surgery with enhanced dexterity and sensitivity,* (1998).

[11] R. Prewitt, V. Bochkarev, C. L. McBride, S. Kinney, and D. Oleynikov, *The patterns and costs of the da vinci robotic surgery system in a large academic institution,* Journal of robotic surgery **2**, 17 (2008).

[12] I. D. Walker, *Continuous Backbone "Continuum" Robot Manipulators,* ISRN Robotics **2013**, 1 (2013).

[13] I. D. Walker, *Some issues in creating "invertebrate" robots,* in *Proceedings of the International Symposium on Adaptive Motion of Animals and Machines* (Citeseer, 2000).

[14] H. B. Gilbert, D. C. Rucker, and R. J. Webster III, *Concentric tube robots: The state of the art and future directions,* in *Robotics Research* (Springer, 2016) pp. 253–269.

[15] P. E. Dupont, J. Lock, B. Itkowitz, and E. Butler, *Design and control of concentric-tube robots,* IEEE Transactions on Robotics **26**, 209 (2010).

[16] T.-D. Nguyen and J. Burgner-Kahrs, *A tendon-driven continuum robot with extensible sections,* in *2015 IEEE/RSJ International Conference on Intelligent Robots and Systems (IROS)* (2015) pp. 2130–2135.

[17] H.-S. Yoon, J. H. Jeong, and B.-J. Yi, *Image-Guided Dual Master–Slave Robotic System for Maxillary Sinus Surgery,* IEEE Transactions on Robotics **34**, 1098 (2018).

[18] K. Ikuta, Y. Matsuda, D. Yajima, and Y. Ota, *Pressure pulse drive: A control method for the precise bending of hydraulic active catheters,* IEEE/ASME Transactions on Mechatronics **17**, 876 (2011).

[19] I. De Falco, C. Culmone, A. Menciassi, J. Dankelman, and J. J. van den Dobbelsteen, *A variable stiffness mechanism for steerable percutaneous instruments: integration in a needle,* Medical & biological engineering & computing **56**, 2185 (2018).

[20] A. Jiang, G. Xynogalas, P. Dasgupta, K. Althoefer, and T. Nanayakkara, *Design of a variable stiffness flexible manipulator with composite granular jamming and membrane coupling,* IEEE International Conference on Intelligent Robots and Systems , 2922 (2012).

[21] N. Simaan, R. Taylor, and P. Flint, *High Dexterity Snake-Like Robotic Slaves for Minimally Invasive Telesurgery of the Upper Airway BT - Medical Image Computing and Computer-Assisted Intervention – MICCAI 2004,* (Springer Berlin Heidelberg, Berlin, Heidelberg, 2004) pp. 17–24.

[22] J. Catherine, C. Rotinat-Libersa, and A. Micaelli, *Comparative review of endoscopic devices articulations technologies developed for minimally invasive medical procedures,* Applied Bionics and Biomechanics **8**, 151 (2011).

[23] P. W. J. Henselmans, S. Gottenbos, G. Smit, and P. Breedveld, *The Memo Slide: An explorative study into a novel mechanical follow-the-leader mechanism,* Proceedings of the Institution of Mechanical Engineers, Part H: Journal of Engineering in Medicine **231**, 1213 (2017).

[24] G. Gerboni, P. W. J. Henselmans, E. A. Arkenbout, W. R. van Furth, and P. Breedveld, *HelixFlex: bioinspired maneuverable instrument for skull base surgery,* Bioinspiration & biomimetics **10**, 66013 (2015).

[25] K. Riojas, P. Anderson, R. Lathrop, S. D. Herrell, C. Ruker, and R. J. Webster, *A Hand-Held Non-Robotic Surgical Tool with a Wrist and an Elbow,* IEEE Transactions on Biomedical Engineering (2019).

[26] C. Fan, D. Dodou, and P. Breedveld, *Review of manual control methods for handheld maneuverable instruments,* Minimally Invasive Therapy & Allied Technologies **22**, 127 (2013).

[27] P. L. Anderson, R. A. Lathrop, and R. J. Webster III, *Robot-like dexterity without computers and motors: a review of hand-held laparoscopic instruments with wrist-like tip articulation,* Expert review of medical devices **13**, 661 (2016).

[28] C. Culmone, G. Smit, and P. Breedveld, *Additive manufacturing of medical instruments: A state-of-the-art review,* Additive Manufacturing **27**, 461 (2019).

[29] J. Mintenbeck, M. Siegfarth, R. Estaña, and H. Wörn, *Flexible instrument for minimally invasive robotic surgery using rapid prototyping technology for fabrication,* IEEE/ASME International Conference on Advanced Intelligent Mechatronics, AIM , 1085 (2014).

[30] T. K. Morimoto and A. M. Okamura, *Design of 3-D Printed Concentric Tube Robots,* IEEE Trans. Robotics **32**, 1419 (2016).

[31] D. B. Roppenecker, A. Pfaff, J. A. Coy, and T. C. Lueth, *Multi Arm Snake - Like Robot Kinematics,* (2013) pp. 5040–5045.

[32] Y. S. Krieger, D. B. Roppenecker, I. Kuru, and T. C. Lueth, *Multi-Arm Snake-Like Robot,* IEEE Int. Conf. Robot. Autom. , 2490 (2017).

[33] A. Schneider and H. Feussner, *Chapter 7 - operative (surgical) laparoscopy,* in *Biomedical Engineering in Gastrointestinal Surgery*, edited by A. Schneider and H. Feussner (Academic Press, 2017) pp. 269–327.

[34] F. Jelínek, R. Pessers, and P. Breedveld, *DragonFlex Smart Steerable Laparoscopic Instrument,* Journal of Medical Devices **8**, 015001 (2014).

[35] J. Gardan, *Additive manufacturing technologies: state of the art and trends,* International Journal of Production Research **54**, 3118 (2016).

[36] J. Jiang, X. Xu, and J. Stringer, *Support structures for additive manufacturing: a review,* Journal of Manufacturing and Materials Processing **2**, 64 (2018).

[37] M. Fernandez-Vicente, M. Canyada, and A. Conejero, *Identifying limitations for design for manufacturing with desktop FFF 3D printers,* International Journal of Rapid Manufacturing **5**, 116 (2015).

[38] J. Kranz, D. Herzog, and C. Emmelmann, *Design guidelines for laser additive manufacturing of lightweight structures in TiAl6V4,* Journal of Laser Applications **27**, S14001 (2015).

[39] M. Cloots, A. Spierings, and K. Wegener, *Assessing new support minimizing strategies for the additive manufacturing technology SLM,* in *Solid Freeform Fabrication Symposium (SFF), Austin, TX, Aug* (2013) pp. 12–14.

[40] M. Langelaar, *Topology optimization of 3D self-supporting structures for additive manufacturing,* Additive Manufacturing **12**, 60 (2016).

[41] D. Chakravorty, *3D Printing Support Structures – All You Need To Know in 2019,* (2019).

Figure 5.14: Video of the motion of the HelixFlex

6

Steering Strategies of 3D Printed Steerable Instruments

Submitted as:
Culmone, C., van Starkenburg R., Smit G., and Breedveld, P. "Comparison of two cable configurations in 3D printed steerable instruments for Minimally Invasive Surgery".

Abstract

In laparoscopy, a small incision size reduces damage to healthy tissues but leads to consequent impairment of the surgeon's maneuverability. Such reduction introduces new challenges, such as the loss of wrist articulation or the impossibility of overcoming obstacles. A possible approach is using multi-steerable cable-driven instruments fully mechanical actuated, which allow great maneuverability while keeping the wound small. In this work, we compared the usability of the two most promising cable configurations in 3D printed multi-steerable instruments: a parallel configuration with all cables running straight from the steerable shaft to the handle; and a multi configuration with straight cables in combination with helical cables. Twelve participants were divided into two groups and asked to orient the instrument shaft and randomly hit six targets following the instructions in a laparoscopic simulator. Each participant carried out four trials (two trials for each instrument) with 12 runs per trial. The average task performance time showed a significant decrease over the first trial for both configurations. The decrease was 48% for the parallel and 41% for the multi configuration. Improvement of task performance times reached a plateau in the second trial with both instruments. The participants filled out a TLX questionnaire after each trial. The questionnaire showed a lower burden score for the parallel compared to multi configuration (23% VS 30%). Even though the task performance time for both configurations was comparable, a final questionnaire showed that 10 out of 12 participants preferred the parallel configuration due to a more intuitive hand movement and the possibility of individually orienting the distal end of the steerable shaft.

6.1. Introduction

Laparoscopic surgery is a minimally invasive procedure in which several small incisions allow access to the human body by means of long and straight surgical tools. The reduction of the incision size reduces the post-operative pain and the recovery time for the patient, minimizes the scar tissue, thus obtaining better cosmetic results, and improves the cost-effectiveness of the procedure. Despite its great advantages, laparoscopy introduces new hurdles, e.g., due to the loss of wrist articulation and the introduction of a fulcrum effect [1, 2].Due to the pivoting point in the abdominal wall, the movement of the end-effector is inverted with respect to the handle. This so-called fulcrum effect results in a steeper learning curve. With the advent of new domains of minimally invasive surgery, such as single-port laparoscopy, transluminal, and intraluminal procedures, new challenges arise. For instance, accessing the target area becomes demanding when its optimal approach direction is not aligned with the rigid instrument shaft inserted through the incision [3].

Many robotic platforms have been proposed to overcome the limits in laparoscopy. One of the most famous platforms is the Da Vinci® robotic system offered by Intuitive Surgical Inc. (Intuitive Surgical Inc., Sunnyvale, Ca, USA) [4]. Robotic platforms give the surgeon additional degrees of freedom (DOF), three-dimensional visualization of the surgical site, and eliminate the fulcrum effect. However, they require a large footprint and high maintenance cost that makes the price-benefit ratio unfavorable for many procedures [5].

An alternative approach is the use of handheld mechanical solutions, in which the surgeon's dexterity is enhanced by a steering mechanism with an additional two DOF close to the end-effector. Many research prototypes and commercialized instruments have been designed, and different solutions have been proposed to control the steerability of the end-effector [6, 7]. The two most used control strategies in handheld instruments are *wrist control*, in which the movement of the wrist is used to steer the end-effector, such as found in the Laparo-Angle [8] or the LaparoFlex [9], and *thumb control*, in which the thumb controls the steering by means of a joystick [10], a trackball [11], or a steering wheel [12, 13]. Comparative studies have been carried out on these two different control strategies to identify the most beneficial handheld control for the surgeon [14–16]. However, despite the 2-DOF steerable end-effector, the shaft rigidity of these instruments still restricts the surgeon's workspace, limiting surgical use to procedures in which no obstacles need to be passed without being touched. To further improve maneuverability, mechanical solutions such as cable-driven mechanisms [17–19], or concentric continuum tubes [20] have been proposed to design a multi-steerable shaft enabling the surgeon to move along complex double-curved paths. In cable-driven solutions, the *cable control strategy* plays an important role [21]. Cables can vary from a minimum of three for steering in two planes [22] to four or more as in the so-called cable-ring configuration [23], Figure 6.1a. In our group, we have explored two different cable control strategies for controlling cable-driven multi-steerable instruments: a control strategy based on cables straightly guided from the steerable shaft to the control handle (*parallel configuration*) [24], and a control strategy based on the combination of straight

and helically cables placed around the backbone of the shaft and the control handle (*multi-actuation configuration*) [18], Figure 6.1b-c.

Whereas control strategy comparisons have been performed for 2-DOF instruments with only one steerable segment, a comparison in the steering and control of multi-steerable instruments with two or more segments has not yet been carried out. As a result, there is a lack of information about which way of controlling multi-steerable instruments is more convenient to the surgeon. In this study, we developed 3D printed multi-steerable instruments using parallel and multi configurations. Using these instruments, we carried out an experiment with 12 participants to compare the two control strategies and identify which one has a steeper learning curve, faster task performance time, requires a lighter workload, and is preferred by the participants.

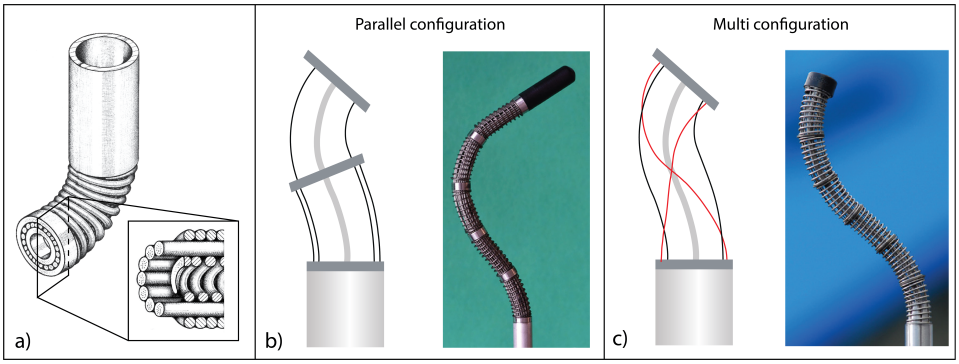

Figure 6.1: Multi-steerable strategies to control surgical instruments. a) Cable-ring mechanism with its cross-section. Cables are placed concentrically to actuate the segments and guide each other along the shaft, adapted from [23]. b) Parallel configuration of a multi-steerable instrument, adapted from [25]. c) Multi configuration of a multi-steerable instrument, adapted from [18].

6.2. Cable configuration strategies

Cable-driven steerable instruments are controlled by actuation forces applied to their steering cables. In multi-steerable instruments, various deformation modes can be generated with different cable configurations, determining the behavior of the steerable shaft. In a 2D representation of one segment, we can define a generic steerable segment as an incompressible compliant backbone, with a length L, in which a rigid end plate of 2R in length is attached at the distal end, Figure 6.2. The proximal end of the backbone is fixed and represents the connection with the shaft. Actuation cables are attached at the outer ends of the end plate. In the case of a 2D symmetrical cable configuration, each segment can have two parallel cables (the parallel configuration), two diagonal cables, or the combination of diagonal and parallel cables (the multi configuration).

6.2.1. Parallel configuration

In the parallel configuration, cables are placed parallel to the backbone, and the pulling force F_p is parallel to the longitudinal axis of the segment, Figure 6.2a. Therefore, the bending moment is constant along the segment length L because the perpendicular distance R between the force application point and the backbone stays constant along the segment length L. The bending moment, therefore, defines the orientation angle of the segment, and the deflection mode will result in a curve with a constant bending radius. Segments with a parallel configuration can be combined by placing them on top of one another so that the base of the first segment acts as the top of the second segment and so on. The combination of the segment angles defines the position and the orientation of the end-effector, i.e., the end plate of the most distal segment, allowing different deformation modes.

6.2.2. Multi-actuation configuration

In the diagonal configuration (Figure 6.2b), cables connect the end plate to the fixed base by crossing each other. Forces Fd are applied along the cable direction and can be split into the F_x and F_y components. When the cables cross each other at L/2, the segment will have a symmetric bending moment and, therefore, symmetric behavior, enabling a double-curved shape deformation mode as shown in Figure 6.2b. In this case, the end plate translates laterally in the direction of the F_x force while the orientation of the end plate remains unchanged. Full control with only one segment can be obtained by combining parallel and diagonal cables, Figure 6.2c. This combination, which will be referred to as the multi configuration [18], results in a mechanical behavior similar to the parallel configuration but with only one segment instead of multiple segments.

6.2.3. Three-dimensional representation

Navigation through confined anatomy requires instruments able to move in a 3D space. For instruments based on the *parallel configuration*, 3D motion can be achieved by using a minimum of three actuation cables per steerable segment. However, the use of four cables per segment concentrically placed at a 90 degrees angle allows antagonist movement of the cables and simplifies control [24]. The steerable segments are placed in series, one after the other, to increase the DOF of the shaft. The combination of a number of segments allows the control of the orientation as well as the position of the end-effector. In an instrument with multiple steerable segments, the actuation cables that control the end-effector run through dedicated slots of the preceding segments, the cables of the first preceding segment through the preceding ones, and so for all segments, Figure 6.3a. To avoid overlap of the actuation cables, each steerable segment of the shaft is rotated slightly, as shown in the close-up of Figure 6.4a.

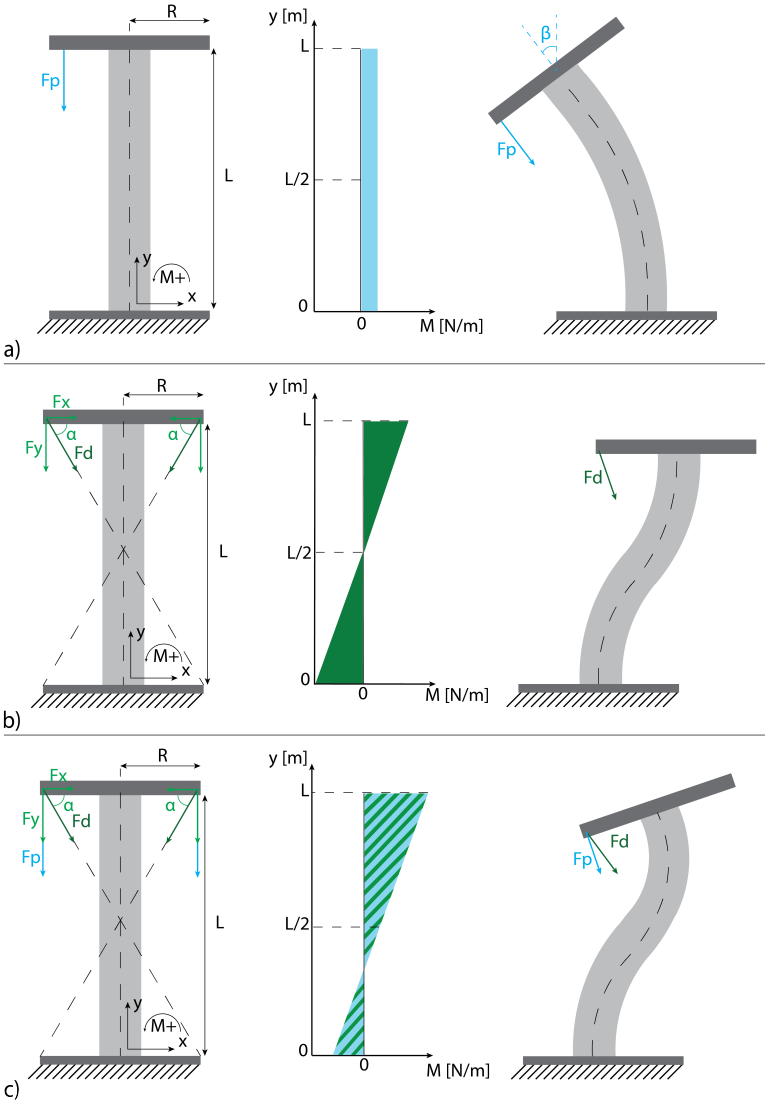

Figure 6.2: The three cable configurations presented in this work. Left: 2D representation of the segment, center: corresponding bending moment diagram, right: segment deforming under the applied pulling force. a) Parallel configuration, b) diagonal configuration, c) multi configuration. For the explanation of the used symbols, see the text.

For instruments based on the *multi configuration*, 3D motion can be achieved by placing the parallel cables concentrically at a 90 degrees angle, similar to the parallel configuration but diagonal cables need a reconfiguration, Figure 6.3b. In fact, the diagonal cables will cross the backbone if positioned like in the 2D representation, and they will not allow any internal lumen to be included in the instrument. A

possible solution, which was successfully investigated by Gerboni *et al.* [18], is to use helically-oriented cables that rotate 180 degrees around the central backbone [26]. Rotation of the helical cables can be either in the clockwise or in the counterclockwise direction. Using only one of the two directions would lead to an undesired torque along the segment backbone. Combining clockwise and counterclockwise helical cables in pairs cancels out this effect. In the parallel configuration, the parallel cables of different segments can be placed at the same distance from the backbone due to the straight nature of the cable slots. In the multi configuration, the helical cables would cross each other, causing overlapping of the cable slots. In order to avoid this arrangement, the three sets of cables (clockwise, counterclockwise, and parallel) are placed concentrically at three different radii, Figure 6.4b. Differently from the parallel configuration in which we need multiple segments to determine the position of the end-effector, in the multi configuration, we can consider the steerable shaft as one long steerable segment due to the possibility of controlling both the position and orientation of the end effector with four actuation cables of each type (clockwise, counterclockwise, and parallel).

6.3. Instrument prototypes

6.3.1. Design

Two prototypes were designed with an identical outer appearance and size: one based on the parallel configuration and one on the multi configuration. Both prototypes contain three components: a compliant handle, a rigid shaft, and a compliant shaft. A detailed description of the compliant shaft and the design in the parallel configuration is described by Culmone *et al.* [24]. Both designs are based on a cable-driven actuation with a serial control strategy, in which the movements of the compliant handle and the one of the shaft are mirrored [21]. The compliant shaft is based on a modular compliant segment, composed of a central flexible backbone and four helicoids that run concentrically around the centerline, Figure 6.5. The helicoids have a T-shaped cross-section that is thin close to the backbone to ensure low bending stiffness and enlarges towards the outer side of the segment to limit the bending angle and prevent failure for excessive bending, Figure 6.5b. Segments with helicoids inversely placed around the backbone (clockwise and counterclockwise helicoids) are alternately placed on top of one another to form the compliant shaft and ensure equally divided torsion stiffness around the backbone. The actuation cables run through holes in the helicoids and are looped into a cross-shaped groove at the top of the steering segment to fix and control them independently, Figures 6.5c-d.

The rigid shaft is connected directly to the compliant shaft. The rigid shaft contains dedicated slots to guide the actuation cables from the compliant shaft to the handle. The compliant handle is based on using wrist control, in which all fingers and the wrist are used to manipulate the handle to define the desired shape of the compliant shaft. The design of the compliant handle is similar to a large version of the compliant shaft. For each compliant segment of the shaft, there is a respective segment for the handle. Similar to the compliant shaft, each segment of the handle has an inner backbone surrounded by an outer helicoid structure. The helicoid struc-

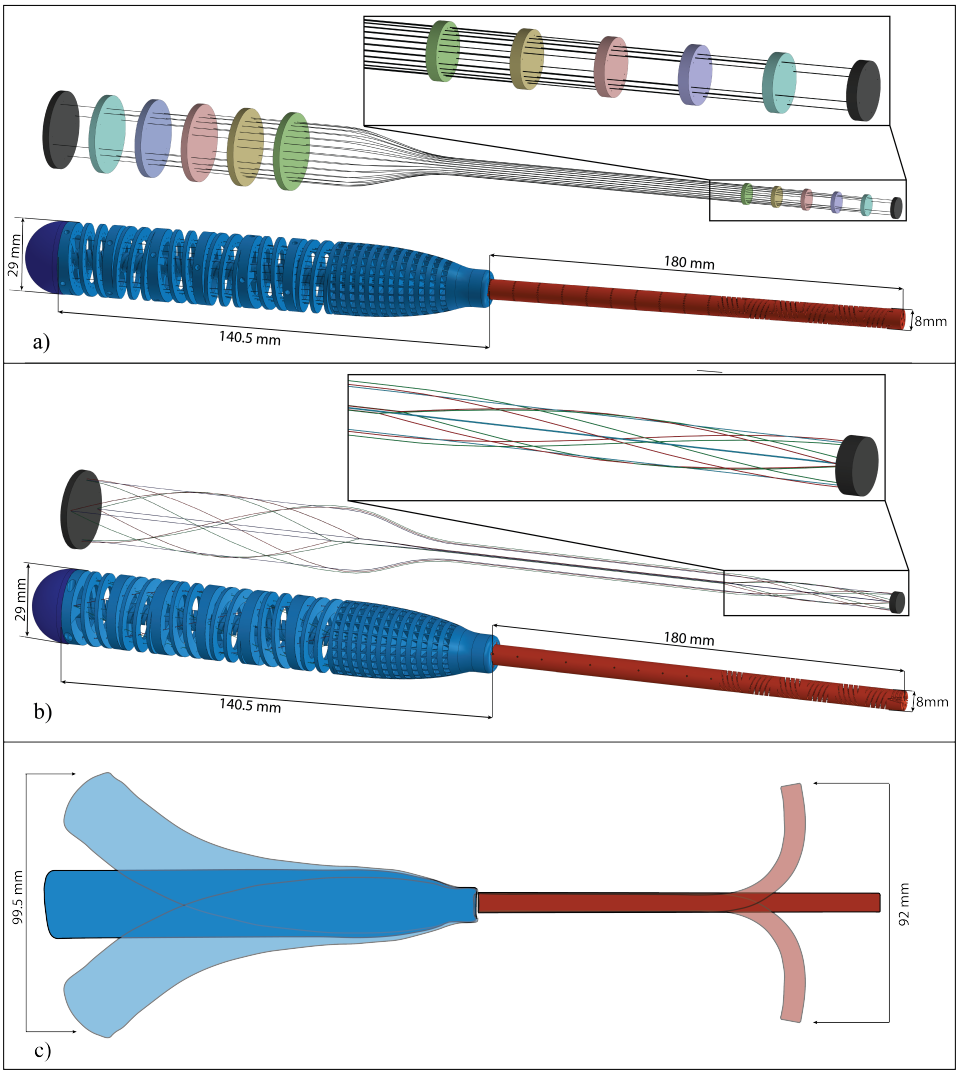

Figure 6.3: Parallel and multi configurations. a) The parallel cable configuration with a close-up on the shaft and the final design of the device. Each color corresponds to a segment mirrored on the control side. b) Multi configuration of the cables and the final design of the device. In this configuration, all cables are connected at the ends. The close-up shows the cable configuration in the steerable shaft. c) Theoretical workspace of both devices at 90 degrees.

ture has the function of guiding the cables as well as creating a cable fixation point. The connection between the rigid shaft and the handle is smoothened by an amplification component that, with an amplification factor of three, guides the cables from the shaft to the handle, amplifying the movement between the handle and the shaft.

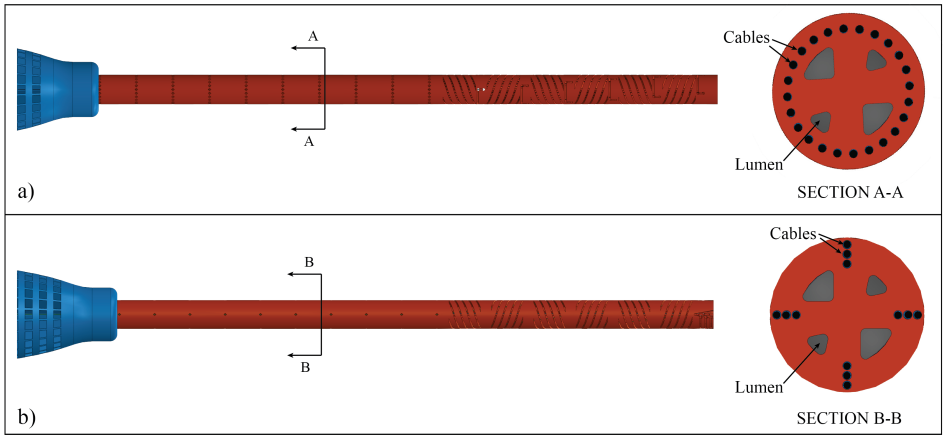

Figure 6.4: Cross-section of the shaft for the parallel and the multi configurations. a) In the parallel configuration all cables are equally distant from the central backbone Segments S are numbered from 1 to 6. In the multi configuration, cables are concentrically placed at three different radii to avoid overlapping. S represents the steerable shaft.

Moreover, both designs have four lumens to insert flexible thin tools for diagnostic or treatment.

In the two prototypes, the steerable shaft shares the same design based on six steerable segments. However, in the parallel configuration, actuation cables control every single segment independently, and the cable fixation point needs to be located directly on the segment itself, in both the compliant shaft and the handle. In the multi configuration, the six segments are considered as one element. All actuation cables run through the entire body of the instrument and are fixed at its two ends: at the distal end, the end-effector, and at the proximal end, the end of the handle. Therefore, while in the parallel configuration, the position and orientation of the end-effector are controlled indirectly by controlling the orientation of the individual segments, in the multi configuration, the position and orientation of the end-effector are directly controlled as if there is only one segment. Moreover, different from the parallel configuration where cables run through straight guiding slots, in the multi configuration, the guiding slots for the cables are both on straight and helical tracks. The parallel configuration uses a serial control strategy based on mirrored movements. The segments of the shaft are mirrored in the handle, Figure 6.3a, resulting in the shaft moving opposite to the handle, i.e., the end of the handle moving upwards resulting in the end-effector moving downwards. Also, the multi configuration is controlled by mirrored movements: when a cable is pulled by bending the handle, it will shorten in its distal end, mirroring the handle movement.

6.3.2. Fabrication

Both instrument prototypes were fabricated using Vat photopolymerization as additive manufacturing technology, Figure 6.6. All parts were printed using Perfactory® Mini

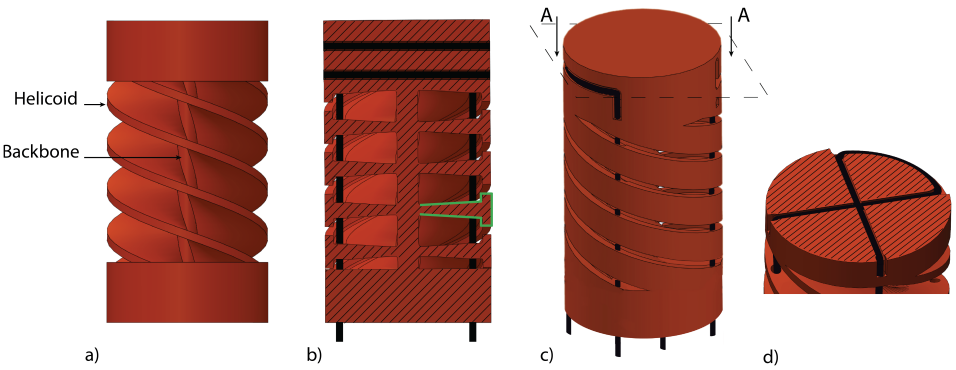

Figure 6.5: 5 Steerable segment with parallel cables. a) Four helicoids concentrically placed around the central backbone. b) Cross-Section of the steerable segments with the T-shape of the helicoids highlighted in green and cables in black. c) 3D model of the steerable segment with d) cross-section A-A showing the looped cables in the fixation point. Adapted from [24].

XL (EnvisionTEC GmbH, Gladbeck, Germany), with 25 µm layer height in the vertical z-axis. The printer, based on the so-called Digital Light Processing (DLP), uses a light source and a projector to harden the liquid resin layer by layer. We used R5 (EnvisionTEC GmbH, Gladbeck, Germany), an epoxy photopolymer resin, which is specifically customized for prototyping. The handle and the shaft were printed in the vertical position, with the main axis parallel to the z-axis of the printer. A total of 24 Ø 0.2 mm stainless-steel cables in the parallel configuration and 12 Ø 0.2 mm stainless-steel cables in the multi configuration, were used to actuate the instruments. After placing them in the 3D printed construction, the cables were straightened using weights of 3 grams and then fixed in the handle by means of dog point set screws. At the end of the assembly, a small steel plate was glued at the end-effectors for use in the experiments.

6.4. Functionality test

6.4.1. Background and goal

A comparative evaluation was carried out to study the maneuverability of the instruments and investigate which cable configuration enables a faster and easier control strategy. We hypothesized that:

- The parallel configuration requires less workload. The straight arrangement of the cables within the instrument generates less friction due to the lower normal forces between the actuation cables and the 3D helical printed structure as compared to the multi configuration.
- The multi configuration would be faster in hitting the target, considering that all cables control the entire steerable shaft at once, whereas, in the parallel configuration, each steerable segment of the handle individually controls the corresponding steerable segment of the shaft.

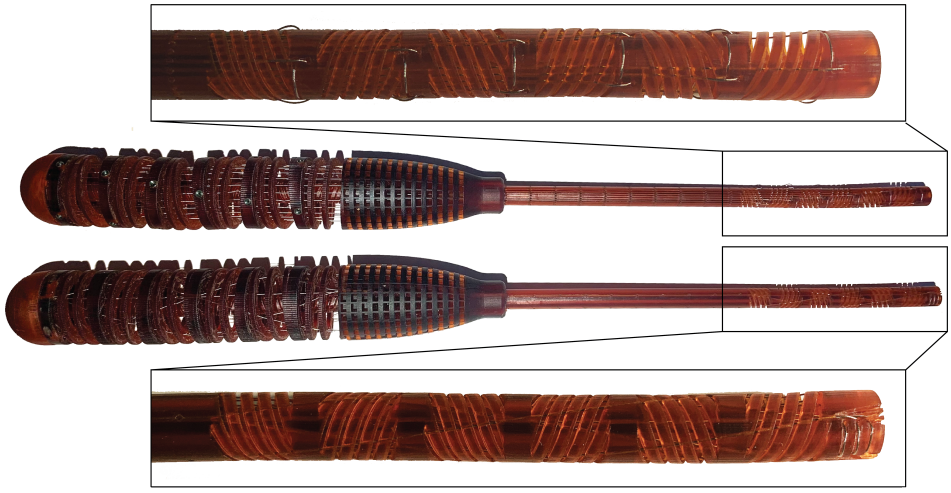

Figure 6.6: Instrument prototypes employing the parallel configuration (top) and multi configuration (bottom). The close-ups show the steerable shafts. Notice that the fixation points in the shafts differ, depending on the configuration. In the parallel configuration, each segment has two fixation points whereas in the multi configuration all cables are fixed at the distal end of the shaft.

The two instruments were tested in a laparoscopic simulator where targets with different orientations and positions were placed. The participants had to hit the indicated targets as fast as possible. The task was repeated 12 times (runs) per trial. Each participant attended four trials, two for each instrument. For each run, we measured the time to complete the task properly. We analyzed and compared the task performance time between the two instruments. Moreover, we examined the learning curve for each instrument and whether the order of use influences the learning curve. Finally, we analyzed the experienced workload and the individual preference of the participants using questionnaires.

6.4.2. Participants

A total of 12 participants (5 men and 7 women, aged 27.4±1.9) were recruited to take part in the experiment. All participants had no prior experience in laparoscopic or open surgery procedures, nor with laparoscopic instruments. The participants were split randomly into two groups, Group A and Group B, of 6 participants each. Each group had a different order of instrument use. Group A started with the instrument with the parallel configuration (PC), whereas Group B started with the instrument with multi configuration (MC). All participants were informed about the purpose, the type of the experiment, and the use of the collected data. The study was approved by the Human Research Ethics Committee at Delft University of Technology (ID:1408).

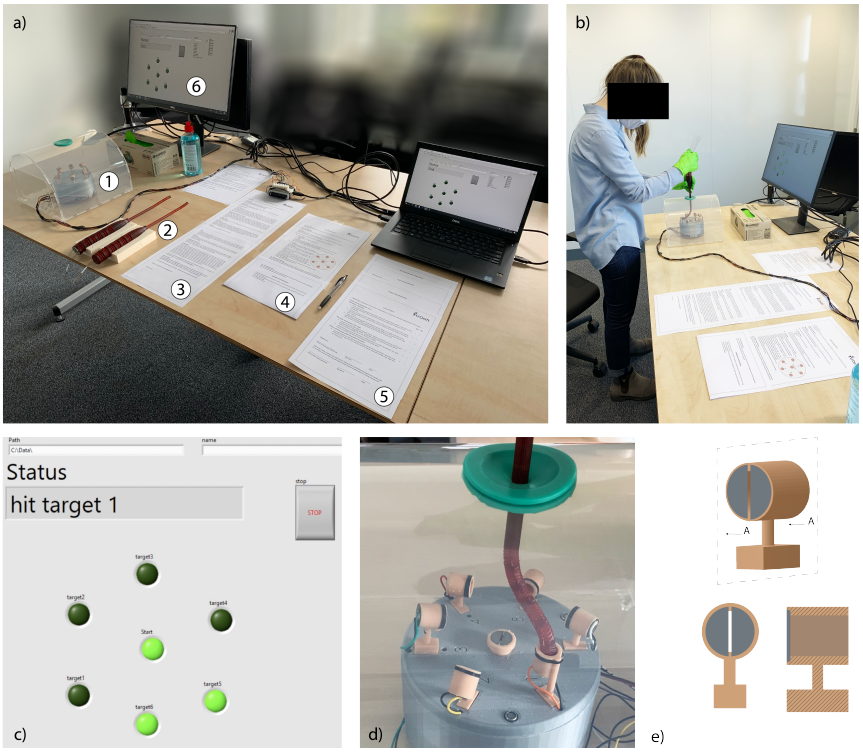

Figure 6.7: Experimental setup. a) Setup and its components: 1. simulator, 2. instruments, 3. participant information letter, 4. general instruction, 5. informed consent and questionnaires, 6. user interface. b) A participant during the test. c) The user's interface during the experiment. Each green circle represents a target. The light green circles are the targets already hit, and the dark green circles are the targets still to be hit. The status bar displays the next target that the participant has to hit. d) The instrument into one of the targets. d) A participant during the test. e) CAD model of the target with back view and cross-section. The two steel plates are represented in grey.

6.4.3. Experimental setup

The experiment was carried out using a laparoscopic simulator, specifically designed for this study. The simulator was made of clear PolyMethylMethAcrylate (PMMA) and PolyPropylene (PP) to replicate an inflated abdomen. We decided to have a transparent simulator to provide participants with direct 3D visualization. Due to their inexperience in laparoscopic surgery, using an endoscope and a monitor could have resulted in additional difficulties related to the loss of depth rather than the instrument maneuverability. A silicon valve placed in the center of the simulator allowed the insertion of the instruments. A 3D printed cylindrical stand with seven targets in different orientations was placed inside the simulator. Six target tubes (20 mm long, Ø 9 mm) were numbered and evenly placed around the stand, while a start flat target was placed center of the stand. The entrance point of the target tubes was marked with a black line. Each target tube contained two steel plates at

its bottom, Figure 6.7e. When the end-effector was parallel oriented to the plates and therefore hit them simultaneously, electric contact was made, and a signal was measured by a Multifunction I/O device (USB-6008, National Instruments, Austin, USA) [27] that was controlled with a laptop via a LabView 2016 program (National Instruments, Austin, USA). A monitor showed the next target to be hit. The setup and the monitor were positioned in front of the participant, and their height could be adjusted to reach a comfortable position, Figure 6.7.

6.4.4. Task and procedure

The task consisted of positioning and orienting the multi-steerable shaft to reach the six targets. The experiment started when the participant hit the start target. Subsequently, the participant was asked to move the shaft towards the indicated target (randomly chosen among the six) and insert the tip into the tube. A low-frequency buzzer indicated that the participant hit the two steel plates of a wrong target, whereas a high-frequency buzzer indicated that the correct target was hit and the participant could move the shaft towards the new target. The time was recorded and was measured from the moment the participant hit the start target until the last target was hit. In each run, the participant hit the start target and the six other targets in a randomized order. Each trial consisted of 12 randomized runs. Each participant performed four trials: two trials for each of the two cable configuration instruments, in total resulting in 48 runs (12 runs x 2 trials x 2 cable configurations) per participant. Prior to the start, a short demonstration and an instruction sheet were given to the participant. The participant filled up an intake questionnaire with general information such as gender, age, educational phase, dominant hand, and video game or musical instruments experience. Before each of the four trials, the participants had two minutes to practice and familiarize themselves with the instrument. For participants of Group A, the experiment sequence was PC instrument followed by MC instrument, and again PC and MC. For Group B, the experiment sequence was MC-PC-MC-PC.

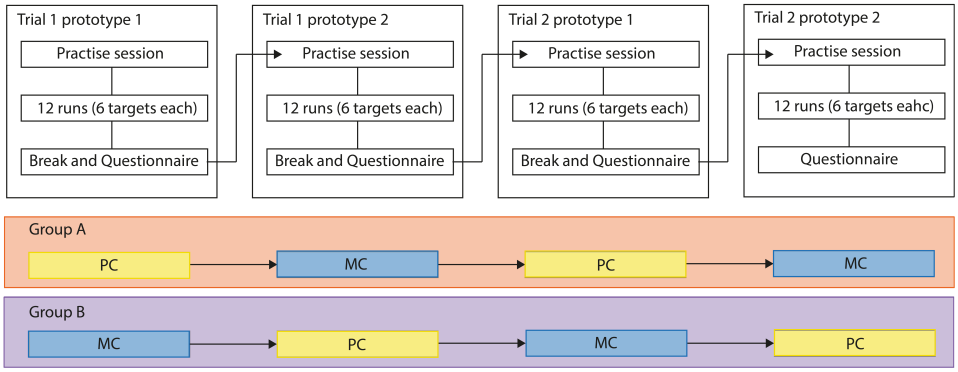

Figure 6.8: Flow chart of the experiment for each participant. Each trial consists of 12 runs and the order of the instruments used for the two groups. Parallel configuration (PC), multi configuration (MC).

Figure 6.8 shows the flow chart of the experiment and the two instruments order for the two groups.

At the end of each trial, the participant had a break of around 10 minutes to fill a self-evaluation questionnaire based on NASA's Task Load Index (TLX) [28]. The six subscales (mental demand, physical demand, temporal demand, performance, effort, and frustration) of NASA TLX were rated from -10 to 10, in which a high score indicated that the task was highly demanding and a low score that was easy to perform. At the end of the fourth trial, the participant filled out a final questionnaire to express a preference between the two instruments, considering the ease of steering and control. Data were analyzed using Matlab R2020a scripts. The QR code at the end of this chapter links to the video of the execution of one run for each instrument.

6.5. Results

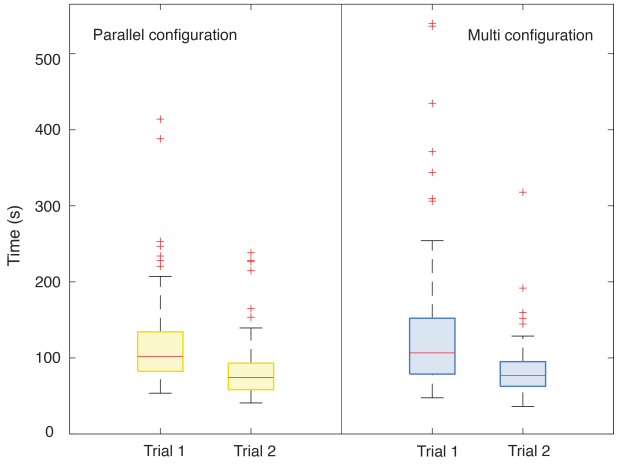

Figure 6.9: Box and whisker plots of the task performance time for the two cable configurations. Yellow represents the parallel configuration (PC), and blue the multi configuration (MC). For each instrument, the participants performed two trials. The red line in the box represents the median and the red crosses, the outliers.

Figure 6.9 shows the task performance time per instrument in the two trials. Yellow represents the PC, and blue the MC. The plot depicts the results as box and whiskers, where the bottom edge of the box indicates the 25th percentile, the top edge the 75th percentile, and the red central line the median. The median time for trial one was 102.05 s for the PC and 106.60 s for the MC. In Trial 2, the median time was 74.15 s and 76.75 s for both configurations, respectively. The median decreased for both instruments between the first and the second trial. Due to the asymmetry of the data calculated with the Shapiro-Wilk test ($p<0.001$), we performed the Mann-Whitney U test for independent groups of non-parametric data. The test revealed no significant difference ($Z= -0.72$, $p= 0.44>0.05$) on the task performance time of the two devices in each trial. Moreover, we compared the two trials of the same cable

configurations. In both cases, the Wilcoxon Signed-Rank test for two dependent groups of non-parametric data showed a significant difference between the two trials ($Z= 8.32$, $p<0.05$), and therefore a significant reduction in time between the first and the second trial for both configurations as the participants got more experienced with the instruments after some training.

Looking at the trend of the runs within the trials, Figure 6.10 shows the learning curve of the participants per each instrument within the 12 performed runs of each of the four trials. The average time shows a reduction of 48% for the parallel and 41% for the MC between the first and the last run of the first trial. Data stabilized in the second trial for both instruments with an average time reduction of 24% for the parallel and 14% for the MC. The time performance for the PC and the MC in the last run of the second trial shows similar results: 76.42±19.87 s for the PC and 74.99±21.99 s for the MC. The minimum task performance time average was 49.92±8.92 s and was achieved by 9 out of 12 participants in the last performed trial, Trial 2 with the MC for Group A, and Trial 2 with the PC for group B. Two participants of Group B achieved the minimum task performance using the MC; one participant in Trial 1 and one in Trial 2. In Group A, one participant achieved the minimum task performance time in Trial 2 with the PC.

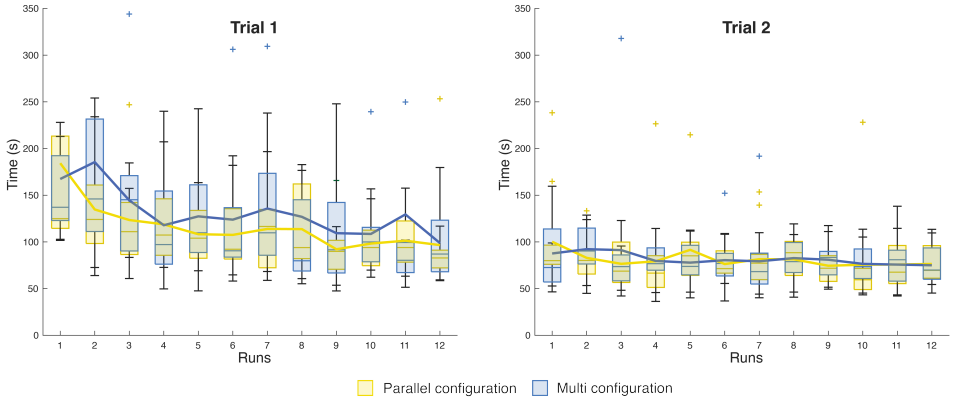

Figure 6.10: Box and whisker plots of the average time per run in the two trials performed by each participant for each instrument. Yellow represents the parallel configuration (PC), and blue the multi configuration (MC). Each box and whisker plot represents the median, the upper and the bottom quartile of the average time for 12 participants. The outliers above 350 s have been cut off in the figure. The full picture can be found in the supplementary material.

The maximum task performance time, with an average of 272.15±124.85 s, was achieved in the first performed trial for 11 out of 12 participants, independently from the instrument. Only one participant of Group A achieved the maximum task performance time in Trial 1 with the MC.

Moreover, we looked at the influence of one instrument over the other, considering their order. Figure 6.11 shows the box and whisker plots of the task performance time for the 12 participants in the four trials for each run. We compared the task performance time of the first run of the two groups, A and B, in Trials 1 and 2 for the

PC and MC, Figure 6.11. We performed the Mann-Whitney U test for independent groups of non-parametric data. The test revealed a significant difference ($Z=2.85$, $p<0.05$) between Group A and Group B in Trial 1 for the PC. Group A (which started with the PC) required more time with an average time of 254.60±119.12 s than Group B (which started with the MC), which required 113.98±9.65 s for the same task in Trial 1. Also, for the MC there was a significant difference ($Z=2.43$, $p<0.05$) between both groups in Trial 1. Group A required 124.30±13.98 s, which is less than Group B, which required 210.47± 84.53 s. Among the four trials, the learning curve of the participants shows a decrease in average task performance time. The curve dropped by more than 55% for the very first instrument used, no matter which configuration, and flattened to a decrease of 3-7% for the very last instrument used in both groups.

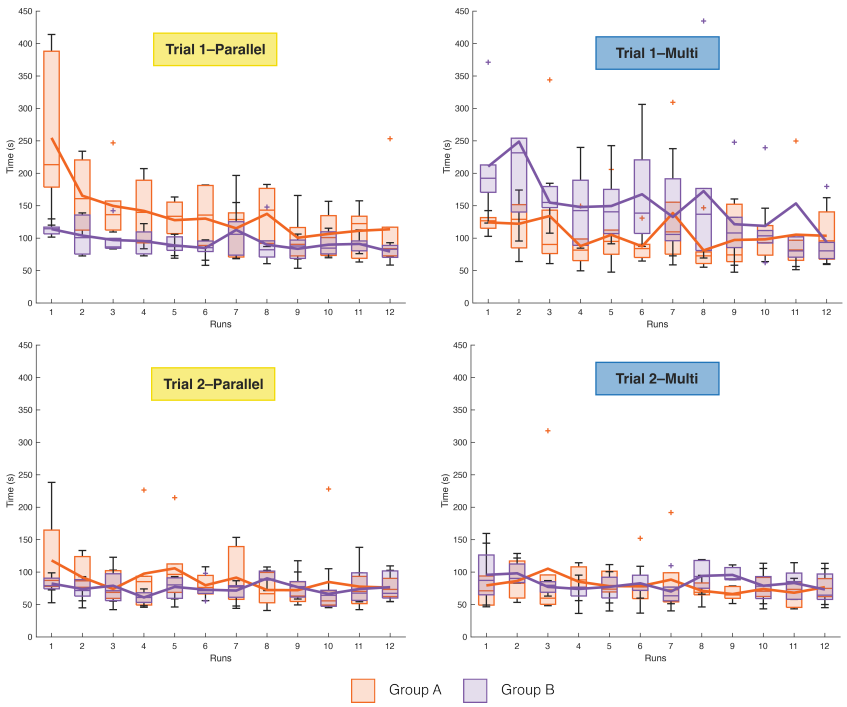

Figure 6.11: Box and whisker plots of the average time per run in the two trials performed by each participant for each instrument in the two different groups. Orange represents Group A and purple Group B. Each box and whisker plot represents the median, the upper, and the bottom quartile of the average time for the six participants of Group A and the six of Group B.

The responses of the TLX self-evaluation that ranged from -10 to 10 were transferred to a percentage scale. High percentages express a high workload, and low percentages express a low workload. The overall Raw TLX score was 34% (SD= 22) for the parallel and 40% (SD= 23) for the MC in Trial 1. In Trial 2, the overall Raw TLX score was 23% (SD= 22) and 30% (SD=23) for the parallel and the MC,

respectively, Figure 6.12. We performed the Mann Whitney U test for independent groups of non-parametric data. The test revealed no significant difference (Z= -1.55 p=0.12>0.05) between the overall workload in the first trials of the two instruments. In the second trial, the overall workload was significantly higher (Z=-2.18, p<0.05) for the MC compared to the PC. The Wilcoxon Signed-Rank test revealed a significant reduction (Zp=4.92 Zm=4.58, p<0.05) in the overall workload of the two instruments from Trial 1 to Trial 2. Participants expressed the maximum workload for both instruments in the effort subscale of Trial 1, 49% (SD=21) for the PC and 57% (SD=25) for the MC, respectively. Finally, Figure 6.13 shows the result of the final questionnaire on the subjective participant preference. The participants expressed a strong overall preference for the PC, 10 out of 12. All participants preferred the PC when considering the response in steering.

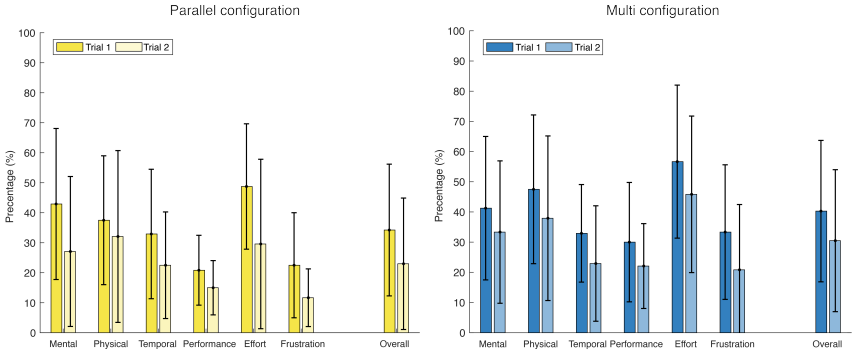

Figure 6.12: Average and standard deviation of the Raw TLX score for the six subscales (mental demand, physical demand, temporal demand, performance, effort, and frustration) in Trials 1 and 2. The average was calculated over the score given by the 12 participants. Yellow represents the parallel, and blue the multi configuration.

6.6. Discussion

6.6.1. Experimental findings

The difference in task performance time was not significant when comparing the parallel and multi configurations to each other over Trials 1 and 2. A significant decrease appeared over time within the two trials when using the same configuration. This data was also confirmed by the learning curve of the two configurations. The two learning curves showed that the task performance time decreased quickly in Trial 1 during the first runs, and the participants reached a plateau after the first runs of Trial 2 for both instruments. It is interesting that for the parallel configuration, the minimum average task performance time was reached during Run 9 of Trial 2, instead of the last run, with a slight increase in average time for the subsequent runs. This effect is probably due to the tiredness of the participants at the end of the test. The flattening of the curves also showed its effect on the decrease in the workload perceived by the participants. The time performance for the parallel and the multi

configurations in the last run of the second trial shows similar results for the parallel and the multi configuration, rejecting our second hypothesis.

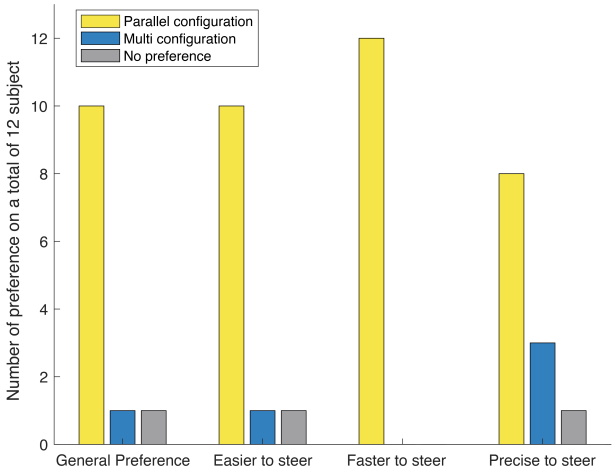

Figure 6.13: Results of the final questionnaire on personal preference.

The workload strongly decreased from Trial 1 to Trial 2 for both configurations. However, even though the task performance time did not show significant differences between the parallel and the multi configuration, the decrease in workload was significantly higher for the parallel configuration. This result can also explain the net difference in the preference of the parallel configuration over the multi configuration.

Looking at the alternation between the two cable configurations over the four trials, it becomes clear that the instruments influence each other over the first trials. In Trial 1, Group A started with the parallel configuration, and the average task performance time is significantly higher than the one in Trial 1 of Group B (which started with the multi configuration) for the same configuration. The same result can be observed for the opposite: the task performance time of Group B with the multi configuration in Trial 1 is significantly higher than the one of Group A. In the very first run, when they used their first instrument for the first time, the participants needed not only to learn to use the instrument and gain dexterity but also needed to familiarize themselves with the setup and the target positions. When they used their second instrument for the first time, they only needed to get used to the different cable configurations.

We also analyzed the performance of the participants within each run. An interesting outcome was the target that required the longest time to be hit and its occurrence within all 48 runs. The analysis revealed that Target 6 was the most difficult target to be hit, 195 times out of the total of 576 recorded runs. This can be explained by the location of Target 6, which was located the closest to the participant, requiring the instrument tip to be pointed towards the participant, mirroring its motion and thus adding an extra layer of difficulty in the maneuverability. The analysis becomes even more interesting when Target 6 is compared to Target 4. Target

4 has the same orientation angle but has an opposite location of Target 6. Target 4 recorded only 66 times the longest time to hit the target, the lowest occurrence among all targets. This result is probably due to its convenient location at the front right of the participant.

The net preference of the parallel over the multi configuration was briefly explained by four participants in the comments at the end of the final questionnaire and was mainly related to steering possibility. The parallel configuration gives the possibility of steering the segments independently, which is especially convenient for the most distal segment. By individually controlling the most distal segment, the participants felt more control over the final shaft orientation during insertion into the target. Therefore, the parallel configuration showed easier maneuverability over the multi configuration as hypothesized. On the other side, the multi configuration was preferred for the higher stiffness of the entire instrument, which allows for stronger haptic feedback of the steerable shaft during the test. The higher stiffness perceived by the participants was probably caused by the friction generated by the higher normal forces between the tensioned helical cables and the 3D printed helical structure in the handle as compared to the parallel cables. This observation is also interesting considering that the total number of cables in the multi configuration is half of the one in the parallel configuration.

6.6.2. Limitation of this study and future recommendation

Additive manufacturing (AM) represents a significant innovation in terms of fast prototyping and the complexity of the design. In our work, AM allowed us to print highly complex compliant structures enabling advanced instrument maneuverability with very limited assembly time - the instruments were printed and assembled in less than one and a half days. Our study was mainly focused on device maneuverability and functionality. Therefore, the instruments were fabricated with an acrylic-based polymeric resin, which was non-biocompatible but specifically designed for easy and precise prototyping. Future work should focus on investigating the use of biocompatible materials able to guarantee the same compliant characteristics of the material used in this study. We think that our instruments should, in the end, be used as disposable devices, opening possibilities for the patient and surgeon-specific designs.

We used the same instrument for more than one participant, and, to always have fully functional instruments, in our experiment, we decided to use a new instrument every time we noticed signs of failing. Most of the time, the breakages were associated with excessive force applied by the participant to hit the target. Another reason for failure was due to the wear of the polymeric-based material induced by the stainless-steel cables.

The test was performed under direct 3D vision due to the inexperience of the participants with laparoscopic procedures. Performing the test with an endoscope and a monitor would improve the resemblance of the task with the clinical setting. Moreover, it would be interesting to further investigate the possible applications of our instruments by using the available lumens to insert flexible instruments to grasp tissues or perform biopsy procedures.

By comparing two cable configurations in 3D printed steerable instruments, this study explores new possibilities for additive manufacturing technology in medical instruments where complex geometries for the single parts simplify the overall design while maintaining, if not enhancing, the instrument's functionalities.

6.7. Conclusion

The goal of this study was to compare parallel and multi cable configurations in multi-steerable laparoscopic instruments in terms of task performance time and workload. Our experiment showed that there was no significant difference in the task performance time for the two configurations. In the used NASA TLX scale, however, the participants expressed a lower workload for the parallel configuration as compared to the multi configuration. Overall, 10 out of 12 participants preferred the parallel configuration. The preference was mainly determined by the increased possibility of individually orienting the most distal segment.

References

[1] A. Gallagher, N. McClure, J. McGuigan, K. Ritchie, and N. Sheehy, *An ergonomic analysis of the fulcrum effect in the acquisition of endoscopic skills,* Endoscopy **30**, 617 (1998).

[2] U. Guller, S. Hervey, H. Purves, L. H. Muhlbaier, E. D. Peterson, S. Eubanks, and R. Pietrobon, *Laparoscopic versus open appendectomy: outcomes comparison based on a large administrative database,* Annals of surgery **239**, 43 (2004).

[3] V. Vitiello, S.-L. Lee, T. P. Cundy, and G.-Z. Yang, *Emerging robotic platforms for minimally invasive surgery,* IEEE reviews in biomedical engineering **6**, 111 (2012).

[4] I. Surgical, *Move surgery forward. again. da vinci sp,* (2020), https://www.intuitive.com/en-us/products-and-services/da-vinci/systems/sp, Accessed 2020-11-25.

[5] G. Schurr, K. Buess, and M. Schwarz, *Robotics in endoscopic surgery: Can mechanical manipulators provide a more simple solution for the problem of limited degrees of freedom?* Minimally Invasive Therapy & Allied Technologies **10**, 289 (2001).

[6] P. L. Anderson, R. A. Lathrop, and R. J. Webster III, *Robot-like dexterity without computers and motors: a review of hand-held laparoscopic instruments with wrist-like tip articulation,* Expert review of medical devices **13**, 661 (2016).

[7] F. M. Sánchez-Margallo, J. A. Sánchez-Margallo, and A. Szold, *Handheld devices for laparoscopic surgery,* New horizons in laparoscopic surgery , 75 (2018).

[8] W. J. Peine and A. Chamorro, *Surgical instrument,* (2011).

[9] DEAM, *Laproflex steerable laparoscopic instrument,* (2019), https://www.deam.com/product-details/laproflex/, Accessed: 2020-05-09.

[10] Indes, *DEAM- Laparoscopic Instrument,* (2020), https://indes.eu/en/portfolio/deam-laparoscopic-instrument/, Accessed: 2020-11-27.

[11] A. Trejo, M.-C. Jung, D. Oleynikov, and M. S. Hallbeck, *Effect of handle design and target location on insertion and aim with a laparoscopic surgical tool,* Applied Ergonomics **38**, 745 (2007).

[12] T. Horeman, M. Aguirre, G. Kerkhoffs, J. Dankelman, and G. Tuijthof, *The sata, a simple, stiff, and rigid steering mechanism,* Journal of Medical Devices **9** (2015).

[13] T. Lenssen, J. Dankelman, and T. Horeman, *SATA-LRS: A modular and novel steerable hand-held laparoscopic instrument platform for low-resource settings,* Medical Engineering & Physics **101**, 103760 (2022).

[14] C. Fan, H. Clogenson, P. Breedveld, J. J. van den Dobbelsteen, and J. Dankelman, *Comparison of two control methods for minimally invasive surgical instruments,* Journal of Medical Devices **6** (2012).

[15] D. Uysal, C. Gasch, R. Behnisch, F. Nickel, B. P. Müller-Stich, M. Hohenfellner, and D. Teber, *Evaluation of new motorized articulating laparoscopic instruments by laparoscopic novices using a standardized laparoscopic skills curriculum,* Surgical endoscopy **35**, 979 (2021).

[16] A. H. Zahraee, J. Szewczyk, and G. Morel, *Simulation for optimal design of hand-held surgical robots,* in *2009 Annual International Conference of the IEEE Engineering in Medicine and Biology Society* (IEEE, 2009) pp. 270–273.

[17] S. Coemert, R. Roth, G. Strauss, P. M. Schmitz, and T. C. Lueth, *A handheld flexible manipulator system for frontal sinus surgery,* International Journal of Computer Assisted Radiology and Surgery **15**, 1549 (2020).

[18] G. Gerboni, P. W. J. Henselmans, E. A. Arkenbout, W. R. van Furth, and P. Breedveld, *HelixFlex: bioinspired maneuverable instrument for skull base surgery,* Bioinspiration & biomimetics **10**, 66013 (2015).

[19] P. W. Henselmans, G. Smit, and P. Breedveld, *Mechanical follow-the-leader motion of a hyper-redundant surgical instrument: Proof-of-concept prototype and first tests,* Proceedings of the Institution of Mechanical Engineers, Part H: Journal of Engineering in Medicine **233**, 1141 (2019).

[20] C. Girerd and T. K. Morimoto, *Design and control of a hand-held concentric tube robot for minimally invasive surgery,* IEEE Transactions on Robotics (2020).

[21] C. Fan, D. Dodou, and P. Breedveld, *Review of manual control methods for handheld maneuverable instruments,* Minimally Invasive Therapy & Allied Technologies **22**, 127 (2013).

[22] M. Neumann and J. Burgner-Kahrs, *Considerations for follow-the-leader motion of extensible tendon-driven continuum robots,* in *2016 IEEE International Conference on Robotics and Automation (ICRA)* (2016) pp. 917–923.

[23] P. Breedveld, J. Sheltes, E. M. Blom, and J. E. Verheij, *A new, easily miniaturized steerable endoscope,* IEEE engineering in medicine and biology magazine **24**, 40 (2005).

[24] C. Culmone, P. W. Henselmans, R. I. van Starkenburg, and P. Breedveld, *Exploring non-assembly 3d printing for novel compliant surgical devices,* Plos one **15**, e0232952 (2020).

[25] A. Sakes, A. Ali, J. Janjic, and P. Breedveld, *Novel miniature tip design for enhancing dexterity in minimally invasive surgery,* Journal of Medical Devices **12** (2018).

[26] D. Stefanchik, O. J. Vakharia, and J. T. Spivey, *Us patent app. 11/458,895 - braided endoscope accessories,* (2008).

[27] N. Instruments, *Usb-6008 8 ai, 2 ao, 12 dio usb multifunction i/o device,* (2017), https://www.ni.com/pdf/manuals/375295c.pdf.

[28] S. G. Hart and L. E. Staveland, *Development of nasa-tlx (task load index): Results of empirical and theoretical research,* in *Advances in psychology*, Vol. 52 (Elsevier, 1988) pp. 139–183.

Figure 6.14: Video of the execution of one run with the parallel configuration instrument and one run with the multi configuration instrument.

7

Fully 3D Printed Compliant Surgical Grasper

Published as:
Culmone C., Lussenburg K., Alkemade J., Smit G., Sakes A., Breedveld P. "SAMPLE: A Fully 3D Printed Steerable Instrument for Minimally Invasive Surgery". Materials, 14.24 (2021): 7910

Abstract

Additive manufacturing is changing the perspective of the design of surgical instruments. The number of components can be drastically reduced while increasing the complexity of the single part and improving its functionalities. In addition, modifications for user's needs or specific procedures become possible by enabling the production of single customized items. In this work, we present a new fully 3D printed handheld steerable instrument for laparoscopic surgery, named SAMPLE. With a shaft diameter of 8 mm, it is fully mechanically actuated using cables. The pistol-grip handle is based on ergonomic principles and allows for single-hand control of both grasping and steering. Compliant joints and snap-fit connectors enable fast assembly and minimal part count. Additive manufacturing allows personalization of the handle to each surgeon's needs by adjusting specific dimensions in the CAD model, which can increase comfort during surgery. During tests, SAMPLE showed that the forces on the instrument handle required for steering and grasping were below 15 N, while the grasping force efficiency was calculated to be 10-30%. SAMPLE combines the advantages of additive manufacturing with regards to personalization and simplified assembly, illustrating a new approach to the design of advanced surgical instruments where the customization for a single procedure or user's need is a central aspect.

7.1. Introduction

7.1.1. State of the art

The advent of Minimally Invasive Surgery (MIS) can be considered one of the most important innovations in the surgical field. In MIS, two or three small incisions, usually between 5 to 10 mm in diameter, act as an entry port to the human body, hereby avoiding a large incision, which is common in conventional open surgery. In the small incisions, a temporary port called trocar is used to facilitate the insertion of the instruments. This minimally invasive approach reduces the risk of complications such as infections or hemorrhages, decreases the hospitalization time, and minimizes the size of the scar; reducing the pain for the patient [1, 2]. However, different from open surgery where the surgeon has direct visualization and access to the operation area, in MIS, the indirect visualization and the limited operational space to maneuver the instruments influence the surgeon's performance.

Instruments conventionally used in MIS are characterized by three main components: a handle to maneuver the device, a long and straight shaft to reach the operation area, and an end-effector to operate; usually containing a grasper or a cutting mechanism. The rigid and slender instruments used in MIS severely reduce the dexterity of the surgeon due to the loss of wrist articulation and the restriction posed by the small incision size. The number of degrees of freedom (DOF) is limited from six in open surgery to four in MIS (Figure 1): 1-2) pivoting on the incision in two perpendicular planes, 3) axial translation, and 4) axial rotation [3]. Aside from the reduced number of DOF, the surgeon has to cope with the fulcrum effect: the inversion of the handle movements at the end-effector due to the pivot point created by the trocar in the abdominal wall.

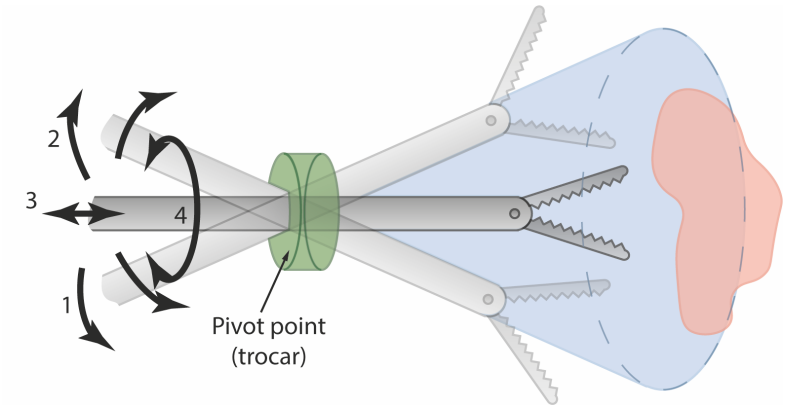

Figure 7.1: Instrument degrees of freedom in Minimally Invasive Surgery:1-2) pivoting around the incision in two perpendicular planes, 3) axial translation and 4) axial rotation.

7.1.2. Challenges in minimally invasive surgery

Solutions have been proposed to overcome the limitations of MIS by enhancing the dexterity of instruments using wrist-like mechanisms. Robotic devices, such as the da Vinci® robotic system (Intuitive Surgical Inc., Sunnyvale, Ca, USA), have the ability to diminish the fulcrum effect and enhance the surgeon's dexterity by providing two ad-ditional DOF to the end-effector of the robotic arm using the so-called EndoWrist mechanism. Still, the high initial costs and the limited lifespan of the robotic instruments [4] push researchers to find solutions able to guarantee the advantages of robotic devices while reducing the costs [5]. Great attention has been given to hand-held mechanically actuated steerable instruments. Examples are the laparoscopic instruments Maestro [6] and the LaparoFlex developed and commercialized by DEAM (DEAM B.V., The Netherlands) [7]. and the LaparoFlex (TU Delft and DEAM B.V., The Netherlands). Both these instruments use rigid joints in their steering mechanism to achieve bending motion in two orthogonal planes, similar to the human wrist. Rigid joints are robust and solid, and therefore widely used in conventional instruments. However, when it comes to MIS, the inability to further miniaturize mechanical components due to friction limits their applications [8].

Next to the limited DOF of conventional MIS instruments, the radically different design and operation of instruments for MIS often cause ergonomic inconveniences for surgeons [9–12]. These inconveniences range from muscle fatigue and musculoskeletal pains to neural injury and worsened performance [10, 13, 14]. Instrument handles are the primary physical interface for the surgeon, and, therefore, many studies have been dedicated to this topic [15]. One of the main conclusions of these studies points to the need for personalization, or at the very least adaptability, of instrument handles [10, 16], since it is impossible to create one handle design that suits every possible hand. Due to the high manufacturing costs associated with conventional manufacturing of personalized products, this has long been out of reach.

7.1.3. Additive manufacturing for surgical devices

Additive Manufacturing (AM) or 3D printing provides new opportunities to change the design paradigm of medical devices. AM allows a 3D model to be directly converted from a Computer-Aided Design (CAD) into an object built with a layer-by-layer process. The possibility of producing complex shapes allows the number of components to be drastically reduced, in addition to increasing the functionality of the entire medical instrument. Examples of 3D-printed medical devices are the continuum robots presented by Kim *et al.* [17], and the 2-DOF steerable grasper DragonFlex created by Jelinek *et al.* [3]. A comprehensive overview of 3D printed surgical instruments has been published previously by our group [18]. AM allows for the possibility of using different approaches, such as non-assembly 3D printed mechanisms [19, 20] or 3D printed compliant solutions [21]; already successfully applied in prosthetics [22] and surgical forceps [23]. In addition, AM enables the production of personalized items at no extra costs [24, 25]. Ranganathan *et al.* [26] 3D printed customized forceps handles based on eight anthropometric hand parameters of Indian males. González *et al.* [27, 28] presented and tested the design of an ergonomic pistol-grip handle that

was customized to the surgeon's specific hand size. They concluded that the use of their ergonomic handle reduced muscle fatigue and improved the ease of use of the instrument. Similarly, Sánchez-Margallo *et al.* [29] compared customized 3D printed handles with standard handles and reported that the customized handles aided the surgeon's hand-eye coordination and led to shorter execution times.

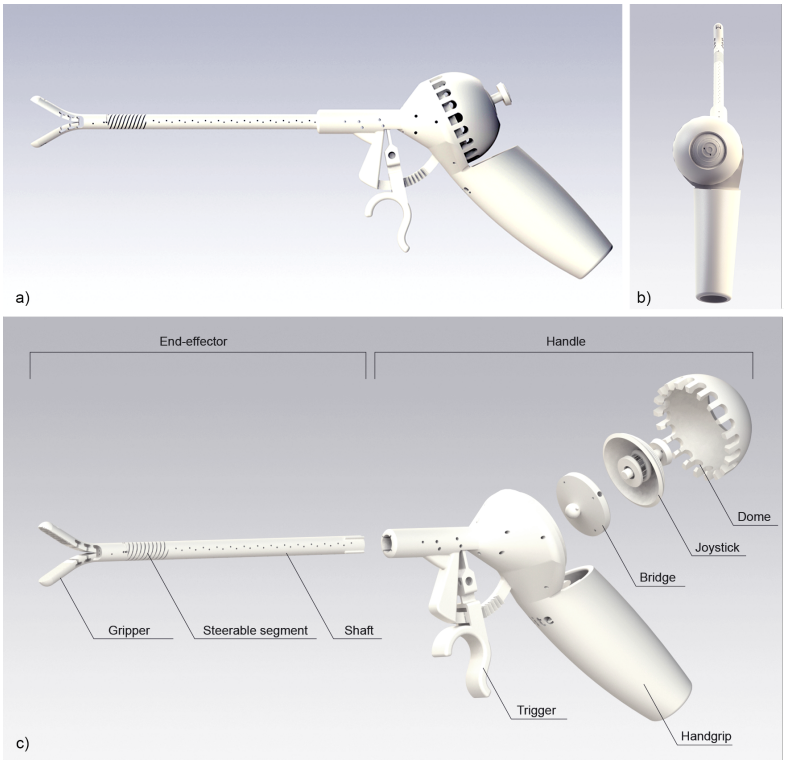

Figure 7.2: Design of 3D-GriP. a) Side view; b) Back view; c) Exploded view with the names of the parts indicated.

7.1.4. Objective

In this work, we propose a design of a handheld 2-DOF cable-driven steerable instrument for MIS that maximizes the advantages of AM by making use of non-assembly design principles. The new steerable instrument (Figure 7.2), called 3D-GriP, is mechanically actuated by means of cables and was designed for AM to minimize the number of assembly steps. In order to comply with the constraints of the laparoscopic environment, it has a maximum omnidirectional bending angle of the end-effector between 40 and 60 degrees [5, 30], an opening angle of the gripper of 60 degrees [7], and a shaft diameter of 8 mm [7, 31, 32]. The surgical instrument allows for single-hand control of both the grasping and steering mechanisms, while the design of the handle is based on ergonomic guidelines and can be customized to specific hand sizes

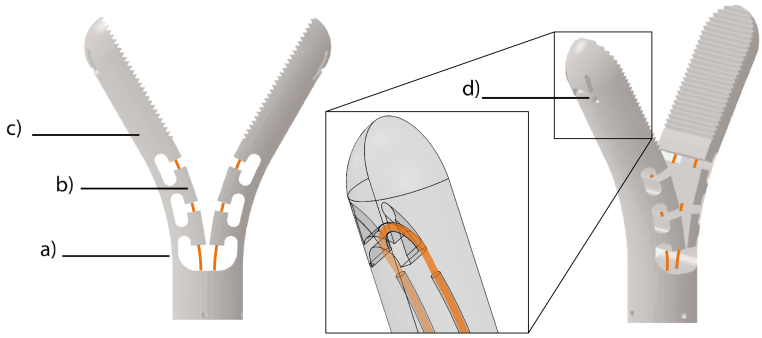

Figure 7.3: Gripper: a) compliant beam, b) T-shape guiding section for the actuation cables, c) jaw, d) cable fixation point with its close-up made transparent. Teeth have been removed for clarity.

due to the use of AM. We used Solidworks as CAD software to design the 3D-GriP.

7.2. 3D-GriP design

7.2.1. Gripper design

For the design of our instrument, compliant joints are used wherever possible in favour of rigid body joints. The advantage of compliant joints is that they do not suffer from the problems with clearances that occur in non-assembly rigid body joints [19, 20]. An additional advantage is that compliant joints can be produced as a single, monolithic part without assembly and can therefore reduce the number of components and assembly steps. Moreover, by using flexible components to achieve motion, friction between sliding elements within the joint can be eliminated [33–36].

The compliant gripper was designed in such a way that in the relaxed position it is in a fully open configuration with a 60-degree opening angle. This way, the forces applied on the actuation cables to close the gripper are directly translated to a (gripping) force on the tissue and can thus be easily controlled by the surgeon. Using a half-open position, as proposed by Lassooij *et al.* [36], has the advantage of reducing the stress on the compliant beam during operation. However, the half-open position is less convenient, as it requires the surgeon to move the gripper both to grasp and to release the tissue. In the fully open configuration, the jaws will passively return to their initial open configuration after the control input is seized due to the compliant flexures, reducing the number of active movements for the surgeon.

The design of the gripper joint was based on a compliant beam, as shown in Figure 7.3a, and consists of two gripper jaws with a closed diameter of 8 mm and length of 20 mm. The tooth profile has a height of 0.5 mm and a tooth angle of 60 degrees, similar to those seen in commercial grippers for MIS [37]. The compliant beam has a thickness of 0.8 mm, in order to minimize the bending stress, while the width was kept as large as possible, to provide torsional and lateral stability. The closing of the gripper is actuated by two Ø 0.25 mm actuation cables, which loop around the distal end of the gripper (Figure 7.3d) to avoid gluing or soldering on

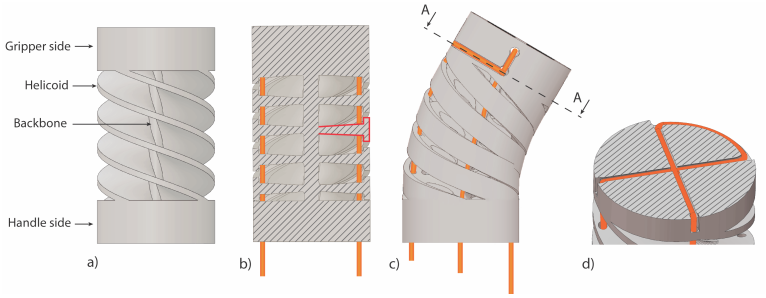

Figure 7.4: Steerable segment design. a) Central backbone with four helicoids evenly placed around. b) Cross-Section of the segments showing the T-shape of the helicoids, highlighted in red. Cables are shown in orange. c) Due to the T-shape, the helicoids touch each other at the inner curve of the segment, limiting the bending angle. d) Cross-Section A-A shows the cable fixation point with the looped cables.

the jaws. T-shaped guiding sections were added to the compliant beams in order to gently guide the actuation cables through the joint without affecting their bendability, see Figure 7.3b.

7.2.2. Steerable segment design

In order to equip the instrument with two additional DOF, a steerable segment was integrated into the shaft of the device. The steerable segment used in this study was designed to achieve high torsional and axial stiffness, to avoid misalignment between the gripper and the shaft, whilst keeping a low bending stiffness to guarantee easy maneuverability. A detailed description of the design of the steerable segment is given by Culmone *et al.* [38]; however, for the clarity of this work, a summary follows. The steerable segment combines a compliant continuous central backbone for high axial stiffness with four helicoids evenly placed around the centerline for high torsional stiffness, homogenously distributed (Figure 7.4a). The helicoids have a T-shaped cross-section (Figure 7.4b). The T-shaped cross-section is thinnest close to the backbone and increases in thickness towards the outer side of the segment. This guarantees a low bending stiffness, while at the same time limiting the maximum bending angle, which prevents failure due to excessive bending.

Two cables are used for steering, which loop around the top of the steerable segment and back down to the shaft (Figure 7.4c). A cross-shaped groove in the top of the segment was used to fixate the cables in place by means of friction, to avoid soldering or gluing (Figure 7.4d). The 20 mm long steerable segment was printed as one part with the rigid shaft, in which dedicated channels guide the steering and gripper cables towards the handle.

7.2.3. Handgrip ergonomics

A pistol-grip is used for the main shape of the handle (Figure 7.2), which is the preferred design for complex or multifunctional instruments [10, 11, 13, 39]. The handle is specifically designed for right-handed use: the asymmetric grip allows for a

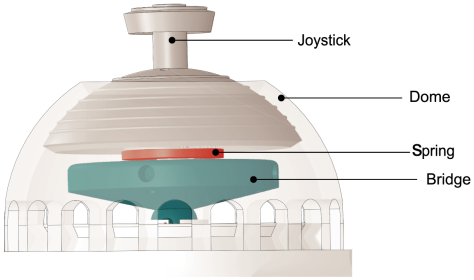

a)

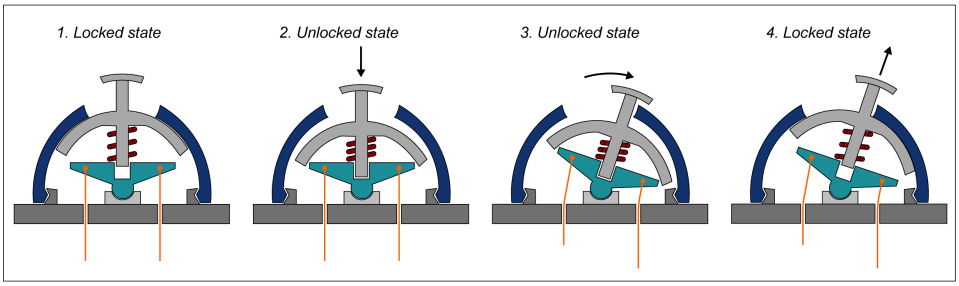

b)

Figure 7.5: Working principle of the steering mechanism. a) 3D-render of the assembled joystick, showing the joystick, the dome (transparent to show the underlying components), bridge (blue), and spring (red). b) Schematic drawing of the working principle of the friction lock showing the bridge (blue), spring (red), and cables (orange). 1-4) show the actions taken to move and lock the steerable segment.

straight alignment of the thumb and the wrist during steering, which increases the user's comfort (Figure 7.2b) [40, 41]. It can easily be converted to left-handed use by mirroring the design [10]. The handgrip has a bulbous shape that follows the shape of the hand [10, 27], without any specific finger grooves for positioning the fingers [42], since the latter limits the positions in which it can be held. Changing the dimensions of the handle length, width, and size of the trigger allows for customization to different hand sizes.

7.2.4. Steering control

A joystick is used for the steering system, actuated by the thumb. In the field of steerable surgical instruments, thumb actuation allows for more precise control in terms of motion, accuracy, and the perception of steering [40, 41, 43, 44]. The steering mechanism itself consists of the joystick with an integrated spring, which is connected to a ball and socket joint, and covered by a dome. The top part of the ball and socket joint, the bridge (Figure 7.5a), is the point of fixation for the cables. Rotating the joystick pulls and releases the actuation cables to steer the end-effector. In order to lock the steerable segment into any angle, an active friction lock mechanism was implemented. When no normal pressure is applied to the joystick, it is held in place by the friction between the joystick and the dome, caused by pre-

tension in the spring (Figure 7.5b). This pre-tension is generated during the assembly when the dome is placed over the joystick mechanism and snapped into place. By applying pressure to the joystick, the friction lock is released, allowing for steering of the end-effector. Releasing the joystick will automatically lock the steerable segment into any angle up to 60 degrees. The rotation of the thumb when steering, and therefore the rotation of the joystick, should be smaller than 45 degrees in order to retain an ergonomic position [45]. Considering the desired steering angle for the end-effector of 60 degrees, the rotation angle of the joystick cannot be transferred in a 1-1 ratio to the end-effector. Therefore, an amplification of the joystick rotation was implemented within the steering control system. To achieve this amplification, the cables' radial distance towards the centerline of the bridge was designed to be three times larger than the cables' radial distance towards the end-effector's centerline. The result of this is that when rotating the joystick 20 degrees in one direction, the end-effector will bend 60 degrees.

7.2.5. Grasping control

The grasping motion of the gripper is driven by a trigger, actuated by the index and/or middle finger (Figure 7.6) [44]. The trigger is automatically locked in position by means of a ratchet mechanism. In order to release the ratchet lock, the trigger needs to be moved sideways until the teeth disengage. Two orthogonal bending flexures were de-signed to allow the trigger to move in these two required directions (Figure 7.6c). Because of the compliancy of the bending flexures, the trigger moves automatically back to the initial position when released, opening the compliant gripper. This means that only active movement for the surgeon is required to close the gripper. The actuation cables were fixated in the rigid part between the bending flexures. Although it is common in lapaoscopic instruments to place the trigger mechanism inside the handle, in this case, we opted to place it outside the handle to be able to produce it with as few assembly steps as possible.

7.3. Prototype fabrication and assembly

The instrument was manufactured using a commercially available Form 3B (Formlabs, Somerville, MA, USA) 3D printer, which uses Stereolithography (SLA) technology. SLA is a process in which a light source, typically a laser, hardens a liquid photopolymer in layers [46]. The handgrip, dome, bridge, and end-effector were printed using the Durable FLDCL02 resin (Formlabs, Somerville, MA, USA), exploiting the high elongation properties of the material for the compliant joints. The total volume for the parts printed with the Durable resin was 132 ml. The joystick with incorporated spring was printed with the Tough 1500 FLTO1501 resin (Formlabs, Somerville, MA, USA), with a total volume of 8.85 ml, due to its ability to produce parts that spring back under loading cycles. All parts were printed with a 50 µm layer height. The print time for the parts in Durable was 43 hours, whereas the joystick was printed in 3 hours and 45 minutes. After printing, isopropanol alcohol was used to remove the uncured resin from the prototype. Only the joystick was cured for 60 minutes at 70 ºC in the curing chamber to enhance the spring back properties of this component.

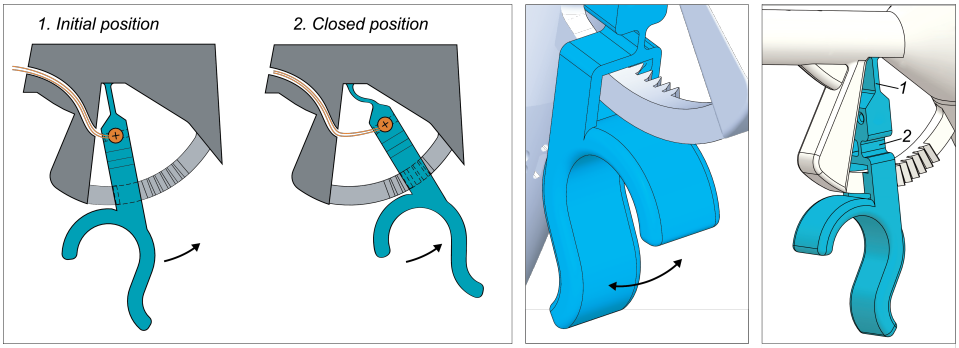

Figure 7.6: Working principle of the trigger mechanism, the trigger and flexures are highlighted in blue, the cables are shown in orange. a) 1. In the initial position of the trigger, the ratchet is not locked, and the gripper is opened. 2. By moving the trigger towards the palm, the gripper closes, and the trigger is locked when the ratchet teeth are engaged. b) Close-up of the internal ratchet-teeth in the locked position. c) Render of the trigger indicating the two orthogonal bending flexures.

The final prototype consists of five 3D printed parts: 1) the end-effector, 2) handgrip with trigger, 3) bridge, 4) joystick with spring, and 5) dome. The end-effector and the handgrip could not be printed as one part because they exceed the printer's build volume. Therefore, they were separated into two pieces and connected by a form-fit closure. The channels for the actuation cables run along the entire length of the shaft and handgrip. In order to be able to remove excess material from inside these channels, we added small drainage holes of 0.1 mm in diameter at regular intervals along the shaft (Figure 2). Furthermore, the shaft and the handgrip were printed with the long axis of the cable holes parallel to the vertical z-axis of the printer. This orientation proved best to keep the cable channels open along their entire length. The joystick and the spring were consolidated so that they could be 3D printed as one part. However, this configuration made it difficult to remove the standard support material generated by the Formlabs software. Therefore, we created custom support pillars between the coils of the spring that could be easily removed after printing.

To assemble the prototype (Figure 7.7), first, the shaft was coupled with the handgrip using the form-fit connection. To actuate the steerable segment, we used stainless steel cables (Ø 0.30 mm). The four ends of the cables were fixed using dog point screws into dedicated grooves of the bridge. Before fixation, the cables were straightened by means of weights. The gripper jaws are actuated with nitinol wires (Ø 0.25 mm) because, due to their high rigidity, they can be used to close the jaws, and help open them. These wires were fixed to the trigger by means of dog point screws. After insertion and fixation of the cables, the joystick and dome were snapped into place.

7.4. Experimental methods and results

To assess the functionalities in steering and grasping, we performed three different measurements. First, we verified the maximum bending angle of the end-effector in four main directions, with different external loads applied to the end-effector. Second, we evaluated the required steering force applied by the user on the joystick when different external loads were applied to the end-effector, simulating steering in a surgical setting. Third, we evaluated the grasping force of the gripper on artificial tissue in relation to the required force applied by the user on the trigger.

7.4.1. Bending angle measurements

We analyzed the maximum bending angle of the end-effector by steering the joystick to its maximum position in the four main directions: upward and downward in the vertical yz-plane and right and left in the horizontal xy-plane. We repeated the measurement three times for each plane. The end-effector was able to reach an angle of approximately ±50 degrees in both directions in the xy-plane (Figure 7.8b) and ±45 degrees in the yz-plane (Figure 7.8c), which is somewhat lower than the desired ±60 degrees. The video linked to the QR code at the end of this chapter illustrates the omnidirectionality and the smoothness of the motion.

In addition, we evaluated the effect of different external loads on the bending performance by attaching different weights to the end of the steerable segment. Three load conditions were tested: 1) 5 grams, 2) 10 grams, and 3) 20 grams. The load was suspended from the distal end of the steerable segment in order to only test its effects on the steerable segment and not the compliant gripper. Only the bending angle in the yz-plane was evaluated, since the direction of the load does not influence bending in the xy-plane. To measure the bending angle, we moved the joystick to its maximum up- and downward position, and repeated this three times for each load condition. It was found that an in-crease in load decreased the bending angle in the upwards direction: 7.1% for 5 grams, 19.8% for 10 grams, and 28.5% for 20 grams (Table 7.1). No considerable differences in the average of the maximum bending

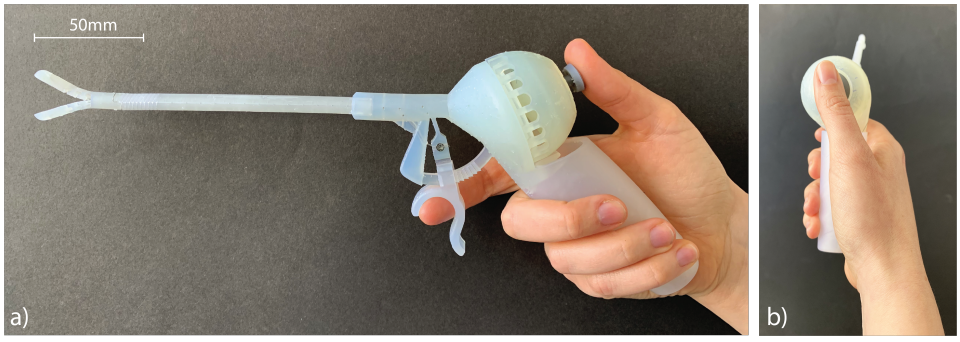

Figure 7.7: The assembled prototype. a) Front view, b) side view that shows the alignment of the wrist and the thumb.

angle (0-2%) were observed when the steerable segment was steered downwards, regardless of the applied load.

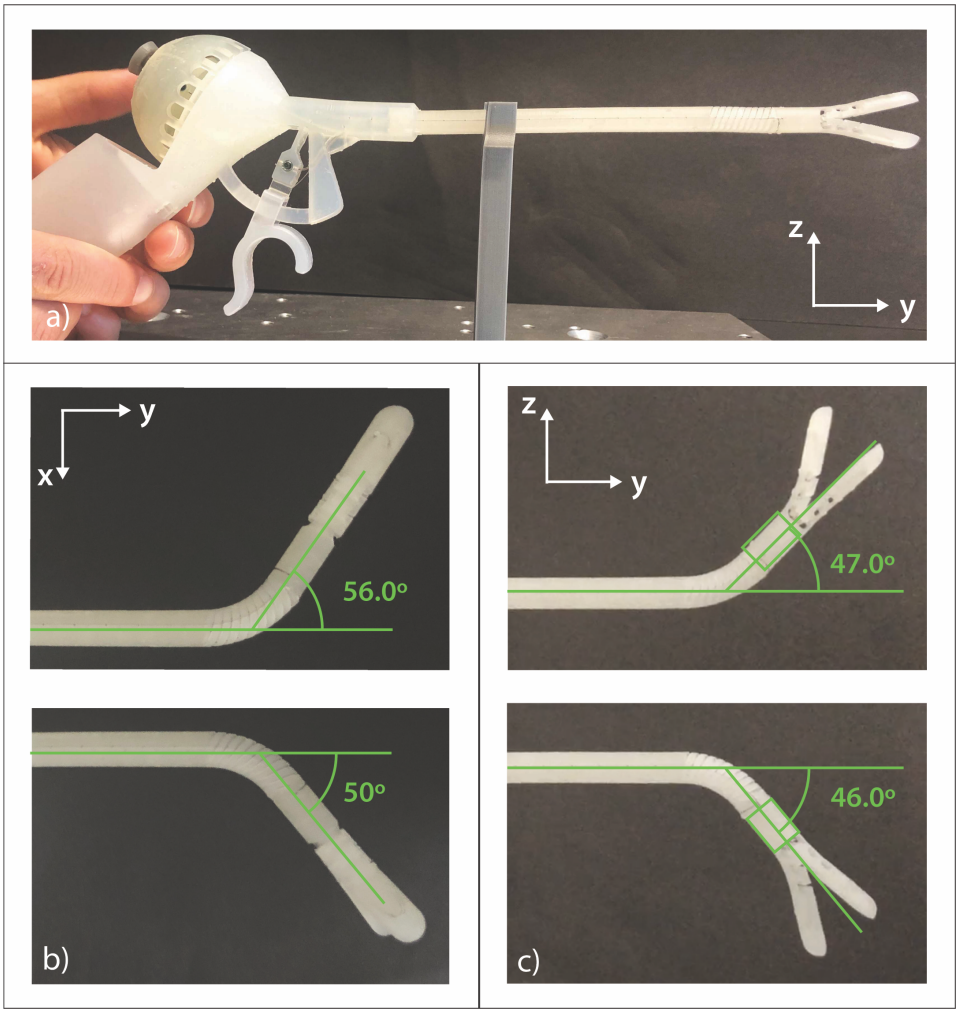

Figure 7.8: Lateral bending evaluation. a) Set-up. b) Lateral left/right bending in the horizontal xy-plane without load, and c) in the vertical yz-plane without load.

7.4.2. Steering force test

Method

In a surgical procedure, it is often necessary to move or stretch the gripped tissue. Therefore, we evaluated the force necessary to operate the joystick with the thumb in relation to the effect of different loads on the steerable segment. For this test, we applied again a load to the end of the steerable segment and moved the joystick in the

Table 7.1: Vertical bending evaluation with different loads applied. Vertical bending in the yz-plane with no load, 5 grams, 10 grams, and 20 grams.

	No Load (degrees)		5 grams (degrees)		10 grams (degrees)		20 grams (degrees)	
	upward	downward	upward	downward	upward	downward	upward	downward
rep. 1	47.0	46.0	42.3	51.2	40.4	49.7	37.0	45.5
rep. 2	46.2	48.7	43.7	50.3	35.8	52.2	34.3	50.8
rep. 3	46.5	53.4	43.9	50.6	36.1	49.5	28.7	52.3
Aver.	46.6 ±0.3	49.4 ±3.8	43.3 ±0.9	50.7 ±0.5	37.4 ±2.5	50.4 ±1.5	33.3 ±4.3	49.5 ±3.5

rep. = repetition, aver. = average

four main directions (upward, downward, left, and right), after which we registered the force required for these four movements combined. We tested the following load conditions: 1) no load, 2) 5 grams, 3) 10 grams, and 4) 20 grams. The force required to operate the joystick was measured by placing a piece of pressure foil with a sensitivity of 0.05 MPa (4LW Fujifilm Prescale, ALTHEN BV Sensors & Control, Leidschendam, the Netherlands) between the fingertip and the joystick (Figure 7.9a). The foil changes color when pressure is applied in a specific location. The pressure foil can be used to calculate the applied force, by analyzing the density of the colored pixels. Using the pressure chart as provided by the manufacturer of the foil, the pressure value corresponding to the density can be determined. In order to calculate the total force on the joystick, the pressure is multiplied by the surface area of the joystick head.

During the test, the instrument was placed on a support that constrained the base of the handle, kept the shaft in straight position, and left the end-effector free to move. The test was performed by one of the authors and repeated three times per load condition. Although the joystick has a circular flat head with a diameter of 20 mm, we used a square piece of foil for the joystick analysis to avoid false imprints while placing and removing the foil during the test. Only the circular area of the pressure foil corresponding to the joystick head was analyzed. The acquired imprints on the pressure foil were digitalized using a calibrated scanner (Canon Canonscan LiDE 110) and analyzed using Matlab R2020a in order to find the corresponding density. We translated the images into black-and-white, with a threshold of 0.8, as used in previous studies [47] where the black pixels represented the colored locations (Figure 7.9b-c). Then the images were masked with a circle with the same diameter as the joystick head (Figure 7.9d). The digitalized figures were divided into nine portions to analyze the force distribution on the joystick, indicating on which part of the joystick the most pressure was applied by the user, see Figure 9e-f. The average black-pixel density over the three repetitions was calculated per portion and normalized for the total number of pixels.

Results

Figure 7.10a shows the pressure concentration per portion for the different load conditions. For all load conditions, the black-pixel density peaks on the edges of the flat head, especially in the top right and bottom left corner (portions 4 and 7), whereas in the central vertical portions (2, 5, and 8), the applied pressure reaches the lowest

value.

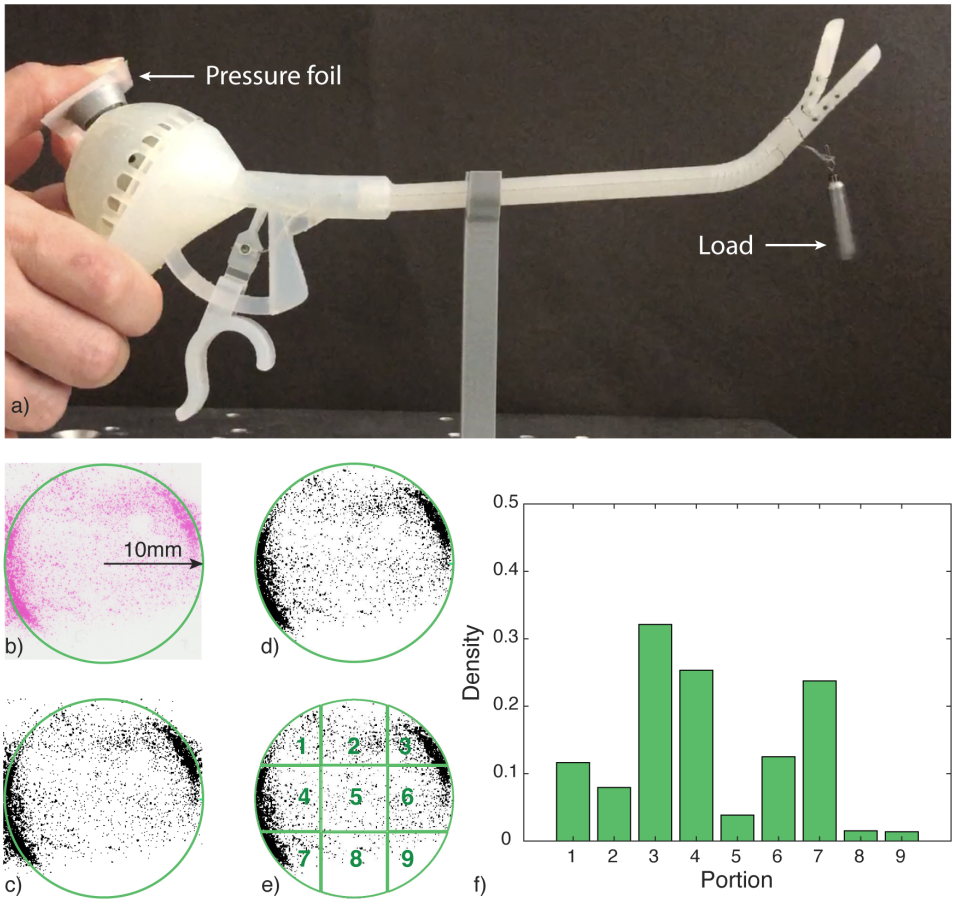

Figure 7.9: Method of force analysis on the joystick during steering. The example shown in this figure is the first repetition at the no load condition. a) Set-up of the steering force measurements. b) Scan of the imprinted pressure foil. The green circle represents the joystick area, the pink color shows the pressure distribution. c) Black-and-white conversion of the scanned foil. d) Applied mask used to analyze the circular area corresponding to the joystick area. e) Segmentation of the pressure foil into nine portions. f) Density of the black pixels per portion for the pressure foil for the no load condition.

7

Subsequently, we analyzed the density of the colored pixels for the entire measured area for the different load conditions (Figure 7.10b). The plot shows that there are no significant differences in black-pixel density (D) when increasing the load: D_{0steer} = 0.17 ± 0.05, D_{5steer} = 0.09 ± 0.04, $D_{10steer}$ = 0.12 ± 0.03, $D_{20steer}$ = 0.10 ± 0.02. Based on the density of the black pixels and the known surface area of the joystick head, we calculated the applied force using the pressure chart given by the manufacturer. The applied force was between 12.5 N and 23.5 N, considering the 10 mm radius of the joystick head. These results indicate that the user does not

need to increase the applied force to steer the joystick when the load increases in the measured range.

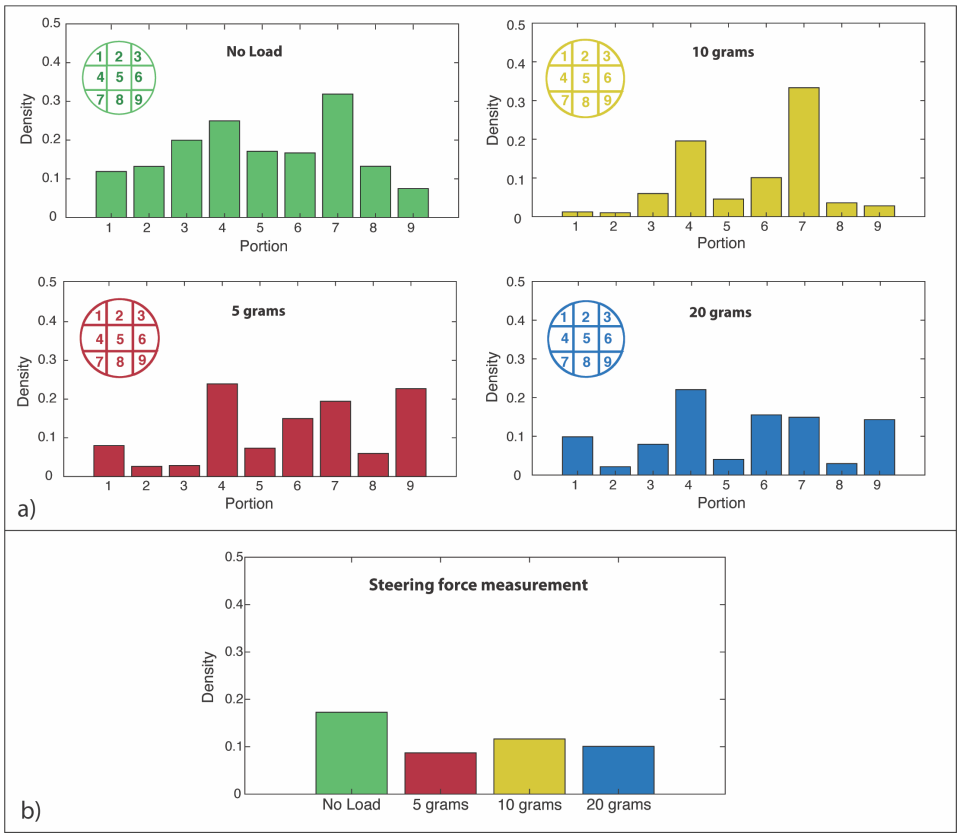

Figure 7.10: Steering force measurement. a) Average of the black-pixel density per portion for each tested condition: no load (green), 5 grams (red), 10 grams (yellow), and 20 grams (blue) applied load. b) Average of the black-pixel density for each load condition on the entire area of the pressure foil.

7.4.3. Grasping force test

Method

Another important aspect during surgery is the force applied by the user in relation to the force at the gripper used to grasp the tissue, i.e., the efficiency of the instrument. To evaluate the grasping functionality in different scenarios, we tested the prototype on artificial silicon-based tissue (DOTFOX Snc, Siena, Italy) with three different thicknesses: 1-2 mm, 2-3 mm, and 3-4 mm. We used a set-up similar to the one used for the steering force measurement (Figure 7.11). Since the pressure foil is one-sided and the grasping force on both jaws of the gripper is identical when gripping, we decoupled the cables actuating the lower jaw of the gripper from the trigger and fixed the lower jaw onto customized support to prevent it from moving. Moreover,

we placed a rigid tube around the steerable segment to prevent bending and analyze only the grasping functionality. We placed the artificial tissue and a piece of pressure foil with a minimum sensitivity of 0.006 MPa (5LW Fujifilm Prescale) between the jaws. The forces exerted by the user on the trigger were also measured using the same type of pressure foil. To digitalize and analyze the acquired imprints, we used the same methodology as for the imprints of the steering test described in Section 7.4.2.

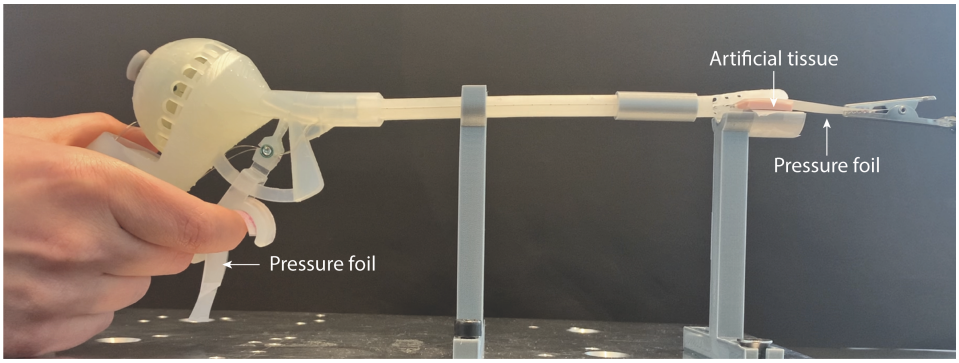

Figure 7.11: Set-up of the grasping force measurement.

Results

The imprints for the gripper show that the pressure was concentrated at the proximal side, close to the steerable segment (portions 7, 8, and 9). For the trigger, the pressure was equally distributed among all the portions with a slightly smaller concentration on the top part of the trigger (portions 1 and 3), see Figure 7.12.

Using the average of the black-pixel density and the surface area of the gripper and the trigger, we calculated the applied force using the pressure chart given by the manufacturer. To calculate the total force exerted by the gripper, we only used portions 7, 8, and 9, since the black-pixel density was close to zero for the gripper on the top and central parts. Therefore, the surface area of the other portions was not included in the calculation to obtain a more realistic value. The average black-pixel density (D) for portions 7,8 and 9 was $D_{1\text{-}2gripper}$=0.04 ± 0.01 for 1-2 mm, $D_{2\text{-}3gripper}$=0.06 ± 0.01 for 2-3 mm, and $D_{3\text{-}4gripper}$=0.09 ± 0.01 for 3-4 mm tissue thickness. The average black-pixel density for the trigger was $D_{1\text{-}2hand}$=0.24 ± 0.001 for 1-2 mm, $D_{2\text{-}3hand}$= 0.21 ± 0.03 mm for 2-3 mm, and $D_{3\text{-}4hand}$=0.27 ± 0.07 for 3-4 mm tissue thickness (Figure 7.13). Based on these values, the force generated by the gripper on the tissue samples was between 1 N and 4.4 N, and the force applied by the user on the trigger was between 10.8 N and 13.2 N. We calculated that the mechanical efficiency, and therefore the efficiency of our instrument, ranges between 10% and 30%.

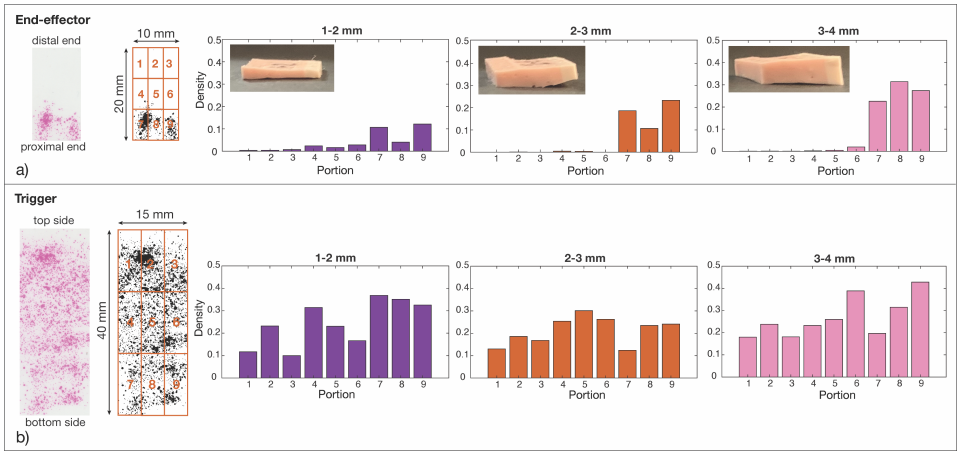

Figure 7.12: Grasping force measurements. From left to right: example of a scan of the imprinted pressure foil for 2-3 mm condition; the segmentation of the corresponding scanned foil converted into a black-and-white image; average of the black-pixel density per portion for each tested condition: 1-2 mm (purple), 2-3 mm (orange), and 3-4 mm (pink) tissue thickness. a) Gripper results. b) Trigger results.

7.5. Discussion

7.5.1. Production and customization

3D-GriP was designed for use as a disposable instrument; therefore, the production process must be as fast and simple as possible. A non-assembly design can save time and costs for the total production process. In our design, the trigger mechanism is completely non-assembly, due to the use of compliant joints. For the fastest route to the total assembly of the instrument, we decided to produce the joystick mechanism out of three separate parts, which gave us access to remove supports and excess material, and place the cables through the instrument. The separate parts can be positioned easily and snapped into place. The solutions that we used for the fastest and simplest assembly can be summarized as the following design rules: 1) make use

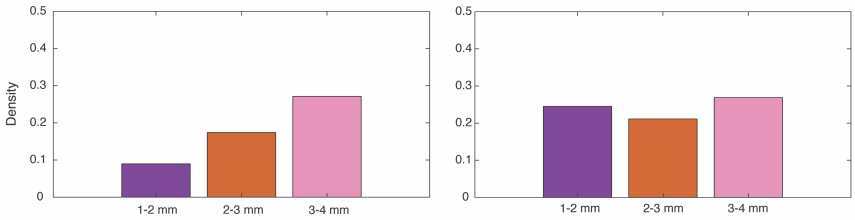

Figure 7.13: Average black-pixel concentration for the grasping force measurements. Left, the average of the black-pixel concentration of the gripper considering portions 7, 8, and 9. Right, the black-pixel concentration of the trigger for each tested tissue thickness:1-2 mm (purple), 2-3 mm (orange), and 3-4 mm (pink).

of compliant joints to create monolithic parts; 2) consolidate parts where possible; 3) 'expose' moving parts to ensure the material can be drained and supports removed; 4) when an assembly is unavoidable, make use of smart solutions such as snap-fit connections for quick and easy assembly.

Being 3D printed, the instrument can be customized to the patient, the procedure, and the needs of the surgeon, for instance, by changing the gripper into a needle holder or fenestrated grasping forceps. Customization of the handle depending on the surgeon's hand size is also possible. Although we took care in our handle to adhere to ergonomic principles, it is impossible to design one handle that fits all. On the other hand, it is not necessary to change the entire design for each surgeon, since the main functionality remains the same. We addressed the customization by enabling certain specific dimensions to be easily adjustable. For instance, the length and width of the handle can be adjusted to the palm size of the surgeon, and the distance of the trigger to the handgrip can be adjusted to the length of the index finger. In addition, by mirroring the trigger design, it can be changed from right- to left-handed. For future implementation, we envision surgeons recording some of their relevant hand measurements in a personal portfolio, which can be easily implemented in the CAD design and 3D printed on-demand to create surgeon-specific instruments.

7.5.2. Performance and improvements

The low bending stiffness of the steerable segment reduces the forces required for steering, and increases the ease of maneuverability. In the steering force test, we found that the force required for steering the end-effector is between 12.5 N and 23.5 N, with the maximum applied force measured in no load condition. This result is counter-intuitive, but since this was the first condition tested, might be explained by the user's inexperience, which led to an excessive force being applied. In fact, excluding the no load condition, the applied force ranges between 12.5 and 15.7 N. The maximum measured force applied by the user on the trigger to operate the gripper was 13.2 N. This force is comparable to the measured forces as applied by the surgeon while using conventional instruments in a laparoscopic setting that varies between 9 and 15 N for gentle pinch [42, 48, 49]. No data are available on the force required to steer the end-effector on commercially available steerable handheld laparoscopic instruments with fully mechanical actuation. In a future study, it would be interesting to perform a test to compare the results of the 3D-Grip to commercially available laparoscopic devices, especially related to the steering force.

An important aspect related to the surgeon's comfort during laparoscopic surgery is the handle-to-tip force ratio [50]. In the grasping force test, we measured the grasping efficiency as the control-force-to-gripper-force ratio. We found that the efficiency ranges between 10% and 30%. This efficiency is comparable to common laparoscopic graspers [51]. However, this efficiency should still be improved: a higher force transmission ratio has been associated with lower muscle fatigue in the forearm, which improves the surgeon's comfort [50], higher force feedback [52], as well as prevention of tissue slipping from the gripper, which improves performance [49]. A possible reason for a low force transmission ratio is the friction of the cables in the

cable channels. Since the cable channels are difficult to clean after printing, the leftover resin may remain in the channels, which cannot be easily removed or cured. Additional drainage holes and more thorough cleaning could aid in this respect.

Using the pressure foil, we were also able to evaluate the pressure distribution on the joystick, trigger, and gripper jaws. The imprints of the joystick showed that the pressure concentration was higher on the edges, especially on the top/right and bottom/left. This result seems to indicate that more force is required for steering in the up- and downwards direction compared to the left/right direction, which can be attributed to the applied load. More research is needed to indicate whether a more equal pressure distribution can be obtained with for instance a customized joystick head. For the trigger imprints, the concentration was equally distributed over all the portions. The imprints of the gripper showed a pressure concentration of the forces at the proximal end of the jaws, which caused localized pinch force on the tissue. The limited areas of the imprints in the other portions of the gripper where too small to evaluate using the pressure foil, considering the supplier's guidelines. To quantitatively evaluate this pressure, a possible solution would be using a pressure sensor on the gripper such as the one used by Jin *et al.* [53]. An interesting option to obtain a uniform distribution of the gripper forces would be an adaptable gripper such as the one proposed by Sun *et al.* [23].

7.5.3. Limitations and future studies

The verification of 3D-GriP showed that it functions comparably to existing laparoscopic instruments; however, there are some limitations to the design and tests described in this article. Since our instrument was designed for disposable use, we did not carry out a dedicated fatigue test for the compliant joints. However, we observed the compliant joint behavior and durability after repeated use of the prototype in both steering and grasping during the tests. The prototype did not experience any sign of fatigue or breakage, however more testing is required to determine the joint fatigue and optimal dimensions for the compliant joints.

For the fixation of the cables, we initially used thread inserts and dog point screws. However, after executing the tests, the metal thread inserts in the trigger tore the material apart. In future instruments, we will experiment with alternative methods of fixating the cables, for instance by applying a small amount of the same photopolymer resin used to print the instrument at the fixation point and letting it cure. The advantage of this method is that it is quicker to apply than the thread inserts and screws, and requires fewer parts and materials. Testing should find out whether this fixation will hold up in repeated use.

The design of the pistol-grip handle is based on well-documented ergonomic principles. However, we did not perform any tests with users to verify its comfort level. We suggest that future tests require multiple participants, preferably surgeons as they are familiar with laparoscopic instruments, with an equal number of instruments customized to their specific hand sizes in order to verify its potential as an ergonomic instrument.

The 3D printer used for our design was a Form 3B, which is based on SLA tech-

nology and optimized for biocompatible materials. However, biocompatible materials that also have the possibility to be sterilized with different technologies, such as autoclave or gamma radiation, are limited. Moreover, since we found that the available biocompatible materials were too brittle for use in the compliant flexures, we decided to print our prototype using non-biocompatible materials to analyze the functionality of our design. In the future, we hope that new biocompatible and sterilizable materials will become available with characteristics similar to the materials we used in this study, for truly biocompatible 3D printed surgical instruments.

7.6. Conclusion

In this work, we have proposed a design of a handheld steerable instrument for MIS that can be fully 3D printed. The new steerable instrument, called 3D-GriP, is fully mechanically actuated using cables. It complies with standard specifications for laparoscopic instruments, such as an omnidirectional bending between 40 and 60 degrees, a gripper opening of 60 degrees, and a shaft diameter of 8 mm. We designed a handle for the instrument based on ergonomic principles, which allows for single-hand control of both grasping and steering. Using AM allows personalizing the handle to the surgeon's preference by adjusting specific dimensions in the CAD model. This flexibility allows the production of customized handles to increase the surgeon's comfort. In addition, the use of AM enables a minimal part count by making use of compliant joints and snap-fit connectors. We tested the required forces to steer and operate the instrument by measuring both the input actuation force and the output grasping force. The results show that the operating forces on the handle remain below 15 N for both steering and grasping, resulting in a grasping efficiency of 10-30% for the force transmission. Although the instrument was developed for laparoscopy, our design can be easily adapted to other fields of minimally invasive surgery.

References

[1] A. Parisi, D. Reim, F. Borghi, N. T. Nguyen, F. Qi, A. Coratti, F. Cianchi, M. Cesari, F. Bazzocchi, O. Alimoglu, *et al.*, *Minimally invasive surgery for gastric cancer: a comparison between robotic, laparoscopic and open surgery,* World journal of gastroenterology **23**, 2376 (2017).

[2] V. Velanovich, *Laparoscopic vs open surgery,* Surgical endoscopy **14**, 16 (2000).

[3] F. Jelínek, R. Pessers, and P. Breedveld, *DragonFlex Smart Steerable Laparoscopic Instrument,* Journal of Medical Devices **8**, 015001 (2014).

[4] R. Prewitt, V. Bochkarev, C. L. McBride, S. Kinney, and D. Oleynikov, *The patterns and costs of the da vinci robotic surgery system in a large academic institution,* Journal of robotic surgery **2**, 17 (2008).

[5] P. L. Anderson, R. A. Lathrop, and R. J. Webster III, *Robot-like dexterity without computers and motors: a review of hand-held laparoscopic instruments with wrist-like tip articulation,* Expert review of medical devices **13**, 661 (2016).

[6] P. L. Anderson, R. A. Lathrop, S. D. Herrell, and R. J. Webster, *Comparing a mechanical analogue with the da vinci user interface: Suturing at challenging angles,* IEEE robotics and automation letters **1**, 1060 (2016).

[7] DEAM, *Laproflex steerable laparoscopic instrument,* (2019), https://www.deam.com/product-details/laproflex/, Accessed: 2020-05-09.

[8] J. Arata, Y. Saito, and H. Fujimoto, *Outer shell type 2 dof bending manipulator using spring-link mechanism for medical applications,* in *2010 IEEE International Conference on Robotics and Automation* (IEEE, 2010) pp. 1041–1046.

[9] S. D. Choi, *A review of the ergonomic issues in the laparoscopic operating room,* Journal of Healthcare Engineering **3**, 587 (2012).

[10] U. Matern and P. Waller, *Instruments for minimally invasive surgery,* Surgical endoscopy **13**, 174 (1999).

[11] F. M. Sánchez-Margallo and J. A. Sánchez-Margallo, *Ergonomics in laparoscopic surgery,* Laparoscopic Surgery. Rijeka: InTech , 105 (2017).

[12] L. Santos-Carreras, M. Hagen, R. Gassert, and H. Bleuler, *Survey on surgical instrument handle design: ergonomics and acceptance,* Surgical innovation **19**, 50 (2012).

[13] T. Emam, T. Frank, G. Hanna, and A. Cuschieri, *Influence of handle design on the surgeon's upper limb movements, muscle recruitment, and fatigue during endoscopic suturing,* Surgical endoscopy **15**, 667 (2001).

[14] A. Park, G. Lee, F. J. Seagull, N. Meenaghan, and D. Dexter, *Patients benefit while surgeons suffer: an impending epidemic,* Journal of the American College of Surgeons **210**, 306 (2010).

[15] R. HM Goossens, MA van Veelen, *Assessment of ergonomics in laparoscopic surgery,* Minimally Invasive Therapy & Allied Technologies **10**, 175 (2001).

[16] A. G. Gonzalez, D. R. Salgado, and L. G. Moruno, *Optimisation of a laparoscopic tool handle dimension based on ergonomic analysis,* International Journal of Industrial Ergonomics **48**, 16 (2015).

[17] Y. Kim, S. S. Cheng, and J. P. Desai, *Towards the development of a spring-based continuum robot for neurosurgery,* Medical Imaging 2015: Image-Guided Procedures, Robotic Interventions, and Modeling **9415**, 94151Q (2015).

[18] C. Culmone, G. Smit, and P. Breedveld, *Additive manufacturing of medical instruments: A state-of-the-art review,* Additive Manufacturing **27**, 461 (2019).

[19] J. S. Cuellar, G. Smit, D. Plettenburg, and A. Zadpoor, *Additive manufacturing of non-assembly mechanisms,* Additive Manufacturing **21**, 150 (2018).

[20] K. Lussenburg, A. Sakes, and P. Breedveld, *Design of non-assembly mechanisms: A state-of-the-art review,* Additive Manufacturing , 101846 (2021).

[21] T. L. Thomas, V. Kalpathy Venkiteswaran, G. Ananthasuresh, and S. Misra, *Surgical applications of compliant mechanisms: A review,* Journal of mechanisms and robotics **13**, 020801 (2021).

[22] J. S. Cuellar, G. Smit, A. A. Zadpoor, and P. Breedveld, *Ten guidelines for the design of non-assembly mechanisms: The case of 3d-printed prosthetic hands,* Proceedings of the Institution of Mechanical Engineers, Part H: Journal of Engineering in Medicine **232**, 962 (2018).

[23] Y. Sun, Y. Liu, L. Xu, Y. Zou, A. Faragasso, and T. C. Lueth, *Automatic design of compliant surgical forceps with adaptive grasping functions,* IEEE Robotics and Automation Letters **5**, 1095 (2020).

[24] I. Gibson, D. W. Rosen, and B. Stucker, *Additive Manufacturing Technologies: Rapid Prototyping to Direct Digital Manufacturing* (Springer US, Boston, 2010) pp. 1–459.

[25] L. Toth, A. Schiffer, M. Nyitrai, A. Pentek, R. Told, and P. Maroti, *Developing an antispastic orthosis for daily home-use of stroke patients using smart memory alloys and 3D printing technologies,* Materials & Design **195**, 109029 (2020).

[26] S. M.P., R. Ranganathan, and A. Pugalendhi, *Individual customization strategy accomplished by developing prototype of a laparoscopic forceps handle using additive manufacturing,* Rapid Prototyping Journal **26**, 689 (2020).

[27] A. G. González, D. R. Salgado, L. García Moruno, and A. Sánchez Ríos, *An ergonomic customized-tool handle design for precision tools using additive manufacturing: a case study,* Applied Sciences **8**, 1200 (2018).

[28] A. González, J. Barrios-Muriel, F. Romero-Sánchez, D. Salgado, and F. Alonso, *Ergonomic assessment of a new hand tool design for laparoscopic surgery based on surgeons' muscular activity,* Applied Ergonomics **88**, 103161 (2020).

[29] J. A. Sanchez-Margallo, A. Gonzalez Gonzalez, L. Garcia Moruno, J. C. Gómez-Blanco, J. B. Pagador, and F. M. Sanchez-Margallo, *Comparative study of the use of different sizes of an ergonomic instrument handle for laparoscopic surgery,* Applied Sciences **10**, 1526 (2020).

[30] F. M. Sánchez-Margallo, J. A. Sánchez-Margallo, and A. Szold, *Handheld devices for laparoscopic surgery,* New horizons in laparoscopic surgery , 75 (2018).

[31] A. Schneider and H. Feussner, *Chapter 7 - operative (surgical) laparoscopy,* in *Biomedical Engineering in Gastrointestinal Surgery*, edited by A. Schneider and H. Feussner (Academic Press, 2017) pp. 269–327.

[32] R. Zhu, M. Maréchal, I. Yamamoto, M. J. Lawn, T. Nagayasu, and K. Matsumoto, *Evaluation of laparoscopic forceps jaw contact pressure and distribution using pressure sensitive film,* Computer Assisted Surgery **24**, 105 (2019).

[33] L. L. Howell, *Compliant mechanisms,* in *21st century kinematics* (Springer, 2013) pp. 189–216.

[34] J. Dearden, C. Grames, B. D. Jensen, S. P. Magleby, and L. L. Howell, *Inverted l-arm gripper compliant mechanism,* Journal of Medical Devices **11** (2017).

[35] S. Kota, K.-J. Lu, Z. Kreiner, B. Trease, J. Arenas, and J. Geiger, *Design and application of compliant mechanisms for surgical tools,* ASME J Biomech Eng. **127**, 981 (2005).

[36] J. Lassooij, N. Tolou, G. Tortora, S. Caccavaro, A. Menciassi, and J. Herder, *A statically balanced and bi-stable compliant end effector combined with a laparoscopic 2 dof robotic arm,* Mechanical Sciences **3**, 85 (2012).

[37] H. Chen, L. Zhang, D. Zhang, P. Zhang, and Z. Han, *Bioinspired surface for surgical graspers based on the strong wet friction of tree frog toe pads,* ACS applied materials & interfaces **7**, 13987 (2015).

[38] C. Culmone, P. W. Henselmans, R. I. van Starkenburg, and P. Breedveld, *Exploring non-assembly 3d printing for novel compliant surgical devices,* Plos one **15**, e0232952 (2020).

[39] K. D. Tung, R. M. Shorti, E. C. Downey, D. S. Bloswick, and A. S. Merryweather, *The effect of ergonomic laparoscopic tool handle design on performance and efficiency,* Surgical endoscopy **29**, 2500 (2015).

[40] C. Fan, H. Clogenson, P. Breedveld, J. J. van den Dobbelsteen, and J. Dankelman, *Comparison of two control methods for minimally invasive surgical instruments,* Journal of Medical Devices **6** (2012).

[41] L. M. Okken, M. K. Chmarra, E. Hiemstra, F. W. Jansen, and J. Dankelman, *Assessment of joystick and wrist control in hand-held articulated laparoscopic prototypes,* Surgical endoscopy **26**, 1977 (2012).

[42] M. Van Veelen, D. Meijer, I. Uijttewaal, R. Goossens, C. Snijders, and G. Kazemier, *Improvement of the laparoscopic needle holder based on new ergonomic guidelines,* Surgical Endoscopy and Other Interventional Techniques **17**, 699 (2003).

[43] C. Fan, D. Dodou, and P. Breedveld, *Review of manual control methods for handheld maneuverable instruments,* Minimally Invasive Therapy & Allied Technologies **22**, 127 (2013).

[44] M. Van Veelen, D. Meijer, R. Goossens, and C. Snijders, *New ergonomic design criteria for handles of laparoscopic dissection forceps,* Journal of Laparoendoscopic & Advanced Surgical Techniques **11**, 17 (2001).

[45] A. R. Tilley *et al.*, *The measure of man and woman: human factors in design* (John Wiley & Sons, 2001).

[46] J. Gardan, *Additive manufacturing technologies: state of the art and trends,* International Journal of Production Research **54**, 3118 (2016).

[47] P. van Assenbergh, C. Culmone, P. Breedveld, and D. Dodou, *Implementation of anisotropic soft pads in a surgical gripper for secure and gentle grip on vulnerable tissues,* Proceedings of the Institution of Mechanical Engineers, Part H: Journal of Engineering in Medicine **235**, 255 (2020).

[48] E. Heijnsdijk, A. Pasdeloup, J. Dankelman, and D. Gouma, *The optimal mechanical efficiency of laparoscopic forceps,* Surgical endoscopy **18**, 1766 (2004).

[49] E. P. Westebring-van der Putten, J. J. van den Dobbelsteen, R. H. Goossens, J. J. Jakimowicz, and J. Dankelman, *Effect of laparoscopic grasper force transmission ratio on grasp control,* Surgical endoscopy **23**, 818 (2009).

[50] R. Berguer, S. Gerber, G. Kilpatrick, and D. Beckley, *An ergonomic comparison of in-line vs pistol-grip handle configuration in a laparoscopic grasper,* Surgical endoscopy **12**, 805 (1998).

[51] W. Sjoerdsma, J. Herder, M. Horward, A. Jansen, J. Bannenberg, and C. Grimbergen, *Force transmission of laparoscopic grasping instruments,* Minimally Invasive Therapy & Allied Technologies **6**, 274 (1997).

[52] J. L. Herder, M. J. Horward, and W. Sjoerdsma, *A laparoscopic grasper with force perception,* Minimally Invasive Therapy & Allied Technologies **6**, 279 (1997).

[53] X. Jin, J. Zhao, M. Feng, L. Hao, and Q. Li, *Snake-like surgical forceps for robot-assisted minimally invasive surgery,* The International Journal of Medical Robotics and Computer Assisted Surgery **14**, e1908 (2018).

Figure 7.14: Video of the omnidirectionality and the motion smoothness of the 3D-Grip

Part 3

Surgical Grippers

8

3D Printed Surgical Grasper for Chordae Tendineae Repair

Published as:
Culmone C., Ali A., Scali M., Menciassi A., Breedveld P. "ChoRe: A Device for Trans-Catheter Chordae Tendineae Repair".Proceedings of the Institution of Mechanical Engineers, Part H: Journal of Engineering in Medicine, 233.7 (2019), 712-722.

Abstract

This work focuses on the design of a new device (called Chore) to place artificial chords in the mitral valve structure during a trans-catheter procedure. The aim of the device is to restore the correct functionality of the valve and solve mitral valve regurgitation, that is a common consequence of chordae tendineae rupture. An analysis of the requirements was carried out and used to design and develop a first functional prototype. The resulting device was able to connect artificial chords at the posterior leaflet of the mitral valve and at the apex of the left ventricle, also allowing the control of the artificial chord length. The ChoRe was tested ex-vivo in bovine hearts. The qualitative assessment of the ChoRe focused on the performance of the device and preliminary evaluation of the procedure time. Results demonstrated that the device is able to create a top and bottom fixation in an average time of 3.45±1.44 minutes. Future improvements will focus on enhancing the connection at the leaflet, as well as the overall functionality, in order to guarantee better control of the artificial chord length. This work shows future potentials for more patient-specific treatments in trans-catheter scenarios for mitral valve repair.

8.1. Introduction

8.1.1. Mitral valve regurgitation

Heart disease is a leading cause of death in industrialized countries. One of the most prevalent heart valve dysfunctions, which causes disturbed blood flow through the heart, is mitral regurgitation in which blood leaks backward through the mitral valve between the left atrium and the left ventricle [1]. Mitral regurgitation increases with age and occurs in 10% of people older than 75 [2]. Figure 8.1 shows a cross-section of the mitral valve structure with the so-called chordae tendineae, i.e. branched chords that connect the mitral valve leaflets to the papillary muscles that form part of the ventricle wall [3]. One of the main causes of mitral regurgitation is a lengthening of the chordae tendineae, resulting in the valve to open in the wrong direction. In mitral regurgitation, the leaflets of the valve do not close completely and are not able to reach the so-called coaptation, which corresponds to the ideal closure of the valve. Chordae tendineae elongation or breakage occurs for 70% in the posterior leaflet [4].

8.1.2. State-of-the-art interventional techniques

Various surgical approaches have been developed to treat mitral regurgitation, ranging from replacing the full valve system to restoring the function by repairing a single element of the valve. During replacement, the diseased mitral valve is substituted by an artificial valve consisting of the annulus and the leaflets made of biological or artificial materials [6, 7]. During repair, single elements of the mitral valve, such as the leaflets or the chordae tendineae are restored in their original functionalities [8]. Both the replacement and the repair approach can be conducted via traditional open-

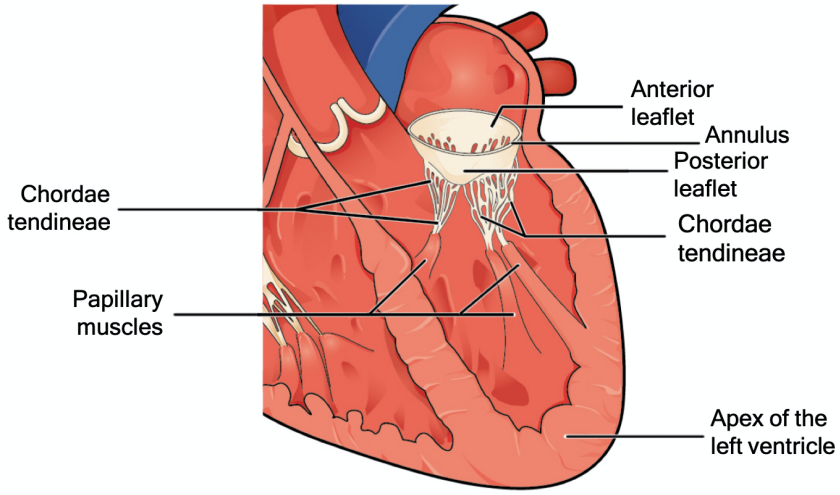

Figure 8.1: Mitral valve structure with the principal elements: the anterior and posterior leaflet, the annulus, the chordae tendineae, the papillary muscles, and the apex of the left ventricle. Adapted from [5].

heart surgery, with a sternal incision of approximately 240 mm [9], or by minimally invasive cardiac surgery (MICS), in which a smaller incision of approximately 75 mm is made under the right breast [10].

In open-heart surgery the surgeon can directly reach the target structures, has freedom of hand movement and a direct view of the operation site. These elements are limited in MICS. In this case, the loss of space and degrees of freedom make the procedure more complex and, in some cases, lead to a longer operative time [11], even if many methodologies such as trans-esophageal echocardiography guidance (TEE) [12, 13] have been developed to help the surgeon in visualizing the operative site. Both open surgery and MICS are performed with the use of cardiopulmonary bypass, a technique that temporarily substitutes the functions of heart and lungs during surgery.

However, due to the invasiveness of the surgery, in almost 50% of patient with mitral valve regurgitation, the surgery is not performed due to the high risk of mortality related to the advanced age and comorbidities [14]. In this scenario, innovative approaches such as trans-apical (a 45 mm incision to reach the apex [15]) and trans-catheter (catheters are guided through the blood vessels to reach the target point, and thereby limiting the invasiveness of the procedure for the patient with an incision in the skin only 5-6 mm long [16, 17]) techniques are gaining momentum. Especially in the trans-catheter techniques, significative successful results have been reported in high-risk patients [18]. Due to a lower level of invasiveness, the patient is generally under local anesthesia in beating heart condition, thus avoiding long recovery time, post-procedural complications, and lowering risks of infection [9, 12, 15].

Even though mitral valve replacement can be achieved successfully, a majority of cardiac surgeons prefer a repair approach in which the valve function is restored with longer durability and without a need for long drug therapy after surgery [19, 20]. Moreover, the damage often involves only one element of the mitral valve, such as the chordae tendineae, which is the one that needs to be repaired. Devices developed and tested, such as the Neochord (Neochord, Inc., St. Luis Park, MN, USA) [21], TSD-5 (Harpoon Medical, Inc. Baltimore, MD, USA) [22], V-chordal off-Pump [23] and Babic device [24], use the trans-apical approach to repair the chordae tendineae. In the trans-apical technique performed by the Neochord, the device is inserted through the apex of the heart to enter the ventricle. Then, the device attaches the artificial chords to the leaflet. Finally, the artificial chords are fixed to the outer wall of the ventricle apex. The trans-apical technique performed by the Neochord device is the only one clinically accepted and is currently in the randomized clinical trial phase [25].

However, the trans-apical approach still needs an incision in the skin, of approximately 45 mm, and in the heart, to insert the 8 mm instrument [26]). Moreover, despite promising results in trans-catheter mitral valve implantation (TMVI) [27] and annulus and leaflet repair [28–31], there is no clinically accepted device that is capable of performing the reconstruction of the chordae tendineae via the trans-catheter route.

Therefore, in this work we design a new device to repair the chordae tendineae, mainly focusing on the working principle of the device to place artificial chords at the required sites in a trans-catheter scenery. Therefore, this work presents the most distal segment of the entire device. The design of the catheter and the guiding sheath

for insertion of the device, as well as the method of positioning the device into the ventricle, are out of our scope at this stage.

8.2. Design of the ChoRe

8.2.1. Conventional procedure

The technique for the repair of chordae tendineae has continuously changed over the years, but, regardless of the level of invasiveness, the main steps of the procedure are similar in all methods [32]. The damaged chordae tendineae are left in place and do not need to be removed, while new artificial chords (usually made of artificial biocompatible material) are installed to repair the valve. In the first step, the artificial chords are fixed to the bottom of the ventricle, the papillary muscle, or the apex of the ventricle (see Figure 8.1). The artificial chords are then connected to the leaflet, their length is adjusted and fixed, and a leakage test is carried out [33]. The number of artificial chords generally placed comes to a maximum of ten [34], with an average of three, depending on the valve defect [35]. One of the most important factors affecting the end-result of the intervention is that the artificial chord length has to be estimated by means of echocardiographic images and adjusted during the procedure depending on the patient's anatomy. The length of the artificial chords is generally in the range of 14-21 mm [34] if the chord is attached to the papillary muscles, or 53-85 mm [36] if the chord is attached to the apex of the ventricle. Moreover, the artificial chords have to be attached to a safe and solid connection to the free edge of the leaflet and the bottom of the ventricle [37, 38]. It is extremely important not to damage the healthy chordae tendineae or the mitral valve, considering that the prolapsing leaflet tissue is very thin and fragile, while the papillary muscle is thick and rather stable [32].

8.2.2. Design requirements

The knowledge of the conventional procedure led to a new design for an innovative device capable of repairing the chordae tendineae in a trans-catheter scenario. The general idea behind the device is that it has to be used in combination with a dedicated steerable catheter that enables the device to reach the target site. The device has been designed considering the possibility of performing measurements in a pre-operative phase by means of echocardiographic images, in order to estimate the required length of the artificial chords. We decided to use an anchorage at the apex of the heart due to the difficulties involved in grasping the papillary muscles having a width of approximately 15 mm [39]. At the start of the design process, we established a set of design requirements:

Functions

- The device must connect an artificial chord to the bottom of the ventricle.
- The device must connect an artificial chord to the mitral valve leaflet.
- The device must adjust the length of the artificial chord depending on the patient's anatomy.

Size constraints

- For insertion in the femoral vein, the inferior vena cava and the heart, the maximum diameter of the device should be 22 F (7.3 mm), as in currently available devices for interventions inside of the heart [40].
- The rigid length of the device must not exceed 25 mm, considering the average physiological size of an adult human heart and the curvature of the inferior vena cava blood vessel.
- The shape of the device must be smooth without any sharp edges.

The assumption here is that the procedure is performed using TEE and fluoroscopy guidance to visualize the surgical site [41] and starts right after the insertion of the device mounted on a catheter with a steerable guiding sheath which has been positioned in the left atrium through a trans-septal puncture. The steerable guiding sheath requires a deflection of approximately 90° to reach the perpendicular position in the left atrium [42]. Once the device reaches its position perpendicular to the plane of the mitral valve, the device is moved forward in order to reach the apex of the left heart through the left ventricle, Figure 8.2.

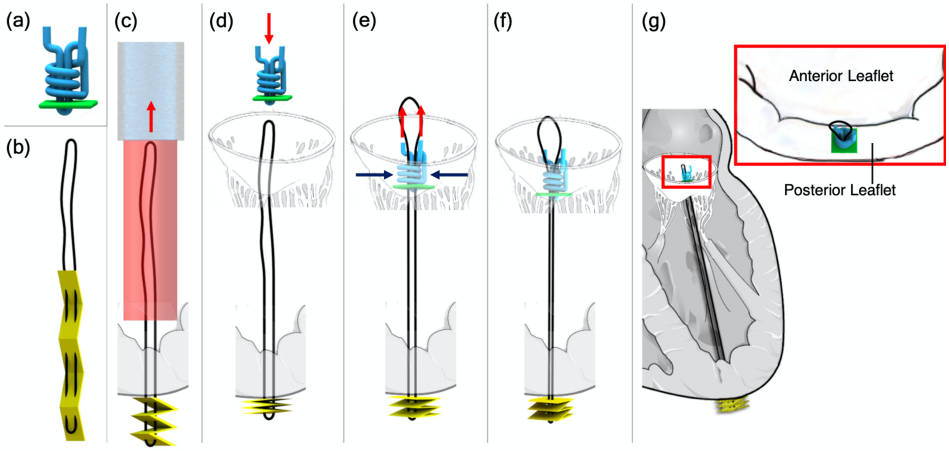

Figure 8.2: Sketches of the ChoRe implant: (a) The pre-constructed knot with the polyester thread in blue and the leaflet pledget in green; (b) The artificial chord with the ePTFE thread in black and the apex pledget in yellow. (c) The apex pledget, previously positioned into the device, is pushed through the ventricle wall using a cannula to create the apex fixation. The apex pledget folds into an accordion-shape due to the movement of the device from the apex to the leaflet and the interaction of the apex pledget with the ventricle wall; (d) the pre-constructed knot is pushed by the surgeon against the leaflet; (e-f) once the length is decided, the surgeon tightens the pre-constructed knot around the artificial chord to finalize the procedure; (g) sketch of the artificial chord installed in the left ventricle, the red box shows a close-up of the implant on the posterior leaflet. The red arrows represent the movements made by the surgeon while the blue arrows the tightening of the pre-constructed knot. The catheter (light blue) and the device (red) are shown only once for simplicity.

8.2.3. Overall design

The overall design of our device, called "ChoRe", was created in Solidworks 2015-2016. Its function relies on first creating the bottom connection at the ventricle wall and then ending with the top connection at the valve leaflet. The procedure can be divided into three main phases: (1) apex fixation, (2) leaflet fixation, (3) length adjustment. The most important component of the ChoRe is the "implant": the component that has to fix the regurgitation. The implant is composed out of two elements: an *artificial chord* and a *pre-constructed knot*, Figure 8.2.

The *artificial chord* is composed of an expanded polytetrafluoroethylene (ePTFE) thread in a loop configuration, black in Figure 8.2b, and an apex pledget (a piece of wad made of felt textile material), yellow in Figure 8.2b. The apex pledget is sewn with the ePTFE thread in a loop configuration and folded into an accordion-shape to allow deployment for creating a stable placement of the apex connection, as presented for a different purpose in Siminiak *et al.* [29], Figure 8.2c.

The *pre-constructed knot* is composed of a leaflet pledget, green in Figure 8.2a and a polyester thread, blue in Figure 8.2a. Inspired by the knot used in Ramponi *et al.* work [43], the pre-constructed knot is an adjustable fixation element at the leaflet side. The polyester thread creates a multiple loops knot using the leaflet pledget as support. The knot is tightened around the artificial chord only when the required chord length has been determined by the interventionist, Figures 8.2d-g. In addition to the implant, the ChoRe has been designed with ten components that can be grouped into three units: an apex fixation unit, a leaflet fixation unit, and a length adjustment unit, Figure 8.3.

Apex fixation unit

The apex fixation unit consists of a needle (1), a cannula (2), and a piston (3), Figure 8.3a. The piston and the cannula are both hollow and fit around the needle. The cannula, 2.3 mm in diameter, ends in a conical shape with an opening. Before the procedure, the cannula is preloaded with the needle, surrounded by the artificial chord. In the first step of the procedure, the needle is inserted through the apex of the heart to define the pathway for the other components. Once the needle is positioned, the cannula is pushed downward over the needle until the entire opening is pushed out of the ventricle wall. Reaching this position, the surgeon can push out the apex pledget by means of the piston to form the apex fixation. When the apex pledget closes in the accordion shape, it creates a solid fixation for the implant, thus preventing bleeding after the extraction of the cannula.

Leaflet fixation unit

The apex fixation unit fits into a dedicated channel of a leaflet clamp, composed of two parts (6 and 7). The leaflet clamp is part of the leaflet fixation unit including also an external shell (4), a thread support (6), and a miniature harpoon-shaped needle (8). The artificial chord, at one side connected to the apex to the heart, is at the other side kept in position in the leaflet clamp by the thread support and the external shell. In order to fix the artificial chord to the leaflet, the ChoRe system is moved upward from the apex to the leaflet. Here, the leaflet is clamped between parts 6

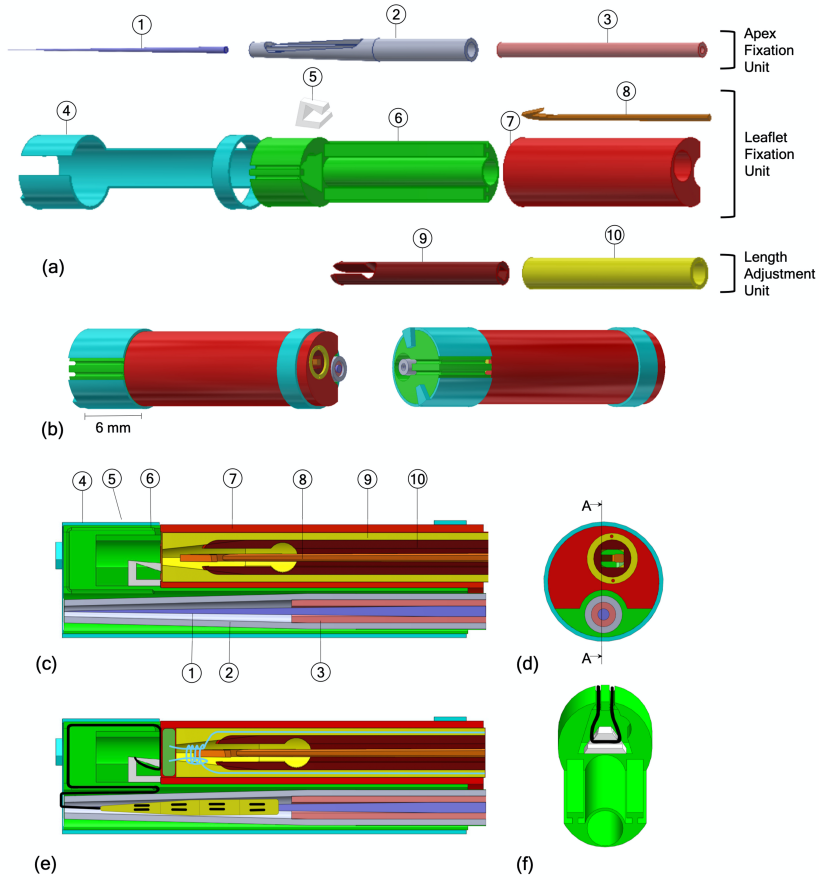

Figure 8.3: (a) Exploded view of the CAD ChoRe model; (1) Needle; (2) Cannula; (3) Piston; (4) External shell; (5) Thread support; (6-7) Leaflet clamp; (8) Harpoon-shaped needle; (9) Clamping tube; (10) Chord grasper; (b) CAD model of the assembled ChoRe device; (c) cross-section view of the CAD ChoRe model; (d) top view of the CAD ChoRe model; (e) cross-section view of the CAD model with the artificial chord, and the pre-constructed knot; (f) a detail of the internal structure of the leaflet clamp and the thread support holding the artificial chord.

and 7. The harpoon-shaped needle is then inserted and pushed through the leaflet to hook the artificial chord and to pull it up through the leaflet. The external shell is then rotated to release the artificial chord from the leaflet clamp.

Length adjustment unit

The length adjustment unit consists of a chord grasper (9) which can slide along the main axis into a clamping tube (10), Figure 8.3a. The main role of these components is to enable the surgeon to tune the length of the artificial chord. When the artificial chord has been pulled up through the leaflet, the harpoon-shaped needle is positioned above the chord grasper and the clamping tube. The harpoon-shaped needle can be

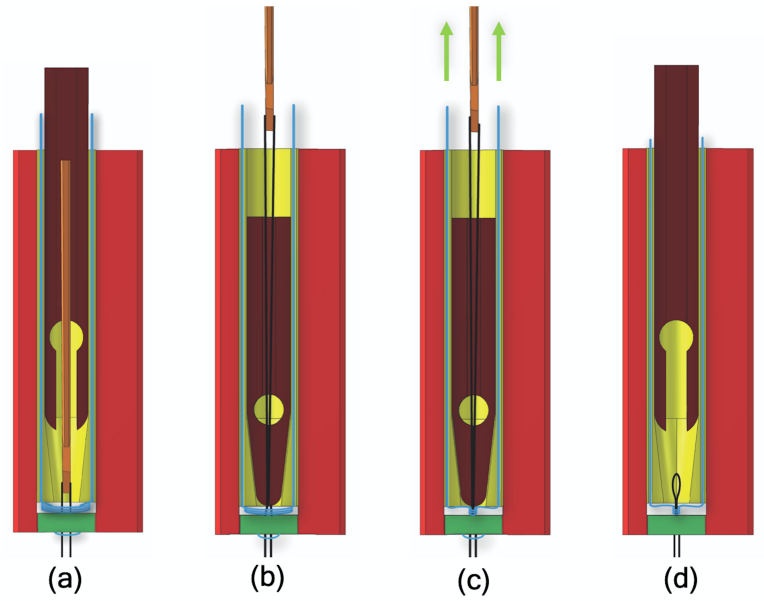

Figure 8.4: (a) The needle passes through the leaflet pledget after capturing the ePTFE thread; (b) the chord grasper closes around the ePTFE thread due to the clamping tube; (c) the pre-constructed knot is closed around the ePTFE thread to finally fix the implant; (d) the chord grasper releases the artificial chord, as well as the harpoon-shaped needle. In the sketches, the whole process is emphasized in displacements.

moved up and down relative to the leaflet to adjust the chord length under ultrasound imaging. During the adjusting, the chord grasper can be closed by pushing it out of the clamping tube, thereby temporarily fixing the chord and setting its length. At the correct chord length, the pre-constructed knot is fastened by pulling at both ends of the knot and the implant is completed. The two ends of the knot are then cut off once ChoRe is retracted, Figure 8.4.

The procedure described above can be summarized into the following 12 steps, Figure 8.5.

Apex fixation

1. The needle is pushed through the apex of the heart to creates the pathway for the cannula.
2. The cannula slides over the needle until the opening is all out of the ventricle wall.
3. The apex pledget is pushed out through the opening by the piston.
4. The needle, the cannula, and the piston are retracted into the leaflet clamp.

Leaflet fixation

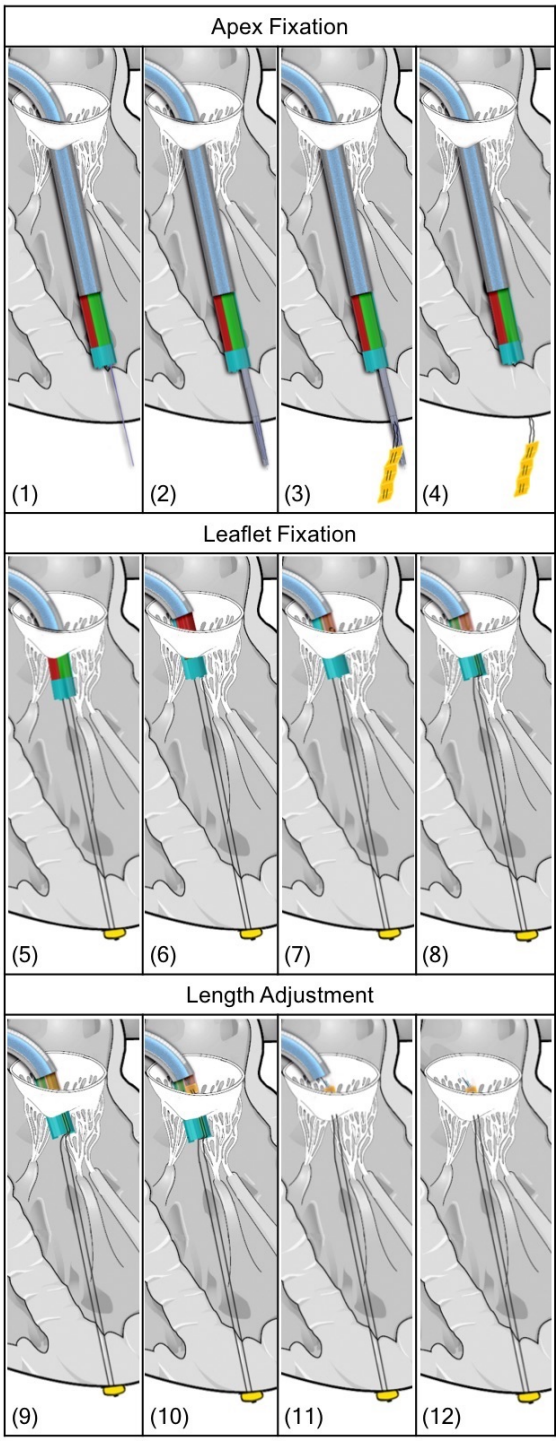

Figure 8.5: (1-12) Drawings of the procedure steps with the Solidworks model of the ChoRe device. The steerable catheter is represented in light blue.

5. The ChoRe is moved up to reach the leaflet plane and the apex pledget folds to create the apex fixation.
6. The leaflet clamp grasps the leaflet.
7. The harpoon-shaped needle is pushed through the leaflet to hook the artificial chord and to pull it up through the leaflet, above the chord grasper and the clamping tube.
8. The external shell is rotated and the artificial chord is released from the leaflet clamp.

Length adjustment

9. The chord grasper can be closed around the artificial chord by pushing it out of the clamping, temporarily fix the length.
10. The pre-constructed knot is fastened by pulling at both ends of the knot.
11. The pre-constructed knot is left on the leaflet.
12. The harpoon-shaped needle releases the artificial chord due to a small movement towards the leaflet and a small rotation. The leaflet clamp is opened to release the leaflet and closed afterward to retract the entire device back in the steerable guiding sheath.

8.2.4. Prototype manufacturing

In order to evaluate its functionality, a ChoRe prototype has been constructed, Figure 8.6. Most parts were manufactured with additive manufacturing technology using the 3D printer Perfactory®4 Mini XL with an Enhanced Resolution Module (ERM) provided by EnvisionTEC (Gladbeck, Germany) at TU Delft. The materials used to print the different parts are liquid photopolymers, R5 and R31, specifically customized for prototyping, Figures 8.6a and b. The RC31 material is stiffer than R5 and was used to make the external shell more rigid. Additionally, the needle for the apex fixation and the harpoon-shaped needle were made of stainless-steel wire. All parts were manufactured twice as large as the designed size due to constraints related to the used 3D-printer (0.06×0.044 mm native pixel size and 0.4 mm in resolution). All elements were printed as separate individual parts, except for the leaflet clamp in which the thread support was glued after the printing.

The geometrical design as described in these sections is the intended design for ChoRe to function in a trans-catheter scenario. Simple hand-pieces were added to operate the device during the test to investigate its functionality.

8.3. Functional test in bovine hearts

8.3.1. Parameters of interest

The functionality of the ChoRe prototype determines the success of the procedure and relies on the correct placing of the implant. The prototype was therefore tested

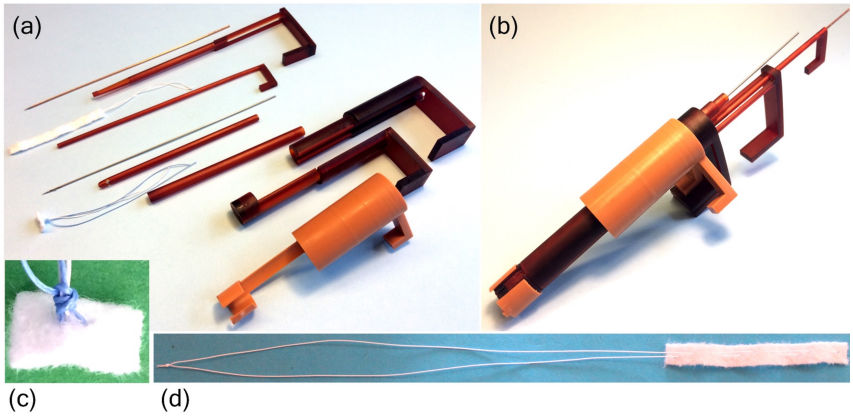

Figure 8.6: The 3D-printed and scaled-up ChoRe prototype with the manipulator part. (a) The disassembled ChoRe prototype. The picture shows all the elements. Starting from the top: the needle, the cannula, the artificial chord, the piston, the harpoon-shaped needle, the chord grasper, the pre-constructed knot, the clamping tube, the leaflet clamp, and the external shell; (b) the assembled ChoRe prototype; (c) an example of the pre-constructed knot structure tightened around the artificial chord; (d) the artificial chord: the apex pledget and the ePTFE in loop configuration.

ex-vivo in bovine hearts due to the scaled-up size of the device (twice as large as the final size). We qualitatively tested the outcome of the procedure by performing it ten times. We also measured the time that is required to conduct the procedure to have a preliminary evaluation of the amount of time the final procedure would take.

8.3.2. Material preparation

Artificial chords preparation

The test was carried out by using GoreTex ePTFE biocompatible suture thread (W. L. Gore and Associates, Inc., Arizona, USA) [44] and Bard®PTFE felt fabric (Bard Peripheral Vascular, Inc., Arizona, USA) for the pledgets [45]. ePTFE is a specific type of thread customized for the repair of the chordae tendineae; it is a highly flexible, non-absorbable, microporous monofilament with high resistance to fatigue and tensile strength, and high bio-integration property. Bard®PTFE felt is a non-absorbable fabric usually applied as buttresses under sutures to reinforce the tissue and avoid tearing, for instance in the repair of left ventricle rupture [46]. The pledget was cut in a rectangular element, folded into an accordion-shape, and sewn together with the ePTFE thread, as shown in Figure 8.6d, to allow its deployment. For the pre-constructed knot, a polyester thread (Medtronic, Minnesota, USA), and the Bard®PTFE felt were used. The polyester thread was sewn into the pledget and the pre-constructed knot was created as shown in Figure 8.6c.

Bovine hearts preparation

The test was performed ex-vivo using bovine hearts. Bovine hearts are commonly used in cardiac studies due to their similarities with the human heart at a larger scale

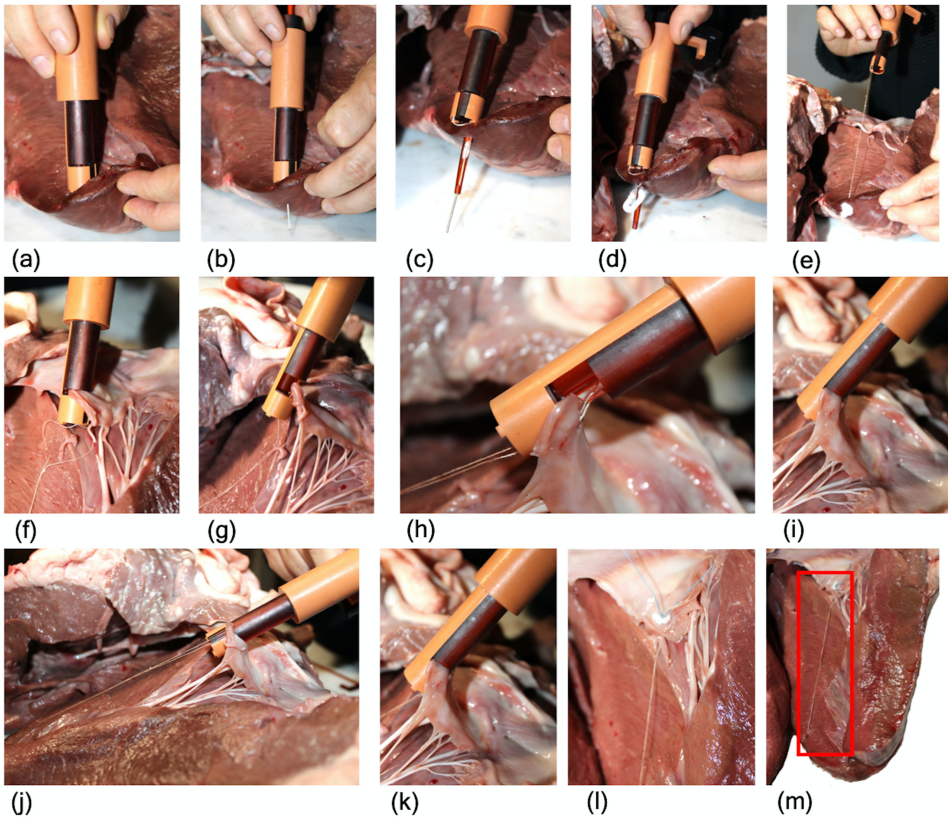

Figure 8.7: Procedural steps of the functional test carried out on bovine hearts. (a) ChoRe is positioned on the apex of the heart; (b) the needle is pushed through the apex; (c) the cannula is pushed through the apex; (d) the apex pledget is pushed out; (e) ChoRe is moved to the leaflet plane; (f) the leaflet is grasped; (g) the harpoon-shaped needle passes through the leaflet; (h) a detail with the clamp opened to show the harpoon-shaped needle after having captured the chord; (i) the chord length is fixed with the chord grasper; (j) the external shell is rotated; (k) the leaflet is released; (l) a detailed of the leaflet fixation of implanted chord; (m) the implanted chord, highlighted by the red square.

[47]. The dissection of each heart was performed following the procedure used by Lodder *et al.* [48], thus to have a better visualization of the left ventricle. Firstly, the right chambers of the heart were taken out, as well as the left atrium. Secondly, the inter-ventricular septum was removed. Then, a portion of the ventricle wall was removed to obtain a better visualization of the mitral valve structure. Finally, the natural chords were cut at the locations at which they commonly break. This included the chords connected to the free margin of the posterior leaflet [49].

Test procedure

The experimental set-up comprised the bovine hearts and a chronometer. A total of ten trials were performed to improve the statistic of the test. However, since

the mitral valve structure of one heart has not enough space to accommodate ten chords, we decided to use three bovine hearts, similar in size, and implant the artificial chords one after the other without removing the previously implanted chord. For practical reasons, a total of ten cannulae were prepared in advance and loaded with pledgets for the apex side, while the pre-constructed knot was inserted into the leaflet clamp every time the procedure was repeated. The procedure was performed by one of the authors of this paper with no experience with the ChoRe when started the functional test. The task completion time was measured with the chronometer. For each implant, the time measuring was started when the ChoRe was positioned in the starting position (in the apex of the left ventricle) and was stopped when the implant was finally attached to the leaflet. The overall procedure was performed according to the method described above, Figure 8.7.

8.4. Results

During the test, all ten artificial chords were successfully implanted. In all the trials, the ChoRe was able to attach the artificial chord first to the apex of the ventricle and then at the leaflet of the mitral valve. The maximum time registered during the first trial was 8.25 minutes, while the minimum time to perform the procedure was 2.34 minutes. The calculated average time was 3.45±1.44 minutes considering all ten trials and 3.14±0.36 minutes without considering the first time (nine trials), as shown in Figure 8.8.

Figure 8.8 shows that a learning factor has a principal role in the collected data of

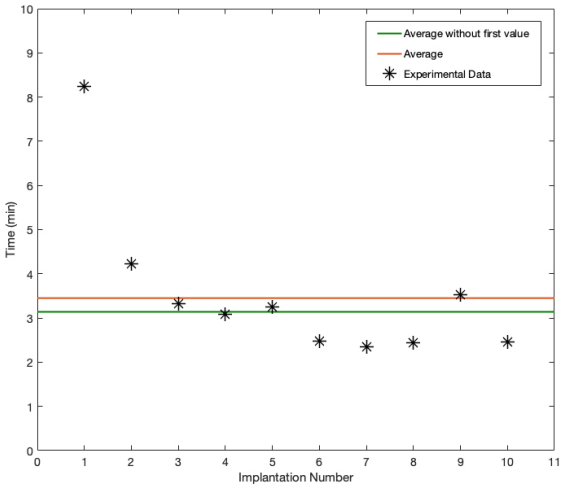

Figure 8.8: Plot of the duration of the procedure, in minutes, for each of the ten trials (black stars). The red line shows the average of the duration considering all ten trials while the green line the average without the first measurement.

the one chord fixation time. As the number of the performed procedures increased, the time decreased accordingly with an average of 3.45±1.44 minutes considering all ten trials (average of ten values) and 3.14±0.36 minutes without the first measurement (average of 9 values). After six trials, the time value stabilizes with an average of 2.59±0.35 minutes (average of the four last values) keeping constant the intra variability of the data. This data gives just an impression of the time the final procedure would take to implant one chord but can be compared to the average of 5 minutes for each implanted chord reported by Rucinskas *et al.* using the clinically accepted Neochord device in a trans-apical procedure [26].

8.5. Discussion

8.5.1. A new concept for chord replacement

This work presents a new device for the treatment of chordae tendineae rupture using trans-catheter approach. The compactness of ChoRe comes without any sharp edges. As such, the resulting device allows for easy motion into the cardiac chambers without creating damage. The simplicity of the design allows for relatively fast production time and assembly using 3D printing technology for the functional test phase. Even though this first prototype of ChoRe has proven its functionality and overall performance, a number of improvements can be made to further develop the design. For example, the length of the opening in the cannula, in the first stage determined considering the thickness of the heart wall, may be designed longer in order to allow relatively easier ejection of the pledget. Another improvement involves the design of the piston, which could have a narrower tip to allow the pledget to be pushed out better. The need for these adjustments became apparent after the first prototype was manufactured and assembled. The dimensions of ChoRe in its intended scale, 22 F in diameter and 25 mm in length, are relatively modest and similar to the ones of devices currently used in mitral valve trans-catheter procedures [40]. These dimensions leave the possibility to use the device in the majority of the patients, retaining its geometry. Moreover, to minimize risks of additional damages to the mitral valve structure, we tried to implement technologies already in use for heart surgery. For example, the harpoon-shaped needle was kept with the same size of the one already used in Neochord [50] and the in accordion-shape pledget is already used in the heart to reduce the size of the annulus of the mitral valve in the Mitralgn system [29]. To conclude, while commercially available devices, such as the Neochord [50], or devices still in a clinical trial phase, such as the TSD-5 [22] or the V-chordal off-Pump [23], are generally intended for trans-apical use, ChoRe was developed to be integrated into a catheter and perform the repair of the chordae tendineae in trans-catheter scenarios. Having the intent to use the device in trans-catheter procedures with a beating-heart condition in the future, the device needs to be further improved for catheterization possibilities; for example, the connection between the flexible shaft and the ChoRe needs to be developed, as well as the controls of each element of the device through a flexible catheter.

8.5.2. Prototyping and testing

With the first prototype being created through additive manufacturing, the quality of the design could be evaluated quickly. This allows ameliorating aspects of the device during the manufacturing phase, such as the size of the chord grasper. Similarly, the test set-up, as well as the results, could be gained relatively fast. For example, it was noticed that the preloading of the cannula with the pledget took approximately 30 minutes on average. This time needs to be reduced to increase the performance of the device, for example by means of a dedicated loading device. Even though manufacturing a 3D-printed model is a relevant opportunity to analyze the device in multiple aspects, there are a number of disadvantages related to this method of manufacturing. The polymeric and resin materials that were used to print the device resulted in breakages during the test phase due to their brittle characteristics. Additionally, it was not possible to print rigid needles due to their small diameters, which resulted in flexible components.

Analyzing the behavior of the prototype during our functional test, we found that the solution to connect the ePTFE thread at the apex of the heart seems to yield good results. This included the mechanical functionality of device components and the robustness of the apex pledget attachment. On the other hand, the upper side of the connection showed some weaknesses. The grasp of the leaflet with the leaflet clamp, the harpoon-shaped needle, and the length adjustment unit functioned according to the requirements, whereas the mechanism of fixation for the leaflet connection has to be re-designed as the pre-constructed knot. In fact, even though the mechanism of the fixation for the leaflet connection was able to fix the length of the artificial chord, it was not able to maintain the length and the point of anchorage when pulled. The reason for this can be found in the slippery properties of the ePTFE thread, as well as in the pre-constructed knot structure which required multiple loops of the thread around the artificial chord. A possible solution to eliminate these problems may be to replace the pre-constructed knot with a clip that is able to fix the thread to the leaflet side. Another important drawback concerns the fixation of a single artificial chord for each insertion of the device. Having a device that is able to place multiple chords during one device insertion could potentially reduce the time and complexity of the procedure.

Moreover, it has been shown that the length of the implanted ePTFE artificial chord affects the outcome of the repair. In the case of an apex connection, as reported by Grinberg *et al.* [51], the length of the artificial chord is approximately two times longer than the chords implanted in a conventional procedure, attached to the papillary muscles. Studies have shown that the increased length leads to a lack of potential shock-absorption and an increase in stiffness that can negatively affect the long-term results and lead to an early failure of the implant [52, 53]. Possible solutions, as suggested by Jensen *et al.* [53], could be to modify the trans-ventricular fixation point in order to reduce the length of the chords, or change the material of the artificial chord. ePTFE is a highly porous suture thread that facilitates the bio-integration of the implant; however, other types of suture threads could be an option due to the adaptability of our design that allows the use of different kinds of threads.

Future research will focus on improving not only ChoRe individual elements, such as the piston shape or the opening of the cannula, but also the functionality of the device, such as reducing the time for preloading the cannula. Moreover, the device will be adapted to be used in beating-heart condition and will be fabricated in its intended scale (22 F in diameter and 25 mm in length), with more resistant, ISO10993 bio-compatible materials, such as AISI 316 or 304 stainless steel for the needles and polymers such as PEEK or PEI for the printed parts, and integrated with a long, flexible catheter shaft that can be used during catheterization. Nevertheless, our ChoRe shows great potential in developing advanced surgical devices using 3D printing technology and packing of complex multi-functionalities in a miniature device for mitral valve repair.

8.6. Conclusion

This paper introduced a novel mitral valve repair device that is intended to operate in a trans-catheter scenario. The device has been designed considering the constraints, given by the biological structures, and the fundamental procedure functions. The artificial chord must be attached to the lower side of the mitral valve structure on the apex of the heart and to the upper side on the prolapsed leaflet of the mitral valve. A research prototype was manufactured with dimensions that were twice the required size to conduct an early evaluation of the properties. The functionality of the prototype was qualitatively tested giving a preliminary evaluation of the procedure time. The resulting data showed that, even if improvements in the design must be done especially for the connection of the artificial chord at the leaflet side in order to guarantee a stable connection, this first prototype of ChoRe is a good starting point for the development of new, multi-functional technology for integrated mitral valve repair. Future work will focus on the integration of the mitral valve repair device with a steerable catheter and a dedicated external manipulating device. This allows a future potential for more patient-specific and less invasive treatments in mitral valve repair.

References

[1] Z. G. Turi, *Mitral Valve Disease,* Circulation **109**, e38 (2004).

[2] V. T. Nkomo, J. M. Gardin, T. N. Skelton, J. S. Gottdiener, C. G. Scott, and M. Enriquez-Sarano, *Burden of valvular heart diseases: a population-based study,* The Lancet **368**, 1005 (2006).

[3] J. H. C. Lam, N. Ranganathan, E. D. Wigle, and M. D. Silver, *Morphology of the human mitral valve,* Circulation **41**, 449 (1970).

[4] M. Enriquez-Sarano, C. W. Akins, and A. Vahanian, *Mitral regurgitation,* The Lancet **373**, 1382 (2009).

[5] J. G. Betts, P. Desaix, E. Johnson, J. E. Johnson, O. Korol, D. Kruse, B. Poe, J. A. Wise, M. Womble, and K. A. Young, *Anatomy and Physiology,* (2017).

[6] D. Jaron, P. Lelkes, R. Seliktar, S. C. Hon, R. Gerbino, and N. Gostola, *Mechanical heart valve,* The Body Synthetic (2008).

[7] P. Bloomfield, *Choice of heart valve prosthesis,* Heart **87**, 583 (2002).

[8] J. Bergsland, E. Mujanovic, O. J. Elle, P. Mirtaheri, and E. Fosse, *Minimally invasive repair of the mitral valve: Technological and clinical developments,* Minimally Invasive Therapy & Allied Technologies **20**, 72 (2011).

[9] D. C. H. Cheng, J. Martin, A. Lal, A. Diegeler, T. A. Folliguet, L. W. Nifong, P. Perier, E. Raanani, J. M. Smith, and J. Seeburger, *Minimally invasive versus conventional open mitral valve surgery: a meta-analysis and systematic review,* Innovations: Technology and Techniques in Cardiothoracic and Vascular Surgery **6**, 84 (2011).

[10] Z. Wu, J. Pan, Q. Wang, Q. Zhou, and D. Wang, *Surgical repair of mitral valve prolapse through a minimal right vertical infraaxillary thoracotomy,* Journal of cardiac surgery **27**, 533 (2012).

[11] A. G. Ahangar, A. H. Charag, M. L. Wani, F. A. Ganie, S. Singh, S. A. A. Qadri, and Z. A. Shah, *Comparing aortic valve replacement through right anterolateral thoracotomy with median sternotomy,* International cardiovascular research journal **7**, 90 (2013).

[12] A. Iribarne, R. Easterwood, E. Y. H. Chan, J. Yang, L. Soni, M. J. Russo, C. R. Smith, and M. Argenziano, *The golden age of minimally invasive cardiothoracic surgery: current and future perspectives,* Future cardiology **7**, 333 (2011).

[13] D. Wang, Q. Wang, X. Yang, Q. Wu, and Q. Li, *Mitral valve replacement through a minimal right vertical infra-axillary thoracotomy versus standard median sternotomy,* The Annals of thoracic surgery **87**, 704 (2009).

[14] A. Vahanian, B. Iung, D. Messika-Zeitoun, D. Détaint, M. Mirabel, G. Baron, P. Ravaud, J.-L. Vanoverschelde, and E. G. Butchart, *What are the characteristics of patients with severe, symptomatic, mitral regurgitation who are denied surgery?* European Heart Journal **28**, 1358 (2007).

[15] D. R. Merk, A. Aidietis, and J. Seeburger, *Off-pump transapical neo-chordae implantation,* Annals of cardiothoracic surgery **4**, 293 (2015).

[16] A. Cribier, H. Eltchaninoff, A. Bash, N. Borenstein, C. Tron, F. Bauer, G. Derumeaux, F. Anselme, F. Laborde, and M. B. Leon, *Percutaneous transcatheter implantation of an aortic valve prosthesis for calcific aortic stenosis: first human case description,* Circulation **106**, 3006 (2002).

[17] O. Oren, M. Oren, and Y. Turgeman, *Transradial versus transfemoral approach in peripheral arterial interventions,* International Journal of Angiology **25**, 148 (2016).

[18] D. S. Lim, M. R. Reynolds, T. Feldman, S. Kar, H. C. Herrmann, A. Wang, P. L. Whitlow, W. A. Gray, P. Grayburn, M. J. Mack, and D. D. Glower, *Improved Functional Status and Quality of Life in Prohibitive Surgical Risk Patients With Degenerative Mitral Regurgitation After Transcatheter Mitral Valve Repair,* Journal of the American College of Cardiology **64**, 182 (2014).

[19] F. Maisano, O. Alfieri, S. Banai, M. Buchbinder, A. Colombo, V. Falk, T. Feldman, O. Franzen, H. Herrmann, and S. Kar, *The future of transcatheter mitral valve interventions: competitive or complementary role of repair vs. replacement?* European heart journal **36**, 1651 (2015).

[20] W. Vongpatanasin, L. D. Hillis, and R. A. Lange, *Prosthetic heart valves,* New England Journal of Medicine **335**, 407 (1996).

[21] J. Seeburger, M. Rinaldi, S. L. Nielsen, S. Salizzoni, R. Lange, M. Schoenburg, O. Alfieri, M. A. Borger, F. W. Mohr, and A. Aidietis, *Off-pump transapical implantation of artificial neo-chordae to correct mitral regurgitation: the TACT Trial (Transapical Artificial Chordae Tendinae) proof of concept,* Journal of the American College of Cardiology **63**, 914 (2014).

[22] J. S. Gammie, P. Wilson, K. Bartus, A. Gackowski, J. Hung, M. N. D'Ambra, P. Kolsut, G. J. Bittle, P. Szymanski, and J. Sadowski, *Transapical beating-heart mitral valve repair with an expanded polytetrafluoroethylene cordal implantation device,* Circulation **134**, 189 (2016).

[23] F. Maisano, M. Cioni, J. Seeburger, V. Falk, F. W. Mohr, M. J. Mack, O. Alfieri, and H. Vanermen, *Beating-heart implantation of adjustable length mitral valve chordae: acute and chronic experience in an animal model,* European Journal of Cardio-Thoracic Surgery **40**, 840 (2011).

[24] G. Panic, M. Ristic, S. Putnik, D. Markovic, I. Divac, and U. U. Babic, *A novel technique for treatment of mitral valve prolapse/flail,* The Journal of thoracic and cardiovascular surgery **137**, 1568 (2009).

[25] ClinicalTrials.gov, *Randomized Trial of the Neochord DS1000 System Versus Open Surgical Repair,* (2017).

[26] K. Rucinskas, V. Janusauskas, D. Zakarkaite, S. Aidietiene, R. Samalavicius, G. Speziali, and A. Aidietis, *Off-pump transapical implantation of artificial chordae to correct mitral regurgitation: early results of a single-center experience,* The Journal of thoracic and cardiovascular surgery **147**, 95 (2014).

[27] O. De Backer, N. Piazza, S. Banai, G. Lutter, F. Maisano, H. C. Herrmann, O. W. Franzen, and L. Søndergaard, *Percutaneous transcatheter mitral valve replacement,* Circulation: Cardiovascular Interventions **7**, 400 (2014).

[28] F. Maisano, M. Taramasso, G. Nickenig, C. Hammerstingl, A. Vahanian, D. Messika-Zeitoun, S. Baldus, M. Huntgeburth, O. Alfieri, A. Colombo, G. La Canna, E. Agricola, M. Zuber, F. C. Tanner, Y. Topilsky, F. Kreidel, and K.-H. Kuck, *Cardioband, a transcatheter surgical-like direct mitral valve annuloplasty system: early results of the feasibility trial,* European Heart Journal **37**, 817 (2016).

[29] T. Siminiak, R. Dankowski, A. Baszko, C. Lee, L. Firek, P. Kałmucki, A. Szyszka, and A. Groothuis, *Percutaneous direct mitral annuloplasty using the Mitralign Bident™ system: description of the method and a case report,* Kardiologia Polska (Polish Heart Journal) **71**, 1287 (2013).

[30] M. Puls, E. Lubos, P. Boekstegers, R. S. von Bardeleben, T. Ouarrak, C. Butter, C. S. Zuern, R. Bekeredjian, H. Sievert, and G. Nickenig, *One-year outcomes and predictors of mortality after MitraClip therapy in contemporary clinical practice: results from the German transcatheter mitral valve interventions registry,* European heart journal **37**, 703 (2015).

[31] D. Wendt, M. Thielmann, A. Melzer, J. Benedik, I. Droc, K. Tsagakis, D. S. Dohle, H. Jakob, and J. E. Abele, *The past, present and future of minimally invasive therapy in endovascular interventions: A review and speculative outlook,* Minimally Invasive Therapy & Allied Technologies **22**, 242 (2013).

[32] M. Ibrahim, C. Rao, and T. Athanasiou, *Artificial chordae for degenerative mitral valve disease: critical analysis of current techniques.* Interactive cardiovascular and thoracic surgery **15**, 1019 (2012).

[33] T. Shibata, *Loop technique for mitral valve repair,* General thoracic and cardiovascular surgery **62**, 71 (2014).

[34] J. Seeburger, M. A. Borger, V. Falk, and F. W. Mohr, *Gore-Tex loop implantation for mitral valve prolapse: the Leipzig loop technique,* Operative Techniques in Thoracic and Cardiovascular Surgery **13**, 83 (2008).

[35] D. Maselli, R. De Paulis, L. Weltert, A. Salica, R. Scaffa, A. Bellisario, and A. Mingiano, *A new method for artificial chordae length "tuning" in mitral valve repair: preliminary experience,* The Journal of thoracic and cardiovascular surgery **134**, 454 (2007).

[36] P. A. Iaizzo, *Handbook of cardiac anatomy, physiology, and devices* (Springer Science & Business Media, 2009).

[37] F. Bizzarri, A. Tudisco, M. Ricci, D. Rose, and G. Frati, *Different ways to repair the mitral valve with artificial chordae: a systematic review.* Journal of cardiothoracic surgery **5**, 22 (2010).

[38] J. Seeburger, S. Leontjev, M. Neumuth, T. Noack, M. Höbartner, M. Misfeld, M. a. Borger, and F. W. Mohr, *Trans-apical beating-heart implantation of neo-chordae to mitral valve leaflets: results of an acute animal study.* European journal of cardio-thoracic surgery : official journal of the European Association for Cardio-thoracic Surgery **41**, 173 (2012).

[39] D. Ozbag, Y. Gumusalan, and A. Demirant, *The comparative investigation of morphology of papillary muscles of left ventricle in different species,* International journal of clinical practice **59**, 529 (2005).

[40] L. Søndergaard, O. De Backer, O. W. Franzen, S. J. Holme, N. Ihlemann, N. G. Vejlstrup, P. B. Hansen, and A. Quadri, *First-in-human case of transfemoral CardiAQ mitral valve implantation,* Circulation: Cardiovascular Interventions **8**, e002135 (2015).

[41] A. J. McLeod, J. T. Moore, and T. M. Peters, *Beating heart mitral valve repair with integrated ultrasound imaging,* (Proc. SPIE 9415, Medical Imaging 2015: Image-Guided Procedures, Robotic Interventions, and Modeling, 2015) pp. 941504–941508.

[42] Abbott, *MitraClip ® NT Clip Delivery System MitraClip ® NT System,* (2016).

[43] F. Ramponi, T. D. Yan, M. P. Vallely, and M. K. Wilson, *Total percutaneous cardiopulmonary bypass with Perclose ProGlide,* Interactive CardioVascular and Thoracic Surgery **13**, 86 (2011).

[44] W. L. Gore & Associates Inc., *INSTRUCTIONS FOR USE FOR : ePTFE Nonabsorbable Monofilament FOR CHORDAE TENDINEAE for Chordae Tendineae Repair or Replacement,* , 5 (2012).

[45] C. R. Bard, *Bard Peripheral Vascular. ☒ Advancing Lives and the Delivery of Health Care™,* (2018), https://www.crbard.com/Peripheral-Vascular, Accessed: 2019-02-28.

[46] D. T. Thorsteinsson, F. Valsson, A. Geirsson, and T. Gudbjartsson, *Major cardiac rupture following surgical treatment for deep sternal wound infection,* Interactive cardiovascular and thoracic surgery **16**, 708 (2013).

[47] J. Hutchison and P. Rea, *A comparative study of the morphology of mammalian chordae tendineae of the mitral and tricuspid valves,* Veterinary record open **2**, e000150 (2015).

[48] J. Lodder, G. J. Verkerke, B. J. M. Delemarre, and D. Dodou, *Morphological and mechanical properties of the posterior leaflet chordae tendineae in the mitral valve,* Proceedings of the Institution of Mechanical Engineers, Part H: Journal of Engineering in Medicine **230**, 77 (2016).

[49] Khalil Fattouch, *CARDIO-CHIRURGIA.COM/IM degenerativa,* http://www.cardio-chirurgia.com/public/IT/im-degenerativa.asp, Acccessed: 2018-09-21.

[50] *NeoChord,* https://neochord.com/, Accessed: 2018-09-21.

[51] D. Grinberg, N. K. Adamou, M. Pozzi, and J.-F. Obadia, *Artificial mitral chordae: When length matters.* The Journal of thoracic and cardiovascular surgery **157**, e23 (2019).

[52] P. P. Caimmi, M. Sabbatini, L. Fusaro, A. Borrone, and M. Cannas, *A study of the mechanical properties of ePTFE suture used as artificial mitral chordae,* Journal of cardiac surgery **31**, 498 (2016).

[53] H. Jensen, M. O. Jensen, F. Waziri, J. L. Honge, E. Sloth, M. Fenger-Gron, and S. L. Nielsen, *Transapical neochord implantation: Is tension of artificial chordae tendineae dependent on the insertion site?* The Journal of thoracic and cardiovascular surgery **148**, 138 (2014).

9

3D Printed Surgical Grasper with Soft Pads for Gentle Grip

Published as:
van Assenbergh P., Culmone C., Breedveld P., and Dodou D. "Implementation of anisotropic soft pads in a surgical gripper for secure and gentle grip on vulnerable tissues ".Proceedings of the Institution of Mechanical Engineers, Part H: Journal of Engineering in Medicine, 235.3, (2021) 255–263.

Abstract

Current surgical grippers rely on friction grip, where normal loads (i.e., pinch forces) are translated into friction forces. Operating errors with surgical grippers are often force-related, including tissue slipping out of the gripper because of too low pinch forces and tissue damaging due to too high pinch forces. Here, we prototyped a modular surgical gripper with elastomeric soft pads reinforced in the shear direction with a carbon-fiber fabric. The elastomeric component provides low normal stiffness to maximize contact formation without the need of applying high normal loads (i.e., pinch forces), whereas the carbon-fiber fabric offers high shear stiffness to preserve the formed contact under the lateral loads (i.e., shear forces) that occur during tissue lifting. Additionally, we patterned the pads with a sub-surface micropattern, to further reduce the normal stiffness and increase shear stiffness. The body of the prototype gripper, including shaft, joints, and gripper tips, was fabricated in a single step using 3D printing, followed by manual attachment of the soft pads to the gripper. The gripping performance of the newly developed soft gripper on soft tissues was experimentally compared to reference grippers equipped with metal patterned pads. The soft-pad gripper generated similar gripping forces but significantly lower pinch forces than metal-pad grippers. We conclude that grippers with anisotropic-stiffness pads are promising for secure and gentle tissue grip.

9.1. Introduction

Secure and gentle soft-tissue grip is imperative in the medical domain. In almost any surgical procedure, from laparoscopy to microsurgery, soft tissues are grasped and pulled for creating space, exposing areas to be treated, or getting access to obstructed contiguous anatomical structures. The vast majority of surgical grippers used in the medical domain are equipped with patterned surfaces made of stainless steel [1]. Such grippers employ friction grip, which relies on the translation of normal load (i.e., pinch forces) to friction forces, for grasping and pulling soft tissues.

Previous studies have shown that the majority of grasping errors with surgical grippers is force-related, with pinch forces being either too low, resulting in slipping of the tissue out of the gripper,[2, 3] or too high, resulting in possible tissue damage[4, 5]. Tissue stresses up to 800 kPa have been measured with laparoscopic grippers,[6] which is considerably higher than the safety threshold of 200 kPa estimated for apoptosis [7].

Studies have shown that high pinch forces can be reduced by replacing the metal forceps of the gripper with soft pads [8, 9]. The grip of such pads on tissue is achieved thanks to their deformability in the normal direction, which enables a large contact area with the tissue. At the same time, the contact formed between the tissue and the pad is homogeneously distributed over the pad surface, eliminating the occurrence of local high peak forces on the tissue [8, 9]. A general disadvantage of a soft pad is that deformations of the pad occur not only in the normal but also in the shear direction, which might lead to tissue slipping out of the gripper during pulling. An ideal soft gripping pad would thus need to be anisotropic, fulfilling two contradictory properties: being deformable in the normal (pinching) direction, so that a large contact is formed, and stiff in the lateral (shear) direction, so that the formed contact is preserved when the tissue is being pulled.

Bartlett *et al.* [10] developed such anisotropic pads for strong grip on rigid substrates. The pads consisted of a carbon-fiber fabric (CFF), part of which was embedded into an elastomeric material (poly-dimethylsiloxane, PDMS); the unembedded CFF part was served as tail via which the pad was pulled along the substrate. PDMS provided deformability in the normal direction, thereby allowing for the formation of a large contact, whereas CFF provided stiffness in the shear direction, thus allowing for the preservation of the formed contact when pulling the pad from the CFF tail along the substrate. These authors found that, on rigid glass substrates, 100 cm^2 elastomeric pads without CFF had a force capacity (i.e., the maximum sustainable force) of about 10 N, whereas the addition of CFF led to a force capacity in the order of 1000 N [10].

Implementation of anisotropic CFF-PDMS pads in surgical grippers is a promising approach for generating secure, yet gentle, grip on biological tissue. The idea herein is to align the CFF with the shear (pulling) direction and guide the loading forces via the CFF tail into the shaft of the instrument in such a way that the elastomeric part of the soft pad is protected from undesirable shear deformations and contact loss (Figure 9.1).

The grip of fiber-reinforced soft pads can be further increased by patterning the

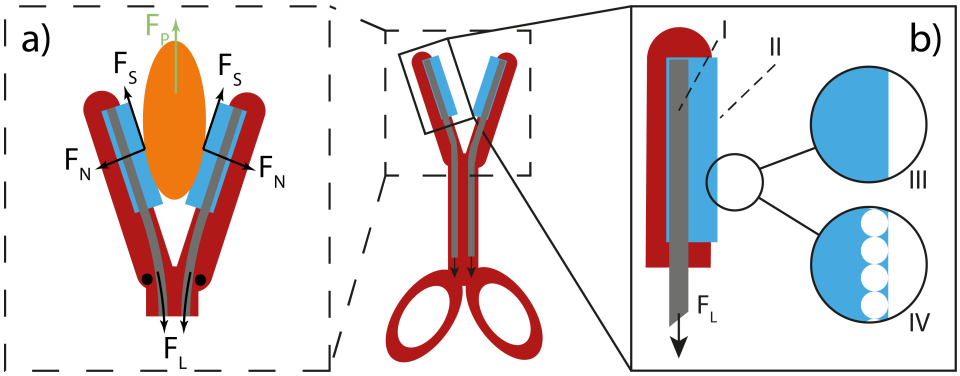

Figure 9.1: A schematic overview of a gripper pad with anisotropic properties. A): Schematic force diagram. Hinges are depicted as black dots. The gripper was closed by loading the CFF using a constant tensile load (FL). By closing the gripper, the pinch force (FN) acts on the tissue in the normal direction. When the tissue sample was pulled upwards using a positioning stage (FP), a shear force (FS) was generated at the soft pad-tissue interface. Gravitational force on the tissue is omitted from the diagram because the load cell to which the tissue was connected via a holder (not visualized here) was zeroed after the tissue was hanged to the holder. B) A stiff carbon-fiber fabric (CFF) (I) is partially embedded into a soft elastomeric material (PDMS) (II). The CFF is aligned with the shear (pulling) direction. The loading forces are guided via the unembedded CFF tail into the shaft of the instrument. The pad is fabricated either without a surface pattern (III) or with a pattern of microscale sub-surface spherical voids (IV). Under shear loading, the internal walls that separate neighboring voids collapse, resulting in lateral stiffening of the adhesive surface.

otherwise plain surface of the elastomer (Figure 9.1). In previous work, we showed that, on soft substrates, the presence of microscale spherical voids in an elastomer, topped with a thin terminal layer, led to higher grip than an unpatterned elastomer [11]. Thanks to its microscale thickness, the terminal layer conforms to microscale irregularities of the substrate's surface, resulting in a higher contact area compared to an unpatterned elastomer, and therefore higher shear forces. At the same time, due to bending and internal sliding of the walls that separate the internal spherical voids under shear loading, the surface structure of the elastomer stiffens in the shear direction, thereby contributing to the preservation of the formed contact during shearing [11, 12].

In this paper, we present the implementation of fiber-reinforced elastomeric soft pads in a modular surgical gripper instrument. We developed two types of fiber-reinforced soft pads, one with an unpatterned surface, and another with sub-surface microscale voids. Additionally, we fabricated a reference gripper by replacing the pads with stainless steel grooved plates. The performance of the three grippers on soft tissue was assessed by measuring their gripping and pinch forces applied to the tissue.

9.2. Design

9.2.1. Soft pads

Unpatterned soft pads were fabricated with a thickness of 0.8 mm, width of 8 mm, and length of 15 mm. A piece of polystyrene plastic foil (50×50 mm^2), acting as an anti-stick layer, was placed on an aluminum base plate (Figure 9.2a). This anti-stick layer was covered by a 200×50 mm^2 piece of CFF (Figure 9.2b; 3K-200 Tex HS fibers, 200 g/m^2, plain woven, purchased from www.carbonwinkel.nl, De Moer, the Nether-lands), which was fixed at the short side of the baseplate using scotch tape. An 8×15 mm^2 rectangular hole was milled from an aluminum plate of 0.8 mm thickness to create a template frame (Figure 9.2d). Sylgard-184 (polydimethylsiloxane, PDMS, purchased from Dow Corning, MI) pre-polymer (base) and crosslinker (curing agent) were mixed in a 10:1 weight-based mixing ratio and degassed in a desiccator. The template frame was placed on top of the aluminum base plate covered with CFF and filled with the pre-polymer/crosslinking mixture. The filled template frame was degassed once more to evacuate air from the CFF, allowing the pre-polymer/crosslinking mixture to fully immerse the CFF. After degassing, the filled template was cured at 70 °C for at least 2 hours, while topped with a plain glass slide to obtain a flat finish (Figure 9.2e). After curing, the soft pad was carefully detached from the frame, anti-stick layer, and topping glass slide. The non-immersed CFF was cut to obtain two lateral flaps and a loading tail (Figure 9.2). To fabricate patterned elastomeric pads, the aforementioned plain glass slide used to top the filled template after degassing was replaced by a coated glass slide to obtain a patterned finish of the soft pad. Thereto, a plain glass slide was coated with a colloidal monolayer, prepared using a dip-coating methodology, as described in earlier work [12]. In brief, styrene divinylbenzene beads (purchased from ThermoFisher Scientific, MA, USA) with a reported diameter of 10 µm and delivered as a 4% (w/v) dispersion in water, were re-dispersed in ethanol at 8% (w/v) before use. The particles were transferred to the surface of a water bath, and compressed to obtain a closely packed floating monolayer of particles. In a dip-coating procedure, the monolayer was transferred to glass slides of 52×76 mm^2. An initial dipping depth of at least 40 mm was used, resulting in monolayers with at least a 52×40 mm^2 area. After curing of the soft PDMS pads, while topped with a coated glass slide, the microparticles were embedded in the pad surface. Removing the microparticles was done by dissolving them in n-methyl-pyrrolidone (NMP, Merck, Darmstadt, Germany). Thereto, the pads were placed horizontally, with the pattern facing up, and a droplet of NMP, large enough to fully cover the pad surface, was deposited for a duration of 10 minutes, before it was rinsed off with ethanol. This washing step was repeated two more times. Pads for reference grippers were milled from stainless-steel with a triangular saw-tooth profile with 0.35 mm tooth height. The height of this surface pattern was chosen based on previous studies, which tested laparoscopic grippers with pattern depths varying between 0.3 and 1 mm [13–15] and showed that a profile of 0.3 mm generated lower peak forces and thus less damage to the tissue [14].

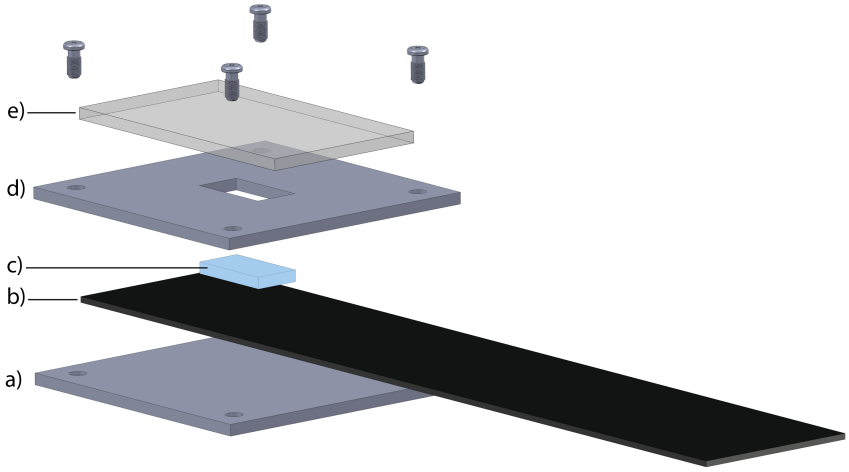

Figure 9.2: Exploded view of soft pad fabrication. An aluminum baseplate, topped with an anti-stick polystyrene foil (a) was covered with a sheet of CFF (b). A template frame in the size and thickness of the envisioned soft pad (d) was placed on the CFF and filled with uncured PDMS (c). The filled frame was covered with a plain or coated glass slide (e) to obtain unpatterned or patterned pads after curing.

9.2.2. 3D printed gripper

Figure 9.3 shows a schematic illustration of the 3D printed gripper, consisting of a shaft, joints, and jaws. Each gripper was 3D printed as a single element, and soft pads or reference pads were implemented in a subsequent manufacturing step. The grippers were printed using a Perfactory® 4 Mini XL printer (EnvisionTEC® GmbH, Gladbeck, Germany) with a layer height in the vertical z-axis of 25 µm. The selected printer is based on Vat photopolymerization technology and uses Digital Light Processing (DLP), in which the build plate moves vertically up and down into a vat of liquid polymer. When the build plate moves down, the liquid polymer is exposed to light, and, depending on the image displayed by a projector, a layer of polymer hardens. The process is repeated layer-by-layer until the object is fully printed. The grippers were printed using R5 epoxy photopolymer resin (EnvisionTEC® GmbH, Gladbeck, Germany), an acrylic resin especially developed for prototyping. The 3D printed grippers were printed in eight hours, with a vertical orientation (i.e., the shaft in a vertical position, and the jaws pointing down).

The gripper shaft contained a central rectangular lumen to guide the CFF tail (Figure 9.3a). The flexural joints were based on a leaf-spring principle and printed in opened condition. The CFF tails were used to actuate the gripper; pulling them resulted in the straightening of both joints via elastic deformation, and closing of the jaws. For the fixation of the soft pads (unpatterned and patterned) to the 3D printed structure, two grooves were added on the long sides of each jaw (Figure 9.3c). The two lateral flaps of the CFFs were folded into the grooves and fixated by gluing with cyanoacrylate. The distal end was left free, and at the joint side of the pad, the CFF tail was guided into the shaft via the joint. Some open space was left between

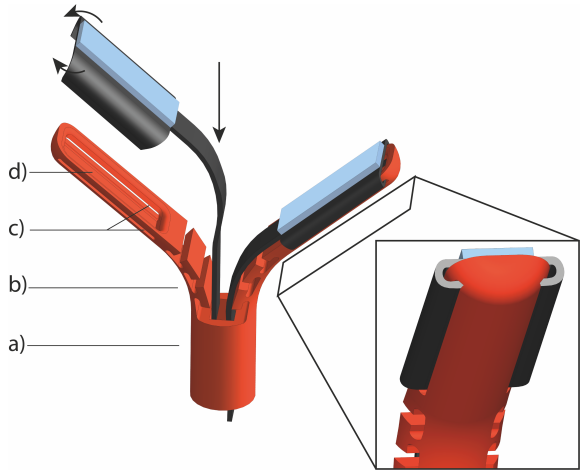

Figure 9.3: Schematic illustration of the gripper design for soft pads, and the positioning of the pads into the gripper. The shaft (a) contained a rectangular lumen, guiding the CFF to the joints. The flexural joints (b) were by default open and straightened by pulling the CFF, resulting in closing of the gripper. Each jaw contained two lateral grooves (c) for fixation of the soft pads. The lateral CFF flaps of the soft pads were folded and glued into these grooves. Underneath the soft pads' center was an open space between jaw and soft pad (d), providing some mobility in the normal direction of the soft pad. The 3D printed gripper for metal pads differed from the grippers for soft pads, in that jaws had a flat surface upon which the metal pads were glued.

the soft pads and the jaw (Figure 9.3d) to allow for some mobility of the fibers to self-align with the shear direction.

Figure 9.4 shows the three printed grippers, with implemented reference. The 3D printed reference gripper had jaws with a flat surface upon which the metal pads were glued (Figure 9.4a). In order to close the reference gripper, two stripes of CFF fibers were glued at the tip of each jaw and guided into dedicated grooves positioned underneath the flat jaw surface. In soft pads, either unpatterned (Figure 9.4b) or patterned (Figure 9.4c), the CFF fibers are embedded in the soft pads, and loaded to close the gripper. All jaws used in this work were 36 mm long, with an outer diameter of 10 mm and an opening up to 90 degrees.

9.3. Methods

9.3.1. Pinch force measurements

To determine the pinch forces generated on the tissue, a pressure-sensitive foil was used (5LW-2M Fujifilm Prescale, purchased from ALTHEN BV Sensors and Controls, Leidschendam, the Netherlands). This foil, consisting of a donor and acceptor sheet, colors at locations where the normal pressure exceeds 0.006 MPa. A PDMS sheet with a thickness of 5 mm was used as a representable tissue phantom in pinch force experiments. The phantom was covered on both sides with sheets of pressure-sensitive foil and placed in between the pads of an opened gripper. The gripper was

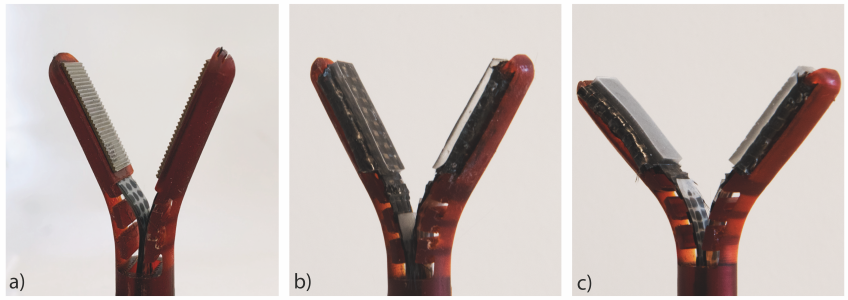

Figure 9.4: The three fabricated grippers. The reference gripper (a) was equipped with a grooved stainless-steel plate. In unpatterned pads (b), the elastomeric pads appear transparent, whereas in patterned pads (c), a white haze can be seen at the pad surface. In soft pads, either patterned or unpatterned, the CFF was embedded in the elastomeric pad.

closed by loading the CFF tails in the tensile direction for 5 seconds with a weight of 1.5 kg, resulting in a tensile load of 14.7 N. Coloring of the pressure foil outside of the gripper area due to deformations of the tissue phantom during grasping is included in our analysis, because these deformations are expected to be present when grasping real tissues. The obtained imprint on the pressure foil was digitalized using a scanner (Canon CanoscanLiDE 110). The digital images were analyzed using Matlab R2018b. The image was converted into black-and-white using the function im2bw in Matlab with a threshold of 0.8. In generated black-and-white images, colored pixels appear black, and uncolored pixels appear white. The number of black and white pixels was counted. The gripper pad was divided into nine equally-sized segments, numbered from 1 to 9. Segments 1-3, 4-6, and 7-9 were located at the distal, middle, and proximal end (i.e., closest to the joint) of the pad, respectively.

The fraction of black pixels per segment was reported as a qualitative image of the applied pressure of different gripper pads. Per gripper type (reference, patterned, unpatterned), six imprints of pressure foil were collected, and per segment, the fraction of black pixels was averaged over these six imprints.

9.3.2. Gripping force measurements

Tissue substrates were prepared by cutting 50×50 mm^2 pieces from the thin end of chicken breast meat. The substrate thickness was in the order of 5 mm. Tissue substrates were preserved at -20 °C and on the day of measuring kept below 0 °C until measuring. A frozen tissue substrate was clamped in a custom-made tissue holder. The tissue holder was connected to a load cell (Futek S-Beam FLLSB 200, controlled by a custom-made LabView script), which was mounted on a positioning stage (Thorlabs PT1/M-Z8, with additional KDC101 controllers, controlled by Thorlabs Kinesis software), allowing vertical displacement of the tissue when connected to the load cell. Before measuring, the load cell was zeroed to correct for the gravitational force acting on the hanging tissue substrate. Forces were recorded at a sampling frequency

of 20 Hz. The process from taking the substrate out of its cooled environment until the start of measuring took about 3-4 minutes, which was sufficient for the tissue to thaw.

The gripper was vertically placed in a holder, with the gripping jaws facing up and the shaft pointing down. The CFF tails came out of the shaft, hanging down, and were clamped together. After hanging the tissue in between the two opened gripping jaws, the gripper was closed by loading the two CFF tails using a tensile load of 14.7 N. Upon closing the gripper, we waited 5 seconds, and then the tissue, mounted on the load cell, was moved up with a speed of 1 mm/s, over a travel distance of at least 15 mm. The gripper was opened by removing the weight directly after the positioning stage came to a stop. A force-time plot was recorded from just before closing the gripper until the gripper was opened again.

Gripping forces of all three grippers (reference, unpatterned, patterned) were each tested on three pieces of tissue, with three subsequent repetitions on each tissue piece. The peak forces obtained in the three subsequent measurements on the same tissue piece were averaged. The three obtained averages were merged into one set of three independent measurements per gripper type. Independent t-tests were conducted to compare the performance of the three gripper types.

9.4. Results

9.4.1. Pinch force measurements

Figure 9.5 shows a scan of a pressure foil after imprinting with a patterned gripper, its transfer to a black-and-white image, the segmentation of the gripper pad, and the fraction of colored pixels for each of 9 segments. It can be seen that for this

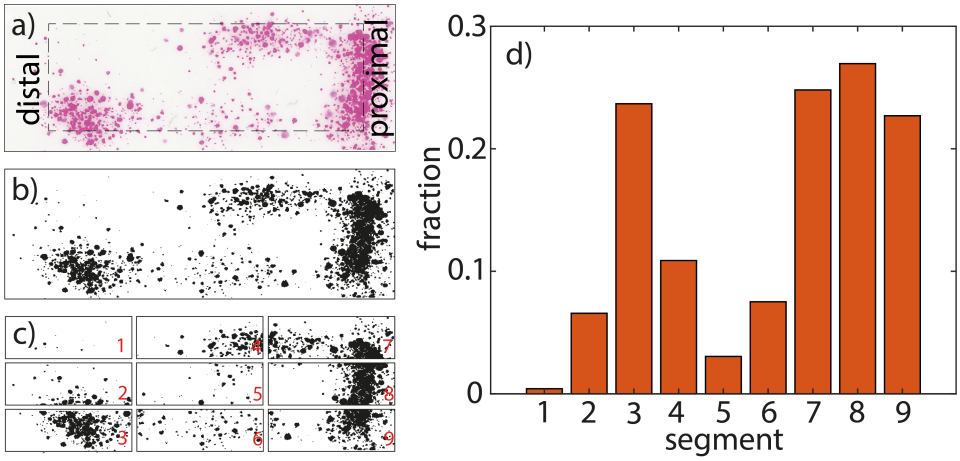

Figure 9.5: Overview of the analysis of imprinted pressure foils. (a) A scan of a pressure foil used with the patterned gripper. The dashed square indicates the outline of the gripper pad. (b) A black-white image of the imprint. (c) Segmentation of the imprint of the gripper pad. Segments 7-9 are at the proximal end of the pad. (d) Fraction of black pixels per segment for this particular imprint.

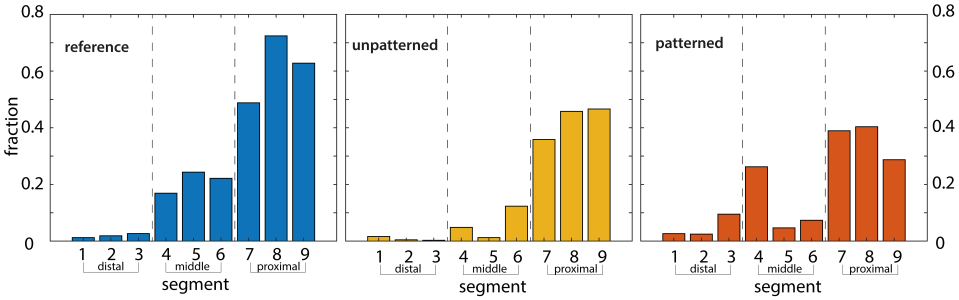

Figure 9.6: Average distribution of pinch forces for three different gripper types. Plots are the mean fraction of black pixels per segment for six imprinted pressure foils per gripper type.

particular imprint, most colored pixels can be found in segments 7, 8 and 9, indicating that pinch forces were highest at the proximal end of the gripper pad.

Figure 9.6 shows the fraction of black pixels per segment for each gripper type (reference, patterned, unpatterned) averaged over the six pressure measurements that were conducted per gripper type. For all three gripper types, we found that the highest pinch forces were present at the proximal size of the pads, that is, closest to the joint (segments 7-9). Pinch forces were lowest at the distal end of the pad. Within each region (distal, middle, or proximal), we did not observe large differences in the generated stresses between the three lateral segments. Pinch forces were found to be higher for the reference gripper compared to the soft gripper pads for the proximal and middle regions.

The fraction of colored pixels throughout the full soft pad, that is, segments 1-9 summed up, was on average 0.28 (standard deviation SD = 0.06) for the metal reference gripper, and 0.17 (SD = 0.03) and 0.18 (SD = 0.06) for the unpatterned and patterned soft grippers, respectively. These values are the means of six pressure measurements per gripper type. t-tests showed that significantly higher pinch forces were generated with the reference gripper compared to the unpatterned gripper ($t(10) = -4.13$; $p = 0.002$) and the patterned gripper ($t(10) = -3.01$; $p = 0.013$). There was no significant difference in the generated pinch force between patterned and unpatterned soft pads ($t(10) = 0.35$, $p = 0.735$).

9.4.2. Gripping force measurements

Figure 9.7a shows a representative force-time plot of the gripping force measurements. Five stages can be distinguished. At Stage I, the gripper closed and made contact with the tissue phantom. During Stages II-IV, the tissue was moving upward. Initially, this resulted in a steep increase in forces (Stage II). At Stage III, the tissue phantom started slipping. At Stage IV, this slipping reached a constant rate. At Stage V, the upward movement of the tissue phantom stopped, and the gripper opened.

Significantly higher gripping forces were generated with the patterned gripper than with the unpatterned gripper ($t(4) = 2.80$, $p < 0.049$ (Figure 9.7b)). The reference

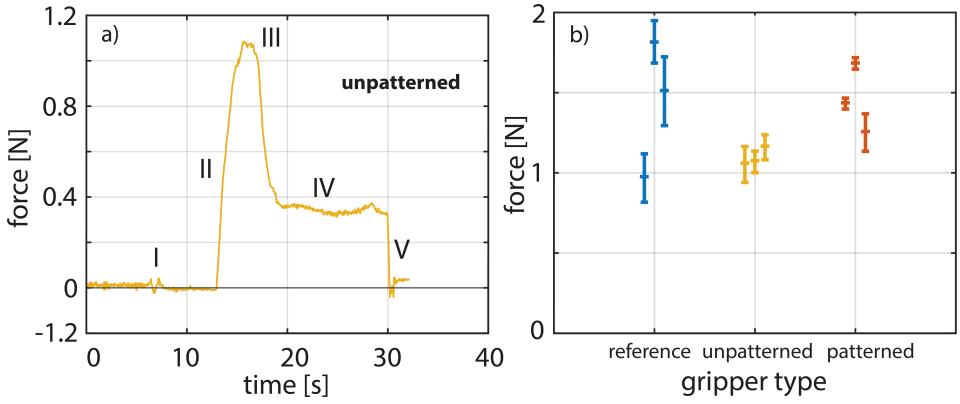

Figure 9.7: Results of shear force measurements. (a) A representative force-time plot of shear force measurements from an unpatterned gripper. First, the gripper closed (I). After around 5 seconds, the phantom was pulled upward with 1 mm/s (II-IV). The peak shear force was reached just before the phantom started sliding out of the gripper (III). The tissue was then gradually sliding out of the gripper (IV). At V, the tissue phantom stopped moving, and the gripper was opened. (b) Generated forces for each gripper type.

gripper generated gripping forces that were not significantly different from the two soft grippers.

9.5. Discussion

We showed that surgical grippers equipped with anisotropic pads, being soft in the normal direction and stiff in the lateral loading direction, generate comparable gripping forces but lower pinch forces than a gripper with metal pads. The gripping forces generated by the grippers were between 1 and 2 N. These forces are suitable for manipulating delicate tissues such as veins or liver tissue [16–18]. For instance, Jia *et al.* generated pinch forces of 1 and 2 N and reported a pinch force threshold of 3.5 N to prevent tissue damage [18].

The gripper was printed in vertical orientation to fit a high number of grippers in the build platform. As a result, the applied load was orthogonal to the plane of binding between printed layers. From a structural strength perspective, printing the grippers in a horizontal orientation would result in applied load parallel to the plane of the printed layers and therefore higher structural strength. If future designs of this gripper are meant for lifting heavier objects, changing the printing orientation of the gripper is advised to obtain stronger joints. The design of the joints is also vulnerable to torsion. We carried out preliminary tests on the mechanical properties of the gripper and found that the torsional stiffness can be increased by adding flaps laterally to the joint, as suggested by Grames *et al.* [19]. In the current design iteration, we decided to keep the design simple by not introducing additional elements, but in future work, it is advised to take torsion considerations into account in the gripper design.

In our measurements, the tissue substrate was used with a frozen core to pre-

vent elastic stretching. In surgical procedures, the higher temperature of the tissue compared to the temperature in our grasping experiments will presumably result in a higher deformation of the tissue. It has to be investigated how such tissue deformation affects the gripping strength. Deformation of the soft gripper pads, on the other hand, is not expected to significantly change with expected temperature fluctuations. Moreover, oscillatory shear tests showed that PDMS with a 10:1 weight-based mixing ratio of base and curing agent exhibited linear elastic behavior up to oscillation frequencies of 102 rad/s, indicating elastic recovery times in the order of 10-2 seconds [20]. These elastic recovery times are well below the time in between subsequent gripping actions, as reported for, for example, cholecystectomies, where Heijnsdijk *et al.* found a mean gripping frequency of 1.9 per minute [21].

Gripping forces were generated using a tensile load of 14.7 N on the CFF tails in the shaft to close the gripper. The height of this load was determined in a pilot experiment, where we found that with loads of 9.8 N or higher, significant grip on grasped tissue substrates was generated. These tensile loads are well in the range of applied handle forces in conventional surgical grippers, [17, 22, 23] although the transfer of forces exerted by a gripper handle to actual pinch forces strongly depends on the closing mechanism of the gripper. We found that applied tensile loads resulted in relatively low stresses on the tissue, due to the used force transfer mechanism, and efficient distribution of pinch forces with soft pads. Due to the use of additive manufacturing, higher pinch forces can be obtained by 3D printing a gripper design in which the same actuation force of 14.7 N results in higher pinch forces at the gripper jaws. 3D printing is a facile method as the instrument can be printed as one piece, and no further assembly of the platform instrument is required. Equipping of the instrument with soft pads can be done in one simple post-manufacturing step. This manufacturing approach allows for variations of the gripper design, including the length of the shaft, the opening angle of the jaws, stiffness of the joints, dimensions of the jaws and soft pads, and mechanical properties of the implemented soft pads. Moreover, pads with various surface patterns could be applied by using different templates.

A pressure-sensitive foil was used to indicate the applied pinch forces. We used this method because, with force sensors, it is complex to measure pinch forces at different locations throughout gripper pads. Between individual imprinting experiments, some variability was observed in the number of colored pixels between different distal (1 vs. 3), middle (4 vs. 6), and proximal (7 vs. 9) lateral segments. These grasping variations between different measurements were found to be random, presumably caused by misalignments of the gripper pads with the substrate. In Figure 9.6, a difference between segments 4 and 6 seems to be present for the patterned gripper, suggesting unequal closing of the gripper. We believe that this difference between segments 4 and 6 for the patterned gripper can be attributed to the small sample size we used, as no difference is present between segments 1 and 3 in the distal region, or between segments 7 and 9 in the proximal region of the same patterned gripper. Furthermore, in the individual imprint of a patterned gripper in Figure 9.5, the difference in colored-pixel count between segments 4 and 6 is small, and for the distal region (segments 1 vs. 3), the highest colored-pixel count is on the bottom

side (segment 3) of the pad, supporting that differences between the lateral segments are random.

One limitation of using this foil is that our gripper pads have smaller dimensions than the applications this foil is designed for. The foil consists of microcapsules that break when a stress threshold of 0.006 MPa is exceeded, resulting in coloring of the foil. Matching the foil color shade with a reference color sample is used to obtain accurate pressures on the foil [24]. As the dimensions of the gripper pad segments and the area of local stress concentrations are too small to determine color shades, we used a more qualitative approach of counting the number of colored pixels and refrained from reporting pinch forces generated by our grippers.

We observed in our measurements that sometimes, the tissue thickness exceeded the separation distance between the two jaws at the proximal end of the gripper. As a result, high pinch forces are present at the proximal end, and low pinch forces or no contact is present at the distal end of the pad. Such local pinch forces could be prevented by using slanted pads, or a prismatic joint movement, resulting in a parallel orientation of the two opposing pads. With parallel pads, a homogeneous distribution of pinch forces is expected, leading to higher gripping forces with lower local pinch forces.

The diameter of the gripper shaft is currently 10 mm, with the gripper tip, when closed, having a slightly larger diameter. In order to allow the use of this instrument in minimally invasive procedures, miniaturization of the instrument is necessary. Limitations of miniaturization are expected to primarily occur at the geometry of the joints of the gripper. The balance between high bendability and high recovery strength is delicate. We expect that, although the main functionality can be maintained, the exact geometry of the joints, especially the shape of the voids, will need optimization. It should be noted that the grasping performance of this gripper also strongly depends on the contact area between gripper and tissue, and thus on the area of the gripper pads. When scaling down the gripper design, the pad area can partially be maintained by using elongated the gripping jaws.

In future work, to make the gripper suitable for in vivo testing, to prevent exposure of the surgical area to CFF, the CFF needs to be fully embedded in the shaft of the instrument, without affecting its mechanical properties. Alternatively, it should be replaced with a fabric-like material with similar mechanical properties consisting of a single component (as opposed to numerous microscale fibers).

The lifespan of the gripper we present here is limited, as the materials the gripper is made of cannot undergo multiple sterilization cycles and joints will get fatigued after repeatable opening and closing. Therefore, we propose the use of the current gripper as a single-use instrument. From an economic perspective, single-use of the instrument is feasible, as 3D printing allows high repeatability and scaling up of manufacturing speed, and also the soft lithographic approach used for fabrication of the soft pads can be easily scaled up [25]. Alternatively, the platform instrument could be fabricated from a material that can be equipped with disposable soft pads and can be easily sterilized.

9.6. Conclusion

Here, we replaced the conventional metal forceps of surgical grippers with gripping pads with anisotropic stiffness. We did so to prevent force-related grasping errors such as slipping of the tissue as a result of too low pinch forces, or damaging of the tissue as a result of too high pinch forces. Soft pads with anisotropic mechanical properties were fabricated, where a low normal stiffness facilitates the generation of a high contact area with tissue, even under low pinch forces, and a high lateral stiffness facilitates preservation of the formed contact when forces in the lateral direction are applied. We found that the use of soft pads in a surgical gripper prototype resulted in a decrease of generated pinch forces on the tissue, while preserving the gripping performance of conventional metal forceps. The prototype gripper, including shaft, joints, and jaws, was fabricated using 3D printing and anisotropic soft pads were post-hoc implemented in the instrument. This modular approach potentially allows for variation of the design parameters of the instrument in future design iterations, thereby enabling a facile and effective optimization of the instrument for a range of application fields.

References

[1] G. Rateni, M. Cianchetti, G. Ciuti, A. Menciassi, and C. Laschi, *Design and development of a soft robotic gripper for manipulation in minimally invasive surgery: a proof of concept,* Meccanica **50**, 2855 (2015).

[2] T. R. Eubanks, R. H. Clements, D. Pohl, N. Williams, D. C. Schaad, S. Horgan, and C. Pellegrini, *An objective scoring system for laparoscopic cholecystectomy,* Journal of the American College of Surgeons **189**, 566 (1999).

[3] K. R. Catchpole, A. E. Giddings, M. Wilkinson, G. Hirst, T. Dale, and M. R. de Leval, *Improving patient safety by identifying latent failures in successful operations,* Surgery **142**, 102 (2007).

[4] E. Heijnsdijk, A. Pasdeloup, A. Van der Pijl, J. Dankelman, and D. Gouma, *The influence of force feedback and visual feedback in grasping tissue laparoscopicauy,* Surgical endoscopy **18**, 980 (2004).

[5] H. Visser, E. Heijnsdijk, J. Herder, and P. Pistecky, *Forces and displacements in colon surgery,* Surgical Endoscopy And Other Interventional Techniques **16**, 14263 (2002).

[6] J. Cartmill, A. Shakeshaft, W. Walsh, and C. Martin, *High pressures are generated at the tip of laparoscopic graspers,* Australian and New Zealand journal of surgery **69**, 127 (1999).

[7] S. De, *The Grasper-tissue Interface in Minimally Invasive Surgery: Stress and Acute Indicators of Injury* (2008).

[8] J. Bos, E. W. Doornebosch, J. G. Engbers, O. Nyhuis, and D. Dodou, *Methods for reducing peak pressure in laparoscopic grasping,* Proceedings of the Institution of Mechanical Engineers, Part H: Journal of Engineering in Medicine **227**, 1292 (2013).

[9] D. D. Marucci, J. A. Cartmill, C. J. Martin, and W. R. Walsh, *A compliant tip reduces the peak pressure of laparoscopic graspers,* ANZ journal of surgery **72**, 476 (2002).

[10] M. D. Bartlett, A. B. Croll, D. R. King, B. M. Paret, D. J. Irschick, and A. J. Crosby, *Looking beyond fibrillar features to scale gecko-like adhesion,* Advanced Materials **24**, 1078 (2012).

[11] P. van Assenbergh, M. Fokker, J. Langowski, J. van Esch, M. Kamperman, and D. Dodou, *Pull-off and friction forces of micropatterned elastomers on soft substrates: the effects of pattern length scale and stiffness,* Beilstein journal of nanotechnology **10**, 79 (2019).

[12] Z. He, C.-Y. Hui, B. Levrard, Y. Bai, and A. Jagota, *Strongly modulated friction of a film-terminated ridge-channel structure,* Scientific reports **6**, 1 (2016).

[13] J. Wang, L. Ma, W. Li, and Z. Zhou, *Safety of laparoscopic graspers with different configurations during liver tissue clamping,* Biosurface and Biotribology **4**, 50 (2018).

[14] E. Heijnsdijk, H. De Visser, J. Dankelman, and D. Gouma, *Slip and damage properties of jaws of laparoscopic graspers,* Surgical Endoscopy **18**, 974 (2004).

[15] H. Chen, L. Zhang, D. Zhang, P. Zhang, and Z. Han, *Bioinspired surface for surgical graspers based on the strong wet friction of tree frog toe pads,* ACS applied materials & interfaces **7**, 13987 (2015).

[16] H. Yamanaka, K. Makiyama, K. Osaka, M. Nagasaka, M. Ogata, T. Yamada, and Y. Kubota, *Measurement of the physical properties during laparoscopic surgery performed on pigs by using forceps with pressure sensors,* Advances in urology **2015** (2015).

[17] I. M. Koc, T. Eray, B. Sümer, and N. Cerci, *An active force controlled laparoscopic grasper by using a smart material actuation,* Tribology International **100**, 317 (2016).

[18] W. Li, Z. Jia, J. Wang, L. Shi, and Z. Zhou, *Friction behavior at minimally invasive grasper/liver tissue interface,* Tribology International **81**, 190 (2015).

[19] C. L. Grames, J. D. Tanner, B. D. Jensen, S. P. Magleby, J. R. Steger, and L. L. Howell, *A meso-scale rolling-contact gripping mechanism for robotic surgery,* in *International Design Engineering Technical Conferences and Computers and Information in Engineering Conference*, Vol. 57120 (American Society of Mechanical Engineers, 2015) p. V05AT08A034.

[20] F. Prabowo, A. L. Wing-Keung, and H. H. Shen, *Effect of curing temperature and cross-linker to pre-polymer ratio on the viscoelastic properties of a pdms elastomer,* in *Advanced Materials Research*, Vol. 1112 (Trans Tech Publ, 2015) pp. 410–413.

[21] E. Heijnsdijk, J. Dankelman, and D. Gouma, *Effectiveness of grasping and duration of clamping using laparoscopic graspers,* Surgical Endoscopy and other interventional Techniques **16**, 1329 (2002).

[22] J. Rosen, M. MacFarlane, C. Richards, B. Hannaford, and M. Sinanan, *Surgeon-tool force/torque signatures-evaluation of surgical skills in minimally invasive surgery,* in *Medicine meets virtual reality* (IOS Press, 1999) pp. 290–296.

[23] E. P. Westebring-van der Putten, J. J. van den Dobbelsteen, R. H. Goossens, J. J. Jakimowicz, and J. Dankelman, *Effect of laparoscopic grasper force transmission ratio on grasp control,* Surgical endoscopy **23**, 818 (2009).

[24] FUJIFILM Corporation, *Fujifilm's measurement film solution,* (2021), https://www.fujifilm.com/products/measurement_film/en/prescale/feature/.

[25] P. van Assenbergh, E. Meinders, J. Geraedts, and D. Dodou, *Nanostructure and microstructure fabrication: from desired properties to suitable processes,* Small **14**, 1703401 (2018).

10

Discussion

10.1. Main findings of this thesis

Original aim of the research

The aim of this thesis was to investigate whether using mechanical solutions, in combination with additive manufacturing technology, would enable the design of steerable surgical instruments while minimizing assembly time and device complexity. Analyzing both the mechanical and the 3D printing aspects, we can conclude that the combination of mechanical solutions with the implementation of additive manufacturing is an interesting pathway to follow for a new generation of steerable surgical instruments.

Real time snake-like control

The first part of this thesis tackled the control of a follow-the-leader (FTL) medical device. Chapter 2 gave an overview of the state-of-the-art of FTL medical devices. A classification has been created based on the three main functions of FTL devices: steering, propagation, and conservation. Most devices with cable-driven mechanisms to control the end-effector use an external actuation unit outside the shaft of the device and, therefore, the body of the patient. For the propagation of the motion, concentric tubes and alternating devices use a deploying propagation method where the proximal segment acts as a guide for the distal segments. Shifting propagation is instead used in devices where the entire device is part of the advancing movement. Different solutions have been found to memorize the shape of the steerable shaft. Even though software constraints are widely used, e.g., holding the tension of the actuation cables, hardware constraints, such as friction or geometrical lock mechanisms, represent a valid alternative, especially for mechanical solutions.

Therefore, in Chapter 3, we investigated how a programmable mechanical memory can control the FTL motion of a flexible shaft. We designed an on-demand adjustable memory mechanism called MemoBox based on geometrical locks. The mechanism guides the actuation cable displacement and creates an FTL motion of the shaft along multi-curved paths. Being an on-demand mechanism, implementing MemoBox into a steerable device gives the surgeon the possibility to adjust the followed path during the insertion and move the device back along the created path during retraction.

Additive manufacturing and compliant solutions

The second part of the thesis started by investigating the use of additive manufacturing in medical devices. Chapter 4 gave a comprehensive overview of the state-of-the-art of additively manufactured surgical and diagnostic instruments. The found devices vary in many aspects: clinical applications, used materials (usually polymer-based), and 3D print technologies, with a preference for material extrusion. The reasons behind the choice of using additive manufacturing are also various. Cost-effectiveness and possible customization represent two of the main motivations expressed. Additive manufacturing gives significant freedom in integrating complexity in the design and represents a powerful component of personalized medicine.

Chapter 5 investigated how the increase in design complexity of a single 3D printed component can lead to a significant design simplification of an entire multi-steerable laparoscopic instrument. We designed modular 3D printed compliant segments to achieve steerability of the shaft and easy assembly. We fabricated a prototype of

the resulting HelicoFlex into two main parts: a ten degrees of freedom shaft and a handle with serial control. We printed the shaft without support to avoid debris in the mechanism. Additive manufacturing highly decreases the number of components and reduces the assembly time to only the cable placement. In the HelicoFlex, each segment of the handle actuates a corresponding segment of the shaft using four parallel cables (parallel configuration). A similar motion of the multi-steerable shaft can be achieved by arranging cables in a different configuration, combining them in a helical and parallel manner (multi configuration).

Chapter 6 investigated which of the two cable configurations has a steeper learning curve, a lower workload, and the user's preference. We performed a comparative analysis with 12 participants. The task consisted of maneuvering the two instruments (with parallel and multi configurations) to reach the targets in the dedicated simulator. The test showed no significant difference between the learning curves of the two instruments for the task performance time. However, participants experienced a significantly lower workload for the parallel configuration as it offers the possibility of independent, more precise steering of the most distal segment of the shaft.

In Chapter 4, we found out that one of the main reasons for using additive manufacturing in the medical field is possible customization. In Chapter 7, we investigated how additive manufacturing can promote the production of customized steerable instruments with easy assembly. The result is a steerable instrument in which the increase in shape complexity of a single element leads to a simplification of the final design itself. We integrated the compliant segment designed in Chapter 5 into a novel surgical steerable laparoscopic gripper. We designed a pistol grip handle with a joystick to control the steering. The entire design contains only five structural components: the gripper and the steerable shaft printed as one element, and the handle, printed out of four elements. The combination of compliant joints and snap-fit connectors simplifies the assembly of the instrument, whereas the CAD model of the handle allows customization towards the surgical needs.

Surgical grippers

In the third part of the thesis, we investigated the possibility of 3D printing highly complex end-effectors for the repair of chordae tendineae in the heart to solve mitral valve regurgitation (Chapter 8) and for a gentle grip with soft tissues (Chapter 9). For the repair of chordae tendineae, we designed a double grip system to recreate a connection between the leaflet of the valve and the apex of the heart. For the gentle grip, we integrated soft adhesive pads with and without sub-surface micropatterns on the gripper designed in Chapter 7. The adhesive pads were made of polydimethylsiloxane (PDMS) and carbon fibers to maximize the contact area with the tissue without creating local high forces and avoiding slippage during gripping.

Main overall findings

This thesis shows that the use of additive manufacturing, in combination with mechanical solutions, paves the way for a new generation of medical devices where the complexity of a single component can significantly simplify the final design without limiting its functionalities but rather enhancing them. Moreover, the implementation

of additive manufacturing in the fabrication of medical devices lays the foundation for patient- and surgeon-specific tools where the device can be adapted and customized to specific individual needs.

10.2. Limitations of the research

Looking at our 3D printed compliant shaft designs and evaluations, a number of limitations can still be identified. In Chapter 5, we performed preliminary studies on the external forces our steerable compliant shaft was able to withstand. The results showed that due to the low bending stiffness of the shaft, those forces were relatively low as compared to devices in which the steerable shaft is designed as a chain of traditional rigid joints. In fact, in a chain of rigid joints, the stiffness of the mechanism increases by increasing the cable tension, whereas, in compliant mechanisms, this method is less effective and may cause unwanted compression or buckling of the structure. Our test highlighted the trade-off between stability and low bending stiffness. Possible solutions could be variable stiffness mechanisms wherein two phases, one rigid and one flexible, alternate depending on the surgeon's needs to increase the stability under external forces while keeping the bending stiffness low during the motion [1]. An improved fine-tuning of the compliant segment dimensions could be an alternative to reach a better balance between stiffness and flexibility. For this purpose, a finite element analysis (FEA) would be interesting to carry out in order to simulate how compliant segments with different backbone radii or helicoids would affect the behavior of the segment under applied loads.

Another significant improvement to the compliant steerable instrument, as proposed in Chapter 5, would be a locking mechanism to fixate the end-effector position without continuously applying forces at the handle. Needing both hands to control one instrument during a minimally invasive procedure is highly unacceptable as the surgeon generally needs to control two instruments at the same time. A possible solution is the one proposed by Gerboni *et al.* in the HelixFlex, where cables are individually clamped, keeping the shape of the handle and the shaft simultaneously locked [2]. Alternatives are the solution in which a spring-based mechanism fixes all cables at once proposed by Ali [3] or a mechanism that automatically locks the instrument position once the steering joystick is released, as proposed in Chapter 7.

In Chapter 6, we carried out an experiment with novice human subjects to observe the actual functionality of the 3D printed steerable instrument proposed in Chapter 5 with different cable configurations. However, we did not have the chance to test and compare possible differences in the performance of novices and expert surgeons. Therefore, an interesting step forward would be to involve surgeons in a scenario that is closer to clinical practice. Similar end-user tests could be performed for the instrument developed in Chapter 7.

10.3. Trends, challenges, and developments

AM technologies and materials

In this work, we have shown the potential of additive manufacturing in the medical instrumentation industry that can lead the way to new approaches from both the engineering and the medical sides. However, additive manufacturing is currently limited by its state-of-the-art. In this section, we will discuss interesting challenges, trends, and developments that might help to overcome these limitations in the future.

Chapter 5 presented the first fully 3D printed steerable instruments able to follow a double-curve path. However, the device was produced using Digital Light Processing (DLP) printing technology with a non-biocompatible resin. A logical step would be the production of the same device in a biocompatible resin. By using another Vat photopolymerization technology, Stereolithography (SLA) with a Form 3B printer (Formlabs), we were able to test a number of the available biocompatible materials. We were able to print the helicoid structure presented in Chapter 5 with the biocompatible Model resin provided by Formlabs, (Figure 10.1). However, the material was too brittle for fabricating the prototype, and the samples broke after a few bending repetitions. Therefore, in Chapter 7, we decided to use non-biocompatible materials to print the 3D-GriP prototype. Different from the available biocompatible materials, the used resins showed high elongation at break, which allowed us to print compliant joints, using spring-back properties in quickly bending and returning to the original shape, which was exploited to integrate a spring in the joystick without the need for an additional assembly step.

Last year, new resins were launched and approved by the FDA for medical use. The interest in biocompatible resins with advanced engineering properties pushes companies and researchers to explore new materials. In recent years, with an emerging interest in soft robotics, the use of PU-based materials, PDMS-based materials, and hydrogel in 3D printing technologies, such as SLA or Direct Ink Writing (DIW), has grown due to their biocompatible, flexible, and stretchable properties [4]. Exploring new biocompatible 3D printable materials for steerable surgical devices would be a logical step to take, together with new advancements in 3D printing technologies to print fast and with high resolution.

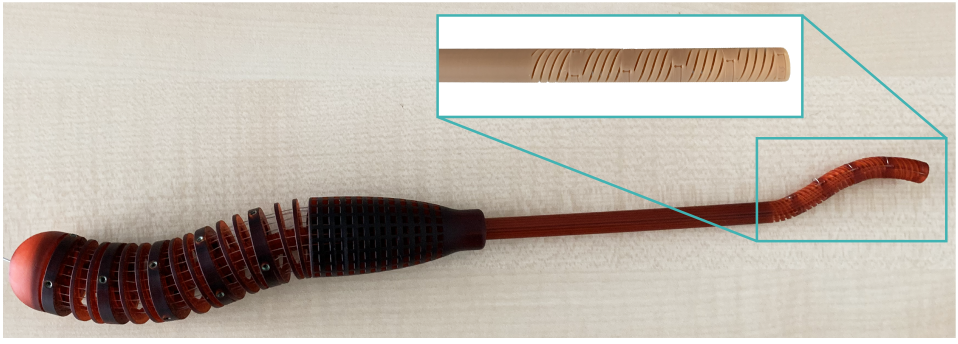

Figure 10.1: HelixFlex. In the close-up the steerable shaft printed with biocompatible Model resin from Formlabs.

The speed of the 3D printing technology becomes highly important when customization of the medical device is a priority. In Chapter 7, we presented a surgical device that can be modified depending on the procedure and the surgeon's needs. However, in our experience, printers are still relatively slow, and the speed decreases when the resolution increases. For instance, the printing process of the handgrip and the end-effector of the 3D-GriP instrument lasted almost two days. New technologies such as Continuous Liquid Interface Production (CLIP) are tackling the problem [5]. CLIP is a Vat photopolymerization technology that exploits oxygen properties to inhibit photopolymerization allowing the build platform to continuously rise without stops in between the layers [6]. The process is 25 to 100 times faster than the common stereolithography technology [7]. The increase in printing speed would allow the surgeon to print the desired tools right before the procedure with specific characteristics tailored for that particular surgery.

Sterilization

In Parts II and III of this thesis, we experimented with additive manufacturing for the fabrication of steerable surgical instruments. Additive manufacturing showed great potential in terms of design freedom, part complexity, and quick feedback for fine-tuning during the design process. Yet, additive manufacturing in a medical scenario still has some crucial aspects to address, such as sterilization. According to the Centers for Disease Control and Prevention, there are many sterilization methods for medical instruments, such as autoclave, hydrogen peroxide gas plasma, ethylene oxide gas, γ -irradiation, and UV sterilization [8]. However, when sterilizing 3D printed instruments, some of these techniques cannot be used due to possible changes in the material properties under certain temperatures or conditions. For example, devices that have been printed in polylactic acid (PLA) cannot undergo the autoclave process due to the low glass transition temperature of PLA that cannot withstand steam sterilization at 120-130 degrees [9].

The devices proposed in this thesis are all manufactured using Vat photopolymerization technology. Vat photopolymerization is based on UV light to cure the resin material layer by layer. Therefore, the use of UV light as a sterilization method might change the properties of the device. Sterilization techniques such as autoclave, γ -irradiation, and ethylene oxide gas, can represent an alternative considering the studies performed on the new materials from Formlabs and EnvisionTEC (companies that produce the printers used in this thesis). A possible solution would also be the use of the 3D printing fabrication process itself as sterilization method. For example, if the fabrication would be in a closed chamber previously sterilized, the use of high temperatures as in the FDM technology, or UV-light in Vat photopolymerization, would lead to the production of pieces directly sterilized by the 3D print process.

Another interesting aspect to take into account is the use of the device in a disposable or reusable manner. If the purpose is to have a disposable device, the sterilization cycle would be limited to one. Therefore, sterilization might be integrated into the post-processing phase after washing and curing or in the 3D printed fabrication process (as mentioned above).

One step fabrication

Additive manufacturing has given the opportunity of printing parts that were difficult, if not impossible, to produce with conventional manufacturing technology. The possibility of printing parts with a complex geometry has paved the way for a new trend in robotics and medical device manufacture: devices without the need for parts assembly (Figure 10.2). Some results have already been achieved in soft robotics to fabricate soft single-part actuators [4, 10] as well as in non-assembly mechanisms [11, 12]. Most of the existing steerable medical instruments are based on tendon-driven mechanisms in which tendons are used to guide and control the end-effector of the device. The devices proposed in Chapters 5 and 7 are all based on tendon-driven mechanisms that allow the control of a large number of degrees of freedom while simplifying the assembly process and omitting the need for additional parts to fix the cables. Finding solutions to directly integrate tendons or other actuation mechanisms in these 3D printed components while keeping the same instrument functionalities would simplify the assembly process even more.

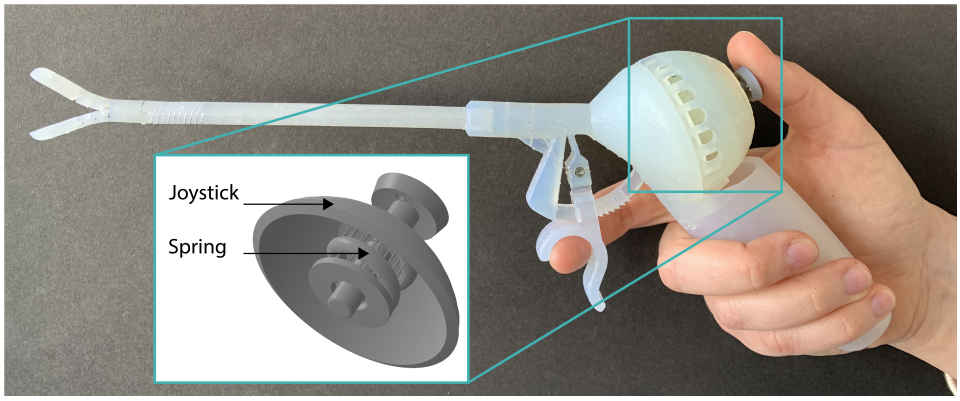

Figure 10.2: 3D-Grip with a close-up of the joystick and the spring. The integration of the spring in the joystick as a single element is an example of a non-assembly mechanism (Chapter 7).

10.4. Conclusion

In the field of minimally invasive surgery, continuous progress is achieved to reduce the invasiveness of the procedure and minimize the trauma for the patient. Follow-the-leader motion into flexible surgical devices allows the instrument to pass through tortuous anatomical paths accessing difficult anatomic areas and avoiding sensitive structures. Still, despite these advantages, these types of devices come with great structural complexity, to the extent that the assembly could be time-consuming, or excessively difficult. To tackle this problem, in this thesis we leveraged the potential of additive manufacturing to design new mechanical solutions for steerable instruments, to minimize the device complexity and assembly time.

We first provided a comprehensive review of the state-of-the-art of follow-the-leader technology to determine the strategies used for steering, memorizing, and

propagating the instrument's shape in the medical field. Finding that mechanical solutions are a viable alternative to electronic devices, we designed a new programmable memory shape mechanism to investigate the potential of mechanical solutions for follow-the-leader medical devices. We successfully built and tested a new surgical instrument, with a path programmable in real-time, which minimizes the assembly components as compared to the previous solutions proposed in the literature. In the second part of the thesis, we tackled the problem of the complex assembly of multi-steerable medical device complex assembly by employing additive manufacturing to reduce the number of device components. We successfully designed a new multi-steerable surgical instrument composed of only two main parts with multiple integrated functionalities. The device is based on a cable-driven mechanism, that was tested to properly function in two different cable configurations. Additionally, we expanded the functionality of the device by integrating a grasper as an end effector, creating a fully 3D printed steerable grasper. In the last part of this thesis, we 3D printed graspers with various functionalities and complex designs, which could potentially be integrated into steerable devices in future works.

In conclusion: the potential of additive manufacturing technology, in combination with the versatility of mechanical solutions, is changing the paradigm of steerable surgical devices, facilitating the design process and their fabrication. While polymer-based 3D printed instruments have the limitation of being less durable, they offer a viable solution to customization and excessive device complexity. We hope our work will inspire future researchers, involved in the design of surgical devices, to further investigate 3D printed solutions that will ultimately benefit surgeons and, more importantly, people's lives.

References

[1] L. Blanc, A. Delchambre, and P. Lambert, *Flexible medical devices: Review of controllable stiffness solutions,* Actuators **6**, 23 (2017).

[2] G. Gerboni, P. W. J. Henselmans, E. A. Arkenbout, W. R. van Furth, and P. Breedveld, *HelixFlex: bioinspired maneuverable instrument for skull base surgery,* Bioinspiration & biomimetics **10**, 66013 (2015).

[3] A. Ali, A. Sakes, E. A. Arkenbout, P. Henselmans, R. van Starkenburg, T. Szili-Torok, and P. Breedveld, *Catheter steering in interventional cardiology: Mechanical analysis and novel solution,* Proceedings of the Institution of Mechanical Engineers, Part H: Journal of Engineering in Medicine **233**, 1207 (2019).

[4] E. Sachyani Keneth, A. Kamyshny, M. Totaro, L. Beccai, and S. Magdassi, *3D Printing Materials for Soft Robotics,* Advanced Materials **33**, 2003387 (2021).

[5] J. R. Tumbleston, D. Shirvanyants, N. Ermoshkin, R. Janusziewicz, A. R. Johnson, D. Kelly, K. Chen, R. Pinschmidt, J. P. Rolland, A. Ermoshkin, *et al.*, *Continuous liquid interface production of 3d objects,* Science **347**, 1349 (2015).

[6] I. Gibson, D. W. Rosen, B. Stucker, and M. Khorasani, *Additive manufacturing technologies*, Vol. 17 (Springer, 2021).

[7] Carbon Inc., *Carbon3D introduces CLIP, breakthrough technology for layerless 3D printing,* (2015), https://www.carbon3d.com/news/press-releases/carbon3d-introduces-clip-breakthrough-technology-for-layerless-3d-printing/.

[8] W. A. W. A. Rutala 1948- and D. J. D. J. Weber 1951-, *Guideline for disinfection and sterilization in healthcare facilities, 2008,* .

[9] V. R. Sastri, *Plastics in medical devices: properties, requirements, and applications* (William Andrew, 2013).

[10] M. Schaffner, J. A. Faber, L. Pianegonda, P. A. Rühs, F. Coulter, and A. R. Studart, *3D printing of robotic soft actuators with programmable bioinspired architectures,* Nature Communications **9**, 878 (2018).

[11] C. Mavroidis, K. J. DeLaurentis, J. Won, and M. Alam, *Fabrication of Non-Assembly Mechanisms and Robotic Systems Using Rapid Prototyping ,* Journal of Mechanical Design **123**, 516 (2000).

[12] K. Lussenburg, A. Sakes, and P. Breedveld, *Design of non-assembly mechanisms: A state-of-the-art review,* Additive Manufacturing , 101846 (2021).

Acknowledgements

At the end of my work, this is the most difficult chapter for me to write. Collecting data, analysing results, writing articles required passion, patience, and dedication. However, this thesis represents also a rich journey from a human point of view. So, I want to thank all of the people without whom this work would have not been possible.

I want to start thanking my supervisor, Paul, for his inspirational mentorship and his staggering brilliance when it comes to device design. Also, I want to thank Gerwin for his co-supervision, constant availability, and punctual feedback. A warm acknowledgment also goes to the members of the committee, Prof. dr. J. Dankelman, Prof. dr. M. van der Elst, Prof. dr. ir. R.H.M Goossens, Prof.dr.ir. J.L. Herder, and Dr. ir. E. van der Poorten who have taken the time to read and provide insightful comments on my work. I would also like to take this occasion to thank other inspiring professors that I have collaborated with along the way that took me here: Prof. dr. Arianna Menciassi, without whom I would have never landed in Delft in the first place, Dr. Dimitra Dodou, and Dr. John van den Dobbelsteen for their collaboration to some of the works published in the thesis.

I feel lucky that I had the possibility to perform my work in a great and dynamic department such as BME, made of enthusiastic and memorable characters. I want to start thanking Kirsten, without whom part of this work would have not seen the light. You have been a tremendous colleague, and more importantly, a very good friend. I will proceed with further acknowledging the other amazing members of the BITE team, starting from Marta, Awaz, Paul, Peter, and Fabian, for the fruitful collaboration and the good times working together. Also, a big thank you to Aimée, Juan, Merle, Jette, and Esther for creating a friendly atmosphere to find at work every morning. I want to thank my office mates: Bob for being such a great help in some dark moments; Steve, for always offering a smile and a positive vibe, no matter the weather; and Ingmar, my excellent fellow in this journey called Ph.D. Moving out from the office, a great thanks goes to my next-door amazing buddies: Françoise, for being the sparkling glue of the social life in the department and keeping her house always open to me; Sebastien, for always listening with a warm and welcoming smile to my complaints at the end of those days that were harder than others; and Niko, that brilliant and unsuspected ingredient that turns the recipe into an unforgivable dish. Moving down a couple of floors, I realize how my social life in the department would have not been the same without the amazing time I had with the people from the fish tank: Pier, a great friend, always listening and speaking only the right, Mauricio, Katerina, Judith, John, Chun-Feng, for putting color to my memories in Delft. A special thanks also to Helda, Jiahui, Mahdiyeh, Mahya, Marike, Pedro, Shahram, Teunis, Yageng, Michelle, Sander, Mohammed, Nazli, Eline, and Khashayar.

I would like also to acknowledge the work of Mirjam, Angelique, Sabrina, and Mar-

jolijn, for being the oil that made operations in our department smooth. Speaking about people without whom everything we did would have just remained an idea, it is my duty to acknowledge all the people working at DEMO, with a particularly warm special thanks to Remi and David, who, with their masterful skills and inextinguishable can-do attitude, brought to life also my wildest and most complicated designs. Outside of work, I have been lucky to find the brotherly love of a one-in-a-million group of friends. I would like to thank them properly, one by one, starting from Zeno: thanks for choosing me (the second time I applied) to be part of the Dojo. It's been the start of the journey together, of which I am always very grateful. Teo, thank you for being such a chill, patient, and warm friend who always infused his positive vibe to the rest of the company. Ale, thanks for showing us how to be brave in life: I wish your dreams come true, as you deserve it. Anna, for your inspirational and silent resilience and for being my only friend I can trust blindly when it comes to organizing holidays together. Also, thank you Federica for bringing a note of lightness and a passion for Prosecco to the team.

Also, I would like to acknowledge the good time I had with the BN team, with a special mention to the cooking mates: Becca and Jochem, Tony and Paola, Alberto and Mireia, whose lovely company kept us lively also during the dark times of pandemic.

Anche se a distanza, anche se divisi da ore di aereo, e anche esplorando nuove strade separati, le poche ore all'anno trascorse con gli amici di sempre sono state fondamentali in tutti questi anni: Baba, Talla, Vio, Claudia, e Mari, mi fate sentire a casa in qualunque posto voi siate. Chiara, Chiara, Giulia, Giulia, Virgi, Miriam, e Michela: per dimostrare che il tempo non ha effetto su alcune cose, quelle importanti.

Per ultimi, ma certamente non ultimi, voglio ringraziare i membri della mia famiglia per il loro costante amore e supporto: Nonno Giovani, per dimostrarmi come si può essere intellettualmente giovani ed entusiasti ad ogni età; Nonna Costanza per essere il pilastro fondante della famiglia Culmone; e Nonna Antonia, per avermi cresciuta. Giovi, per la non apparente, ma sempreverde e mal nascosta sensibilità e affetto che mi dimostra. Infine, mamma e papà, per essere stati una figura di ispirazione, supporto, e silente amore tutta la mia vita.

Ah quasi dimenticavo: grazie Fede ;)

Curriculum Vitae

Costanza Culmone

11-06-1990 Born in Tolentino, Italy.

Work Experience

2021–Present
Development Engineer
Sensors and Disposables Unit, Sentec AG, Therwil, Switzerland

2019–2021
Ph.D. Council Member
Delft University of Technology, Delft, The Netherlands
Faculty of Mechanical, Maritime, and Material Engineering (3mE)

2015–2016
Master Thesis Traineeship Erasmus+ Scholarship
Delft University of Technology, Delft, The Netherlands
Department of BioMechanical Engineering,
BioInspired Technology Group (BITE)

2015
Internship
Delft University of Technology, Delft, The Netherlands
Department of BioMechanical Engineering,
Minimally Invasive Surgery and International Techniques (MISIT Lab)

Education

2017–2022
Ph.D. BioMechanical Engineering
Delft University of Technology, Delft, The Netherlands
Department of BioMechanical Engineering,
BioInspired Technology Group (BITE)

2013–2016
Master in Biomedical Engineering
University of Pisa, Pisa, Italy

2009–2013
Bachelor in Biomedical Engineering
University of Pisa, Pisa, Italy

2003–2009
High School, Liceo Classico F. Filelfo
Tolentino, Italy

List of Publications

Publications part of this thesis

- **C. Culmone**, R. van Starkenburg, G. Smit, P. Breedveld, *Comparison of two cable configurations in 3D printed steerable instruments for Minimally Invasive Surgery*, submitted, (2022).
- **C. Culmone**, D. J. Jager, P. Breedveld, *MemoBox: A Mechanical Follow-the-Leader system for Minimally Invasive Surgery*, accepted, Frontiers In Medical Technology, (2022).
- **C. Culmone**, K. Lussenburg, J. Alkemade, G. Smit, A. Sakes P. Breedveld, *SAMPLE: A Fully 3D Printed Steerable Instrument for Minimally Invasive Surgery*, Materials, **14.24**, 7910, (2021).
- **C. Culmone**, S. F. Yikilmaz, F. Trauzettel, R. I. B. van Starkenburg, P. Breedveld, *Follow-The-Leader Mechanisms in Medical Devices: A Review on Scientific and Patent Literature*, IEEE Reviews in Biomedical Engineering, (2021).
- P. van Assenbergh,**C. Culmone**, P. Breedveld, D. Dodou, *Implementation of anisotropic soft pads in a surgical gripper for secure and gentle grip on vulnerable tissues*, Proceedings of the Institution of Mechanical Engineers, Part H: Journal of Engineering in Medicine, **235(3)**,255-263 (2021).
- **C. Culmone**, P. W. J. Henselmans, R. I. B. van Starkenburg, P. Breedveld, *Exploring non-assembly 3D printing for novel compliant surgical devices*, PLOS ONE, **15(5)**, e0232952 (2020).
- **C. Culmone**, G. Smit, P. Breedveld, *Additive manufacturing of medical instruments: A state-of-the-art review*, Additive Manufacturing **27**, 461–473 (2019).
- **C. Culmone**, A. Ali, M. Scali, A. Menciassi, P. Breedveld, *ChoRe: A device for transcatheter chordae tendineae repair*, Proceedings of the Institution of Mechanical Engineers, Part H: Journal of Engineering in Medicine, **233(7)**, 712–722 (2019).

Other publications

- I. De Falco, **C. Culmone**, A. Menciassi, J. Dankelman, J. J. van Den Dobbelsteen, *A variable stiffness mechanism for steerable percutaneous instruments: integration in a needle*, Med Biol Eng Comput **56**, 2185–-2199 (2018).
- A. Sendrowicz, M. Scali, **C. Culmone**, P. Breedveld, *Surgical drilling of curved holes in bone – a patent review*, Expert Review of Medical Devices **16:4**, 287–298 (2019).
- P. W. J. Henselmans, **C. Culmone**, D. J. Jager, R. I. B. van Starkenburg, P. Breedveld, *The MemoFlex II, a non-robotic approach to follow-the-leader motion of a snake-like instrument for surgery using four predetermined physical tracks*, Medical Engineering & Physics, **86**, 86–95 (2020).

International Conferences

- **C. Culmone**, P. W. J. Henselmans, R. I. B. van Starkenburg, P. Breedveld, *Towards Non-assembly 3D Printing for Multi-Steerable Surgical Devices*, 32th International Conference of Society for Medical innovation and Technology (SMIT). 3-10 December 2020, On-line (Oral presentation).
- **C. Culmone**, L. Bazuin, M. Scali, P. Breedveld, *Towards Non-Assembly 3D Printed Medical Instruments*, Health Innovative. 23 January 2020, Delft, The Netherlands (Poster).
- **C. Culmone**, P. W. J. Henselmans, R. I. B. van Starkenburg, P. Breedveld, *Compliant 3D Printed Surgical Instruments*, Medical 3D-printing and Innovative Technologies. 6-7 December 2019, Vienna, Austria (Oral presentation).
- **C. Culmone**, L. Bazuin, M. Scali, P. Breedveld, *Towards Non-Assembly 3D Printed Medical Instruments*, 41st Conference of the IEEE Engineering in Medicine and Biology Society. 23-27 July 2019, Berlin, Germany (Poster).
- **C. Culmone**, P. W. J. Henselmans, R. I. B. van Starkenburg, P. Breedveld, *3D Printing of Highly Complex Medical Instruments*, 7th Dutch Bio-Medical Engineering Conference. 24-25 January 2019, Egmond aan Zee, The Netherlands (Oral presentation).
- **C. Culmone**, P. W. J. Henselmans, R. I. B. van Starkenburg, P. Breedveld, *3D Printing of Highly Complex Medical Instruments*, 30th International Conference of Society for Medical innovation and Technology (SMIT). 8-9 November 2018, Seoul, South Korea (Oral presentation).
- **C. Culmone**, I. De Falco, A. Menciassi, J. Dankelman, J. J. van Den Dobbelsteen, *A variable stiffness mechanism for minimally invasive surgical needles*,The Hamlyn Symposium on Medical Robotics. 25-28 June 2017 London, United Kingdom (Oral presentation).